Ralf Heinrich *Editor*

AeroStruct: Enable and Learn How to Integrate Flexibility in Design

Contributions to the Closing Symposium of the German Research Initiative AeroStruct, October 13–14, 2015, Braunschweig, Germany

Springer

Notes on Numerical Fluid Mechanics and Multidisciplinary Design

Volume 138

Notes on Numerical Fluid Mechanics and Multidisciplinary Design publishes state-of-art methods (including high performance methods) for numerical fluid mechanics, numerical simulation and multidisciplinary design optimization. The series includes proceedings of specialized conferences and workshops, as well as relevant project reports and monographs.

Ralf Heinrich

Editor

AeroStruct: Enable and Learn How to Integrate Flexibility in Design

Contributions to the Closing Symposium of the German Research Initiative AeroStruct, October 13–14, 2015, Braunschweig, Germany

 Springer

Editor
Ralf Heinrich
DLR, Institute of Aerodynamics and Flow
   Technology
Braunschweig
Germany

Preface

Within Europe's Aviation Vision, ambitious goals have been set for air traffic of the next decades. These include a reduction of emissions by 75% and a decrease of the perceived external noise by 65% relative to a typical aircraft in 2000. Continuous improvement of conventional technologies will not be sufficient to achieve these goals, however, a technological leap forward is required. Combined efforts of industry and academia will be necessary to harness revolutionary technologies and entirely new configurations for use in future aircraft design and development. This will require a significant investment in enhancing the capabilities and tools of numerical simulation, which has become a key technology in recent years. In current aircraft design cycles, the structural layout and aerodynamic design is usually done separately by different groups, leading to sequential and error prone processes requiring a huge amount of communication and "hand work". A key challenge is to combine the structural layout and the aerodynamic design in integrated process chains taking into account the interaction of both disciplines in an early stage of the design cycle, making use of high-fidelity methods.

In order to meet future requirements of German aircraft industry, the German research initiative AeroStruct was set up within the frame of the fourth aviation program of the German Federal Government. The initiative was coordinated by the German Aerospace Center (DLR) and promoted collaboration between the aircraft industry and academia. An essential goal of the project was the development of an integrated multidisciplinary simulation environment for analysis and optimization of aircraft using high-fidelity methods. In contrast to previous projects the process chains to be developed shall run with a high level of automatism. Of special importance is a description of aircraft geometry independent from the disciplines involved, an automated CFD mesh generation and an automated structure model generation including a sizing process. As common software platform the FlowSimulator environment was used.

The software and process chains developed was be demonstrated by the industrial partners and DLR using test cases of relevance for industry. Eg., DLR used the software environment for the design of a forward swept wing of highest aerodynamic quality making use of the potential of aeroelastic tailoring.

The reader will find separate chapters for each of the four industrial use cases ForSWING (DLR), FlexCraft (Airbus), OPTIMALE (Airbus Defence and Space) and DIMENSyon-P (Rolls-Ryce). The fifth chapter is dedicated to technological development work related to all use cases. The important results of this 3 year initiative published in this book were also presented during the AeroStruct closing symposium, which took place at the DLR in Braunschweig, Germany, on 13–14th October 2015.

Braunschweig, Germany   Ralf Heinrich
July 2016

Acknowledgements

Contents

Part I
Use-Case FORSwing

Chapter 1
Integrated Process Chain for Aerostructural Wing Optimization and Application to an NLF Forward Swept Composite Wing

Tobias Wunderlich and Lars Reimer

Abstract   This contribution introduces an integrated process chain for aerostructural wing optimization based on high fidelity simulation methods. The architecture of this process chain enables two of the most promising future technologies in commercial aircraft design in the context of multidisciplinary design optimization (MDO). These technologies are natural laminar flow (NLF) and aeroelastic tailoring using carbon fiber reinforced plastics (CFRP). With this new approach the application of MDO to an NLF forward swept composite wing will be possible. The main feature of the process chain is the hierarchical decomposition of the optimization problem into two levels. On the highest level the wing planform including twist and airfoil thickness distributions as well as the orthotropy direction of the composite structure will be optimized. The lower optimization level includes the wing box sizing for essential load cases considering the static aeroelastic deformations. Additionally, the airfoil shapes are transferred from a given NLF wing design. The natural laminar flow is considered by prescribing laminar-turbulent transition locations. Results of wing design studies and a wing optimization using the process chain are presented for a forward swept wing aircraft configuration. The wing optimization with 12 design parameters shows a fuel burn reduction in the order of 9% for the design mission.

T. Wunderlich (✉) · L. Reimer
German Aerospace Center, Institute of Aerodynamics and Flow Technology,
Lilienthalplatz 7, 38108 Braunschweig, Germany
e-mail: tobias.wunderlich@dlr.de

L. Reimer
e-mail: lars.reimer@dlr.de

1.1 Introduction

The environmental impact of aviation increases with the rapid growth of air travel and transport. For this reason efficiency of future air transport must be improved significantly. The research and development of future transport aircraft have to meet this challenge. A Strategic Research Agenda has been developed by the Advisory Council for Aeronautics Research in Europe (ACARE). The goals of the European aeronautical research have been formulated in this research agenda and have been published in the "Vision 2020" [1, 2] and the "Flightpath 2050" [3]. In order to protect the environment and to preserve the energy supply a 50% reduction of the CO_2 emissions per passenger kilometer has been requested for the year 2020 based on the values of the year 2000. The airframe contribution should be in the order of 20–25% in terms of fuel consumption reduction.

To achieve these challenging goals the development timescales for new technologies including new aircraft concepts have to be reduced significantly. For the assessment of an aircraft configuration it is essential to consider all relevant disciplines and their interactions on overall aircraft level. The consideration of new technologies and aircraft concepts requires a physics based approach because no statistics are available anymore. In order to represent the physics in a realistic manner, accurate simulation tools have to be applied. With increasing accuracy of the disciplinary simulations the geometrical description has to be improved, too. This inherently leads to increased computational costs. The development of accurate and fast numerical simulation and optimization processes is getting more and more important. In this context new capabilities in the areas of process architecture, program interfaces, parallelization and the usage of high performance computing (HPC) are required.

The combination of increasing computer resources and advanced numerical simulation tools enables the accurate prediction of flight performance of a transport aircraft configuration [4]. The use of these high fidelity simulation programs for aerodynamic design and optimization has been demonstrated in the MEGADESIGN project (Kroll et al. [5–8] and Gauger [9]).

State of the art high fidelity analysis methods already routinely include fluid-structure coupling of the aircraft wing for a given structural model. The consideration of fluid-structure interactions gets more important for the accurate performance and load prediction of highly flexible wings.

Improvements in automation and coupling of accurate simulation methods in combination with advances in numerical optimization strategies lead to the emergence of MDO based on high fidelity methods.

Multidisciplinary wing optimizations for realistic aircraft configurations under consideration of static aeroelasticity have been shown for example by Piperni et al. [10] for a large business jet and by Chiba et al. [11] for a regional jet.

The challenge in using MDO based on highly accurate methods is the large number of design parameters and the increased computing effort. To overcome this issue, the adjoint method enables the efficient calculation of the flow variable gradients as a function of the design parameters for gradient based optimizations. The adjoint

method was used by Jameson, Leoviriyakit and Shankaran [12] for a gradient based multidisciplinary wing optimization with fluid-structure coupling. Up-to-date applications of the adjoint approach for multidisciplinary wing optimization have been shown in the publications of Kenway and Martins [13], Kenway, Kennedy and Martins [14] and Liem, Kenway and Martins [15]. These publications show that the gradient based optimization using the adjoint approach is an adequate method for multidisciplinary wing optimization with high fidelity simulation programs and a large number of design parameters.

In this contribution an alternative MDO approach is introduced for cases in which gradients cannot be computed efficiently for all relevant disciplines. This applies particularly to cases which involve laminar-turbulent transition prescription and structural sizing of composite structures using proprietary codes. Furthermore, a certain degree of flexibility in the process architecture and optimization strategy is desired. Especially the option to use optimization strategies seeking for the global optimum is important.

The application of MDO to new aircraft concepts and technologies using high fidelity methods is very promising. By using MDO an accurate comparison between optimal solutions based on conventional and new technologies will be possible. This facilitates an adequate assessment of new concepts and technologies on the one hand. On the other hand, this requires the availability of physics-based simulation models and efficient programs with adequate interfaces.

To improve the aerodynamic efficiency of commercial aircraft, modern technologies for drag reduction have to be applied. A short overview of aerodynamic wing design and corresponding technologies is given for example by Horstmann and Streit [16]. One of the most promising drag reduction technologies is laminar flow control (LFC). The potential of this technology for drag reduction of commercial aircraft has been described by Schrauf [17] and Green [18] for example.

In 1979, Boeing already investigated the benefit of NLF on large transport aircraft [19]. This study shows that the aircraft having an NLF wing design was not competitive against a turbulent wing design taking the top level aircraft requirements as a basis for comparison. In the DLR project LamAiR [20], however, the concept of forward sweep for laminar wings as proposed by Redeker and Wichmann [21] shows significant potential for efficiency improvements. In this project an aerostructural wing design of a forward swept wing having NLF and a composite structure including aeroelastic tailoring has been performed. The results have been published by Kruse et al. [22].

The work on aeroelastic tailoring is summarized by Shirk et al. [23]. In this publication aeroelastic tailoring is described as

> ...embodiment of directional stiffness into an aircraft structural design to control aeroelastic deformation, static or dynamic, in such a fashion as to affect the aerodynamic and structural performance of that aircraft in a beneficial way.

Additionally, the advantages of composite materials on forward swept wings are explained. Tailoring the primary stiffness direction relative to the structural reference axis introduces a bend-twist-coupling that can be used to counteract the susceptibil-

ity of forward swept wings to static divergence. Dähne et al. [24] investigated the influence of aeroelastically tailored composites on structural mass. In this study an automated structural sizing process has been applied with the simplification that the aerodynamic loads remained fixed.

In striving for the capability to assess new wing technologies by development and application of an integrated process chain has been one of the main topics in DLR's contribution to the LuFo IV joint research project AeroStruct. In the scope of the project an integrated process chain for aerostructural wing optimization considering new wing technologies such as forward sweep, NLF, composite materials and aeroelastic tailoring have been developed. In the setup of the process chain it was made sure that the aerodynamic loads of all load cases entering the structural sizing always result from fluid-structure coupled simulations. Wunderlich [25] showed that this has crucial influence on the aerostructural wing optimization results.

1.2 Process Chain for Aerostructural Wing Optimization

An integrated process chain for aerostructural wing optimization based on high fidelity simulation methods has been developed. The developed process chain can be characterized by the following items:

- Usage of a central file format for parametric aircraft description,
- Automated grid generation for aerodynamic simulation,
- Automated structural model generation for structural simulation,
- Parallel static aeroelastic analysis for an arbitrary number of load cases,
- Structural wing box sizing for composite structures,
- Consideration of NLF by prescribing laminar-turbulent transition locations,
- Applicability for large geometrical changes and global optimization strategy.

The selected MDO architecture falls in the category of MDF-optimization (Multi-Disciplinary Feasible) and can be described as ASO (Asymmetric Subspace Optimization) according to Martins and Lambe [26]. In the MDF architecture a full multidisciplinary analysis (MDA) is performed for each optimization iteration. This means that the investigated design fulfills all constraints in each optimization step and hence is called a feasible design.

In Fig. 1.1 the process chain is illustrated with an XDSM-diagram (Extended Design Structure Matrix) [27]. This type of diagram combines the information of process flow between computational components with the information of data dependency. Each component in the diagram takes input data from the vertical direction and provides output data from the horizontal direction. Input and output data are marked by parallelograms. Thick gray lines show the data flow. Thin black arrows indicate the process flow, and a numbering system is used to define the order in which the components are executed.

The starting point for an aerostructural wing optimization is normally a detailed geometrical model of a given reference aircraft configuration. From this non-parametric model a fully parametric description of the aircraft using the Common
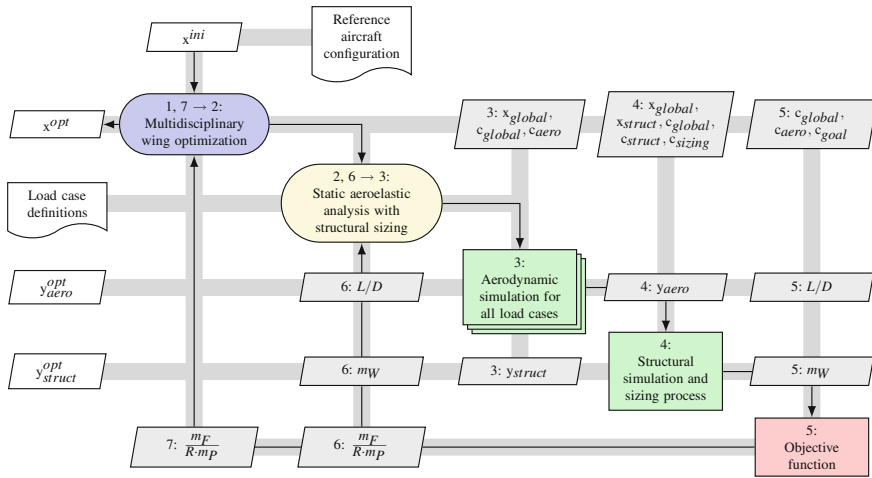
Fig. 1.1 Flow chart of the process chain for aerostructural wing optimization

Parametric Aircraft Configuration Schema (CPACS) has to be generated manually or with a program in an automated way. Furthermore, the initial vector of design parameters $\mathbf{x}^{ini}$ is determined by the reference aircraft configuration. The load case definitions for the structural sizing have to be identified and stored in the CPACS dataset.

All disciplinary simulation programs in the process chain provide interfaces to this central hierarchical and human readable file format. In Sect. 1.2.2 the parametric model and the CPACS dataset are described in more detail.

The driver component controls the optimization iteration and is represented in Fig. 1.1 by a blue rounded rectangle. Based upon a design parameter variation and a following transfer to the CPACS dataset the disciplinary models are built or updated automatically. Thereby, the vector of design parameters $\mathbf{x}$ describes the wing planform including twist and airfoil thickness distributions and the orthotropy direction of the composite structure.

The static aeroelastic analysis is then run in parallel for all load cases including the design point under cruise flight conditions. In the actual implementation, the process chain is limited to steady state maneuver load cases and only the wing-fuselage configuration is analysed within the high-fidelity simulation process.

For each load case the surface pressure distribution and aerodynamic coefficients of the wing are determined by solving the Reynolds-averaged Navier–Stokes equations (RANS) within a numerical flow simulation. Elastic characteristics of the wing and its internal loads are determined using the finite element method (FEM). Subsequently, the wing mass is deduced by processing these internal loads. The interactions between the aerodynamic forces and the structural deformations of the elastic wing are taken into account in the static aeroelastic analysis. The fluid-structure interaction belongs to the category of loosely coupled analysis as described in [28, 29]. Thereby, the fluid-structure coupling loop stops when the values for the lift-to-drag
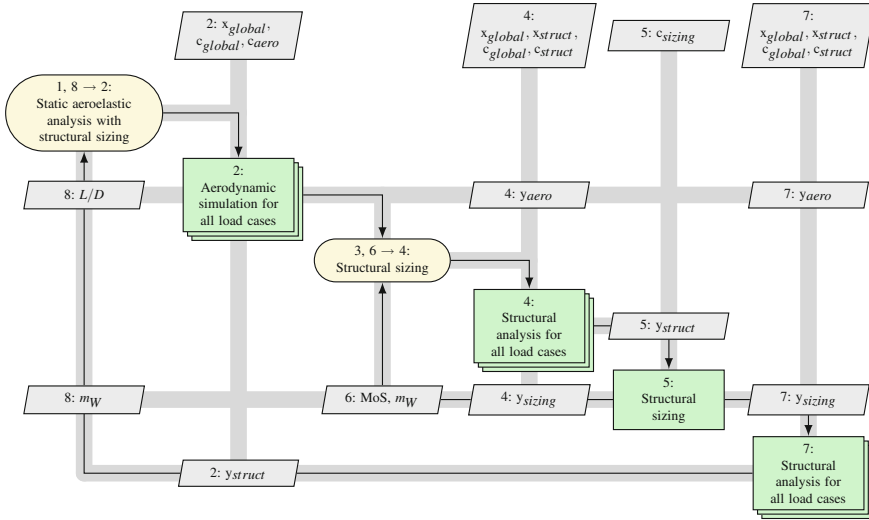
Fig. 1.2 Flow chart of the parallel static aeroelastic analysis including structural sizing

ratio, wing mass and fuel consumption are converged. The fluid-structure coupling loop is shown in Fig. 1.1 by a yellow rounded rectangle.

Figure 1.2 gives more insight into the parallel static aeroelastic analysis including structural sizing. Within the parallel static aeroelastic analysis the wing box structure is sized and the bending and torsional stiffness of the wing converge in the fluid-structure coupling loop. Thereby, the structural sizing forms an inner loop to fulfill the structural constraints in terms of failure criteria and converge the margins of safety (MoS) and the wing mass m_W for a fixed aerodynamic load.

The main results of this parallel analysis are the wing mass m_W and the deformed wing shape for the design point under cruise flight conditions, which is normally called "1g-flight shape". Based on this 1g-flight shape the aerodynamic performance in terms of lift-to-drag ratio L/D is determined.

The last step in the process chain is the evaluation of the objective function f for the multidisciplinary assessment of the wing design. The optimization algorithm then calculates a new set of values for the design parameters based on the value of the objective function. After the optimization run has been finished the optimized vector of design parameters $\mathbf{x}^{opt}$ represents the main result of the process chain for the corresponding optimization problem.

1.2.1 Flight Mission and Objective Function

For the evaluation of the objective function a simplified model of the flight mission has been used. This model is described in the textbook by Raymer [30] and is often used for preliminary aircraft design.

Table 1.1 Flight mission segments and mass fractions

Segment number	Mission segment	Aircraft mass fraction
1	Warm-up, taxi and take-off	m_1/m_0
2	Climb and accelerate	m_2/m_1
3	Cruise	m_3/m_2
4	Descent for landing	m_4/m_3
5	Landing and taxi	m_5/m_4

In this work, the flight mission consist of five segments. Table 1.1 gives an overview of these flight mission segments and the corresponding aircraft mass fractions. With the exception of the cruise flight segment the values for the aircraft mass fractions have to be prescribed depending on the optimization problem.

For the cruise flight segment a constant flight speed V and a given constant lift coefficient C_L have been assumed. The flight speed V is determined by the selected design cruise Mach number Ma and the flight altitude H at the beginning of cruise flight. In combination with the assumption of constant thrust specific fuel consumption $TSFC$ this leads to the well known Breguet range equation:

$$R = \frac{1}{g} \frac{V}{TSFC} \frac{L}{D} \ln \frac{m_2}{m_3} \tag{1.1}$$

The lift-to-drag ratio L/D of the aircraft for the given lift coefficient C_L and the wing mass m_W are results of the parallel static aeroelastic analysis. Furthermore, the selected flight mission corresponds to the design mission. The outcome of this is that the aircraft mass m_0 at the start of the mission is equivalent to the maximum take-off mass m_{MTO}. For an aircraft the maximum take-off mass m_{MTO} is the sum of the residual mass m_{Res} (structural mass without the wing), the wing mass m_W, the payload m_P, the fuel mass m_F and the reserve fuel mass $m_{F,res}$:

$$m_{MTO} = m_{Res} + m_W + m_P + m_F + m_{F,res} \tag{1.2}$$

In the presented applications the maximum take-off mass m_{MTO} is held constant. Furthermore, the residual mass ratio m_{Res}/m_{MTO} is also assumed to be constant, because the optimization is limited to the wing. In accordance with the simple model of the flight mission, the reserve fuel mass fraction $m_{F,res}/m_F$ is assumed to be constant as well. The fuel mass m_F corresponds to the fuel mass which is required for the design mission and has been calculated with the following equation:

$$m_F = m_0 - m_5 = m_{MTO} - m_5 \tag{1.3}$$

The objective function has to be selected based on the lift-to-drag ratio and the wing mass. Options for this selection are the minimization of fuel burn for a given range or the maximization of range for a given payload. Thereby, the objective function has to be derived for fixed maximum take-off mass.

For the transfer of the simulation results to the aircraft level the three following assumptions have been made.

Firstly, it has been assumed that the tailplane lift coefficient $C_{L,T}$ is constant. This means that the adaptation of tailplane lift for aircraft trimming has been neglected. The sum of wing and fuselage lift coefficients $C_{L,W} + C_{L,F}$ results from the flow simulation and matches the prescribed target lift coefficient for the cruise flight.

Secondly, a constant sum of tailplane and engine cowling drag coefficients (here denoted by $C_{D,res}$) has been assumed. The sum of wing and fuselage drag coefficients $C_{D,W} + C_{D,F}$ is a result of the flow simulation and includes pressure and viscous parts. With these assumptions the aerodynamic performance in terms of lift-to-drag L/D ratio is calculated with the following equation:

$$
\frac{L}{D} = \frac{C_L}{C_D} = \frac{\overbrace{C_{L,W} + C_{L,F}}^{\text{flow simulation}} + \overbrace{C_{L,T}}^{=const.}}{\underbrace{C_{D,W} + C_{D,F}}_{\text{flow simulation}} + \underbrace{C_{D,T} + C_{D,E}}_{C_{D,res}=const.}}
\tag{1.4}
$$

Thirdly, the wing mass m_W is the sum of the wing box mass $m_{W,box}$ and the secondary wing masses $m_{W,sec}$. The secondary wing mass consists of the wing leading and trailing edge masses, which have been prescribed in terms of mass per projected area. Additionally, the wing box mass is computed based on the sized finite element (FE) model and is multiplied by a correction factor of 1.25 to get a more realistic wing mass. This correction factor accounts for additional structural mass, which is not modeled in the idealized wing box model.

1.2.2 Parametric Model

For the parameterization of the aircraft the Common Parametric Aircraft Configuration Schema (CPACS) [31] has been selected. This aircraft parameterization scheme uses the widely spread Extensible Markup Language (XML). Hence, the CPACS dataset represents a hierarchical organized and human readable file format.

The usage of CPACS offers a generic and fully parametric description of the aircraft. The geometrical description in CPACS is section based and developed for low-fidelity tools in conceptual design. For the usage in the context of high-fidelity simulation methods this geometrical description is not accurate enough. Therefore, some extensions have been introduced to the geometry description in CPACS through the definition of guide curves. These guide curves describe the surface geometry between the fuselage and wing sections respectively and will be used for the surface lofting. The resulting quality of the outer surface geometry is therefore appropriate for aerodynamic simulations with CFD methods.

In CPACS the inner geometry is defined based on the outer geometry description. This includes for example the parametric arrangement of spars and ribs. Also the

used materials with their properties have to be defined in the CPACS dataset. The structural model generation process is linked to the CPACS dataset and is introduced in Sect. 1.2.5.

For the aerodynamic simulations a CAD model has been built automatically within the commercial software system CATIA® V5 based on the geometry description in CPACS. This parametric CAD model represents an equivalent representation of the geometrical description in CPACS with the same parametric description. The main task of the CAD model is the computation of the resulting surfaces and intersections for a given set of geometrical parameters in CPACS. In addition the CAD model includes the auxiliary geometry for the aerodynamic grid generation process.

This approach allows the fast and automated construction of a parametric CAD model, which provides the necessary interfaces to the CPACS dataset and the aerodynamic grid generation. Furthermore, the parametric CAD model allows fast and robust geometrical changes based on the CPACS parameters for a fixed aircraft topology.

1.2.3 Aerodynamic Grid Generation Process

The automated CAD model generation in CATIA® includes the construction of the auxiliary geometry for the structured grid generation as mentioned before. Additionally, this CAD model generation program writes the control script for the structured aerodynamic grid generation using the commercial program Pointwise®.

In combination with the generated control script the extended CAD model forms the input for the automatic aerodynamic grid generation with Pointwise®. The control script includes all commands for the automatic generation of the structured aerodynamic grid.

In Fig. 1.3 the surface grid of the reference aircraft configuration is shown as an example. It also includes some details of the leading and trailing edge.

To minimize the number of grid points an O-O-topology is used. Each airfoil section is discretized with 170 points. The resulting aerodynamic grid consists of $2.5 \cdot 10^6$ points. This grid resolution represents an appropriate trade-off between accuracy and computing effort for wing optimizations.

The introduced approach allows the fast and automatic grid generation for geometrical changes controlled by design parameters within the optimization loop. Furthermore, the number of grid points is kept constant and the optimization process can be accelerated by using a fully converged flow solution as the starting point for solving the flow field around the modified aircraft geometry. With the usage of structured aerodynamic grids the grid dependent numerical noise is very low for geometrical changes, which is essential for accurate optimization results.

The actual implementation of the automated structured grid generation process is limited to the wing-fuselage configuration. However, the introduced procedure is of general applicability to aerodynamic grid generation in the context of MDO.

Fig. 1.3 Aerodynamic
surface grid of the reference
aircraft configuration with
some details of the leading
and trailing edge
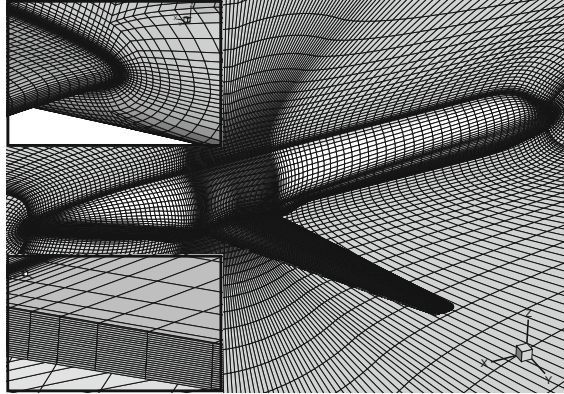
1.2.4 Flow Solver

The transonic flow around the wing-fuselage configuration is simulated with the DLR
TAU-code [32–34], which has been developed at the DLR Institute of Aerodynamics
and Flow Technology. The TAU-code solves the compressible, three-dimensional
Reynolds-averaged Navier–Stokes equations. It is a well established tool for aero-
dynamic applications at DLR, universities and aerospace industry [4, 35, 36]. The
TAU-code uses a vertex centered dual mesh formulation. For spatial approximation,
a finite volume method with second order upwind or central discretization is used.

For the flow simulation within the aerostructural process chain the central dis-
cretization schema and the negative Spalart–Allmaras turbulence model [37] is cur-
rently being used.

1.2.5 Structural Model Generation Process

For the generation of structure models, the software DELiS (Design Environment
for thin-walled Lightweight Structures) has been selected. The core of DELiS is a
parametric model generator that supports various levels of detail. Based on a CPACS
dataset, DELiS creates an abstract and object oriented model of the aircraft. This
model contains all the structurally relevant CPACS information and enriches it with
required data for finite elements. Due to the abstract and FE-centric definition of
the lightweight structure, models for various FE solvers can be created, such as
MSC Nastran™ and ANSYS® [38].

In Sect. 2.2 the structural model generation process is described in more detail.

1.2.6   Structural Analysis and Sizing

The aim of the structural sizing and optimization process is the minimization of the wing box mass $m_{W,box}$ with respect to a set of failure criteria. Based on the CPACS file an FE model of the wing is automatically generated as described in Sect. 2.2. With the external loads, which are calculated within the flow simulation and afterwards mapped onto the FE model, the internal loads are calculated with linear-static FE calculations. Subsequently the FE model with its geometry, material properties and loads is passed to the sizing and optimization module.

The sizing and optimization module is described in Sect. 2.3. Structure mechanical criteria for global buckling, local buckling and maximum strain for skin and stiffener are used for the sizing of the structural components. All criteria are evaluated at ultimate load. Damage tolerance constraints are covered by adapted strain allowables. For the strain allowable at ultimate load a conservative value of $3500 \mu m/m$ has been chosen as proposed in Military Handbook [39]. Furthermore criteria from manufacturing and operations like minimum and maximum ply share in $0°/90°/+45°/-45°$ direction, minimum and maximum height for stringer webs and a minimum skin thickness for repair are considered.

The component sizing itself is performed within the commercial computer-aided engineering (CAE) software HyperSizer® [40]. The structural analysis and sizing process is iterated until all failure criteria are fulfilled and the mass change is lower than the convergence threshold.

1.2.7   Fluid-Structure Coupling

The fluid-structure interaction loop to be carried out in each of the parallel static aeroelastic analyses of Fig. 1.1 involves the following operations:

1. Compute the aerodynamic loads on the given CFD grid for every load case,
2. Interpolate the loads from the CFD surface grid to the structural model,
3. Perform the structural sizing (once the loads of all load cases are available),
4. Compute the structural deformations for the newly sized structure for every load case and
5. Adjust the CFD volume grid according to the resulting structural deformations.

Then the loop starts over again. In step 2, an efficient classical nearest-neighbor interpolation is applied. It ensures equilibrium of forces on fluid and structural side. The existing defect in the equilibrium of moments is negligible. In step 5, a fast and robust grid deformation method is used which is based on the scattered data interpolation technology using radial basis functions. Based on the occurring structural deformations, a volume spline is determined which is then evaluated in parallel at all CFD volume grid points. Consult the publication by Barnewitz [41] for more detailed information on the grid deformation method.

The outlined fluid-structure interaction procedure is scripted in the FlowSimulator environment. The FlowSimulator has been designed particularly for massively-parallel multidisciplinary simulations with high-fidelity tools [42]. It is being jointly developed by Airbus, ONERA, DLR and universities. Its core, a c++ layer, provides parallel data containers and associated methods that support an efficient in-memory data exchange between involved process components. A Python scripting layer representing the users' level of access facilitates a fast creation of complex multidisciplinary process chains [43].

For the convergence of the fluid-structure coupling loop several convergence criteria have been used in parallel. A list of all considered physical quantities and their corresponding convergence criteria is shown in Table 1.2. If all these convergence criteria are fulfilled simultaneously, the aeroelastic equilibrium will be considered as having been achieved and the fluid-structure coupling loop will be terminated.

The selected values represent an appropriate trade-off between accuracy and computing time for the wing optimizations. The application of the process chain shows 4–8 fluid-structure coupling iterations n_{cpl} in practice to reach convergence. Figure 1.4 gives an example for the fluid-structure coupling convergence. Thereby, the used convergence criteria are shown as error bars.

Table 1.2 Convergence criteria of the fluid-structure coupling

Physical quantity		Convergence criterion[a]
Lift-to-drag ratio	L/D	$\frac{\Delta(L/D)}{L/D} \leq 0.001$
Wing mass	m_W	$\frac{\Delta m_W}{m_W} \leq 0.005$
Fuel consumption	$FC = m_F/(R \cdot m_P)$	$\frac{\Delta FC}{FC} \leq 0.002$

[a]The Δ symbol indicates the difference between the values of two consecutive fluid-structure coupling iterations
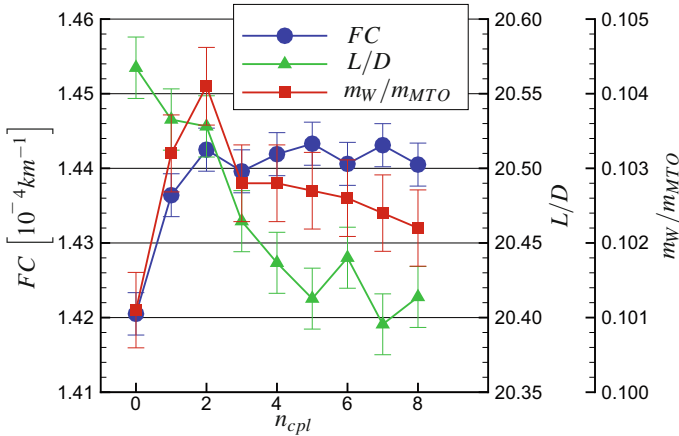
Fig. 1.4 Fluid-structure coupling convergence with used convergence criteria as error bars

The increase of wing mass at the beginning of the fluid structure coupling can be explained with the aeroelastic bending-torsion coupling of the forward swept wing. With increasing bending deformation the center of lift moves outboard and the resulting structural load increases. Additionally, Fig. 1.4 shows a decreasing lift-to-drag ratio under cruise flight conditions. This is a consequence of the elastic wing deformations. The convergence of the fuel consumption is reached after 4 fluid-structure coupling iterations. With the usage of several convergence criteria for the fluid-structure coupling up to the aeroelastic equilibrium the comparability of results for different geometries can be guaranteed within the aerostructural wing optimization.

1.2.8 Optimization Method

To control the process chain the program POT (Powerful Optimization Toolkit) [44] has been integrated. This program has been developed by the DLR Institute of Aerodynamics and Flow Technology and provides several optimization methods.

A surrogate based optimization (SBO) method has been selected for the aerostructural wing optimizations. This optimization method searches the global optimum and offers a high level of robustness. A similar optimization method named EGO (Efficient Global Optimizer) has been introduced by Jones et al. [45] and is discussed in Forrester et al. [46].

The optimization method starts with a design of experiments (DoE) for a selected number of samples. For the calculated objective function values, a surrogate model based on kriging [47] is built. This surrogate model is able to model nonlinear function behavior and includes a statistical error estimation.

The resulting surrogate model is then used for the optimization with a hybrid optimization strategy. Thereby, the expected improvement (EI) is used as the objective function. The optimization starts with a global optimization method and the localization of the optimum is improved by the application of a local optimization method. For the resulting global optimum of the surrogate model a recalculation is performed. The result of this recalculation is then used to improve the surrogate model. The described procedure is iterated until convergence is reached.

1.3 Reference Aircraft Configuration

Within the scope of the DLR project LamAiR [20] an aerostructural wing design of an NLF forward swept wing for short and medium range transport aircraft has been performed [22]. It has been shown, that the forward swept wing design enables for wide extend of laminar flow at transonic flight conditions. By aeroelastic tailoring of the composite wing structure, a divergence free design has been achieved.

For the present study of aerostructural wing design and optimization, the LamAiR aircraft configuration has been selected as the reference. Furthermore, the top level

Table 1.3 Top level aircraft requirements of the reference aircraft configuration

Design cruise Mach number	Ma	0.78
Design mission payload	m_P	150 passengers
Design range	R	4815 km
Maximum payload	$m_{P,max}$	150 passengers and 5 t cargo
Range with maximum payload	R_{mP}	3056 km
Take-off field length	s_{TOFL}	≈1900 m
Landing field length	s_{LFL}	≈1600 m
Propulsion	–	CFM56 class turbofan
Airport conformity	–	FAA Group III and ICAO Code C

aircraft requirements and the design mission are identical to this aircraft configuration. Table 1.3 gives an overview on the top level aircraft requirements.

The reference aircraft configuration has a low wing, rear mounted engines and a T-tail as shown in Fig. 1.5. To fulfill the surface requirements for laminar flow and the requirements for take-off and landing performance, the reference aircraft features a smart leading edge high-lift system as proposed by the DLR Institute of Composite Structures and Adaptive Systems [48].

The selected reference aircraft configuration represents a short and medium range commercial aircraft in the Airbus A320 and Boeing 737 class.

Key figures of the aircraft's flight envelope are summarized in Table 1.4. Flight envelope data give the basis for the selection of critical load cases for the structural sizing of the wing box.

The aerodynamic wing design of the reference aircraft configuration has been published by Kruse et al. [22]. With the objective of drag reduction by maximizing the extension of laminar flow for a design cruise Mach number of $Ma = 0.78$, the choice for a forward swept wing configuration is well-founded. For tapered wings, the forward swept wing design allows the favorably low leading edge sweep angle of $\varphi_{LE} = -17°$ for a passive control of cross flow instabilities in the leading edge region. Simultaneously, a sufficiently high sweep angle near the midchord shock position in the order of $\varphi = -25°$ is maintained, to meet the requirement of low wave drag in cruise flight for realistic wing thickness distributions and lift coefficients. Regarding these aspects, the forward swept wing design offers a clear advantage for NLF design under transonic cruise flight conditions in comparison to backward swept configurations. Some penalty in high-lift efficiency is expected due to the pronounced sweep of the trailing edge. However, the straight trailing edge of the mono-trapezoid wing planform and the rear mounted engine layout allow an efficient continuous trailing edge flap design. Aerodynamic cruise performance is shown to benefit from up to 19% drag reduction in comparison to a conventional backward swept aircraft design. The predicted laminar-turbulent transition locations at the design point ($Ma = 0.78$ and $C_L = 0.5$ at $FL = 350$) reach values between $x_T/c = 45\%$ and $x_T/c = 60\%$ on the wing's upper surface and values of $x_T/c = 50\%$ on the lower surface.

Fig. 1.5 Reference aircraft
configuration
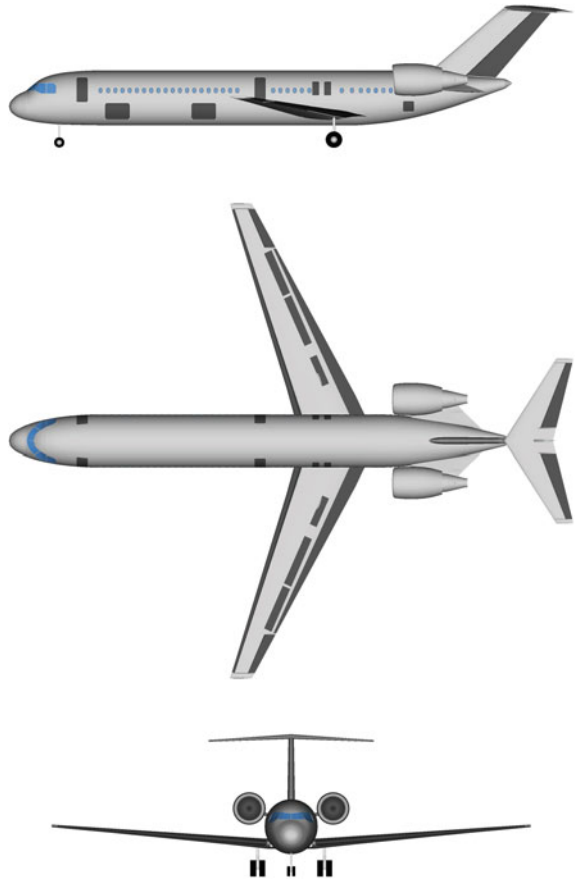
Table 1.4 Key figures of the flight envelope

Altitude		
Maximum flight altitude	H_{max}	41000 ft = 12500 m
Design speeds		
Maximum operating Mach number	Ma_{MO}	0.8
Maximum operating limit speed	$V_{MO,CAS}$	350 kn
Design diving Mach number	Ma_D	0.87
Design diving speed	$V_{D,CAS}$	395 kn

The wing box structure of the reference aircraft configuration has been derived
from the structural design and sizing of the LamAiR configuration [22]. For the
composite wing box the material properties of the CYCOM® 977-2 Epoxy Resin
System from Cytec Industries Inc. have been used. The percentage ply share of the
composite material is shown in Table 1.5 for the wing box of the reference aircraft
configuration.

Table 1.5 Percentage ply share of the wing box composite material

	Dimensionless span coordinate $\eta = 2y/b$	Percentage ply share $0°/\pm 45°/90°$
Upper skin	0.0000−0.3876	70/20/10
	0.3876−0.8157	60/20/20
	0.8157−0.8871	50/30/20
	0.8871−0.9584	40/40/20
Lower skin	0.0000−0.3520	70/20/10
	0.3520−0.7444	60/20/20
	0.7444−0.7801	50/30/20
	0.7801−0.9584	40/40/20
Front spar	0.0000−0.6730	50/30/20
	0.6730−0.9584	40/30/30
Rear spar	0.0000−0.9584	70/20/10
Ribs	0.0000−0.2101	10/80/10
	0.2101−0.3163	20/60/20
	0.3163−0.3876	30/50/20
	0.3876−0.4947	40/40/20
	0.4947−0.9584	60/20/20

1.4 Design Task

1.4.1 Design Parameters and Constraints

The parametric model of the reference aircraft configuration is generated based on the selection of 12 fuselage sections and 9 wing sections. Additionally, 5 guide curves have been used for the geometry description between the fuselage sections and 3 guide curves for the geometry description between the wing sections. Thereby, the guide curves of the wing form the wing leading edge and the upper and lower line of the blunt trailing edge. In Fig. 1.6 the positions of the selected wing sections are shown for the reference aircraft configuration.

The selected design parameters for the wing design studies and the wing optimization are:

- Aspect ratio A,
- Taper ratio λ,
- Twist and thickness distribution ε_i, $(t/c)_i$,
- Orthotropy angles of the composite material $\varphi_{OD,middle}$ and $\varphi_{OD,outboard}$.

For the variation of the twist and thickness distribution the values in 4 wing sections have been used respectively. This leads to a total number of 12 design parameters.
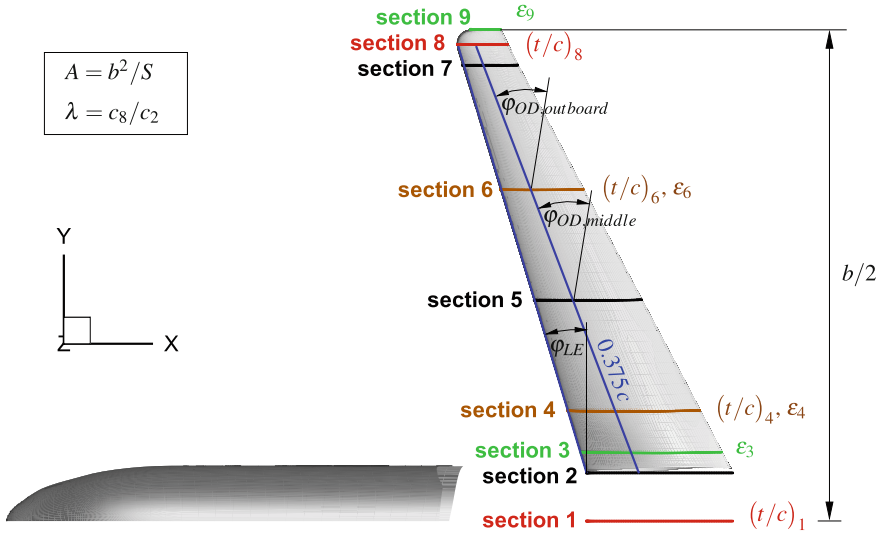
Fig. 1.6 Definition of design parameters

The optimizer does not directly control the design parameters. Scaling factors are used for the control of the aspect ratio, taper ratio and thickness distribution, and differences are used for the control of the twist distribution and the orthotropy angles. Thereby, the scaling factors and the differences are based on the corresponding values of the reference aircraft configuration.

In Fig. 1.6 the selected definition of design parameters is shown. The twist distribution parameters control the twist angles ε_i in the wing sections 3, 4, 6 and 9. For the control of the thickness distribution the thickness parameters $(t/c)_i$ of the wing sections 1, 4, 6 and 8 have been used. In the wing sections between the values for the twist angle and relative thickness are calculated by linear interpolation of the corresponding scaling factors and differences.

For the aeroelastic tailoring of the wing the complete orthotropic material including the stringers of the upper and lower wing box skin is rotated. The orthotropy angle of the composite material φ_{OD} is defined relative to the mean line of the wing box as shown in Fig. 1.6. In the unswept center wing and the inboard wing the orthotropy angle of the composite material has been held constant. The aeroelastic tailoring has been applied to the middle and outboard wing regions. This is achieved by using the orthotropy angles of the composite material $\varphi_{OD,middle}$ and $\varphi_{OD,outboard}$ to control the bend-twist-coupling of the wing. Thereby, the middle wing starts at approximately 40% wing span and ends at approximately 70% wing span. Consequently the outboard wing starts at approximately 70% wing span.

The optimization constraints are listed in Table 1.6 and are based on the top level aircraft requirements of Table 1.3 and the results of the conceptual aircraft design published in [22]. This includes the specifications of the maximum take-off mass m_{MTO}, wing loading m_{MTO}/S and the cruise Mach number Ma.

Table 1.6 Constraints for the wing design studies and wing optimization

Aircraft		
Maximum take-off mass	m_{MTO}	73 365 kg
Maximum payload	$m_{P,max}$	19 250 kg
Wing loading	m_{MTO}/S	556 kg/m^2
Residual mass ratio	m_{Res}/m_{MTO}	0.4604
Drag coefficient of tailplane and engine cowling	$C_{D,res}$	0.0025
Specific mass of leading edge high lift device	m_{le}/S_{le}	30 kg/m^2
Specific mass of trailing edge high lift device	m_{te}/S_{te}	50 kg/m^2
Leading edge sweep angle	φ_{LE}	$-16.8°$
Relative front spar position	x_{FS}/c	0.15
Relative rear spar position	x_{RS}/c	0.60
Number of ribs	N_{Ribs}	$2 \cdot 27 + 1 = 57$
Design mission		
Mach number	Ma	0.78
Range	R	4815 km
Range cruise segment	R_{23}	3726 km
Lift coefficient aircraft	C_L	0.5
Lift coefficient tailplane	$C_{L,T}$	-0.0022
Thrust specific fuel consumption	$TSFC$	0.0589 kg/(Nh)
Take-off and climb mass fraction	m_2/m_0	0.9589
Descent and landing mass fraction	m_5/m_3	0.9906
Reserve fuel mass fraction	$m_{F,res}/m_F$	0.4604

Table 1.7 Cruise flight design point and load cases for the structural sizing of the wing

Load case	Altitude H (m)	Mach number Ma	Lift coefficient $C_{L,W} + C_{L,F}$	Aircraft mass m (kg)	Load factor n
Cruise[a]	10668	0.780	0.502	68640	1.0
LC 2	0	0.717[b]	0.374	73365	2.5
LC 3	4725	0.772	0.571	73365	2.5
LC 4	0	0.717[b]	-0.149	73365	-1.0

[a] Design point with laminar-turbulent transition prescription
[b] $V = 1.2 \cdot V_D$ for divergence prevention from CS-25/FAR 25

For the structural sizing of the wing box three maneuver load cases with minimum and maximum load factors from the certification specifications CS-25/FAR 25 have been selected. The definitions of the cruise flight design point and the selected load cases are specified in Table 1.7 and are based on the flight envelope of the reference aircraft configuration.

The NLF wing sections have been adopted from the reference aircraft configuration. For the flow simulations, spanwise transition locations are prescibed at $x_T/c = 0.3$ for the inboard wing and $x_T/c = 0.4$ for the middle and outboard wing. Furthermore, the leading edge sweep angle is limited to $|\varphi_{LE}| \leq 17°$ to

Table 1.8 Equations for the calculation of fuel consumption

Mass fraction cruise	$\dfrac{m_3}{m_2} = e^{-\frac{g\,TSFC\,R}{V\,(L/D)}}$
Mass fraction fuel	$\dfrac{m_F}{m_{MTO}} = 1 - \dfrac{m_3}{m_2}\dfrac{m_1}{m_{MTO}}\dfrac{m_2}{m_1}\dfrac{m_4}{m_3}\dfrac{m_5}{m_4}$
Mass fraction payload	$\dfrac{m_P}{m_{MTO}} = 1 - \dfrac{m_{Res}}{m_{MTO}} - \dfrac{m_W}{m_{MTO}} - \left(1 + \dfrac{m_{F,res}}{m_F}\right)\dfrac{m_F}{m_{MTO}}$
Fuel consumption	$FC = \dfrac{1}{R}\dfrac{m_F}{m_{MTO}}\dfrac{m_{MTO}}{m_P}$

preclude excessive growth of crossflow instabilities and potential attachment line transition [17].

The topology of the wing box structure (relative spar positions and number of ribs) and the ply share of the composite material are transferred from the reference aircraft configuration. The values for this percentage ply share of the composite material are indicated in Table 1.5. Within the structural sizing process the wing box topology and the ply share of the composite material is held constant. The wing box mass $m_{W,box}$ resulting from the structural sizing process is multiplied by a factor of 1.25 to account for additional masses which are not modeled in the idealized finite element model [49]. This is required to obtain a realistic wing mass for the evaluation of the objective function.

1.4.2 Objective Function

Based on the simplified model for the flight mission as introduced in Sect. 1.2.1 the fuel consumption FC has been selected as the figure of merit for the aerostructural wing optimization. The fuel consumption FC is here defined in terms of fuel burn per range and payload $m_F / (R\, m_P)$ for a given range R.

The minimization of the fuel burn is an appropriate objective for the aerostructural wing optimization of future commercial aircraft as shown in [50].

For the calculation of the fuel consumption the required equations are listed in Table 1.8. Thereby, the fuel mass m_F is computed from the given range R and the lift-to-drag ratio L/D. The payload m_P results from this fuel mass m_F and the wing mass m_W. As mentioned before, the lift-to-drag ratio L/D and the wing mass m_W are outputs of the parallel static aeroelastic analysis. With all these calculated values the fuel consumption per range and payload $m_F / (R\, m_P)$ follows directly from the last equation shown in Table 1.8.

1.5 Wing Design Studies

The wing design studies have been performed with the introduced process chain and the selected design parameters and constraints. Each study has been executed for a constant taper ratio and a constant orthotropy angle distribution of the composite material. In each design study wings with 2–3 aspect ratios, 2–3 thickness distributions and 2 twist distributions have been investigated.

The results for the orthotropy angle distribution of $\varphi_{OD} = (0°; 0°; 0°)$ are summarized in Figs. 1.7 and 1.8 in terms of wing mass ratio m_W/m_{MTO}, lift-to-drag ratio L/D and fuel consumption FC.

As expected, the increasing aspect ratio shows an increase of lift-to-drag ratio and wing mass ratio due to induced drag reduction and a higher level of structural loads. The results for different thickness distributions show the trend of increased lift-to-drag ratios and wing mass ratios for reduced airfoil thicknesses. Furthermore, twist distributions with increased outboard loading lead to increased wing mass ratios.

The design mission fuel consumption depends on aerodynamic performance and structural wing mass ratio. Consequently, the minimization of design mission fuel consumption is equivalent to the search for the best trade-off between aerodynamic performance in terms of lift-to-drag ratio and structural wing mass ratio. It can be observed that different wing geometries with the same design mission fuel consumption exist. These solutions are equivalent with regard to the objective function. Additional criteria have to be considered for a further assessment.

In all figures the solutions for the baseline and the optimized wing geometries are included. The baseline wing geometry is transferred from the reference aircraft configuration, which is described in Sect. 1.3. Thereby, no aeroelastic tailoring has been considered. This means that the orthotropy angles of the composite material are set to $\varphi_{OD} = (0°; 0°; 0°)$. The optimized wing geometry is the result of the wing optimization including aeroelastic tailoring, which is presented in Sect. 1.6.
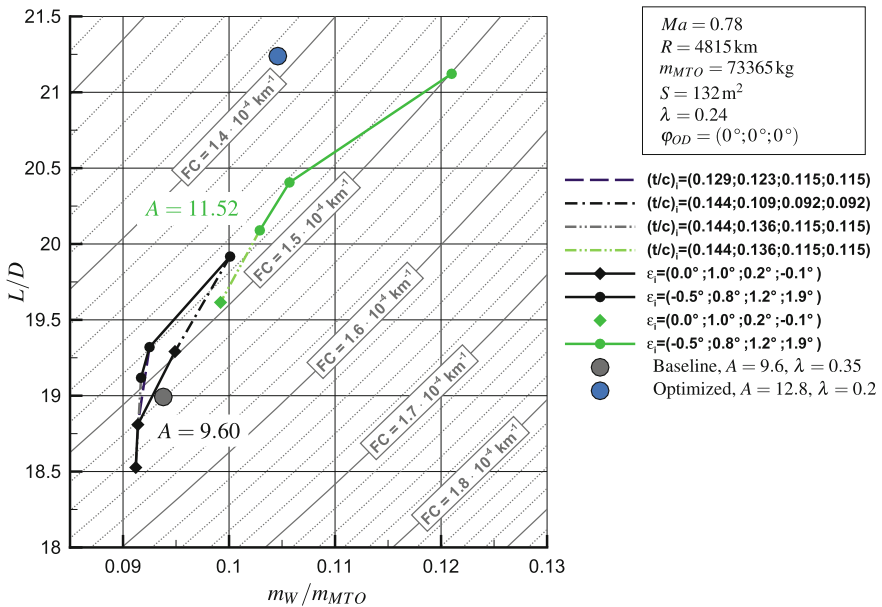
Fig. 1.7 Variation of aspect ratio, thickness and twist distribution for a taper ratio of $\lambda = 0.24$ and an orthotropy angle distribution of $\varphi_{OD} = (0°; 0°; 0°)$
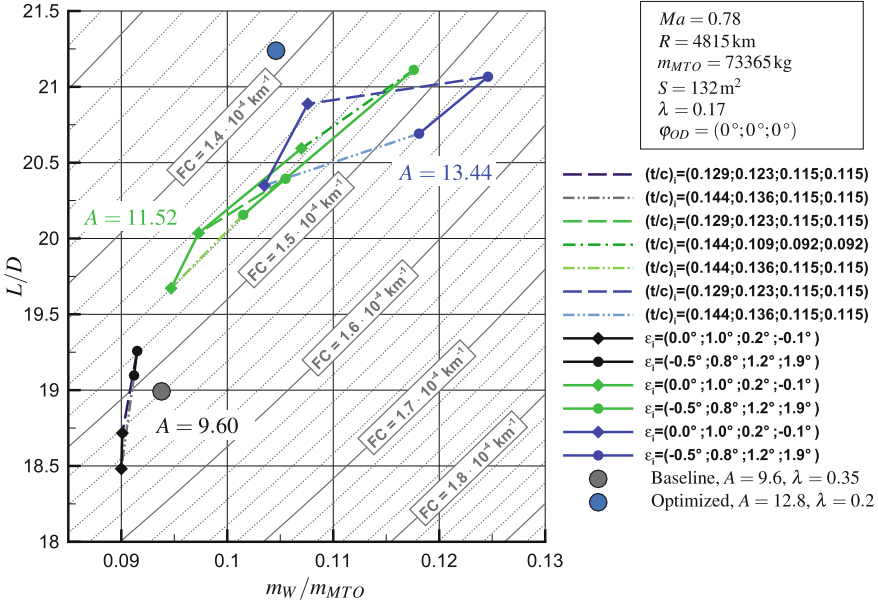
Fig. 1.8 Variation of aspect ratio, thickness and twist distribution for a taper ratio of $\lambda = 0.17$ and an orthotropy angle distribution of $\varphi_{OD} = (0°; 0°; 0°)$

The influence of taper ratio variation can be observed by comparing the results of Figs. 1.7 and 1.8. This taper ratio reduction shows the trend to almost unchanged lift-to-drag ratios and decreased wing mass ratios. Only for the lower taper ratio of $\lambda = 0.17$ the calculations with the high aspect ratio of $A = 13.44$ have been performed.

To investigate the influence of aeroelastic tailoring the studies have been repeated for wings with different orthotropy angle distributions. The results for an orthotropy angle distribution of $\varphi_{OD} = (0°; -5°; -5°)$ are shown in Figs. 1.9 and 1.10.

The aeroelastic tailoring leads to a significant wing mass reduction and similar aerodynamic performance. In comparison to the results with an orthotropy angle distribution of $\varphi_{OD} = (0°; 0°; 0°)$ the results show the same trend of increased lift-to-drag ratios and wing mass ratios for reduced airfoil thicknesses. The main difference can be observed for the twist distribution variations. In contrast to the results with an orthotropy angle distribution of $\varphi_{OD} = (0°; 0°; 0°)$ the results for the aeroelastic tailored wings show that twist distributions with increased outboard loading lead to increased lift-to-drag ratios with minor effect to the wing mass ratios.

In Figs. 1.11 and 1.12 the results for the orthotropy angle distribution of $\varphi_{OD} = (0°; -5°; -10°)$ are presented. These results show further fuel consumption reductions in comparison to the results with an orthotropy angle distribution of $\varphi_{OD} = (0°; -5°; -5°)$. The reason for the fuel consumption reductions is the decrease of wing masses due to maneuver load reduction.
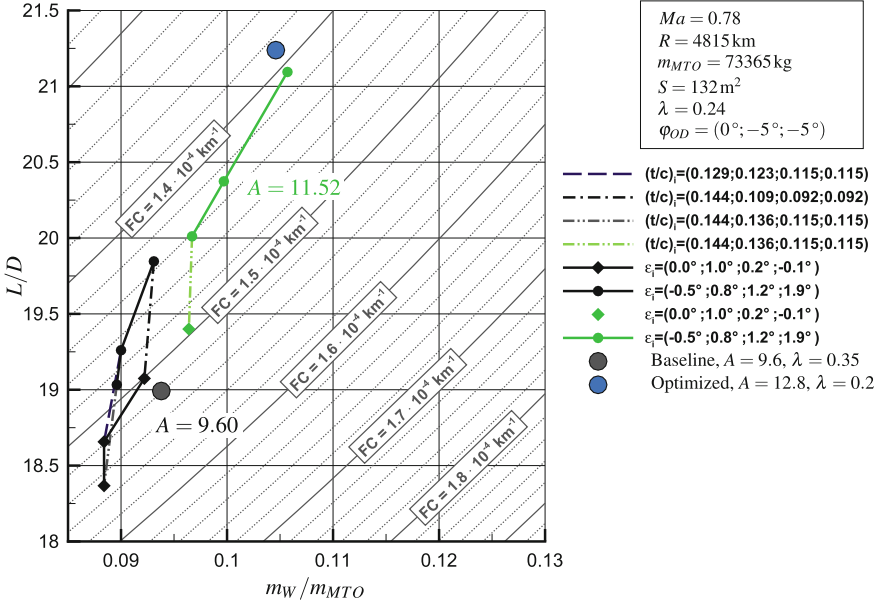
Fig. 1.9 Variation of aspect ratio, thickness and twist distribution for a taper ratio of $\lambda = 0.24$ and an orthotropy angle distribution of $\varphi_{OD} = (0°; -5°; -5°)$
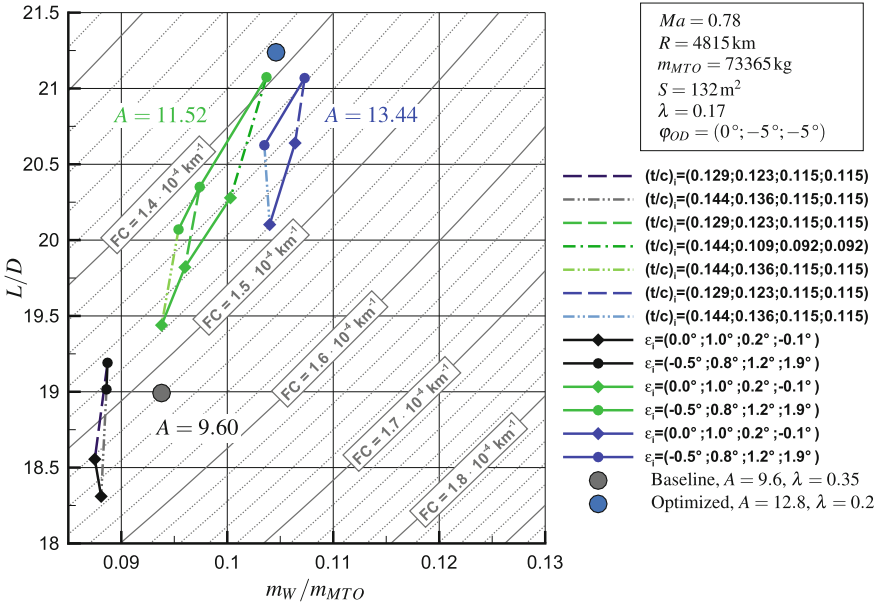
Fig. 1.10 Variation of aspect ratio, thickness and twist distribution for a taper ratio of $\lambda = 0.17$ and an orthotropy angle distribution of $\varphi_{OD} = (0°; -5°; -5°)$
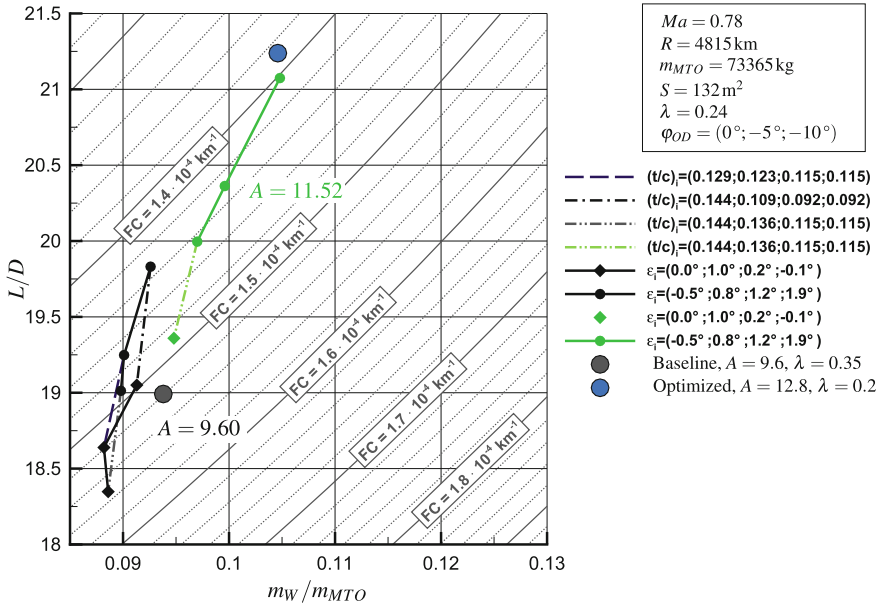
Fig. 1.11 Variation of aspect ratio, thickness and twist distribution for a taper ratio of $\lambda = 0.24$ and an orthotropy angle distribution of $\varphi_{OD} = (0°; -5°; -10°)$
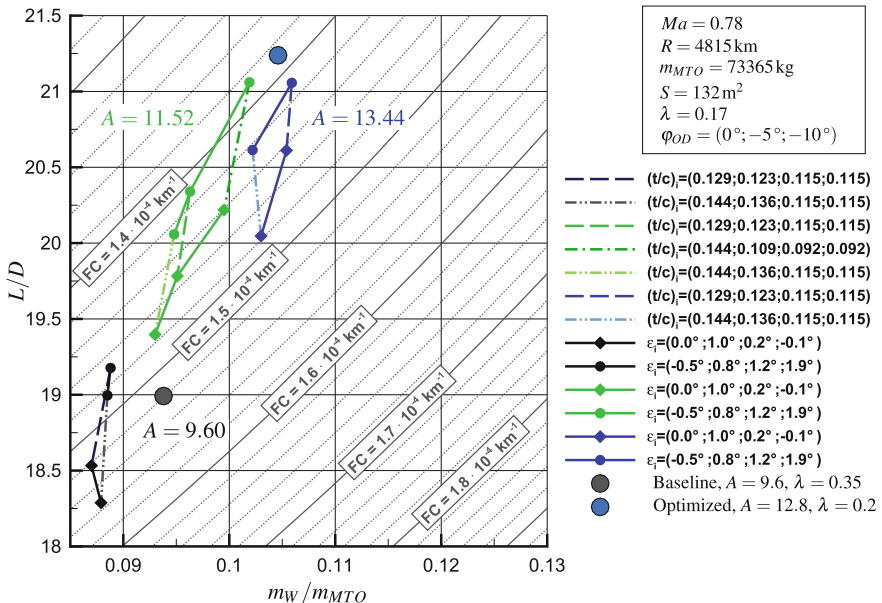
Fig. 1.12 Variation of aspect ratio, thickness and twist distribution for a taper ratio of $\lambda = 0.17$ and an orthotropy angle distribution of $\varphi_{OD} = (0°; -5°; -10°)$

The best solutions of the wing design studies including aeroelastic tailoring achieve nearly the same fuel consumption as the optimized wing resulting from the wing optimization in Sect. 1.6.

1.6 Wing Design Optimization

The wing optimization has been performed successfully for the selected design parameters and constraints. Figure 1.13 gives an overview of the wing optimization results in terms of fuel consumption FC, lift-to-drag ratio L/D, wing mass ratio m_W/m_{MTO} and payload ratio m_P/m_{MTO} depending on the aspect ratio A.

The increase of aspect ratio shows the trend of increasing lift-to-drag ratio and wing mass ratio. Minimum values for the fuel consumption can be observed for wings with an aspect ratio between 11 and 13. For the specified constraint of constant maximum take-off mass the payload ratio is an output of the process chain and reaches maximum values for aspect ratios between 10 and 12.

The wing optimization has been performed without a span limit. This leads to optimal wing geometries with wing spans greater than the span limit of $b \leq 36$ m for FAA Group III and ICAO Code C aircraft. Technical solutions for folded wingtips exist and have to be considered for wings with the highest level of fuel efficiency. The span limit of FAA Group III and ICAO Code C aircraft is additionally drawn in Fig. 1.13. Furthermore, the wing with minimum fuel consumption is marked in Fig. 1.13 and further referred to as "optimized".

In Table 1.9 the wing planform parameters resulting from the optimization are shown for the baseline and the optimized wing. The aspect ratio A of the optimized
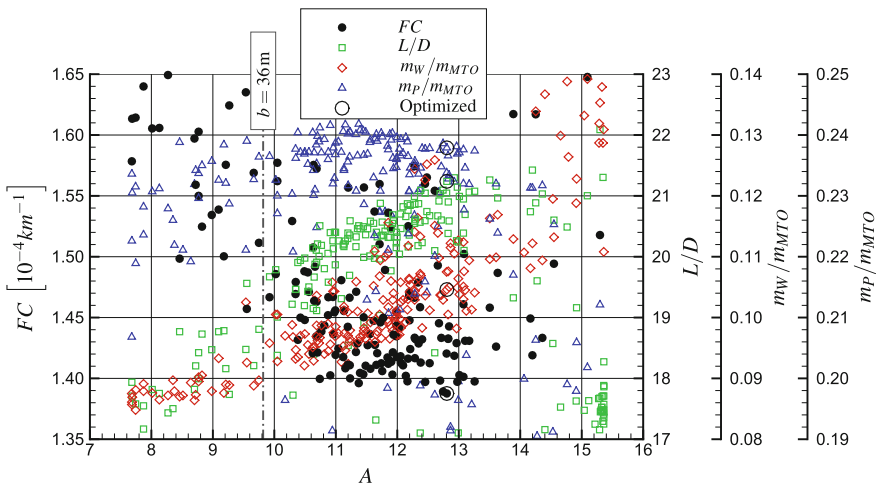
Fig. 1.13 Overview of wing optimization results

Table 1.9 Results of wing optimization for baseline and optimized wing

		Baseline	Optimized	Difference
Aspect ratio	A	9.601	12.806	+33.4%
Taper ratio	λ	0.345	0.196	−43.1%
Orthotropy angle middle wing	$\varphi_{OD,middle}$	0.0°	−4.7°	−4.7°
Orthotropy angle outboard wing	$\varphi_{OD,outboard}$	0.0°	−5.8°	−5.8°
Lift-to-drag ratio	L/D	18.992	21.239	+11.8%
Wing mass ratio	m_W/m_{MTO}	0.0938	0.1046	+11.5%
Fuel mass ratio	m_F/m_{MTO}	0.2121	0.1972	−7.0%
Payload ratio	m_P/m_{MTO}	0.2338	0.2379	+1.8%
Fuel consumption	FC	$1.519 \cdot 10^{-4}\,\mathrm{km}^{-1}$	$1.388 \cdot 10^{-4}\,\mathrm{km}^{-1}$	−8.6%
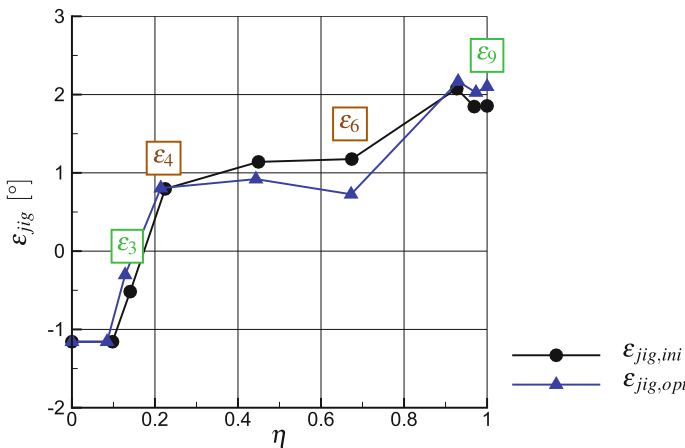
Fig. 1.14 Twist distributions for baseline and optimized wing

wing has been increased in comparison to the baseline wing. Furthermore, the taper ratio λ of the optimized wing is lower than the value of the baseline wing.

In Fig. 1.14 the twist distributions of the baseline and optimized wing are shown for the undeformed jig-shape geometry. The twist angles of the optimized wing are nearly identical in the inboard and outboard regions in comparison to the baseline wing. In the middle wing region the twist angles of the optimized wing are slightly smaller than the twist angles of the baseline wing.

Figure 1.15 shows the relative and absolute thickness distributions of the baseline and the optimized wing. The absolute thickness is nearly identical in the symmetry plane of both wings. With the exception of the symmetry plane and the wing tip the relative and absolute thickness of the optimized wing are decreased in comparison to the baseline wing. In principle the relative airfoil thickness reduction leads to
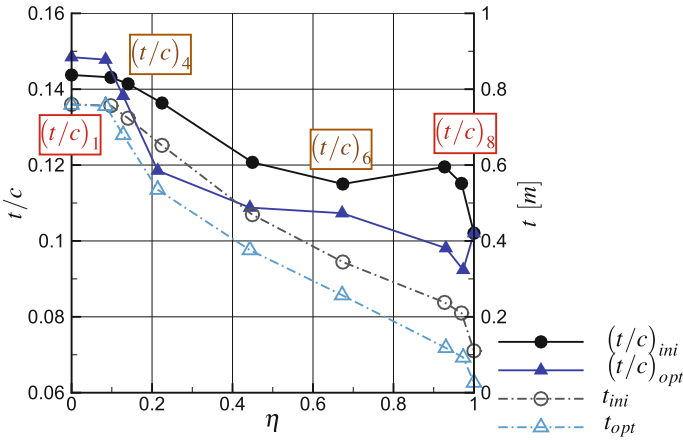
Fig. 1.15 Relative and absolute thickness distributions for baseline and optimized wing

aerodynamic performance improvement and the absolute airfoil thickness reduction results in increased wing mass. Additionally, the thickness reduction of the wing leads to a smaller fuel tank volume.

The optimization results for the lift-to-drag ratio, the wing mass ratio, the fuel mass ratio, the payload ratio and the fuel consumption are also given in Table 1.9. These results show an increased aerodynamic performance in terms of lift-to-drag ratio L/D and simultaneously an increased wing mass ratio m_W/m_{MTO} for the optimized wing in comparison to the baseline wing. The increased lift-to-drag-ratio can be explained with the induced drag reduction resulting from the increased span and leads to the reduced fuel mass ratio. It can be observed that the reduced fuel mass ratio m_F/m_{MTO} overcompensates the increased wing mass ratio m_W/m_{MTO}. Consequently the payload ratio m_P/m_{MTO} increases. The main result of the wing optimization is the reduction of the fuel consumption FC in the order of 9%.

In Fig. 1.16, an overview of the wing optimization results for cruise flight condition is given. This includes the comparison of the baseline and the optimized wing in terms of isentropic Mach number distribution for the upper wing, the deformations for the 1g-cruise flight and the corresponding lift and lift coefficient distributions in span direction. Furthermore, the isentropic Mach number distributions and airfoil shapes are presented in four wing sections.

For each lift distribution the related elliptical lift distribution is shown by a dot-dashed line as a reference. The elliptical lift distribution is the optimum for planar wings in terms of induced drag. Additionally, the prescribed laminar-turbulent transition line is shown in the isentropic Mach number distribution of Fig. 1.16 as a long-dashed line. The relative position in chord direction of the laminar-turbulent transition has been held constant during the optimization process. The optimized wing shows an inboard load shift and increased bending deformations in comparison to the baseline wing. In the isentropic mach number distributions of the four sections a shock strength reduction can be observed for the optimized wing. With the exception of the wing tip region the isentropic mach number distributions show
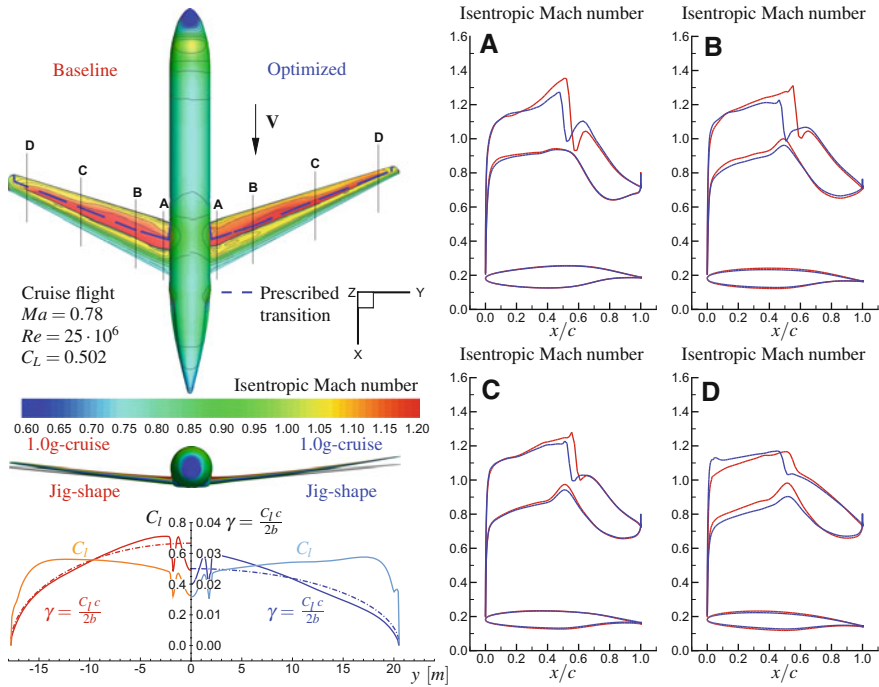
Fig. 1.16 Overview of wing optimization results for cruise flight

accelerated flow up to 50% chord, which is necessary to limit the growth rate of Tollmien–Schlichting instabilities and maintain laminar flow.

Figure 1.17 shows the results for load case LC 2 and LC 4 in a similar form. An outboard load shift is observed for both wings and both maneuver flight conditions in comparison to the cruise flight. This outboard load shift of both wings can be explained with the geometrical bending-torsion coupling of the forward swept wing. Thereby, the optimized wing is more inboard loaded in comparison to the baseline wing. The reason for the reduced bending-torsion coupling of the optimized wing is the aeroelastic tailoring with the orthotropy angle of the composite material. The lift distributions of these maneuver load cases show the importance of considering the static aeroelastic effects in the loads computation for the structural wing sizing. Furthermore, an increased bending deformation of the optimized wing is observed for both maneuver flight conditions.

1.6.1 Computing Time

The aerostructural wing design studies and wing optimization based on high-fidelity methods require a relative high computing effort. For the aerodynamic simulations and the fluid-structure coupling the HPC-cluster $C^2A^2S^2E$ (Center for Computer Applications in AeroSpace Science and Engineering) of the DLR Institute of Aero-
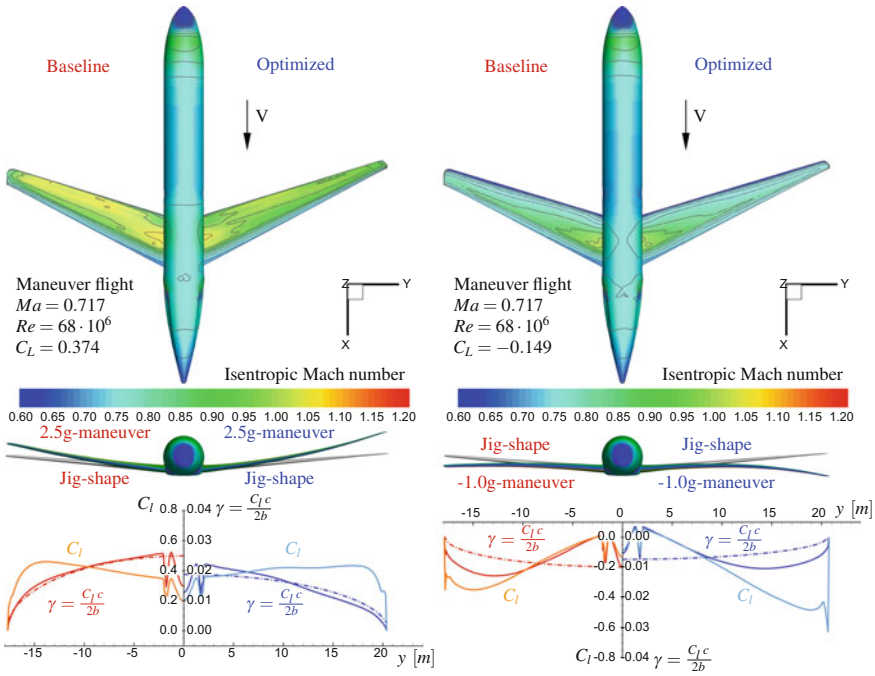
Fig. 1.17 Overview of wing optimization results for load case LC 2 and LC 4

Table 1.10 Example of the required computing time of the disciplinary simulation programs for an aerostructural wing analysis

Process	Program	Program calls	Computing time (min)	Computing time ratio (%)
CAD model update	CATIA® V5	1	1.2	1.3
Aerodynamic grid generation	Pointwise®	1	1.8	1.9
Structural model generation	DELiS	1	3.3	3.5
Flow simulation and fluid-structure coupling	FlowSimulator (TAU-Code)	7	53.4	56.7
Structural analysis and sizing	MSC Nastran™ and HyperSizer®	6	32.2	34.2
Data transfer	–	–	2.3	2.4
			94.2	100

dynamics and Flow Technology is used. In this work the aerodynamic simulations use 8 nodes of the $C^2A^2S^2E$-cluster, which equates to 192 processor cores. All other simulation programs are executed on local workstations.

An example of the required computing time and the corresponding computing time ratio of the disciplinary simulation programs for an aerostructural wing analy-

sis is given in Table 1.10. In this example 6 fluid-structure coupling iterations have been performed to reach the aeroelastic equilibrium of all considered load cases. With approximately 55%, the aerodynamic simulation including the fluid-structure coupling requires the largest percentage of the computing time. Nevertheless, the computing time for the aerodynamic simulation is relatively short for aerostructural coupled simulations based on the Reynolds-averaged Navier–Stokes equations (RANS) due to the high degree of parallelization. The structural analysis and sizing using the finite element method (FEM) is comparatively efficient. It only needs a percentage of computing time in the order of 35%.

To summarize, it can be stated that an aerostructural wing optimization with 12 design parameters requires an overall computing time in the order of 2 weeks.

References

1. European Commission, *European Aeronautics: A Vision for 2020* (Office for Official Publications of the European Communities, Luxembourg, Belgium, 2001)
2. European Commision, *2008 Addendum to the Strategic Research Agenda* (2008), http://www.acare4europe.com
3. European Commision, *Flightpath 2050 Europe's Vision for Aviation* (Office for Official Publications of the European Communities, Luxembourg, Belgium, 2011)
4. N. Kroll et al., The MEGAFLOW-project - numerical flow simulation for aircraft. Prog. Ind. Math. ECMI **2004**, 3–33 (2005)
5. N. Kroll et al., Ongoing activities in shape optimization within the German project MEGADESIGN, in *ECCOMAS 2004* (2004)
6. N. Kroll et al., Flow simulation and shape optimization for aircraft design. J. Comput. Appl. Math. **203**, 397–411 (2005)
7. N. Kroll et al., Ongoing activities in flow simulation and shape optimization within the German megadesign project, in *25th International Congress of the Aeronautical Sciences, ICAS* (2006)
8. N. Kroll et al., *MEGADESIGN and MegaOpt - German Initiatives for Aerodynamic Simulation and Optimization in Aircraft Design* (Springer, Berlin, Heidelberg, 2009)
9. N.R. Gauger, Ongoing activities in shape optimization within the German project MEGADESIGN, in *EUCCO2004, Dresden (de), 29.-31.03.2004* (2004)
10. P. Piperni et al., Preliminary aerostructural optimization of a large business jet. J. Aircr. **44**(5), 1422–1438 (2007)
11. K. Chiba et al., Multidisciplinary design optimization and data mining for transonic regional-jet wing. J. Aircr. **44**(4), 1100–1112 (2007)
12. A. Jameson et al., Multi-point aero-structural optimization of wings including planform variations, in *45th Aerospace Sciences Meeting and Exhibit, AIAA 2007-764* (Reno, Nevada, USA, 2007)
13. G.K.W. Kenway, J.R.R.A. Martins, Multipoint high-fidelity aerostructural optimization of a transport aircraft configuration. J. Aircr. **51**, 144–160 (2014)
14. G.K.W. Kenway et al., Scalable parallel approach for high-fidelity steady-state aeroelastic analysis and adjoint derivative computations. AIAA J. **52**, 935–951 (2014)

15. R.P. Liem et al., Multi-point, multi-mission, high-fidelity aerostructural optimization of a long-range aircraft configuration, in *14th AIAA/ISSMO Multidisciplinary Analysis and Optimization Conference* (Indianapolis, USA, 2012)

16. K.H. Horstmann, T. Streit, in *Aerodynamic Wing Design for Transport Aircraft - Today: Hermann Schlichting - 100 Years*, vol. 102, ed. by R. Radespiel et al. (Springer, Berlin, Heidelberg, 2009), pp. 130–144

17. G. Schrauf, Status and perspectives of laminar flow. Aeronaut. J. **109**(1102), 639–644 (2005)

18. J.E. Green, Laminar flow control - back to the future? in *38th Fluid Dynamics Conference and Exhibit, AIAA 2008-3728* (Seattle, Washington, USA, 2008)

19. G.W. Hanks et al., *Natural laminar flow analysis and trade studies*. Tech. rep. NASA CR-159029 (National Aeronautics and Space Administration, 1979)

20. A. Seitz et al., The DLR project LamAiR: design of a NLF forward swept wing for short and medium range transport application, in *29th AIAA Applied Aerodynamics Conference, AIAA Conference Paper AIAA 2011-3526* (2011)

21. G. Redeker, G. Wichmann, Forward sweep - a favourable concept for a laminar flow wing. J. Aircr. **28**, 97–103 (1991)

22. M. Kruse et al., A conceptual study of a transonic NLF transport aircraft with forward swept wings, in *30th AIAA Applied Aerodynamics Conference, AIAA Conference Paper AIAA 2012-3208* (New Orleans, Louisiana, 2012)

23. M.H. Shirk et al., Aeroelastic tailoring - theory, practice, and promise. J. Aircr. **23**(1), 6–18 (1986)

24. S. Dähne et al., Steps to feasibility for laminar wing design in a multidisciplinary environment, in *ICAS 2014* (2014)

25. T.F. Wunderlich, Multidisciplinary wing optimization of commercial aircraft with consideration of static aeroelasticity. CEAS Aeronaut. J. **6**(3), 407–427 (2015)

26. J.R.R.A. Martins, A.B. Lambe, Multidisciplinary design optimization: a survey of architectures. AIAA J. **51**, 2049–2075 (2013)

27. A.B. Lambe, J.R.R.A. Martins, Extensions to the design structure matrix for the description of multidisciplinary design analysis and optimization processes. Struct. Multidiscip. Optim. **46**, 273–284 (2012)

28. R. Kamakoti, W. Shyy, Fluid-structure interaction for aeroelastic applications. Prog. Aerosp. Sci. **40**(8), 535–558 (2005)

29. X.B. Lam et al., Coupled aerostructural design optimization using the kriging model and integrated multiobjective optimization algorithm. J. Optim. Theory Appl. **142**(3), 533–556 (2009)

30. D.P. Raymer, *Aircraft Design: A Conceptual Approach* (Third Edition, American Institute of Aeronautics and Astronautics, 1999)

31. C.M. Liersch, M. Hepperle, A unified approach for multidisciplinary preliminary aircraft design, in *CEAS European Air and Space Conference* (Manchester, United Kingdom, 2009)

32. M. Galle, *Ein Verfahren zur numerischen Simulation kompressibler, reibungsbehafteter Strömungen auf hybriden Netzen*. Tech. rep. DLR-Forschungsbericht 99-04. Braunschweig: DLR Institut für Aerodynamik und Strömungstechnik (1999)

33. T. Gerhold, in *Overview of the Hybrid RANS TAU-Code*, vol. 89, ed. by N. Kroll, J. Fassbender, MEGAFLOW - Numerical Flow Simulation Tool for Transport Aircraft Design. Notes on Multidisciplinary Design (2005)

34. D. Schwamborn et al., The DLR TAU-code: recent applications in research and industry, in *ECCOMAS CFD 2006 Conference European Conference on Computational Fluid Dynamics* (Delft, The Netherlands, 2006)

35. N. Kroll, J.K. Fassbender, MEGAFLOW - Numerical flow simulation for aircraft design, Braunschweig, in *Notes on Numerical Fluid Mechanics and Multidisciplinary Design (NNFM)*, vol. 89 (2002)

36. N. Kroll et al., MEGAFLOW - a numerical flow simulation tool for transport aircraft design, in *ICAS Congress 2002* (Toronto, Canada, 2002), pp. 1.105.1–1.105.20

37. S.R. Allmaras et al., Modifications and clarifications for the implementation of the Spalart-Allmaras turbulence model, in *Seventh International Conference on Computational Fluid Dynamics (ICCFD7)* (2012), pp. 1–11

38. S. Freund et al., Parametric model generation and sizing of lightweight structures for a multidisciplinary design process, in *NAFEMS Konferenz: Berechnung und Simulation - Anwendungen, Entwicklungen, Trends* (2014)

39. M.-H.-1.-3. Military. *Composite Materials Handbook, Polymer Matrix Composites: Materials Usage, Design, and Analysis*. Vol.3 of 5. US Department of Defense, June 2002

40. *HyperSizer Documentation*. Collier Research Corporation. Newport News (2015)

41. H. Barnewitz, B. Stickan, in *Improved Mesh Deformation*, ed. by B. Eisfeld et al. Notes on Numerical Fluid Mechanics and Multidisciplinary Design, vol. 122 (2013), pp. 219–243

42. M. Meinel, G.O. Einarsson, The FlowSimulator framework for massively parallel CFD applications, in *PARA 2010 conference* (Reykjavik, Iceland, 6–9 June 2010)

43. L. Reimer et al., Multidisciplinary analysis workflow with the flow simulator, in *Proceedings of the Onera Scientific Day 2012—CFD Workflow: Mesh, Solving, Visualizing*, ed. by C. Benoit et al., vol. 19 (Amphithéâtre Becquerel, École Polytechnique, Palaiseau, 2012), pp. 23–30

44. G. Wilke, Multi-objective optimizations in rotor aerodynamics using variable fidelity simulations, in *39th European Rotorcraft Forum* (2013), pp. 1–13

45. D.R. Jones et al., Efficient global optimization of expensive black-box functions. J. Global Optim. **13**, 455–492 (1998)

46. A. Forrester et al., *Engineering Design via Surrogate Modelling: A Practical Guide* (Wiley, New York, 2008)

47. D.G. Krige, A statistical approach to some basic mine valuation problems on the witwatersrand. J. Chem. Metall. Min. Soc. S. Afr. **52**(6), 119–139 (1951)

48. M. Kintscher et al., Design of a smart leading edge device for low speed wind tunnel tests in the European project SADE. Int. J. Struct. Integr. **2**(4), 383–405 (2011)

49. G.K.W. Kenway et al., Aerostructural optimization of the common research model configuration, in *15th AIAA/ISSMO Multidisciplinary Analysis and Optimization Conference* (Georgia, USA, 2014)

50. T.F. Wunderlich, Multidisziplinärer Entwurf und Optimierung von Flügeln für Verkehrsflugzeuge, in *Deutscher Luft- und Raumfahrtkongress, Aachen*. DGLR-Tagungsband - Ausgewählte Manuskripte DLRK2009-1181 (2009)

Chapter 2
Automated Structural Design of Composite Forward Swept Wings

Sascha Dähne and Lars Heinrich

Abstract This article describes the structural design process within a multidisciplinary environment. A forward swept wing configuration is considered where static divergence has to be avoided by using anisotropic properties of stiffened panels made of CFRP (carbon fibre reinforced plastic). The structural design includes parametric model generation and automated sizing of composite wings. An analytical formulation of stiffened panels is used to investigate different stiffener concepts, where fast analytical failure criteria are applied. The goal is to minimize weight and provide accurate deformations for a coupled process. A parametric study shows the flexibility of the approach as well as the validity of the design concept and the approach for bend twist coupling. Furthermore, the influence of neglecting the load redistribution due to the wings deformation on the wing mass is shown.

2.1 Introduction

Shirk et al. [1] summarized the work on aeroelastic tailoring as: *"...embodiment of directional stiffness into aircraft structural design to control aeroelastic deformation, static pressure or dynamic, in such a fashion as to affect the aerodynamic and structural performance of that aircraft in a beneficial way."* They explained the advantages of composite materials on forward swept wings. Tailoring the primary stiffness direction relative to the structural reference axis introduces a bend-twist

S. Dähne (✉) · L. Heinrich
German Aerospace Center, Institute of Composite Structures and Adaptive Systems,
Lilienthalplatz 7, 38108 Braunschweig, Germany
e-mail: sascha.daehne@dlr.de

L. Heinrich
e-mail: lars.heinrich@dlr.de

coupling which can be used to counteract divergence tendencies of forward swept wings and to increase the aerodynamic performance.

Kruse et al. [2] investigated the bend-twist coupling for various tailoring angles on the forward swept wing LamAiR configuration. It was shown, that the aeroelastic tailoring can eliminate the divergence tendency of a forward swept wing. The influence of aeroelastic tailoring on the structural mass was not investigated because of a missing automatization of the sizing process.

The significant influence of different stiffener concepts on the twist distribution is shown by Bach et al. [3]. Based on identical loads, they examined the differences in deformation behavior of two stiffener concepts on the same wing configuration. The stiffener concept affects the aerodynamic performance, which shows the necessity of taking stiffener concepts into account in early design stages of fluid structure interaction applications.

To consider different stiffener concepts, Collier [4] developed an approach for fast analytical analysis of complex stiffened panels and an integrated finite-element-analysis and design optimization system [5]. The commercial Software HyperSizer [6] is based on such analytical formulations of stiffened panels and provides an interface to various finite-element-solvers.

A first application of an automated structural optimization based on HyperSizer is given in [7], where the influence of aeroelastically tailored composites on structural mass is investigated. An automated sizing was applied on the LamAiR configuration [8]. The mass and the corresponding deformation concerning bending and twist are evaluated and show primary effects of aeroelastically tailored wings. The interaction of aerodynamic loads and deformation was not considered at this point.

Computational Fluid Dynamics (CFD) and Computational Structural Mechanics (CSM) are the two disciplines to be coupled for wing design. In this article a structural analysis in a CFD-CSM coupled iterative process is presented which addresses the required needs of automatization, performance and the structural level of detail required to satisfy the desired needs regarding bend-twist coupled deformations and operational evaluations, like fuel capacity check and fuel mass modeling.

2.2 Model Generation

For interdisciplinary communication, a common dataset is required. The Common Parametric Aircraft Configuration Schema (CPACS) has been developed to establish a unified data model for Multidisciplinary Design Optimization (MDO) [9].

For the creation of structure models, the software DELiS (design environment for thin-walled lightweight structures, written in Python) has been chosen [10]. The core of DELiS is a parametric model generator that supports various levels of detail. Based on a CPACS dataset, DELiS creates an abstract, object oriented model of the aircraft. This model contains all structurally relevant information and enriches it with required data for finite elements. Due to the abstract and finite-element-centric
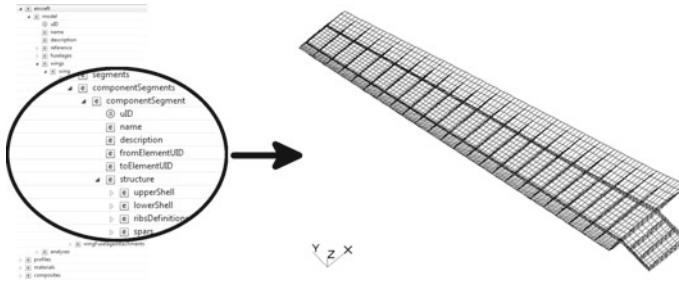
Fig. 2.1 CPACS with structural part highlighted and FE model created by DELiS

definition of the lightweight structure, models for various FE solvers can be created, such as Nastran and Ansys [10].

As starting point for the multidisciplinary optimization, the final configuration from the DLR internal project LamAiR was taken [2]. Neither CPACS nor automated model generation were part of LamAiR, so the outer hull and the structure of that final configuration were translated to CPACS syntax manually. In Fig. 2.1, the conversion of this data set to an FE model by DELiS is shown exemplarily. From the structural side only the wing is being regarded. In the scope of the LuFo IV joint research project AeroStruct, two major enhancements to the automated model generation were implemented, namely the configuration-specific evaluation of fuel masses and secondary masses. As run time plays an important role in pre-design where numerous configurations have to be regarded, the aim in terms of efficiency was to consider load relief by fuel and secondary masses while keeping the overall model generation as fast as possible. For the calculation of the fuel distribution, fuel tanks need to be defined in the data set. Tank regions are based on references to existing ribs and spars. Together with a maximum fill level, accounting for unusable volumes, unmodelled components like pumps, fuel expansion reserves etc., the available volume can be calculated per rib bay and tank. In the next step, the fuel for each load case is then successively distributed on the tanks, whereby the outermost tank is filled first. When fill levels have been determined the fuel mass of each rib bay is applied to a point in the middle of the rib bay, which in turn is connected to the corner points by a Nastran RBE3 element. No rotational inertia is being considered due to the liquid phase of the fuel. In the last step, point masses are converted to forces based on the acceleration of the specific load case. This is necessary to handle different fuel distributions in one FE calculation.

Leading and trailing edge high lift devices are not explicitly modelled. For considering their respective masses, a simplified approach has been chosen which is well established in predesign. Semi-empirical values for these regions are taken from the literature in terms of mass per unit area [11]. Based on these values and the projected areas of the individual configuration, the span wise mass distribution is evaluated. Finally point masses are created per rib bay with the same modeling approach as for the fuel masses (except the conversion to forces as the secondary masses are the same
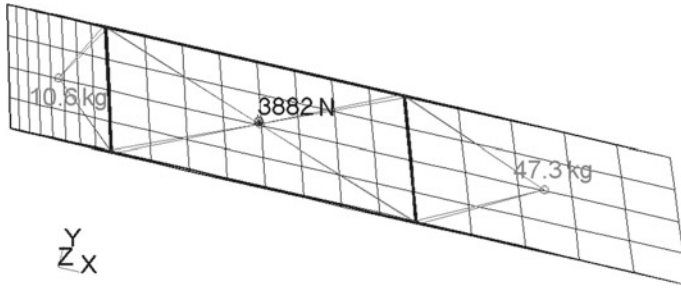
Fig. 2.2 Rib bay with fuel load and secondary masses

across all load cases). Rotational inertia is neglected as it is hardly assessable without further information about the type of high lift device. In Fig. 2.2, the FE representations of fuel and secondary masses are shown exemplary. It should be mentioned, that rib positions are constant along the chord in this case but that is not necessarily the case.

2.3   Composite Sizing

Aeroelastic tailoring is indispensable for natural laminar flow on a forward swept wing like the reference configuration, described in [8]. The strategy to obtain the desired behavior of bend-twist coupling (BTC) is to rotate the primary stiffness direction of the skin and stringer materials. Varying the primary stiffness direction leads to a different behavior of twist and bending. Furthermore the resulting mass due to the sizing process will change.

The aim of the structural sizing and optimization process is the minimization of the structural weight W_{struct} with respect to a set of failure criteria, where all Margins of Safety (MoS) must be above the required limit ($MoS_{required}$). The problem formulation is shown in Eqs. (2.1) and (2.2).

$$\underset{x}{\text{minimize}} \qquad W_{struct}(x), \qquad (2.1)$$

$$\text{subject to } \text{MoS}_{criteria,i}(x) \geq \text{MoS}_{required,i}(x) \qquad (2.2)$$

The developed optimization module, embedded into the global process, is shown in Fig. 2.3. Based on the CPACS file a finite element (FE) model of the wing is automatically generated as described in Sect. 2.2. Wing covers, ribs and spars that are present in the FE model can be used as an optimization region. The external loads are calculated by CFD. These external loads are then mapped to the FE model, where the internal loads are calculated using linear-static FE calculations. Subsequently the
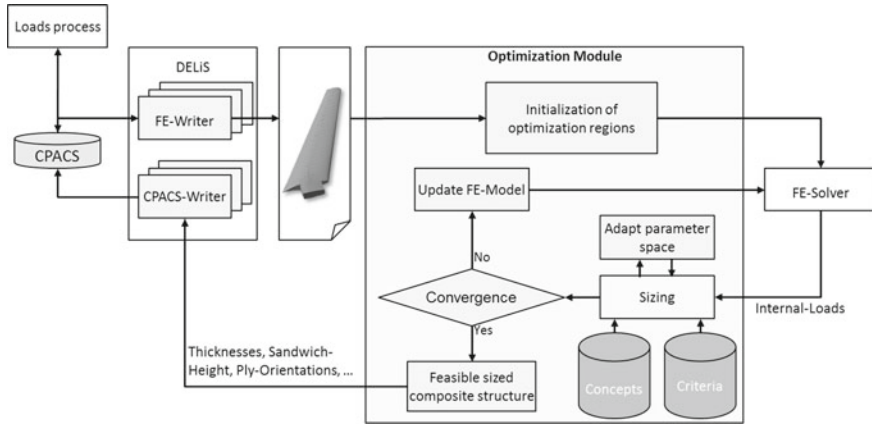
Fig. 2.3 Structural process with CPACS interface, modelgeneration and iterative optimization module

FE model with its geometry, material properties and loads is passed to the sizing and optimization module. Both MSC Nastran and Ansys models are supported.

In the optimization module the geometry is preprocessed and analytical optimization regions, called components and assemblies are created. A component for example can be a panel of a wing cover, confined by two ribs and two spars, or a section of a spar or a rib. Components are the most important subunits as all calculations are performed per component. An assembly comprises all the components of the same part like the wing upper cover or the front spar.The panel concept is assigned to each component in the initialization. By considering the design concept implicitly in the optimization module, it is possible to investigate different design concepts with the same FE model. The stiffness of a stiffener is smeared into the overall panel stiffness matrix, hence the stringers don't have to be discretized and the effort of model generation is reduced. Furthermore an optimization of stringer dimensions and pitch based on a single FE model becomes possible.

Every component has to have failure criteria assigned to it, serving as constraints for the optimization. Necessary failure criteria are evaluated in [7], where global buckling, local buckling and strength are found to be essential in order to obtain reasonable results for mass and deformation. The failure criteria used for structural analysis are shown in Table 2.2. The material used is a CYCOM 977-2 from Cytec Industries Inc. with epoxy resin. There properties are given in Table 2.1. All criteria are evaluated at ultimate load. Damage tolerance constraints are covered by adapted strain allowables. 3500 μm/m are chosen as conservative value for strain allowable at ultimate load as proposed in military handbook [12]. Furthermore it is possible to consider restrictions from manufacturing and operations like minimum and maximum ply share per layer orientation, minimum and maximum height for stringer webs and a minimum skin thickness for repair.

Table 2.1 CFRP material data used

977-2_HTS_MT_025			
Properties		Allowables	
E_x [GPa]	144	F_{t1} [μm/m]	3500
E_y [GPa]	7.5	F_{c1} [μm/m]	3500
G [GPa]	5.03	F_{t2} [μm/m]	3500
ν_{12} [−]	0.29	F_{c2} [μm/m]	3500
ρ [kg/m³]	1660	F_s [μm/m]	7000

Table 2.2 Failure criteria for component analysis

Failure criteria	Limit load	Ultimate load
Global buckling	–	x
Local buckling	–	x
Max strain skin	–	x
Max strain stiffener	–	x

The component sizing itself is performed within the software HyperSizer [6]. An internal object model is created for each component, exemplarily shown in Fig. 2.4 for an integral blade-stiffened panel concept. Other approaches like [13] with discrete stiffeners are not able to consider skin and stiffener simultaneously. For every design parameter of each component, a minimum and maximum value is specified. The number of discrete (equidistant) values between these bounds needs to be specified as well. The parameter can vary between these discrete values. In addition, fixed material sets are provided to consider different ply shares of composite materials. The number of permutations of each component design parameter generates the number of design candidates of a component. It should be noticed that skin and stringer are optimized together. With this approach a change in the stiffness distribution between skin and stringer results in stress redistribution so an optimum design can be found. The stresses are calculated from the internal loads distribution coming from FE calculations and the stiffnesses of the panel objects, like skin, stringer web, etc.

After a sizing step, when all parameter values are chosen, the FE model is updated with the new stiffness results and new internal loads are calculated for the next iteration. Convergence checks, based on the mass of the wing box, are done in every iteration considering all MoS as shown in Eq. (2.3). The allowed change of mass is determined by the process in dependence on current fluid structure iteration step. At the first iteration $\Delta m \leq 10\%$ leads to a good first mass and stiffness estimation for the next aerodynamic load calculation. Step by step the Δm-criteria is reduced down to $\Delta m \leq 0.5\%$ for the final convergence of aerodynamic and structural analysis.

$$\Delta m = (m_i - m_{i-1})/m_{i-1} \, MoS \geq MoS_{required} \qquad (2.3)$$

Fig. 2.4 Panel parameter of a integral-blade-stiffened concept

t_{skin}	skin thickness
t_{web}	web thickness
$s_{stringer}$	stringer spacing
$h_{stringer}$	stringer height
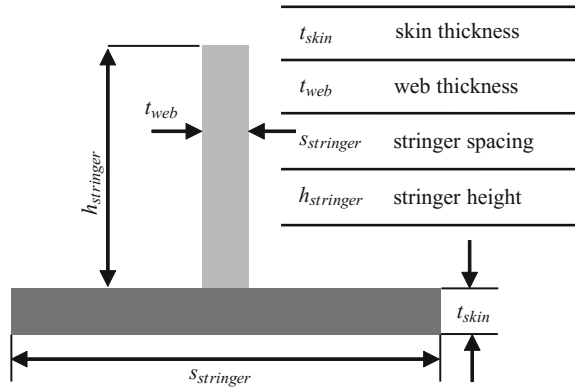
To improve the performance, results from prior fluid-structure-iteration steps are used as restart points. This increases the convergence speed due to decreasing aerodynamic load changes at further iterations. A faster convergence of structural sizing and the overall coupled process is achieved this way. If the convergence criterion is fulfilled the results are exported from the optimization module and the CPACS file is updated with the results.

2.4   Iterative Loads Process

The automated coupling between structural design and CFD-loads calculation is mighty tool. This coupling allows to investigate the effects of bend-twist coupling. CFD-analyses are performed for the calculation of aerodynamic loads. FE analyses and sizings ensure that the structure is able to withstand these loads and yield expected deformations. As loads and deformations are dependent on one another, both have to be considered. Therefore, an explicitly coupled iterative process, composed of the following steps, is applied.

1. Aerodynamic loads calculation with CFD,
2. structural sizing considering the previously calculated loads,
3. return to step 1 with resulting deformed shape of step 2.

The first aerodynamic loads are calculated for the undeformed wing. The structural optimization process allows the determination of deformations. These global deformations are used for the next CFD-calculation until a balance in load and deformation is achieved. The converge loads allows a accurate wing mass, deformations and the corresponding aerodynamic performance estimation. The complete fluid-structure interaction process is described in Sect. 1.2.7. The resulting aerodynamic forces are mapped on the outer surface nodes of the structural FE-model. Figure 2.5 exemplarily shows the aerodynamic loads mapped on the upper surface of a panel segment.
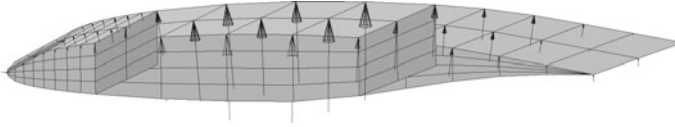
Fig. 2.5 Aerodynamic loads maped on FE panel segment

Four load cases are considered, which are described in detail in Sect. 1.4.1. One cruise load case and three structural relevant design load cases are taken into account with positive and negative accelerations. The performance assessment is conducted for the cruise load case. The structural optimization considers all loadcases in parallel and provides the corresponding deformations for all of them.

2.5 Approach for Structural Bend-Twist Coupling

The approach for introducing a bend-twist coupling is to rotate the principal stiffness direction of the material. Thereby the complete composite layup is rotated around the z-axis.

This rotation leads to a structural coupling of wing bending and twist. The rotation is realized by defining a reference coordinate system for the material orientation in the finite element model. The material properties are defined symmetrical and balanced with respect to the reference coordinate system. The global structural BTC of the wing is then obtained by rotating the whole reference system around it's z-axis. In addition to LamAiR the structural concept is evaluated in more detail, while besides the global stiffness effects of stiffeners, which are considered in LamAiR as well, additionally the akin local buckling and strength and stability of stiffeners are taken into account. The evaluation of analytical concepts as described in Sect. 2.3, allows considering detailed failure modes and the correct representation of the global panel stiffness.

The angle between the reference orientation and the rotated one is called orthotropy angle in the following. The zero degree direction is the 50% chord line. A positive angle means that material orientation axes will be rotated more aft ward. Negative angles mean that the principal stiffness direction will be rotated forward in flight direction as shown in Fig. 2.6.

The stringer orientation is directly coupled with the material orientation, due to the analytical formulation. While rotating the principal stiffness direction, the material orientation is rotated and therefore the stiffener orientation is rotated as well. The stiffener rotation increases the bend-twist coupling. Simultaneously the load capability of the stiffener decreases due to the off axial loading. Additional load has to be carried by skin, due to load redistribution.

Fig. 2.6 Definition of orthotropy angle definition of left wing (top view)
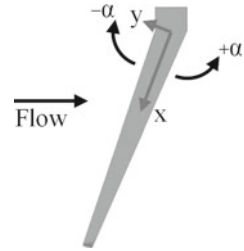
Fig. 2.7 Comparisson of I- and T-stiffener concepts in deformation behavior in cruise condition
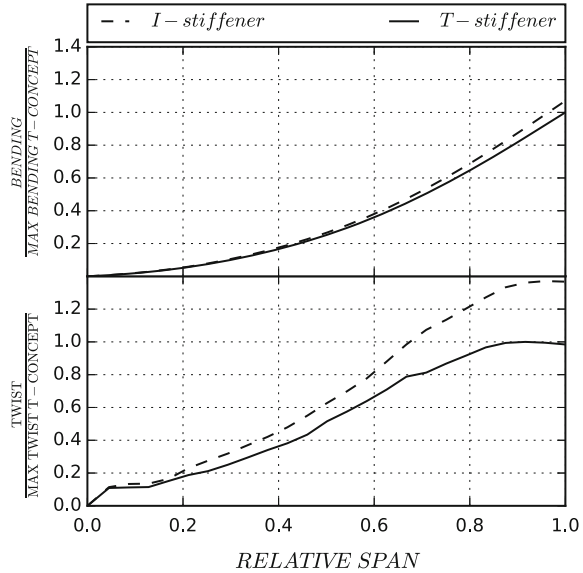
2.6 Structural Design Study

To clarify the influence of different stiffener concepts, Bach et al. [3] investigated T- and I-stiffener concepts for the wing cover on the same wing configuration. The wing configuration equals the LamAiR reference [2]. It is a forward swept wing with 36 m span and a leading edge sweep angle of $-17°$. The structural sizing process described in Sect. 2.3 is used to size the structure against fixed aerodynamic loads given by a coupled fluid-structure-interaction process performed once in the LamAiR project. Figure 2.7 shows the deformation behavior of the different concepts after sizing, where similar masses are achieved with only 1.5% difference. The heavier T-stiffener concept is used as reference to illustrate the difference in the deformations. The I-Stiffener concept leads to lower bending and torsional stiffness. In contrast to the small difference in mass, the I-stiffener has up to 37% higher twist in the tip region and 7% higher vertical deflection.

Evaluating the stiffener type and mass breakdown discussed in detail in [3], it can be stated that the I-stiffener generates a high local bending stiffness preventing the upper cover panels from global buckling. On the other hand the longitudinal stiffness of upper cover is smaller compared to the T-stiffener so more panels are dimensioned by local buckling. This reduced inplane stiffness is one of the reasons for the higher twist. Furthermore the feet of the T-stiffeners are wider and thicker than the ones of the I-stiffeners, so this additional material with a larger distance from the wing box neutral axis increases torsional and bending stiffness. As a last point, the additional flange of the I-stiffeners help preventing the stiffeners' webs from local buckling, so the I-stiffener webs are thinner than the T-stiffener webs. As a results, the area moment of inertia of the I-stiffened wing cover is smaller and hence the global bending stiffness is smaller too.

A forward swept wing has a geometrical bend-twist coupling, which produces a wash-in effect. Wash-in means that bending leads to nose-up twist and an increased angle of attack. This behavior can cause static divergence, where nose-up twist leads to higher aerodynamic loads which can not be compensated by the structural stiffness anymore and the wing fails through strength. The idea is compensate this wash-in effect with superimpose structural bend-twist coupling that causes a wash-out behavior. The effectiveness of the structural bend-twist coupling approach is now investigated by applying the coupled multidisciplinary process explained in Sects. 1.2 and 2.4 on a model with integral blade stiffeners as shown in Fig. 2.4. Two studies are discussed in the following:

1. A variation of the principal stiffness direction and it's impact on wing mass and deformation. Therefore, the abovementioned iterative coupled process is applied.
2. A comparative study with fixed loads to evaluate the impact of the fluid-structure-interaction.

The coupled process performs until the mass and the loads does converge and the deformations and loads are in balance. The uncoupled study considers only the uncoupled loads from the undeformed reference configuration to illustrate the difference of aerodynamic-structure coupled analyses.

The outer shape is taken from the LamAiR reference and is held constant for the present studies to show only the structural influences. The FE model is generated automatically by the model generation process described in Sect. 2.2. The principal stiffness direction has been varied between -30 and $+5°$. The material ply-share of the ribs, spars and the wing cover skins are fixed at LamAiR reference results given in Table 1.5. In the root region, the effectiveness of bend-twist coupling is higher than in the tip region. From root to tip, the percentage of $0°$-plies decreases from 70 to 40% at wing covers, to ensures a distinct principal material stiffness direction of the skin material to ensure bend-twist coupling. The web material ply share is not fixed because a reference does not exist for stiffener material distribution.

Figure 2.8 shows the results of the coupled and uncoupled processes for the same wing configuration. The desired wash-out behavior is present if the orthotropy angle is rotated forward for both processes as desired to compensate the geometrical bend-

Fig. 2.8 Comparisson of coupled and uncoupled results with given orthotropy angles and deformations from cruise load case
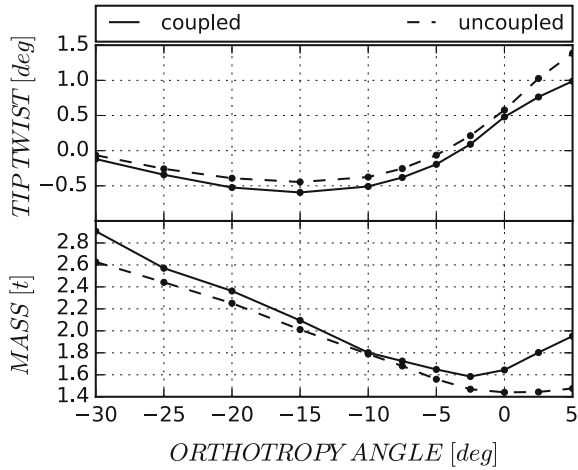
twist-coupling. Between −5° and all positive angles a global wash-in behavior is present. The coupled process leads to smaller tip-twist angles.

The masses in Fig. 2.8 show that the coupled process has over the whole range of orthotropy angles higher masses. In the uncoupled process, the minimum is found around 0° or higher. The coupled process considers the elastic deformations and therefore the load increase through the geometrical bend-twist coupling. The minimum mass in the coupled process is around −2.5°, which shows the load relief through structural wash-out behavior. At −10° the masses of the coupled and the uncoupled processes are equal. Here the structural bend-twist coupling compensates the geometrical coupling completely and yields to nearly equal loads. −10° was also found by LamAiR-project to be the most efficient angle for BTC [2].

The tip bending behavior is different to twist and mass as shown in Fig. 2.9. This different behavior results from the parallel rotation of principal stiffness of skin and stringer orientation. Figure 2.9 shows on the middle plot the portion of stringer volume relative to the panel volume. Because of equal ply-material the volume is representative for mass. To clarify the effect the results are split in three nearly equal distanced regions over the wing span. The values from upper and lower wing cover are averaged for each region and plotted over the orthotropy angle. A clear correlation between the mean inner wing relative stringer volume and the bending deflection in Fig. 2.8 can be found. From 0 to −10° the relative stringer portion decreases, which increases the bending stiffness. In association with the increased skin thickness, due to higher shear loads in the skin, the bending deflection decreases. With an increased area moment of inertia, the associated bending deflection decreases. For angles lower than −10° the portion of stringer volume increases again and the skin volume increases further as shown in Fig. 2.9 on the lower side, but the overall stiffness decreases due to the rotation of the principal stiffness direction off the load axis.

Fig. 2.9 Bending behavior
in cruise condition in
conjunction with stringer
volume ratio and skin
thickness
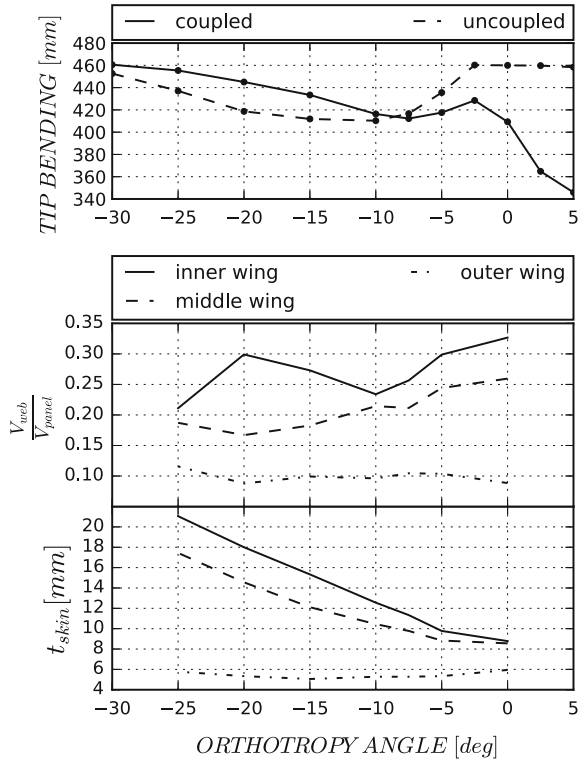
Fig. 2.10 Masses and fuel
consumption for design
mission
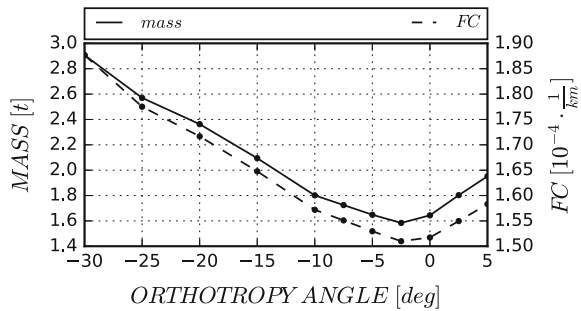
The mission performance is represented by the fuel consumption per payload mass and range. The mission objective is described in more detail in Sect. 1.4.2. In Fig. 2.10 the fuel consumption is plotted in conjunction with wing mass. A close correlation between wing mass and fuel consumption can be found for small orthotropy angels. A minimum fuel consumption is found at $-2.5°$, which shows the positive effect aeroelastic tailoring.

2.7 Conclusion

The present article shows the influence of structural details, like stringer orientations and stiffener concept, on the global deformation behavior for a forward swept composite wing. The complexity of structural coupling with regard to structural sizing and load redistribution between skin and stringer have been shown. With an analytical approach for stiffened panel analysis, effects of different stiffener concepts are taken into account. An optimal wing mass is found slightly off the reference axis, through coupled analyses at $-2.5°$. The possibilities of stiffened composite panels to counteract static divergence and the improvement of mission performance show the effects of aeroelastic tailoring in accordance to the description of Shirk et al. [1].

References

1. M.H. Shirk, T.J. Hertz, T.A. Weisshaar, Aeroelastic tailoring - theory, practice, and promise. J. Aircr. **23**(1), 6-18 (1986). https://doi.org/10.2514/3.45260. ISSN 0021-8669
2. M. Kruse, T. Wunderlich, L. Heinrich, A Conceptual study of a transonic NLF transport aircraft with forward swept wings, in *Fluid Dynamics and Co-located Conferences* (American Institute of Aeronautics and Astronautics, 2012). https://doi.org/10.2514/6.2012-3208
3. T. Bach, L. Heinrich, S. Dähne, C. Hühne, Structural optimization of composite wings in an automated multi-disciplinary environment, in *AIAA Aviation Technology, Integration, and Operations Conference* (American Institute of Aeronautics and Astronautics, 2014). https://doi.org/10.2514/6.2014-2295
4. C.S. Collier, Thermoelastic formulation of stiffened, unsymmetric composite panels for finite element analysis of high speed aircraft. in *Proceedings of 35th conference AIAA/ASME/ASCE/AHS/ASC structures, dynamics, and materials conference. AIAA* (1994), S. 941579
5. C.S. Collier, An integrated FEA and design optimization system for composite structures / DTIC Document. Forschungsbericht (1996)
6. HyperSizerHelp, *HyperSizer Documentation*. Newport News: Collier Research Corporation (2015)
7. D. Sascha, B. Tobias, H. Christian, *Steps to Feasibility for Laminar Wing Design in a Multidisciplinary Environment, ICAS* (St. Petersburg Russia, 2014)
8. A. Seitz, M. Kruse, T. Wunderlich, J. Bold, L. Heinrich, The DLR project LamAiR: Design of a NLF forward swept wing for short and medium range transport application, in *Fluid Dynamics and Co-located Conferences* (American Institute of Aeronautics and Astronautics, 2011). https://doi.org/10.2514/6.2011-3526
9. B. Nagel, D. Böhnke, V. Gollnick, P. Schmollgruber, A. Rizzi, G. La Rocca, J.J. Alonso, Communication in aircraft design: can we establish a common language? in *28th Congress of the International Council of the Aeronautical Sciences 2012* Bd. 1, 2012. ISBN 978-1-62276-754-0, S. 443–455
10. S. Freund, F. Heinecke, T. Führer, C. Willberg, Parametric model generation and sizing of lightweight structures for a multidisciplinary design process, in *NAFEMS Konferenz: Berechnung und Simulation - Anwendungen, Entwicklungen, Trends* (2014)

11. E. Torenbeek, *Synthesis of Subsonic Airplane Design* (Delft University Press, Delft, 1982). ISBN 9024727243
12. Military, MIL-HDBK-17-3F, Composite Materials Handbook, Polymer Matrix Composites: Materials Usage, Design, and Analysis. in *US Department of Defense* 17 (2002)
13. A. Deblois, M. Abdo, Multi-Fidelity multidisciplinary design optimization of metallic and composite regional and business jets. in *Multidisciplinary Analysis Optimization Conferences* (American Institute of Aeronautics and Astronautics, 2010). https://doi.org/10.2514/6.2010-9191

Chapter 3
Design Procedure for Optimum Fiber Composite Airframe Structures Within an Automated Multidisciplinary Design and Optimization Process

Michael Seibel

Abstract This paper presents a concept and setup of a design procedure for optimum fiber composite airframe structures within an automated multidisciplinary design and optimization process. The optimization procedure is based on the Three-Columns-Concept, using a state-of the-art Finite-Element-Method (FEM) software for structural analysis purposes embedded into a multidisciplinary optimization software. The optimization model is formulated for traditional civil aircraft designs, providing maximum design flexibility in order to tailor-made the characteristics of fiber composite materials, including aeroelastic tailoring. Therefore, the design domain includes both, geometry and laminae related design variables. In doing so, a strict separation of the design model from the analysis model is implemented. The evaluation model includes all important structural design objectives, like mass, deformations (e.g. wing bending and twisting), local and global buckling behavior (classical eigenvalue analysis), strength as well as damage tolerance. Aggregation methods are applied to reduce the tremendous number of constraints and to improve the robustness of the optimization process. Finally, optimization results of a forward swept wing configuration, optimized with respect to structural design objectives, are presented.

3.1 Introduction

The optimization of large and complex aerospace structures made from fiber composite materials, considering multidisciplinary design requirements, is the starting point of the methods and procedures outlined hereafter. One of the fundamental disciplines

M. Seibel (✉)
University of Applied Sciences, Hamburg, Germany
e-mail: michael.seibel@haw-hamburg.de

is the structural design in order to fulfill basic demands throughout the development process. Therefore, the requirements posed on the structural optimization procedure to be used in a multidisciplinary tool chain are described as well as the structural design features to be considered within the optimum structural design (Sect. 3.2). A brief literature survey (Sect. 3.3) provides an insight into past and current work concerning relevant topics. Subsequently (Sects. 3.4 and 3.5) the main features of the design and optimization procedure are outlined. The developed numerical optimization tool is finally applied to optimize a forward swept wing (Sect. 3.6). The achieved results and findings are summarized (Sect. 3.7) in order to conclude the documentation.

3.2 Requirements of the Structural Optimization Procedure

A structural optimization procedure to be used in a multidisciplinary tool chain has to cope with basic requirements, independent from the software framework used for its implementation. The top level requirements of an optimization procedure may be defined as:

- Parameterized, in order to:
  - fully control the optimization procedure and the optimization model,
  - automatically generate the structural model via the design model,
  - efficiently evaluate analyses results via the evaluation model.

- Modular, in order to enable:
  - a straightforward implementation in a multidisciplinary optimization software, or an usage as a stand-alone tool,
  - an easy implementation of self-made modules and extensions,
  - a subsequent substitution or enhancement of applied mathematical models.

- Flexible, in order to allow:
  - the usage of different structural analysis types or models, varying properties or net densities of Finite-Element-Models,
  - the usage of different optimization algorithms or global optimization methods.

- Robust and efficient, in order to provide:
  - a reliable optimization process,
  - short to moderate analysis and optimization times.

3.3 Literature Survey

A brief survey of relevant topics related to *optimum structural design of fiber composite airframe structures* is provided. Emphasis is put on the formulation of efficient optimization models that allow to extend the design domain of fiber composite structures as much as possible.

Structural and Multidisciplinary Optimization

The fundamentals of structural optimization, developed in the second half of the 20th century, can be found in [2, 7, 13]. They describe in detail relevant optimization concepts, methods and formulations for constrained and unconstrained problems. In [5], an overview of multicriteria optimization is provided that may serve as a basis for coupled aero-structural problems. Furthermore, several optimization problems from various engineering disciplines are presented as challenging applications with respect to structural and multidisciplinary optimization.

An excellent survey concerning different architectures of how to solve problems of *Multidisciplinary Design Optimization (MDO)* is given in [12].

For solving large, multidisciplinary optimization problems, the so-called *Three-Columns-Concept* is proposed in [4], that suggests to strictly separate between the three tasks, i.e. three columns, structural model, optimization algorithm and optimization model. An example of a high-performance computing platform for systems analysis and multidisciplinary optimization is OpenMDAO [10], developed at the NASA Glenn Research Center.

Optimization of Fiber Composite Airframe Structures

For optimizing airframe structures very different approaches and methods may be found in the literature. The most common objective function is the minimization of the weight, while the most common constraints are strength, buckling and stiffness. The design objective damage tolerance may only be found occasionally.

Optimizations of a multispar high aspect ratio wing were conducted in [25], by introducing the above mentioned constraints through penalty functions. Minimum mass designs were obtained and compared for aluminum-alloys and fiber composite materials. An optimization of a typical long range transport aircraft wing using a two-level approach and a non-gradient based, probabilistic optimization algorithm (particle swarm) is presented in [28]. The aerodynamic optimization takes place at system level, while the structural optimization is conducted in form of a subproblem. An alternative two-level approach for optimizing a simple composite wing-box is applied in [15]: at wing level, a layer thickness optimization based on response surfaces was performed, while at panel level the number of layers and stacking sequence was genetically optimized. A multilevel optimization of a blended wing body aircraft is analyzed in [8], using an evolutionary strategy in the first level for optimizing the wing topology and a gradient-based optimization in the second level for optimizing the layer thicknesses. The separation of topology variables from sizing variables in two different levels indicated a better efficiency than mixing them in one optimization task. A two-level optimization strategy is also documented in [30]

for large-scale composite wing structures. The objective is the minimization of the structural efficiency (i.e. efficiency factor calculated based on the failure coefficients of buckling and strength). A Finite-Element-Model is used for the load extraction, buckling loads are calculated using an energy method and a surrogate model, and empirical formulas are used for static strength. In [3] a preliminary optimization routine for optimizing aircraft stiffened panels is developed. The upper stringer-stiffened panels are optimized using analytical local and global buckling constraints, while the lower panels are optimized considering fatigue constraints. An adapted genetic algorithm was applied in [1] for the design optimization of composite panels, associated with FE-analyses to cope with weight and stiffness related objectives.

Parametric Optimization Models for Fiber Composite Structures

In order to take full advantage of fiber composite material capabilities, their design domain with respect to optimum layer thickness distributions and fiber orientations must be exploited. The latter one may consider straight or curvilinear fiber paths.

A fundamental elaboration about constructive design models for multidisciplinary optimization of fiber composite structures is provided in [19, 20]. Thickness distributions of individual layers of the considered laminae are described with Beziér functions. The resulting, continuously defined Beziér surfaces are translated into individual element thicknesses of the applied Finite-Element-Model. The same approach is used to define the curvilinear fiber path of individual layers, whereas only one path of a unidirectional tape (prepreg) must be described mathematically. All other tapes to be applied in one layer must string together (without gap or overlap).

The application of cellular automata for curvilinear fiber design of fiber composite laminae for in-plane responses are investigated in [24]. In [11] a cubic polynomial function is introduced to define curvilinearly shaped fibers. These publications pursue the objective to optimally orientate the fiber paths in accordance with the main stress axis, simultaneously considering the manufacturing capabilities and limitations of fiber placement technologies.

The flexibility of these parametric design models is used in [21, 26] to not only define the fiber design of composite laminae, but to describe geometrical and sizing properties of the structural model as well. Thus, having the same approach for treating geometrical as well as laminae specific design features within the optimization loop.

Aggregation Methods for Large Scale Problems

Constraint aggregation is suggested as the key for efficiency, when treating large structural optimization problems. The traditional constraint aggregation method, the Kreisselmeier–Steinhauser function (KS-function), is described in [14]. It reduces the number of constraints drastically and returns a conservative estimate of the considered constraints. Its disadvantage is the poor accuracy of the conservative estimate, that is most prominent when constraints are active and increases with the number of active constraints. A variety of publications deal with this shortcoming and suggest improvements. Three of them may be cited as representative: [6, 16, 23].
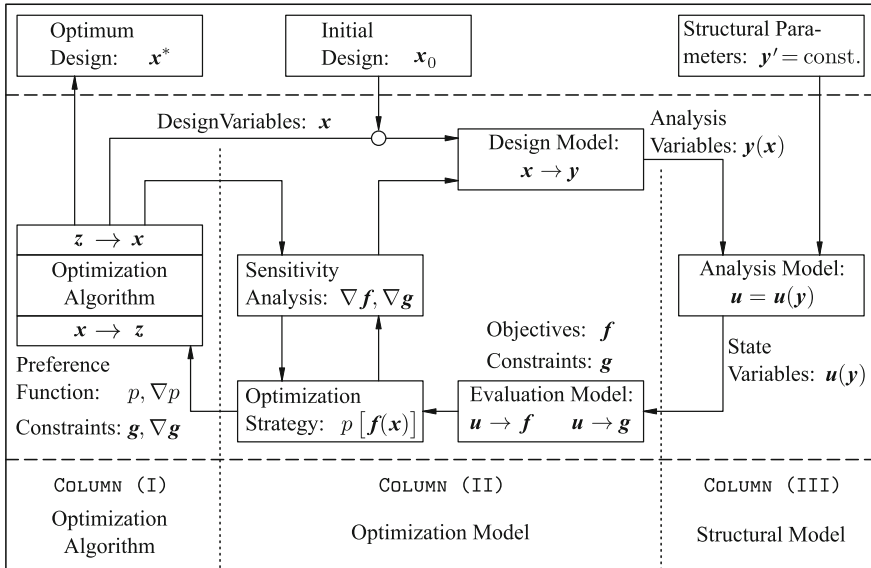
Fig. 3.1   Control loop of the Three-Columns-Concept for solving problems in optimum structural design, according to [4]

3.4   Optimization Model for Fiber Composite Airframe Structures

The implementation of the top level requirements defined in Sect. 3.2 is achieved by applying the so-called *Three-Columns-Concept* as outlined in [4] and depicted in Fig. 3.1. The concept strictly distinguishes between the three tasks of an optimization procedure, namely:

- Column (I): *Optimization Algorithm*
  Regarding the development and availability of optimization algorithms, extensive publications have been made and their programming is implemented in state-of-the-art optimization software suites. Hereafter, gradient-based algorithms are of special interest, as they are applied for the conducted optimization work, i.e. sequential quadratic programming (SQP) algorithms, as described in [18].
- Column (II): *Optimization Model*
  The optimization model, as outlined in further detail in Sect. 3.4, consists mainly of the design model (translating design variables into analysis variables), the evaluation model (translating analysis results into objective functions and constraints) and the optimization strategy (e.g. treatment of multi-objective optimization problems or aggregation of constraints).
- Column (III): *Structural Model*
  The applied structural model is a Finite-Element-Model, in order to provide the

required level of structural detail. A description of its configuration and structural features is given in Sect. 3.5.

3.4.1 Design Model Using the Example of an Aircraft Wing

The design model provides a full-parametric mathematical model that describes essential parts of the structural geometry and the laminae definitions of individual structural components.

Laminar Design Features

For all wing components, i.e. covers, spars, ribs and stringers, individual laminae layer thicknesses and layer orientations may be used as design features, whereas the stacking sequence is treated as fixed.

The thickness distributions of the layers are described by means of parametric Beziér functions, whereas the coordinates of the control points serve as design variables. Thus, a decoupling of the design model from the analysis model is achieved, i.e. the design variables are not directly associated with analyses properties. By implication, a dedicated step to map the thickness distributions to the Finite-Element-Model becomes mandatory. Figure 3.2 describes the approach, using the upper cover as example.

Furthermore, each layer of the laminae may have an offset angle as design variable, or alternatively, the complete laminae may have one uniform offset angle.

Geometric Design Features

Throughout the structural optimization process, the geometry data describing the general wing configuration, like sweep angle, airfoil geometry and wing-span, are not considered as design features. That applies also to geometry data described by discrete numbers (number of spars, ribs, stringers). Design features that are considered in the optimization process are:

- Positions of front and rear spar
- Positions of ribs in span-wise direction
- Positions of stringers in chord-wise direction
- Heights of stringers (T-stringers assumed)

3.4.2 Evaluation Model Using the Example of an Aircraft Wing

The evaluation model comprises essential responses that are mandatory for a sound structural optimum design:
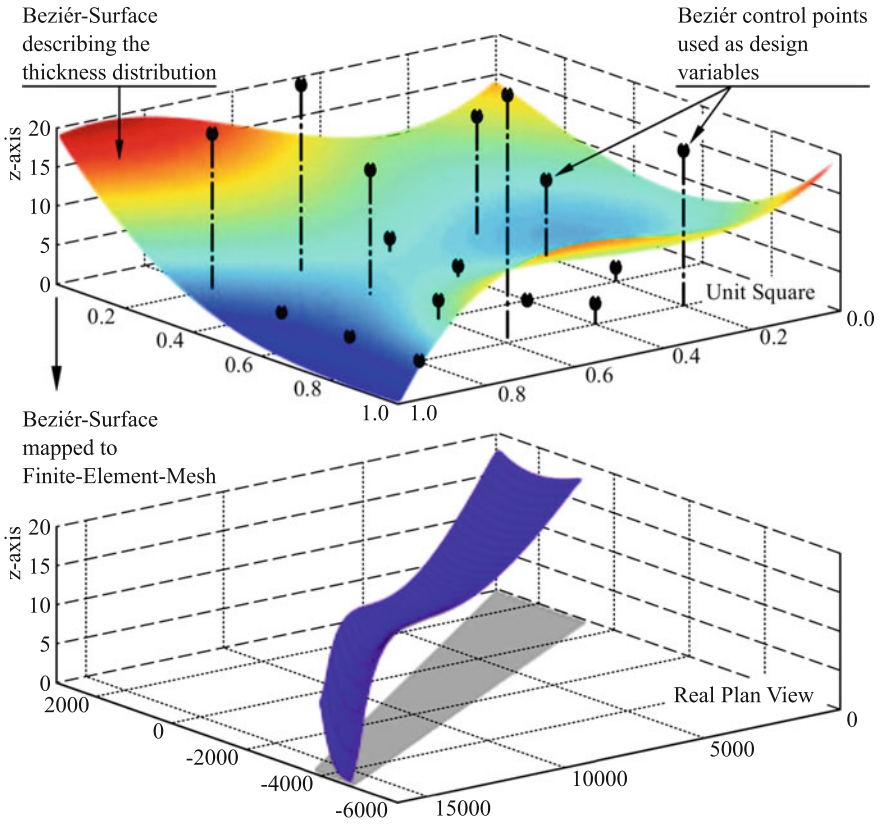
Fig. 3.2 Fiber composite material: thickness distribution of a layer, continuously described in form of a Beziér surface and mapped to a FE-mesh

- Mass
  The mass is extracted from the FE-analysis output (without any contingency) and represents the structural mass exclusively.
- Strength
  The strength assessment is done for each finite element and each layer based on the first-ply-failure approach. The applied failure hypotheses are Hashin [9] and Puck [17]. In order to reduce the number of individual results, constraint aggregation is applied.
- Damage tolerance
  The damage tolerance assessment is a based on strains, targeted to guarantee the no growth policy of laminae. As every finite element may have individual results, aggregation methods are used as well.
- Stability (Buckling)
  The consideration of buckling phenomena is based on a classical eigenvalue analysis, that allows to identify local and global buckling modes. Thus individual

constraints and associated limits are considered. A global mode is characterized through:

- Buckling of upper or lower cover with stringers
- Buckling of ribs
- Buckling of front or rear spar

- Stiffness, elastic deformation (aeroelastic tailoring)
  The objective aeroelastic tailoring is embedded by limiting the elastic deformations at designated positions (wing stations). The torsion of the wing is explicitly evaluated at the ribs by processing the circumferential rib deflections.
- Constraint aggregation
  Constraint aggregation is applied to cope with the tremendous number of constraints resulting from strength and damage tolerance results as well as to cope with local and global buckling constraints. The applied mathematical method utilizes the function of Kreisselmeier and Steinhauser (KS-function) [14].

3.5 Structural Model

FE-analyses are mandatory due to the complex structural configuration of the wing and the envisaged analysis types and results. All structural components as depicted in Fig. 3.4 (covers, spars, ribs, stringers) are modeled using 2D rectangular linear shell elements, whereas the individual components are joined by coincide FE-nodes. The geometry of the wing describes its outer contour, thus all surface normal vectors are oriented to the inside of the wing box and the reference surfaces of the associated laminae are defined accordingly.

External loads are introduced into the wing structure by means of rigid body elements placed at every rib station. The resultant transverse forces and torsion moments are derived for specific load cases from calculated pressure distributions.

The fiber composite materials are T800/M21 (unidirectional prepreg) for the $0°$ and $90°$ layers and HTA M-21 (fabric) for the $±45°$ layers. The stacking sequence is identical for all structural components: [$0°$ $±45°$ $90°$]$_s$.

The parametric setup of the Finite-Element-Model is depicted in Fig. 3.3, that shows seven dedicated modules for the its generation and four data files, containing the following data:

- Control:
  Contains data to run the Finite-Element-Model generation within the optimization procedure.
- Wing data:
  Contains geometry data (e.g. wing-span, sweep angle, airfoil, etc.), that may result from a superior multidisciplinary design procedure, or from the design model of the structural optimization (e.g. position of spars, ribs and stringers).
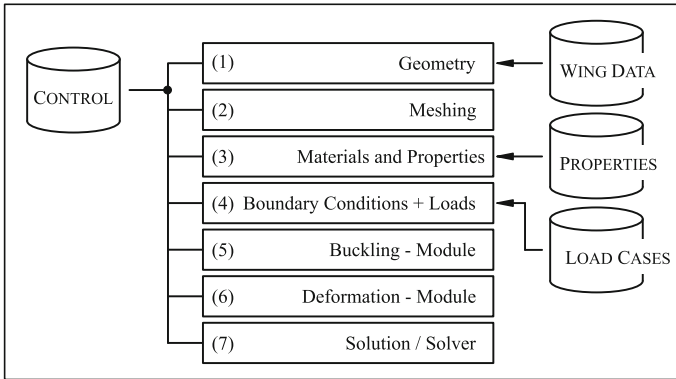
Fig. 3.3 Automated and parameter based Finite-Element-Model generation

- Properties:
  Contains property data necessary for the structural analysis (e.g. layer thicknesses, layer orientations, etc.).
- Load cases:
  Contains loading conditions for different load cases, e.g. derived from calculated pressure distributions. The data may result from a superior multidisciplinary design procedure.

3.6   Use Case: *ForSwing*

A forward swept wing (so-called *ForSwing*) made of fiber composite materials is the use case considered hereafter. The overall objective is to develop an optimum design, considering aerodynamic and structural requirements simultaneously, employing natural laminar flow characteristics at minimum structural weight. However, the main focus of the work documented is solely put on optimum structural design.

3.6.1   Baseline Design of the Use Case

The baseline structural design of the use case *ForSwing* is based on [22]. It represents a traditional 2-spar wing box configuration with ribs and stringer-stiffened covers, as shown in Fig. 3.4. The leading and trailing edges as well as the high-lift devices are not considered in the structural model. Furthermore, the center wing box is not included in the optimization model. The size of the wing box as well as the airfoil is based on a single aisle civil aircraft, like an Airbus A320. One of the fundamental
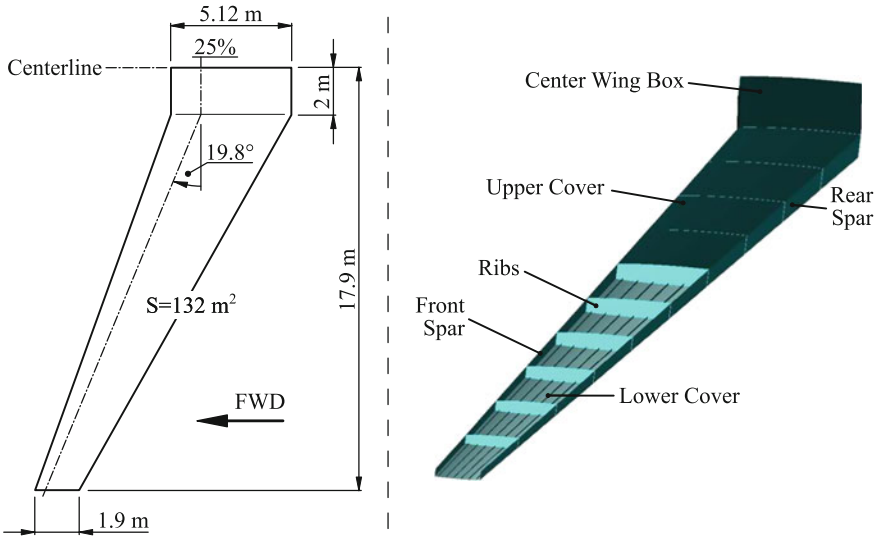
Fig. 3.4 Use-case *ForSwing*: top view of the baseline wing geometry (on the left) and structural configuration, with upper cover partly removed (on the right)

load cases is a gust load case, equivalent to $n_z = 3.44$ (*Limit Load*), that will as well be used for optimization purposes in the subsequent sections.

3.6.2 Definition of the Optimization Model

The purpose of the model definition shown hereafter is to illustrate the performance of the developed structural optimization process. Due to the coarse FE-mesh and the simplified laminae definitions, the achieved results are derived for demonstration purposes rather than serving as an input for a substantiation report. The model settings are defined as:

(A) Objective function:
Mass (as derived from the Finite-Element-Model)
(B) Design variables (86 overall):
z-coordinates of the Beziér control points (c.f. Fig. 3.2), used to describe the layer thickness distributions of individual layers of laminae used for the wing components: upper and lower cover; front and rear spar; ribs.
Generally applied stacking sequence: [0° ±45° 90°]$_s$
(C) Aggregated constraints (via KS-functions)
   – Strength
   – Damage tolerance
   – Local and global buckling

(D) Non-aggregated constraints
      Stiffness, aeroelastic tailoring (bending and torsion)
 (E) Finite-Element-Model
      – Model size: 28152 d.o.f.
      – Ribs: 15
      – Stringers: 12 (6 per upper and lower cover)
      – Load case: Gust with $n_z = 3.44$ (*Limit Load*)
 (F) Optimization algorithm
      NLPQL (Non-linear Programming by Quadratic Lagrangian)

3.6.3   Optimization Results

The optimization results are focusing on three topics that have been highlighted in
Sect. 3.4, viz. the parametric thickness distribution of individual layers, the aggre-
gation of constraints and the independent consideration of local and global buckling
modes.

Thickness Distribution of Individual Layers (Laminae of Upper Cover)

The thickness distributions of $0°$, $\pm45°$ and $90°$ fiber orientations of the upper cover
at four stages in the optimization process are plotted in Fig. 3.5. They are projected
over the wing top view, whereas the height represents the thickness of the individual
layers in each finite element. The optimization process starts (initial design) with
equally thick layers and reaches an almost converged solution after 14 iterations.
The remaining iterations are for the sake of numerical accuracy only.

Aggregated Constraints (Strength)

The optimization behavior of a strength constraint is described by means of the $0°$
layer of the upper cover using the failure hypotheses of Hashin (Tape). The strength
requirements are not directly (for each individual element and layer) considered in
the optimization model, but in form of aggregated constraints. Thus, as shown in
Fig. 3.6, 924 individual reserve factors (drawn as red lines) are aggregated in one
single constraint (blue line, lower limiting curve) using a KS-function.

Local and Global Buckling Constraints

The consideration of the stability behavior is based on a classical eigenvalue analysis.
The optimization results shown in Fig. 3.7 indicate that the applied method is able
to identify local and global buckling modes as defined in Sect. 3.4.2 from a set of
eigenvalues (approx. 30) at the lower bound of the spectrum. The eigenvalues of the
local buckling modes are aggregated in a single constraint by means of a KS-function,
requiring a minimum eigenvalue of

$$\lambda_{\text{min, local}} \geq 1.0 \cdot (\text{Limit Load}) \, .$$
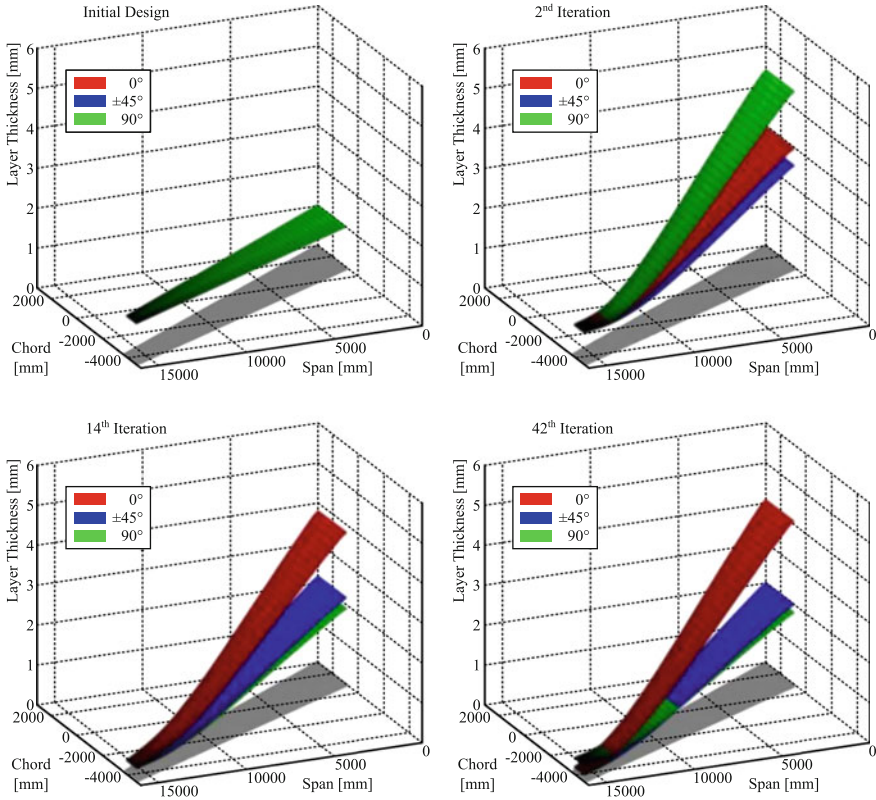
Fig. 3.5 Thickness distributions of 0°, ±45° and 90° fiber orientations of the upper cover at four stages in the optimization process

The eigenvalues of the global buckling modes are treated accordingly with a constraint limit of

$$\lambda_{\text{min, global}} \geq 1.2 \cdot (\text{Limit Load}) .$$

3.7 Achievements and Findings

The work presented herein shows, that major objectives of the optimization procedure for designing optimum fiber composite airframe structures within a multidisciplinary optimization process have been achieved:

- The optimization process is strictly applying the rules of the *Three-Columns-Concept*. Thus, the developed procedures may be used as a stand-alone
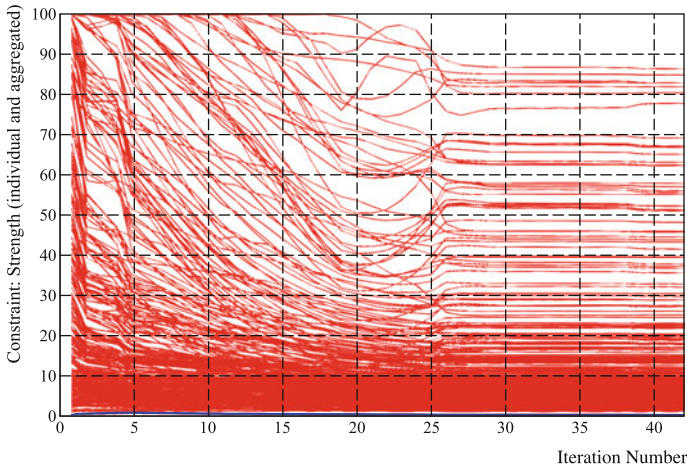
Fig. 3.6 Evolution of a strength constraint during the optimization: individual finite element constraints (red lines) aggregated by means of a single KS-function (blue line)
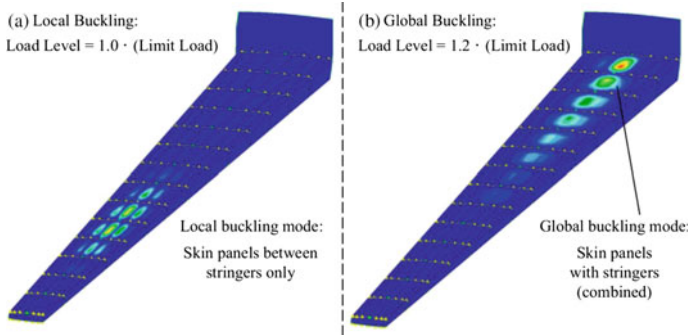
Fig. 3.7 Buckling modes of the optimum design: **a** Mode No. 1 (first local mode); **b** Mode No. 6 (first global mode)

optimization tool or they may be implemented in a multidisciplinary optimization tool without modifications.

- The design model contains a parameterized mathematical description of major design features. As such, geometrical and laminae-specific design variables are implemented, simultaneously keeping the numerical effort extremely low.
- Based on the mathematical descriptions used for the design model, fiber composite manufacturing limitations may be introduced into the optimization process. In this regard, limitations of the taper ratio (layer thickness) are possible.
- The evaluation model is, as well as the design model, independent from the structural analysis model or -in case of FE-analyses- independent from the net density.

- The following structural items can be used as objective functions or constraints: mass, strength, damage tolerance, stability (classical buckling analysis with eigen-mode identification) and stiffness (elastic deformation, aeroelastic tailering).
- The robustness of the optimization process is enhanced by using an aggregation method (KS-function) for constraints like strength and damage tolerance. Hence, only dozens of constraints must be handled instead of thousands (or tens of thousands).
- The aggregation of constraints is done area by area in conjunction with the definition of the design variables, in order to provide coherent sensitivities.
- The structural optimization has been executed as a stand-alone tool for demonstration purposes using the example of the use case *ForSwing*.

It can be summarized that the objectives of the envisaged work have been achieved successfully. Nonetheless, further developments may be considered in order to improve the robustness and efficiency of the optimization process (c.f. [6]), or to extend the design capabilities of the automated optimization loop (c.f. [27, 29]).

References

1. F.S. Almeida, A.M. Awruch, Design optimization of composite laminated structures using genetic algorithms and finite element analysis. Comput. Struct. **88**, 443–454 (2009)
2. J.S. Arora, *Introduction to Optimum Design*, 2nd edn. (Elsevier Academic Press, London, 2004)
3. S. Chintapalli, M. Elsayed, R. Sedaghati, M. Abdo, The development of a preliminary structural design optimization method of an aircraft wing-box skin-stringer panels. Aerosp. Sci. Technol. **14**, 188–198 (2010)
4. H.A. Eschenauer, The three columns for treating problems in optimum structural design, in *Optimization: Methods and Applications, Possibilities and Limitations: Proceedings of an International Seminar Organized by Deutsche Forschungsanstalt für Luft- und Raumfahrt (DLR)* ed. by H.W. Bergmann (Springer, Berlin, 1989)
5. H.A. Eschenauer, J. Koski, A. Osyczka (eds.), *Multicriteria Design Optimization (Procedures and Applications)* (Springer, Berlin, 1990)
6. H.-G. Goanţă, Optimization strategies for robust design of structural elements based on finite element analysis models and carbon fiber composite materials. Master Thesis, University of Applied Sciences Hamburg (2015)
7. R.T. Haftka, Z. Gürdal, *Elements of Structural Optimization* (Kluwer Academic Publishers, Dordrecht, 1990)
8. L.U. Hansen, P. Horst, Multi-level optimization in aircraft structural design evaluation. Comput. Struct. **86**, 104–118 (2008)

9. Z. Hashin, Failure criteria for unidirectional fiber composites. ASME, J. Appl. Mech. **47**(2), 329–334 (1980)
10. C.M. Heath, J.S. Gray, OpenMDAO: framework for flexible multidisciplinary design, analysis and optimization methods, in *8th AIAA Multidisciplinary Design Optimization Specialist Conference (MDO)*. (Honolulu, Hawaii, 2012)
11. S. Honda, T. Igarashi, Y. Narita, Multi-objective optimization of curvilinear fiber shapes for laminated composite plates by using NSGA-II. Compos. Part B Eng. **45**(1), 1071–1078 (2013)
12. R. Joaquim, R.A. Martins, A.B. Lambe, Multidisciplinary design optimization: a survey of architectures. AIAA J. **51**(9), 2049–2075 (2013)
13. U. Kirsch, *Structural Optimization* (Springer, Berlin, 1993)
14. G. Kreisselmeier, R. Steinhauser, Systematic control design by optimizing a vector performance index, in *International Federation of Active Controls Syposium on Computer-Aided-Design of Control Systems* (Zürich, Switzerland, 1979)
15. B. Liu, R.T. Haftka, M.A. Akgün, Two level composite wing structural optimization using response surfaces. Struct. Multidiscip. Optim. **20**, 87–96 (2000)
16. J.R.R.A. Martins, N.M.K. Poon, Adaptive constraint aggregation for structural optimization using adjoint sensitivities, in *Canadian Aeronautics and Space Institute Annual General Meeting Aircraft Design and Development Symposium* (Toronto, Canada, 2005)
17. A. Puck, *Festigkeitsanalyse von Faser-Matrix-Laminaten. Modelle für die Praxis* (Hanser-Verlag, München, 1996)
18. K. Schittkowski, *Optimization in Industrial Engineering: SQP-Methods and Applications. Radioss User Meeting* (Nice, France, 2005)
19. G. Schuhmacher, Multidisziplinäre, fertigungsgerechte Optimierung von Faserverbund- und Flächentragwerken. Bericht T07-03.95. TIM-Forschungsberichte, University of Siegen (1995)
20. G. Schuhmacher, H.A. Eschenauer, J. Krammer, Constructive design models for multidisciplinary optimization of fiber composite structures, in *AIAA/USAF/NASA/OAI Symposium on Multidisciplinary Analysis and Optimization*, (Cleveland, Ohio, 1992)
21. M. Seibel, H.-G. Goanţă, H. Velásquez, C. Hühne, L. Heinrich, T. Bach, Structural optimization of a forward swept elastic wing made of composite materials (Paper no. 301365), in *Annual Meeting of the German Society for Aeronautics and Astronautics (DGLR)* (Stuttgart, Germany, 2013)
22. A. Seitz, M. Kruse, T. Wunderlich, J. Bold, L. Heinrich, The DLR project LamAiR: design of a NLF forward swept wing for short and medium range transport application (Paper no. 2011-3526), in *29th AIAA Applied Aerodynamics Conference* (Honolulu, Hawaii, 2011)
23. S. Sethi, A. Striz, On using the Kreisselmeier-Steinhauser function in simultaneous analysis and design, in *38th Structures, Structural Dynamics and Materials Conference* (Kissimmee, Forida, 1997)
24. S. Setoodeh, Z. Gürdal, Design of composite layers with curvilinear fiber paths using cellular automata, in *44th AIAA/ASME/ASCE/AHS Structures, Structural Dynamics and Materials Conference* (Norfolk, Virginia, 2003)
25. J.H. Starnes Jr., R.T. Haftka, Preliminary design of composite wings for buckling, strength and displacement constraints. J. Aircr. **16**(8), 564–570 (1979)
26. H. Velásquez, Structural design optimization of an aircraft composite wing-box using curvilinear stiffeners. Master Thesis, University of Applied Sciences Hamburg (2014)
27. H. Velásquez, M. Seibel, H.-G. Goanţă, Structural design optimization of an aircraft composite wing box using curvilinear stiffeners (Paper no. 340064), in *Annual Meeting of the German Society for Aeronautics and Astronautics (DGLR)* (Augsburg, Germany, 2014)
28. G. Venter, J. Sobieszczanski-Sobieski, Multidisciplinary optimization of a transport aircraft wing using particle swarm optimization (Paper 2002-5644), in *9th AIAA/ISSMO Symposium on Multidisciplinary Analysis and Optimization* (Atlanta, Georgia, 2002)
29. T. von Ahlen, Optimum design of airframe structures made of composite materials using curvilinear fiber paths. Master Thesis, University of Applied Sciences Hamburg (2016)
30. Q. Zhao, Y. Ding, H. Jin, A layout optimization method of composite wing structures based on carrying efficiency criterion. Chinese J. Aeronaut. **24**, 425–433 (2011)

Chapter 4
Development of Flight Control Functions for Integration in Gust Load Simulations

Alexander Hamann

Abstract Within the joint project AeroStruct, the Department of Flight Mechanics, Flight Control and Aeroelasticity at TU Berlin developed generic flight control modules for considering the influence of flight control functions in preliminary aircraft design. In order to improve the methods used for the design process, an automated tool chain was set up, that builts a flight-mechanical model of the airplane, calculates controller parameters according to consistent criteria and automatically implements flight control functions in a high fidelity simulation environment.

Acronyms

D	Damping ratio [-]
p	Roll rate [°/s]
q	Pitch rate [°/s]
r	Yaw rate [°/s]
α	Angle of attack [°]
β	Sideslip angle [°]
ζ	Rudder deflection [°]
η	Elevator deflection [°]
Θ	Pitch angle [°]
ξ	Aileron deflection [°]
Φ	Roll angle [°]
ω_0	Natural frequency [rad/s]
CFD	*Computational Fluid Dynamics*
FCF	*Flight Control Functions*
PH	*Phugoid mode*
SP	*Short-period mode*

A. Hamann (✉)
Department of Flight Mechanics, Flight Control and Aeroelasticity,
Marchstraße 12, 10587 Berlin, Germany
e-mail: alexander.hamann@ilr.tu-berlin.de

4.1 Introduction

The Flight Control System of modern commercial aircraft strongly influences the aircraft's flight-dynamical characteristics. Control surface deflections are not directly commanded by the pilot, but calculated according to commanded parameters like a load factor or roll rate, instead. Modern Flight Control Systems contain both functions, that influence the aircraft's flight-dynamical behavior (e.g. damping functions), and functions, that ensure safe flight operations (e.g. maintain flight boundaries). Furthermore, it influences the aircraft's behavior in atmospheric disturbances. For realistic gust encounter or maneuver load simulations, it is therefore necessary to include flight control functions into the simulation. The Department of Flight Mechanics, Flight Control and Aeroelasticity at TU Berlin developed generic flight control functions for implementation in existing simulation tools for load calculations. Figure 4.1 shows the automated steps that are performed to design those functions. In the beginning of the process, geometrical and structural data are imported from a finite elements model of the aircraft. With those data a simulation model for investigations of the aircraft's flight-dynamical behavior without flight control functions is formed. This model is then used to calculate the parameters of flight control functions, that improve the aircraft's flight-dynamical behavior and control pitch angle, roll angle and sideslip angle. For the calculation and optimization steps, consistent criteria are used in order to achieve consistent flight-dynamical characteristics under different flight conditions within the flight envelope.
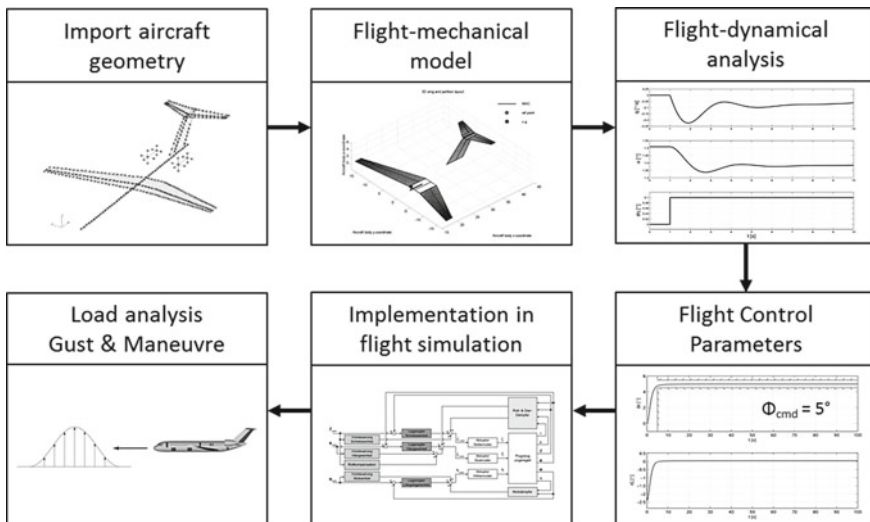
Fig. 4.1 Process chain

The flight control functions were implemented in a simulation environment of higher accuracy at DLR Göttingen to perform gust encounter simulations with and without influence of control functions.

4.2 Flight-Mechanical Modeling

For analyzing the aircraft's flight-dynamical behavior and for calculating parameters of the flight control functions, a flight-mechanical model of the aircraft was built. All necessary data were read from condensed finite elements (FE) models provided by DLR Göttingen, that contain the aircraft's geometry, mass, moments of inertia and elastic modes for nine different loading conditions.

In order to use the Matlab based, in-house software FlexSim, the FE data was processed into a compatible data structure. With those standardized data, aerodynamic coefficients for the aerodynamic two-point model (wing/fuselage, tailplane) were calculated using the vortex lattice method. Furthermore a strip model was set up for considering the influence of the aircraft's elastic deformation. After processing the FE data, all steps shown in Fig. 4.2 are automated. This allows an automated examination of different load conditions, structural stiffness or even different geometries, as long as the structure of the FE model remains the same. For the following steps, trim calculations for different flight conditions (altitude and velocity) were performed. System matrices were calculated by linearising the model for each trim point and used for examining the aircraft's flight-dynamical characteristics. Furthermore the linearized models were used for the computationally intensive optimization of the flight controller parameters.
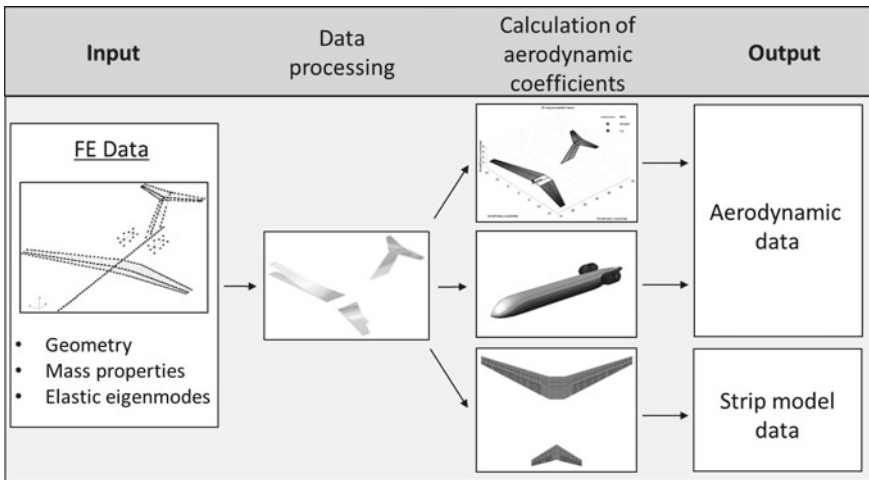
Fig. 4.2 Flight-mechanical model

4.3 Flight-Dynamical Analysis

For analyzing the aircraft's flight-dynamical behavior, the eigenvalues of the system matrices were calculated. Those eigenvalues contain characteristic values for the aircraft's flight-dynamical eigenforms (short-period and phugoid mode in longitudinal motion and dutch roll, spiral and roll mode in lateral-directional motion). The characteristic values are compared to flying quality requirements from MIL-F-8785C and MIL-HDBK-1797A. In those documents, flying quality requirements can be found for different flight phases and classes of aircraft. The aircraft examined here falls under Class III aircraft ("Large, heavy, low-to-medium maneuverability airplanes"). For this class Tables 4.1 and 4.2 list requirements for three levels of flying qualities, assessing the ability to fulfill the operational mission for which the airplane is designed. An aircraft with Level 1 flying quality is "clearly adequate for the mission flight phase", consequently those values shall be achieved.

For each of the different FE input files, flight-mechanical models were set up, trimmed and linearized for three different flight phases (Cruise, Approach and Landing). For most of the examined flight conditions the aircraft fulfilled Level 1 qualities without a flight control system. In some cases, the requirements were missed: With a forward position of the aircraft's center of gravity, the damping ratio of the short-period mode comes below the specified value for Level 1 qualities in cruise flight. With an aft center of gravity and a high take-off mass, the aircraft tends to miss the short-period mode minimum frequency criterion. In lateral-directional motion the aircraft complies with Level 1 flying qualities for almost all examined load and flying conditions. In three cases the product of frequency and damping ratio is too low in cruise flight. In order to achieve Level 1 qualities, flight control functions are used, that specifically increase the damping ratio of certain eigenforms and adjusts the associated frequency.

Table 4.1 Longitudinal flying qualities

Short-period mode	Flight phase	D $[-]$	Min. ω_0 [rad/s]
Level 1	Cruise	**0.30−2**	**−**
	Approach, landing	**0.35−1.3**	**0.7**
Level 2	Cruise	0.20−2	−
	Approach, landing	0.25 − 2	0.4
Level 3	Cruise	>0.15	−
	Approach, landing	>0.15	−
Phugoid mode	Flight phase	D $[-]$	
Level 1	All	**>0.04**	
Level 2	All	>0	
Level 3	All	$T_2 > 55s$	

Table 4.2 Lateral-directional flying qualities

Dutch roll mode	Flight phase	Min. D [−]	Min. ω_0 [rad/s]	Min. $D \cdot \omega_0$ [rad/s]
Level 1	Cruise	**0.08**	**0.4**	**0.15**
	Approach, landing	**0.08**	**0.4**	**0.10**
Level 2	All	0.02	0.4	0.05
Level 3	All	0	0.4	0
Roll mode	Flight phase	Max. time constant [s]		
Level 1	All	**1.4**		
Level 2	All	3		
Level 3	All	10		
Spiral mode	Flight phase	Min. time to double amplitude [s]		
Level 1	Cruise	**20**		
	Approach, landing	**12**		
Level 2	All	8		
Level 3	All	4		

4.4 Flight Control Functions

In order to improve the aircraft's flying qualities and to command and control pitch, roll and sideslip angle, flight control functions were defined. Instead of directly commanding control surface deflections in a simulation, those flight control functions calculate the deflections depending on the commanded and the current flight condition. As can be seen in Fig. 4.3, the functions are built around the flight-mechanical simulation model of the aircraft. The gray boxes depict the different parts of the flight controller. The damper functions are implemented to adjust the damping ratios and frequencies of the flight-dynamical eigenforms. The demand controller and feedforward controller are implemented to command and control the flight state the aircraft is in. For a realistic behavior of the control surfaces, actuator blocks are used. Those blocks model the movement of the control surfaces by PT_2 elements, bring in a delay time and limit the rates and deflections of each surface.

In order to achieve consistent flight qualities within the flight envelope, the parameters of the flight control functions are calculated depending on the current flight conditions. At first the gains of the inner control loop with the damping functions are calculated. The influence of the feedbacks, that are used for adjusting damping ratios and frequencies of short-period mode and phugoid mode, are shown in the root locus plot in Fig. 4.4. A feedback of the pitch rate q to the elevator deflection η increases the damping ratio of the short-period mode and reduces the frequency of the phugoid mode. A feedback of the pitch angle Θ to the elevator deflection η increases the damping of the phugoid mode and the frequency of the short-period mode. By
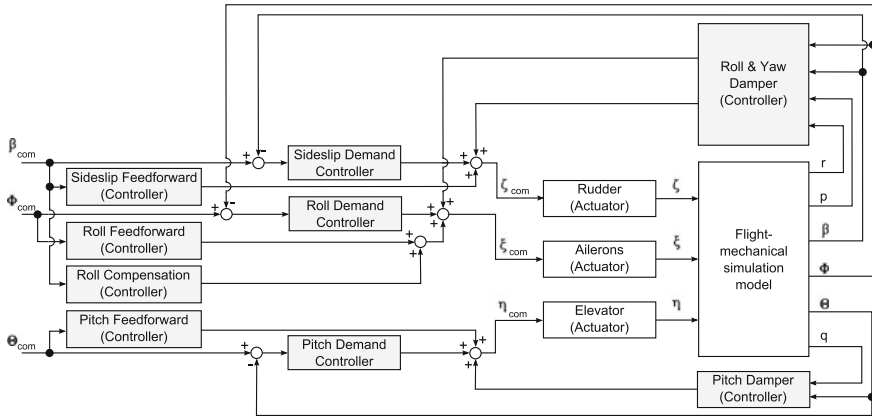
Fig. 4.3 Flight control functions

Fig. 4.4 Feedbacks for adjusting damping ratios and frequencies of short-period mode (SP) and phugoid mode (PH)
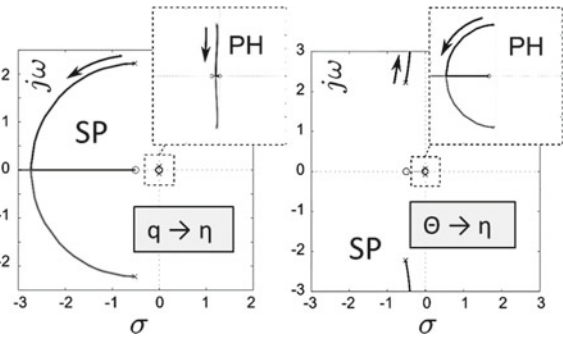
using a combination of both, the longitudinal flight-dynamical characteristics are specifically adjusted.

The influence of the damping functions on the short-period mode is illustrated in Fig. 4.5. The plot shows the aircraft's reaction to an elevator step input with and without activated damping functions. All other parts (feedforward and demand controller) are deactivated in this case. The solid line represents the aircraft with damping functions, the dashed line the aircraft without those functions. During the first seconds after the elevator input, the short-period oscillation can clearly be seen, especially for the aircraft without damping functions. Due to the negative pitch rate, the dampers reduce the elevator deflection command, that is sent to the actuator and further to the flight-mechanical model. As a result the damping of the short-period is increased, and less oscillations occur.

Due to the strong coupling between the lateral-directional eigenmodes, a full set of feedbacks from roll angle Φ, sideslip angle β, roll rate p and yaw rate r to aileron and rudder deflection ξ and ζ are used to adjust the flight-dynamic behavior. This allows to apply the eigenstructure assignment method to calculate gain factors. With
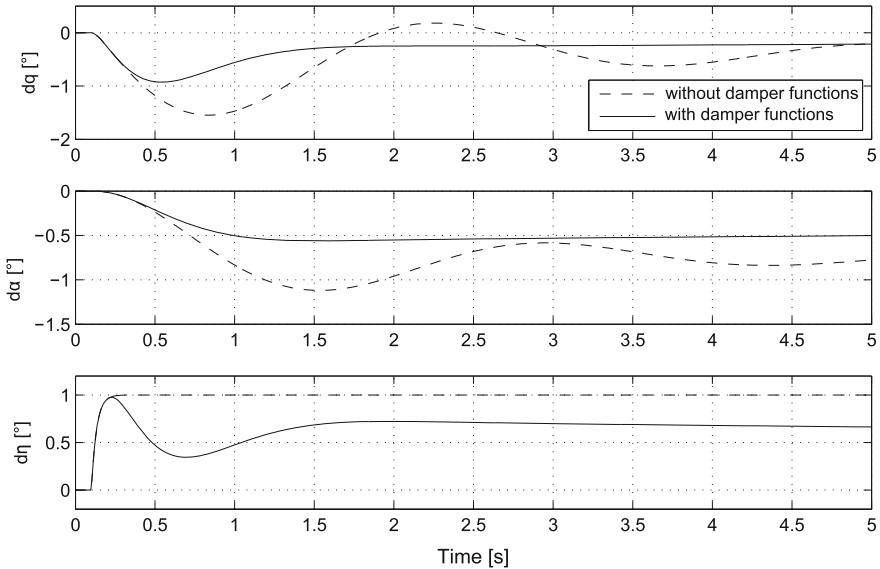
Fig. 4.5 Simulation results for elevator step input of 1°

this method both eigenvalues and eigenvectors can be influenced specifically, so that the flight-dynamical behavior meets the requirements listed in Table. 4.2.

Figure 4.6 shows simulation results for an aileron step input, again for both the unaugmented aircraft (dashed line) and the aircraft with damping functions (solid line). Here several effects concerning the flight-dynamical characteristics can be observed. Directly after the positive aileron step input, the aircraft starts rolling to the left (negative roll rate p). The roll rate then decreases slightly, which indicates a stable spiral mode. During the first 15s the dutch role can be seen as an oscillation of sideslip angle β and role rate p. The decaying character of the oscillation indicates a stable dutch role mode. For the aircraft with damping functions an indifferent spiral mode, a stronger damped dutch roll and a consistent roll time constant, independent from the current flight conditions, was chosen as desired behavior. Furthermore the sideslip angle is suppressed. The effects can be seen in the plots: In order to achieve this chosen behavior, both ailerons and rudder are deflected. Due to the indifferent spiral mode the aircraft now rolls with a constant roll rate. Furthermore the stronger damping and the suppression of the sideslip angle can be observed (Fig. 4.7).

After calculating the gains of the damping functions, the optimization of the feedforward and demand controller parameters is performed. Both feedforward and demand controller are used to adjust and maintain the aircraft's sideslip angle, roll angle and pitch attitude angle. The corresponding controller parameters are calculated using the optimization toolbox MOPS. Requirements to evaluate the controller were extracted from MIL-F-9490D. The commanded value has to be reached within five seconds with a maximum deviation of 5% in longitudinal motion and 10% in lateral-
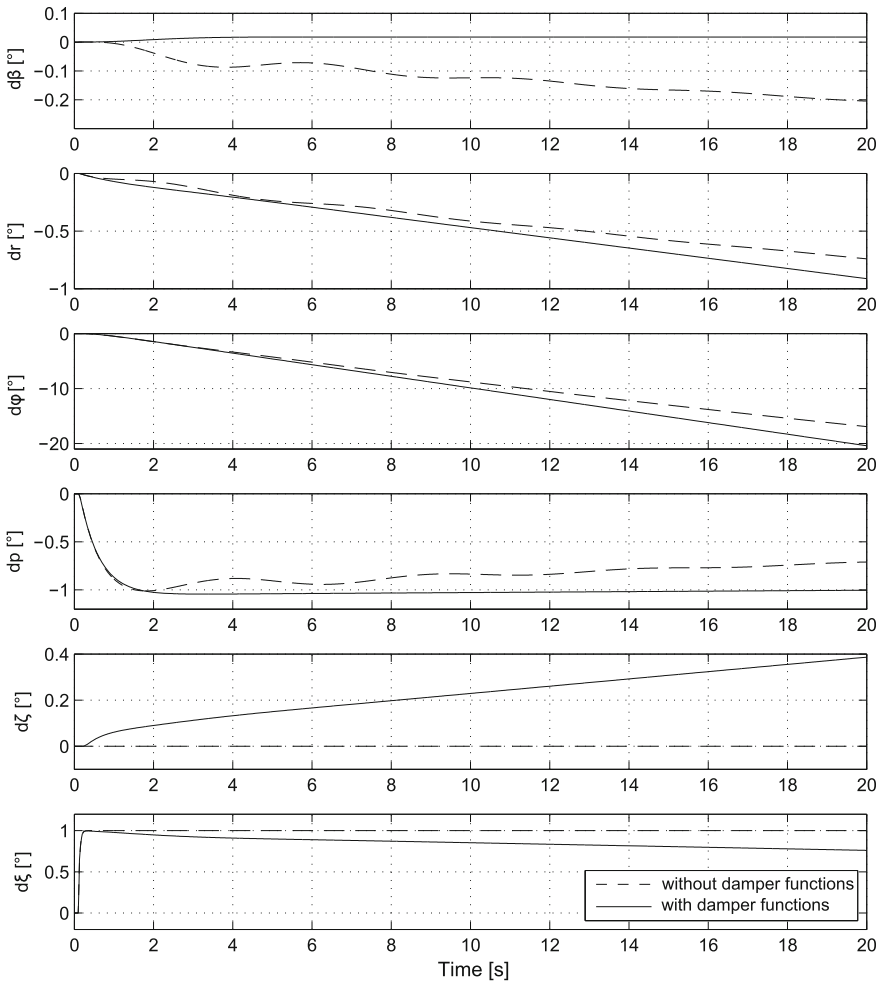
Fig. 4.6 Simulation results for ailerons step input of 1°

directional motion. By optimizing the controller parameters with the same criteria for every flight condition leads to a consistent flight-dynamical behavior within the flight envelope. Figure 4.8 shows a set of flight velocities and altitudes, for which trim calculations and calculations of flight controller parameters were performed.
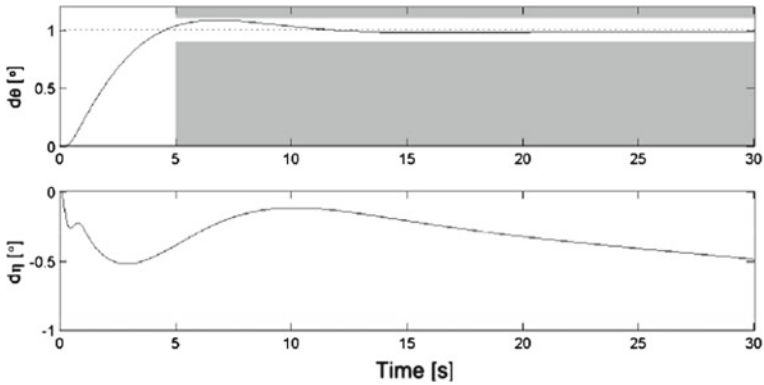
Fig. 4.7 Criteria for longitudinal control functions
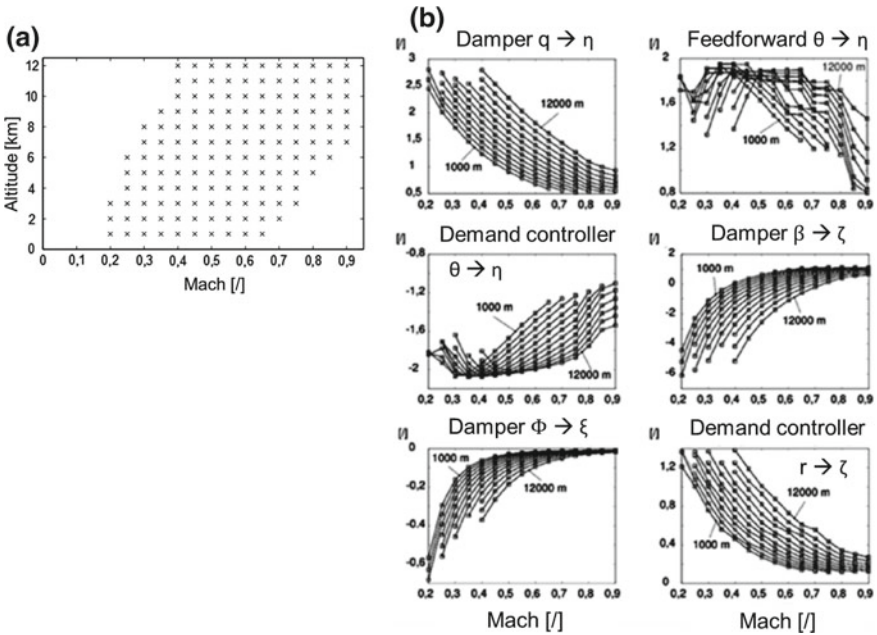
Fig. 4.8 **a** Analized combination of velocities and altitudes, **b** Flight control function parameters for those different flight conditions

4.5 Implementation of Flight Control Functions in Gust Simulations

In order to compare gust encounter simulations with and without the influence of flight control functions, the flight control module was implemented in a simulation environment at DLR Göttingen. The programm structure corresponds to the DLR Flow Simulator, that is used for high fidelity CFD simulations, but for a shorter simulation time this model uses the vortex lattice method to calculate aerodynamic forces. As a first step the structure of the flight control module was directly coded into the simulation model. In order to be able to simulate different aircraft configurations, numerical parameters are loaded at the beginning of the simulation. Consequently changes in the flight controller structure are work-intensive, but different aircraft configurations, positions of the center of gravity or higher or lower take-off masses can be investigated by using the automated process chain for the investigated, current aircaft. The parameter file contains values for all flight conditions shown in Fig. 4.8, for altitudes and velocities between these values, the controller parameters are interpolated.

For a higher level of automation, the implementation of the flight control functions was automated as well. For this purpose the flight control functions were converted from Simulink to C-Code, which can be integrated into the Python code of the
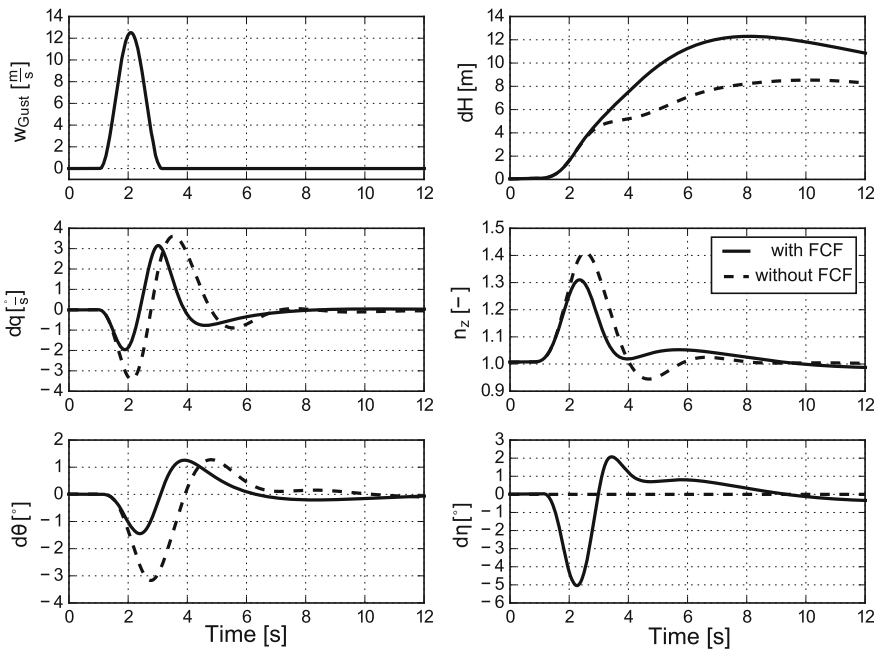
Fig. 4.9 Gust encounter simulation with and without flight control functions (FCF)

simulation environment. Here only an interface has to be defined which connects the in- and outputs of simulation model and flight control module, which can be done automatically. Doing so, not only different aircraft configurations, but also different control structures can be investigated and compared.

In Fig. 4.9 results of gust encounter simulations with and without active FCF are compared. The results show the aircraft's reaction to an upwind gust at Mach 0.3. When the gust hits the horizontal tailplane, the airplane takes down its nose (negative pitch rate dq and pitch angle $d\Theta$). The flight control functions command an elevator deflection $d\eta$ to compensate these changes and to bring the airplane back into the trimmed flight condition. The airplane without FCF does not deflect any control surface. In this case the elevator deflection reduces the gust induced loads by approximately 25%, as can be observed in the course of the load factor n_Z.

References

1. Flying Qualities of Piloted Aircraft, MIL-HDBK-1797A, US Navy (1997)
2. Military Specification: Flying Qualities of Piloted Airplanes MIL-F-8785C, US Navy (1980)

Part II
Use-Case FlexCraft

Chapter 5
Introduction to Airbus Use-Case "FlexCraft"

Frank Theurich and Klaus Becker

Abstract Within the joint project AeroStruct Airbus studied a concept for best exploitation of wing or aircraft flexibility for aircraft performance purposes. An important aspect was to improve the collaboration between the disciplines like Aerodynamics, Loads or Structure. There was a lot of learning on requirements on fidelity and accuracy, but also about effects of uncertainties on the design. Multiple layer models of different fidelity helped to understand and optimize the design process. For the design case aerodynamic optimization was conducted on the basis of a surrogate model using a quite large number of parametric variations of shape and flow parameters. Loads and flutter studies were performed with advanced CFD methods like LFD (linear frequency domain). The design of a more flexible wing was evaluated from an overall aircraft point of view, in particular taking into account the drag and weight changes. All together the AeroStruct project provided not only a much better insight to potential future design but also delivered a better understanding of product behavior and discipline interactions.

5.1 Introduction

The AeroStruct project provides an excellent opportunity to Airbus to investigate and develop a concept for best exploitation of wing or aircraft flexibility for aircraft performance purposes while optimizing also towards handling qualities and loads. Since there is a must to integrally consider major disciplines like aerodynamics, structures, systems etc. within the design process a completely integrated simulation capability is needed, which covers discipline simulation and their full interaction.

AeroStruct intends to elaborate the opportunity to progressively use higher flexibility on wings. It is not only intended to provide a full analysis of the flexibility

F. Theurich · K. Becker (✉)
Airbus Operations GmbH, Bremen, Germany
e-mail: klaus.becker@airbus.com

F. Theurich
e-mail: frank.theurich@airbus.com

The more flexible aircraft
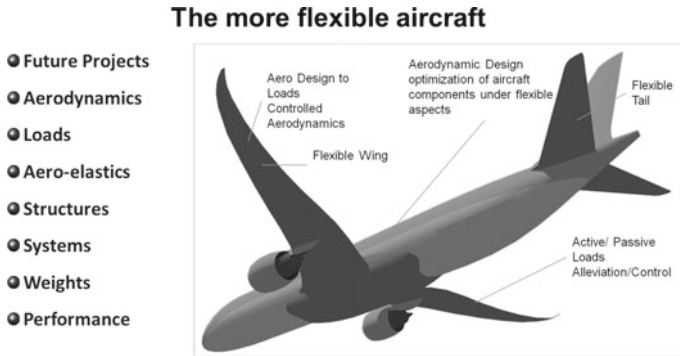
Fig. 5.1 The more flexible aircraft, a multidisciplinary design

effects and their potential for design but also to develop a process and the capability to perform such kind of design. Together with other partners in the project it is planned to develop the numerical simulation and optimization, and to let people exercise and learn on how to cope with this kind of challenge.

AeroStruct brings together disciplines like Aerodynamics, Aeroelastics, Mass Properties, Structures, Systems, Flight Dynamics, etc. (see Fig. 5.1). It targets at a qualified investigation on the background of experience from previous aircraft design. The designer shall directly cooperate with the developer of simulation capabilities which will deepen the common understanding and development of best practice.

Since some time Airbus has worked on the "more flexible aircraft" topic, which has already led to a number of requirements on process and capabilities. Airbus could therefore jump into the project right from the start. Walking through a sequence of multi-disciplinary integration a successively refined concept for such kind of design philosophy will be elaborated.

The more flexible aircraft or wing use case has been selected since it provides a substantial potential for product improvement. Obviously we would like to answer the question on how much an aircraft design would gain in terms of performance if we optimize the use of modern materials like CFRP and related production processes. Looking at the wing, Airbus could imagine a much more efficient component than available today. We think that considerable weight savings will be possible, and a more sophisticated use of targeted wing deformation could lead to a better aircraft performance.

Our use case is a classical aircraft configuration, however, with more flexible wing. Based on an internal study Airbus will perform a targeted new component design which shall demonstrate the opportunities. High fidelity simulation methods will help to arrive at a robust judgment of the product but also provide insight to all disciplinary effects and interactions. We also intend to learn a lot about requirements on fidelity and accuracy as well as effects of uncertainties on the design. Multiple layer models of different fidelity shall help to understand and optimize the design

process. Single steps and results will be validated on an existing design as well as on principal experiments, wherever available.

All together the AeroStruct project will not only provide a much better insight to potential future design but also deliver a better understanding of product behavior and discipline interaction. Finally it prepares the ground for a more intensive use and exploitation of computational simulation of the overall product.

5.2 Specification of the Product Target

In the frame of the specification of the product target the reference case needs first to be defined. Only on the basis of a reference case, an aircraft development progress can be adequately judged. Therefore the starting point for a more flexible aircraft specification has to be defined carefully at the beginning of the project. In the AeroStruct project a configuration has been selected as reference case, which corresponds to a classical and typical Long Range aircraft.

On the basis of the reference configuration modifications are performed in order to stepwise achieve the targeted product. The following geometric and aerodynamic parameters are particularly taken into account: wing bending, wing twist, wing thickness, wing section design, wing tip device design.

To assess the wing behaviour at design and off-design conditions aerodynamic-structure coupled simulations (CFD/CSM) are performed. For CFD/CSM the structure model is also derived and developed from the reference model in order to achieve the targeted behaviour wrt increased wing flexibility.

The target in terms of aero performance is on one hand to mitigate penalties potentially implied by the increased wing flexibility, e.g. span loss due to the increased wing bending, movement of centre of lift (CoL) inboard or due to any other additional flexibility effects on wing aerodynamics. On the other hand aerodynamic drag potentials and opportunities are explored.

5.3 Design Case

For the design case of a more flexible aircraft the modifications also include changes to the aircraft design, for example wing position relative to the fuselage and HTP size in order to account for flexibility effects on handling qualities. The wing planform as well as the fuselage is maintained unchanged within the project due to the comparability reasons to the reference case.

In the loads studies different loading cases, like maneuvers, continuous turbulence and discrete gusts are investigated for the more flexible wing. Nonlinear structural modelling and flutter phenomena are also considered and studied, because a more flexible wing is a potential candidate for a flutter problem. The flutter process is verified with CFD and a full-flex coupling method. With the introduction of the

LFD (linear frequency domain) solver the simulation time of the CFD process is significantly reduced. Comparisons of the results with established methods confirm the good quality of the LFD solver.

For the optimization non-adjoint process chains are further developed and applied for flexible wing configurations. For a so-called POD-based (Proper Orthogonal Decomposition) surrogate model a quite large number of parametric variations of shape and flow parameters are performed. Based on the post-processed surrogate model data the designer is able to explore the design space and provides a significant support for design decisions. As CFD usually consumes a significant time in an automated, numerical optimization process and is always risky wrt stability, the use of a robust surrogate model is a significant improvement.

An aerodynamic optimization is performed for a fully flexible Airbus-type aircraft with engines running. The objective is to perform multi-point / multi-objective design optimization for flexible wings. The optimization is conducted based on a surrogate model that is created using the PODRacer proper orthogonal decomposition (POD) method. The approach is described in [1].

A fully flexible configuration is studied, where the wing structure, fuselage structure and horizontal tail plane (HTP) structure are modelled using Nastran [2]. To describe the design space five geometrical parameters are considered (see also Fig. 5.2), namely: inner and outer flap angle, inner and outer aileron angle and HTP deflection angle, and one flow parameter is considered: the angle of attack. HTP trimming is considered to be essential to account for trim drag. The design space is located around the design point.

A computational campaign based on Design of experiments is performed to cover design space with 219 snapshots. For each snapshot a turbulent flow solution is computed using an aero-structural coupling approach. Target lift values are used to compute the angle of attack for the flexible wing for fixed flap, aileron and HTP settings. The engine thrust is taken into account in the trimming of the aircraft. Engine thrust has a contribution to the moment, see also Fig. 5.3.

Fig. 5.2 Illustration of changes in wing bend and HTP setting variations
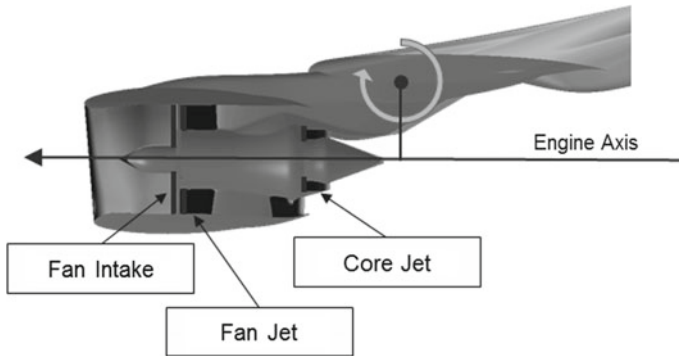
Fig. 5.3 Contribution of engine thrust to the moment around the centre of gravity

In the optimization constraints like maximum wing bending moments can be taken into account without re-computing the CFD/CSM campaign.

It is concluded that a drag reduction is feasible for specific areas in the design space. The optimization approach reduces the lead time for trades and trade responses by using surrogate modelling techniques. The surrogate model approach allows to perform trades around the design point considering the changes for the aerodynamic shape.

The design of a more flexible wing is based on assumptions of different wing stiffness. The maximum strains for the wing structure are demonstrated by theoretical methods (simulations) and tests. Trade study results are obtained from a systematic exploration of different skin/stringer laminate combinations with the use of stringer laminates as a mean to achieve both weight savings and a design solution with a higher flexibility.

5.4 Evaluation of the Design Case

The design of a more flexible wing is evaluated from an overall aircraft point of view.

For the evaluation the data of the drag polar in cruise condition which are used are Reynolds-number, Mach-number, lift coefficient and dynamic pressure. The drag data are well known for the reference configuration. For the design case incremental data are determined based on semi-empirical methods, which are calibrated by more sophisticated methods and tools, e.g. CFD and wind tunnel tests.

On the CFD side significant work is performed in relation to the use of the RSM (Reynolds Stress Transport Turbulence Model). Advantages of RSM versus k-based turbulence models, like Menter SST, are demonstrated. Comparisons with High Reynolds No. wind tunnel results of an industrial configuration show better results at design and off-design conditions for a RSM based model as with the Menter-SST model.

The relevant weight data of the wing and the tails are also based on semi-empirical methods. The calculated increments due to the more flexible wing in comparison to the reference wing are used for the estimation of the weight impact.

All the other relevant data for the calculation of the aircraft performance and mission data are taken or slightly changed from the reference configuration.

The process starts with a known reference configuration. In parallel the new configuration to be investigated is described (in general the changes compared to the reference). The direct effect of these design modifications on key performance indicators (e.g. weight, drag, etc.) are analysed resulting in changes of the aforementioned key performance indicators.

These changes are applied to a so called aircraft sizing loop: A process in which the actual aircraft performance with the required performance are compared and appropriate changes to the design are derived. These changes are an indirect effect of the design modifications. The indirect effects and direct effects are applied to the design and the sizing loop is repeated until all requirements are achieved. The effects of all these changes on a figure of merit (for example fuel consumption) are analysed and used for the evaluation of the new design.

The high speed drag and weight difference is taken into the mission calculation, in a first step with the same engine. After a first analysis with the mass-performance loop only, the engine is resized to achieve the same performance targets (mass-performance loop + engine resize). This leads to some further weight decrease. Low Speed performance is evaluated for take-off and landing.

References

1. K. Bobrowski, H. Barnewitz, E. Ferrer, E. Valero, in *Proceedings AIAA-Aviation and Aeronautics Forum and Exposition*, Aerodynamic shape optimization using geometry surrogate model and adjoint methods, 2016
2. http://www.mscsoftware.com/product/msc-nastran; MSC Nastran: Multidisciplinary Structural Analysis

Chapter 6
On Recent Advances in Industrial High-Fidelity Aeroelasticity

Bernd Stickan, Frank Schröder, Sebastian Helm and Hans Bleecke

Abstract   The paper shows for steady and unsteady tasks the usage of high-fidelity CFD-CSM interaction. While for steady scenarios CFD is the standard method for nowadays aerodynamic prediction, the level of detail in the structural model is often limited to linear FEM models with, by definition, rigid airfoils. Here the usage of multi-body models with nonlinear body motion and single-body nonlinear structural models is presented. For dynamic applications like flutter prediction, an approach which allows using purely unsteady CFD data, is presented. In this connection the combination of linearised CFD and unsteady data recycling results in a very efficient and accurate unsteady aerodynamic ROM.

6.1   Introduction

Computational Fluid Dynamics (CFD) is used in a wide area of different industrial application in aircraft development. While the focus is still on rigid and static application, more and more interdisciplinary applications like static and dynamic fluid-structure interaction are on the rise.

The papers [15, 16] give for a wind-tunnel model an impression about the accuracy which can be reached with high-fidelity CFD-CSM interaction for static and dynamic cases. The documents show for the examined clean-wing case the importance of high-fidelity aerodynamic and structural modelling for transonic flow with shock-induced separation and cross-sectional deformations of the wing structure.

B. Stickan (✉) · F. Schröder · H. Bleecke
Department of Aeroelasticity, Airbus, Bremen, Germany
e-mail: bernd.b.stickan@airbus.com

S. Helm
TU Braunschweig, Institute of Aircraft Design and Lightweight Structures,
Braunschweig, Germany

85

In the industrial context the same challenges appear. Hence, Sect. 6.3 deals with the pure usage of CFD for flutter computations and Sect. 6.4 handles the usage of very detailed structural models in static CFD-CSM computations. Here the dynamic case focusses on the efficient usage of CFD for flutter applications, while for the second case the challenges lie more on the structural and CFD-CSM coupling part.

But beforehand a short introduction in the used methods and tools is presented in Sect. 6.2.

6.2 Methods and Tools

6.2.1 CFD Solver: TAU

As CFD solver the DLR TAU-code is applied to solve the steady and the unsteady Reynolds Averaged Navier Stokes (RANS) equations [7]. For the unsteady aerodynamic modelling performed in Sect. 6.3 the Linearized Frequency Domain (LFD) solver of TAU is the most important feature to mention. As shown in [9, 17], the LFD solver allows to compute the unsteady aerodynamics induced by a harmonic forced motion for very small amplitude with strongly reduced costs.

6.2.2 CSM Solvers

For different applications the most suitable structural solver is used in the following sections. These commercial solvers are:

- MSC-NASTRAN is the classical structural FEM solver in the context of aircraft aeroelasticity. In the context of this document the eigenvalue decomposition (modal analysis) is used as input for the flutter analysis: The eigenmodes Φ_s are the main input for the aerodynamic model which is used in combination with the generalized mass and stiffness in the p-k-flutter solver. Additionally the eigenmodes of different components are combined by ADAMS (see next item) to create a flexible multibody model [11].
- MSC-ADAMS is a multi-body solver, which allows to combine multiple structural components from different regular structural models. The components itself are represented in generalized format and, therefore, of linear type. But the interaction between the components due to body contact and motion is handled nonlinearly [10].
- DS-ABAQUS (DS = Dassault Systèmes) is used additionally due to its more powerful features concerning nonlinear structures. For the here presented study the coping with geometrical nonlinearities is the main target [6].

6.2.3 CFD-CSM Coupling

The coupling method for the aerodynamic and structural model uses a coupling matrix which interpolates the structural displacements or structural eigenmodes to the aerodynamic surface. The methodology allows to combine different interpolation methods for different model component. The selection of the interpolation method depends mainly on the present structural fidelity. The different coupling domains are united with blending and relaxation functions to keep a smooth and watertight CFD surface.

To transfer the aerodynamic loads to the structural surface either the transposed interpolation matrix or a nearest-neighbour mapping can be applied.

More details about the used method can be found in [14].

6.2.4 CFD-CSM Interaction

The here presented application examples of CFD-CSM interaction are either performed for static or transient analysis. While the static analysis is simply performed by iterating between the structural and the aerodynamic solver until convergence is reached, the transient analyses are performed in the frequency domain.

6.2.4.1 Static Interaction

The static simulation chain combines the structural and aerodynamic solver by using the coupling method sketched in Sect. 6.2.3. Since the coupling method only involves the model surfaces, the aerodynamic deflection must be transferred into the volumetric CFD mesh by mesh deformation. For this purpose RBF-interpolation is used again, combined with a nearest-neighbour correction scheme, see [2]. Additionally the model parameters can be used for trimming. For this purpose an outer iteration loop is installed. An overview of the interaction setup can be seen in Fig. 6.1.

6.2.4.2 Transient Interaction

The transient analyses are performed in the frequency domain. For this purpose the p-k-method [8] is applied to compute the aeroelastic frequencies and damping values of the flutter equation:

$$\left[\left(p \frac{v_\infty}{c_{ref}} \right)^2 \mathbf{M} + p \frac{v_\infty}{c_{ref}} \mathbf{D} + \mathbf{K} - q_\infty \mathbf{A}(k) \right] \cdot \mathbf{q} = 0 \,. \qquad (6.1)$$

Fig. 6.1 CFD-CSM loop
sketch
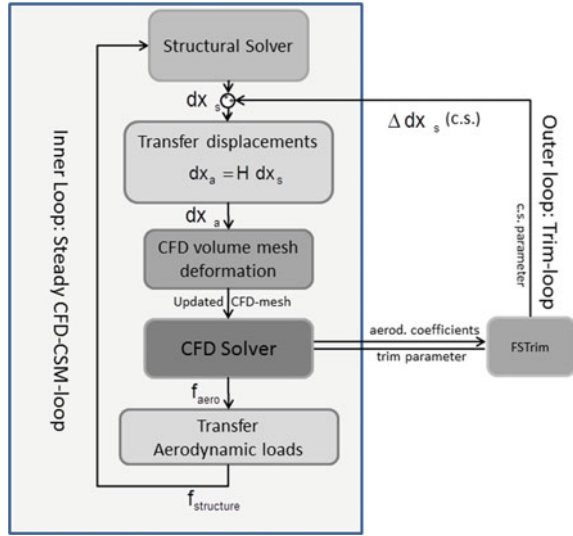
q_∞ denotes the dynamic reference pressure, v_∞ the reference farfield flow speed, c_{ref} the reference length, $\mathbf{M}$, $\mathbf{D}$ and $\mathbf{K}$ the generalized mass, damping and stiffness matrices. $\mathbf{q}$ is the vector of generalized coordinates and k the reduced frequency: $k = \frac{2\pi f c_{ref}}{v_\infty}$. The most important matrix (-function) for the here presented studies is $\mathbf{A}(k)$, which is the aerodynamic influence matrix or generalized air force (GAF) matrix. The entries of $\mathbf{A}(k)$ are interpolated from several sampling point matrices $\widehat{\mathbf{A}}^k$ for different reduced frequencies k. An entry (m, n) of the GAF matrix $\widehat{\mathbf{A}}^k$ for an in coordinate $\mathbf{q}_m$ harmonically oscillating eigenmode Φ_m, exciting the generalized forces of eigenmode Φ_n, is defined by the first harmonic of the transfer function

$$\widehat{\mathbf{A}}^k_{m,n} = \frac{1}{q_\infty} \frac{\mathscr{F}_1(\Phi^T_{s,n} f_s(\mathbf{q}_m(t)))}{\mathscr{F}_1(\mathbf{q}_m(t))} \tag{6.2}$$

whereas $\mathscr{F}_1$ symbolizes the first harmonic of the fourier transformation. For the case of the here used TAU-LFD solver, such frequency domain entries are computed directly by the CFD solver by solving a large, but linear equation system.

For this linear frequency domain analysis the structural and aerodynamic matrices are constant, hence the application sketch in Fig. 6.2 does not contain a loop (loop only inside p-k-method).

6.2.5 Least-Squares Approximation for Unsteady Aerodynamics

For the certification of aircraft plenty of different structural settings must be investigated. This various conditions include different mass cases and stiffness settings,

Fig. 6.2 Flutter process sketch
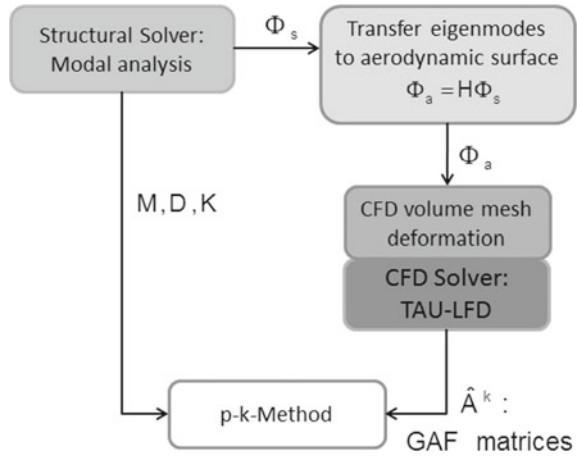
Fig. 6.3 Flutter process sketch
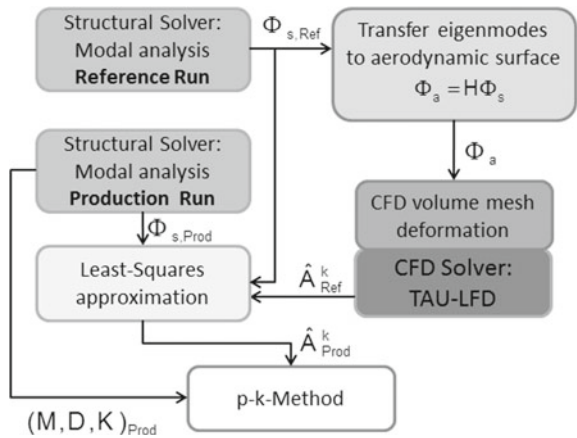
e.g. due to failure cases. Since CFD aerodynamics are still costly and by far the most expansive part of the flutter process sketched in Fig. 6.2, a least-squares based aerodynamic approximation method is used to approximate the aerodynamics for different structural conditions without re-running CFD. Instead the CFD aerodynamics of one reference mass case is reused for production purposes with the mentioned various structural conditions.

The method works in the manner that the eigenmodes of the structural production run $\Phi_{s,\mathrm{Prod}}$ are approximated with the eigenmodes of the structural reference run $\Phi_{s,\mathrm{Ref}}$ with the least squares method:

$$G = \left(\Phi_{s,Ref}^{T}\Phi_{s,Ref}\right)^{-1}\Phi_{s,Ref}^{T}\Phi_{s,Prod} \tag{6.3}$$

The production modes can be approximated by

$$Phi_{s,Prod} \approx \Phi_{s,Ref} G \ .$$ (6.4)

For the case of small amplitude aerodynamics superposition of aerodynamic forces is possible. Hence the generalized air force matrices $\widehat{\mathbf{A}}^k_{Prod}$ are approximated by

$$\widehat{\mathbf{A}}^k_{Prod} \approx G^T \widehat{\mathbf{A}}^k_{Ref} G \ .$$ (6.5)

The overall process with least-squares approximation is shown in Fig. 6.3.

6.3 Application of Direct CFD for Flutter

To gain aerodynamic models for flutter it is common practice to use aerodynamic models based on panel methods. The most spread method is the Doublet Lattice Method (DLM), [1], which is usually corrected with windtunnel or CFD data, see for example [12]. This section shows validation results for the direct usage of CFD without correcting less expansive aerodynamic methods, which is a step-change in unsteady aero modelling.

The already in Sect. 6.2.1 mentioned TAU-LFD solver is an enabler for the direct usage of unsteady forced motion CFD aerodynamics. It is not only reducing the computation time dramatically, but also lowers the parameter space to investigate to find a time-converged unsteady solution. For a classical harmonic time domain method parameters like the time step size, the convergence level in each time step and the number of overall time steps/periods must be investigated. Since the LFD result is the limit value of such studies, no trade-off between accuracy and performance is necessary.

But as already mentioned in Sect. 6.2.5, the direct usage of CFD for flutter aerodynamics is still too expansive with nowadays computing power. To solve the issue the least-squares approximation method for different mass cases etc. has been introduced. This means absolutely 'Direct CFD' cannot be achieved, but the least-squares method is used to build a reduced order model which should deliver accuracy close to 'Direct CFD'.

In this section the method should be validated for different mass cases and structural setting. Underlying assumptions are:

- Steady flow conditions equal for all cases including aircraft shape, trim angle etc. (not realistic, but acceptable)
- Small amplitude motion: Linear unsteady aerodynamics (necessary for LFD usage)

Compared are always the p-k-method result of a directly with CFD computed aero model with an approximated aerodynamic model. A CFD run for one model includes 150 eigenmodes and 7 eigenfrequencies per mode. So approximately 1000 CFD com-
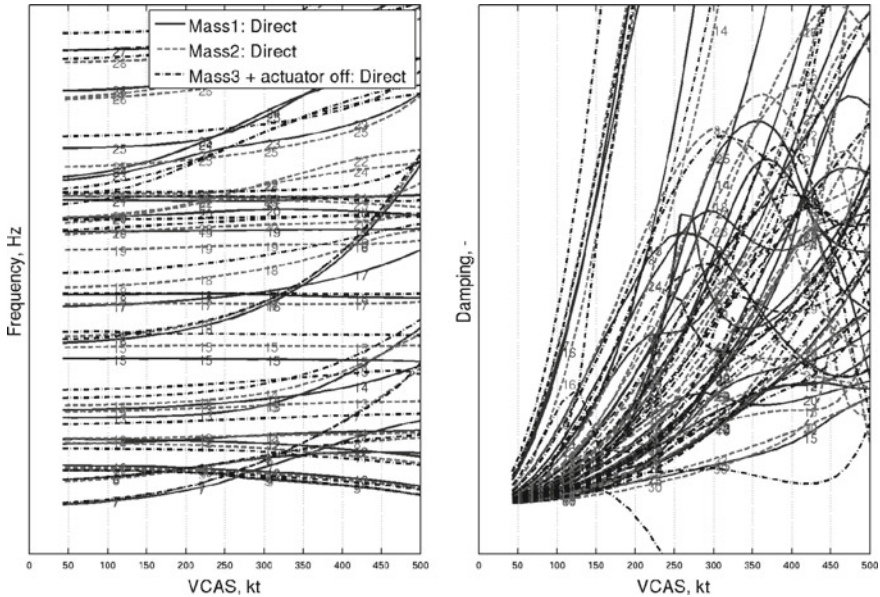
Fig. 6.4 Difference of structural cases

putations are performed per case. This value underlines the need for an approximation method.

Used are 3 different mass cases of a transport aircraft model with distinct differences in the flutter results as one can observe in Fig. 6.4. All cases are computed at $C_{Lift} = 0.3$ and Mach $= 0.91$.

As first case the mass case 2 (Mass2) is approximated by the reference mass case 1 (Mass1). Figure 6.5 presents the result. It can be observed that for the low frequency couplings the accuracy of the method is very high. The agreement between the directly with CFD computed case and the results approximated from a different mass case is very good. The higher the frequencies get, the lower the accuracy gets.

In Fig. 6.6 it can be seen that the mode approximation error increases with increasing mode number. This explains the decreasing accuracy with increasing mode number.

But to make clear: The differences for the high-frequency modes in the p-k-method results are still relatively small. Additionally, if a higher accuracy is needed for higher frequency eigenmodes, the reference mode set can be increased.

In Figs. 6.7 and 6.8 not only the mass case has changed, but also the stiffness of the structural model is modified. In the first case an actuator of a control surface is turned off, in the second example a complete control surface can move freely without an active actuator. It can be observed that even for such disruptive changes in the FEM model the approximation method provides a very good agreement compared to the directly computed results.
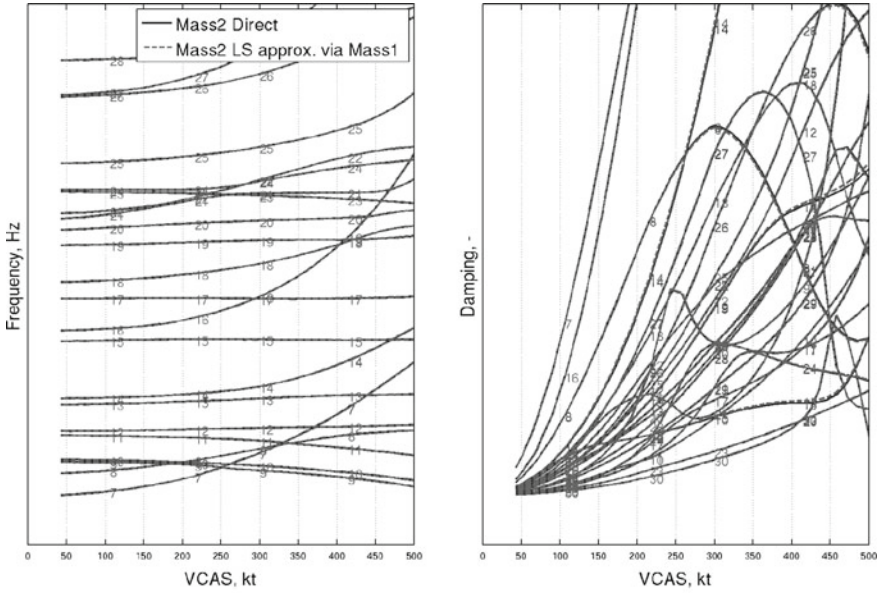
(a) Low frequencies: Modes 7-30
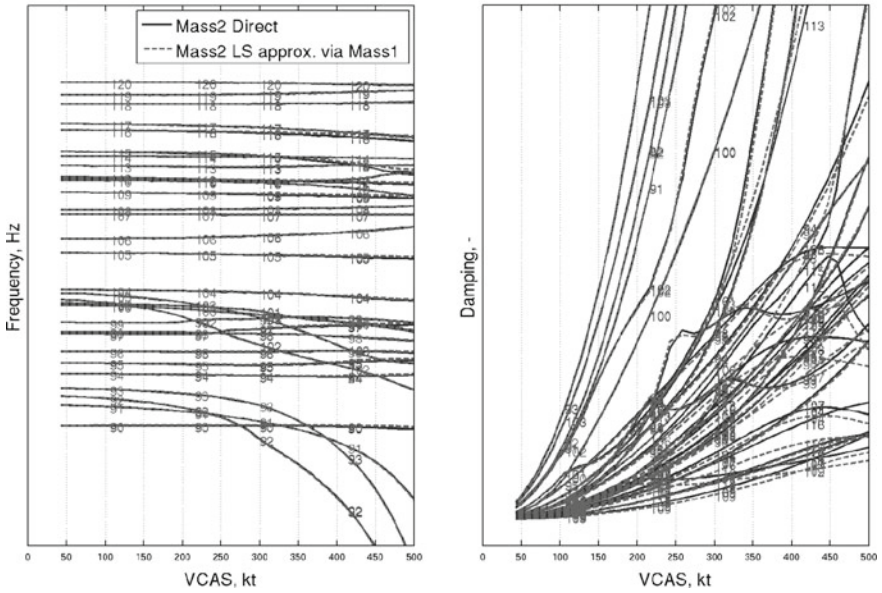
(b) High frequencies: Modes 90-120

Fig. 6.5 Least-squares approximation result for mass case 2
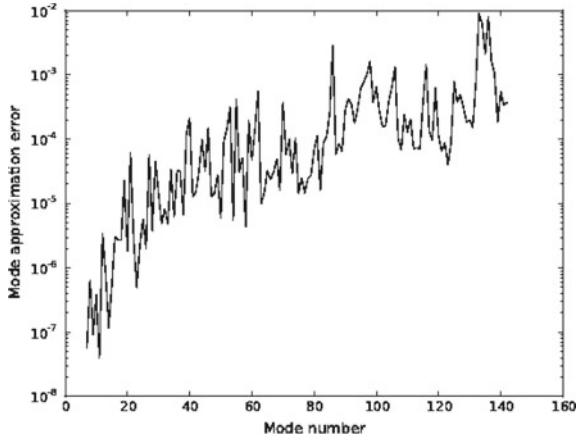
Fig. 6.6 Approximation error of eigenmodes
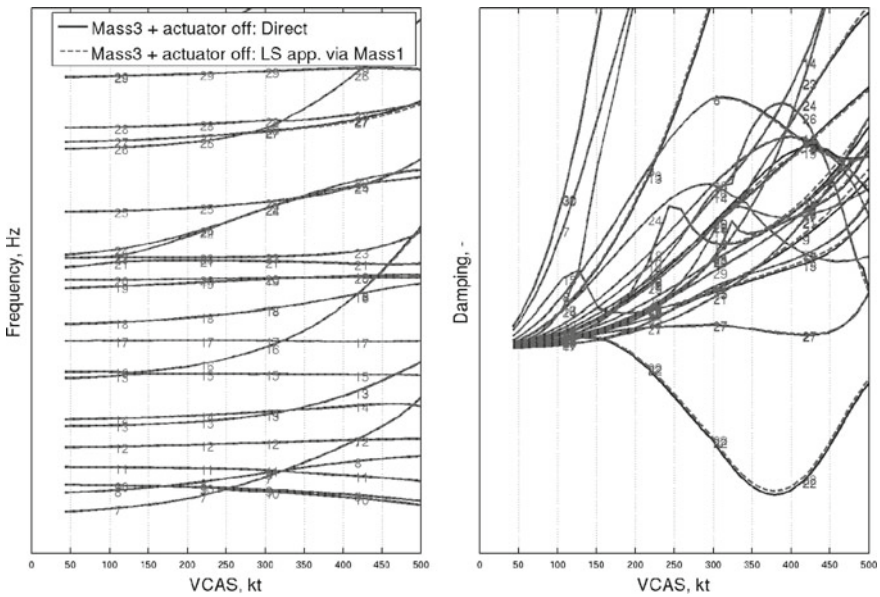
Fig. 6.7 Least-squares approximation result for mass case 3 with additionally deactivated actuator in control surface (CS)

Overall the accuracy of the least-squares method is very good and therefore a reduced order model based on it can be used for all structural conditions. Therefore this straightforward approach allows using only CFD data instead of correcting Doublet-Lattice method results.
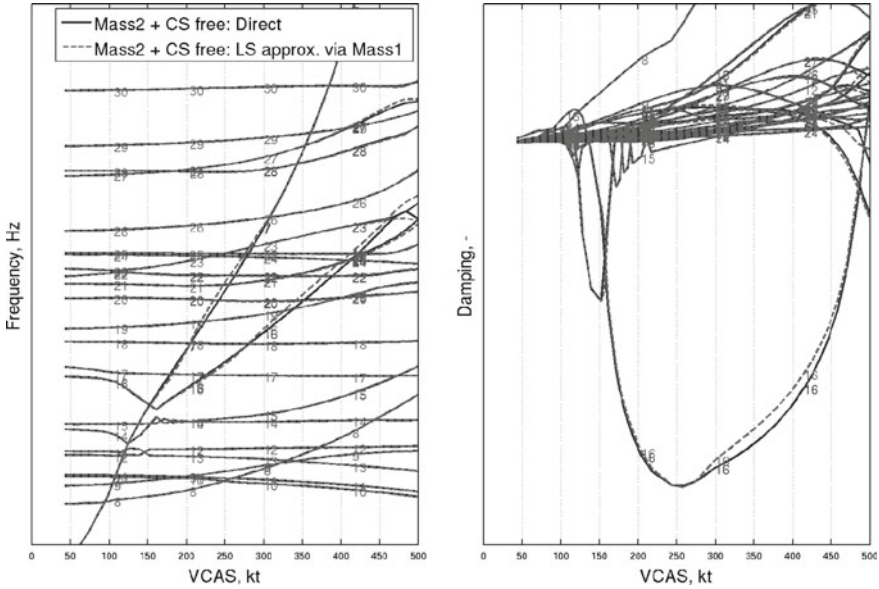
Fig. 6.8 Least-squares approximation result for mass case 2 with free control surface (CS)

6.4 Application of Static High-Fidelity CFD-CSM

The high accuracy for performance, loads and stability predictions, which is intended to be computed by RANS-CFD aerodynamics with varying resolution of turbulent scales, is today more and more limited by the accuracy of the structural modelling. The usual usage of linear beam-node line methods does not fit to the expected accuracy of the aerodynamic methods. Although it must be mentioned that still aerodynamic modelling shortcomings at the edges of the flight envelope exist.

This section is presenting two examples where the two main structural limitations are tackled. In the first subsection the reduction to beam-node line FEM and coupling is overcome by using a multi-body structural model including all structural components. The shortcoming of the linear structure assumption is handled in the second subsection.

6.4.1 Multi-body Simulation (MBS)

In a previous investigation by Bleecke, CFD-CSM coupling based on a structural model of Finite Elements (FE) revealed deficiencies to capture the cross-sectional deformation of an aircraft wing accurately over the whole chord, i.e. including leading- and trailing edge devices [3]. This work showed as well that this defor-

mation of an aircraft wing at transonic speeds might have a considerable influence on shock prediction and, thus, on wave drag. The additional assembly of movable leading- and trailing edge devices to the fixed wing main structure in an integrated multi-body model resolves the common limitation of FE models. It facilitates the representation of structural deformation (and coupling) over the whole chord and, thus, allows the analysis of the wing cambering effect on aerodynamics.

Multi body simulation is a "versatile gluing tool" [4] which allows large non-linear motion of parts, i.e. classically interconnected rigid bodies. Here the extension to flexible bodies is used [13, 18].

MBS is offering some advantages compared to conventional FEM:

- The straight-forward modelling based on Commercial Off-The-Shelf (COTS) construction kit for joints and contacts including nonlinearities, such as friction or backlash.
- Co-simulation offers the possibility to incorporate sub-systems such as control- or drive systems.
- The complete multi body model usually copes with far less degrees of freedom than a comparable FE model.

A multi body model of a complete aircraft wing is presented here. In the industrial environment FE models are usually available for the wing main structure (wing box) and for all subcomponents (movable surfaces) separately. These can be easily reused in a flexible multi-body model. Modelling efforts are, hence, restricted to the assembly of these flexible bodies, i.e. it is focused on the definition of their connection.

The coupling of multi-body systems and finite element models is realized in commercial software, such as SIMPACK or MSC ADAMS. The latter is used in this work in combination with MSC-NASTRAN taking care of component mode synthesis of the flexible bodies. The Craig–Bampton method [5] is used allowing the selection of interface degrees of freedom for which additional static modes are generated. This was found to be a particularly suitable and efficient means to incorporate small linear-elastic body deformation into multi body systems. As a result the modal matrix Φ_i is generated for the N linear-elastic bodies of the system. It is used to express the physical coordinates $\bar{u}_i$ in terms of the generalized coordinate q_i.

$$\bar{u}_i = \sum_{i=1}^{N} \Phi_i q_i, \ \ i = 1, \ldots, N \tag{6.6}$$

The generalized mass matrix $\mathbf{M_i}$ and the generalized stiffness matrix $\mathbf{K_i}$ are computed once in the pre-process.

$$\mathbf{M_i} = \Phi_i^T \bar{\mathbf{M_i}} \Phi_i \tag{6.7}$$

$$\mathbf{K_i} = \Phi_i^T \bar{\mathbf{K_i}} \Phi_i \tag{6.8}$$
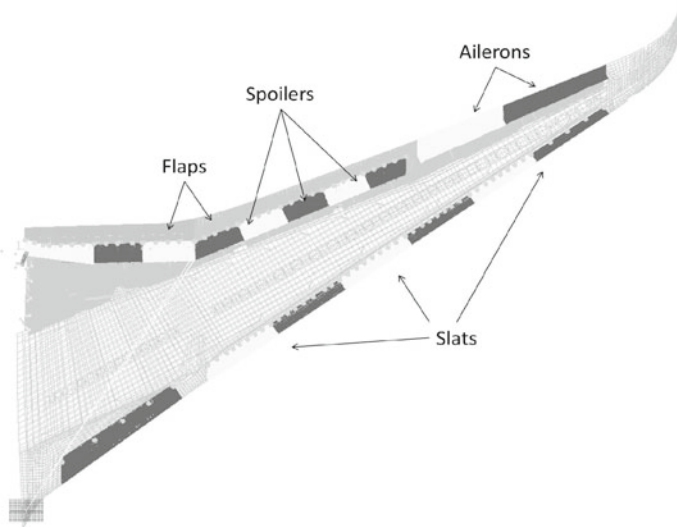
Fig. 6.9 Multi body model of an aircraft wing

In every step of the CFD-MBS loop, distributed aerodynamic forces $\bar{F}_i$ are applied to the linear-elastic bodies using modal transformation and for each flexible body the equation of motion, which is linear, is solved.

$$f_i = \Phi_i^T \bar{F}_i \tag{6.9}$$

$$\mathbf{M_i}\ddot{q}_i + \mathbf{K_i}q_i = f_i \tag{6.10}$$

Furthermore, the kinematic equations of motion in Lagrangian formulation are solved in MSC ADAMS, including nonlinear equations [10].

Figure 6.9 shows the multi-body model of a complete aircraft wing composed of $N = 28$ Flexible bodies. Additionally, rigid bodies, different kinds of joints, force elements (e.g. springs), contacts and constraints are used to reflect the real assembly of the wing.

A steady level flight condition at a typical cruise flight point ($Mach = 0.85$) is investigated. After about 10 CFD-MBS coupling iterations the loop (cf. Fig. 6.1) is converged. The resulting flight shape is depicted in Fig. 6.10 with respect to the unloaded and weightless jig shape.

Absolute bending (dz) and local angle of attack (ry) over the wing span are shown in Fig. 6.11. A good overall agreement between multi-body coupling (CFD-MBS), finite element coupling (CFD-FEM) and flight test measurement is observed.

In Fig. 6.12 the chord-wise deformation is presented as relative displacements in z-direction (z), i.e. absolute bending and local angle of attack (as depicted in Fig. 6.11) are subtracted. It reflects the deformation of leading- and trailing edge

Fig. 6.10 Aerodynamic surface shapes
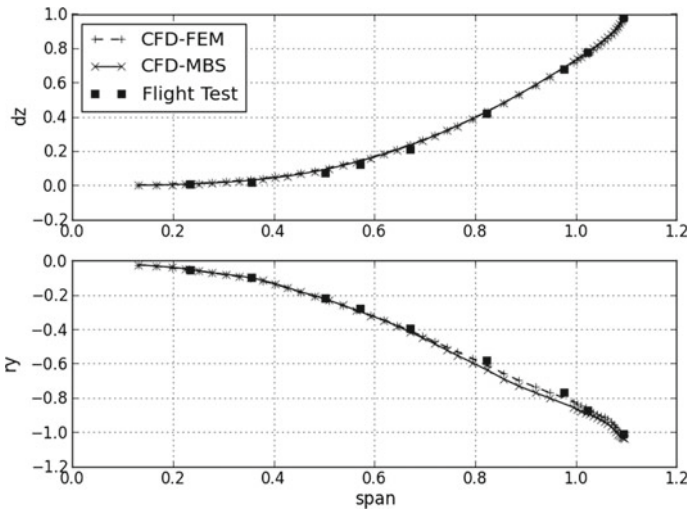
Fig. 6.11 Wing bending and local angle of attack

movables and the transition between the wing and movable surfaces in detail. The largest deflections are observed at the trailing edge. This upward deflection of trailing edge devices, essentially a decambering, is observed over the whole wing span. Another observation is the occurrence of steps at the transition between fixed wing and movable surfaces. As can be seen in the bottom part of Fig. 6.12, the deformation is globally well transferred to the CFD surface. The CFD model and the mesh deformation are, however, limiting the precise transfer of sharp edges due to mesh quality constraints. Therefore, the blending introduced by the coupling method leads to a smearing of steps.

For the present application multi body simulation facilitates an unprecedented level of detail of the static aeroelastic wing deformation. Cambering over the whole chord as well as steps between the fixed wing and movable surfaces can be resolved.
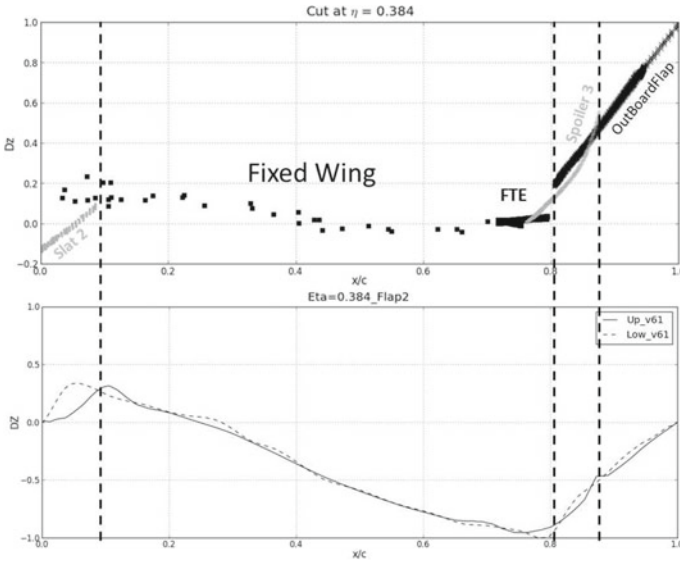
Fig. 6.12 Cambering at wing cut; Top: Structural deformation; Bottom: CFD surface deformation

This enables the quantification of these effects on aerodynamic characteristics which will be subject to future work. In order to better exploit the CSM capabilities in a coupled scheme, enhanced aerodynamic methods are to be applied.

6.4.2 Nonlinear CSM

As application example for nonlinear deformations a transport aircraft CFD model is coupled with an ABAQUS structural model of a relatively flexible wing-box. The flow conditions are subsonic at $Mach = 0.5$.

Here the results of 3 investigated C_{lift} values are presented. To get an impression of the overall deformation, the deformed CFD surface for the highest C_{lift} is plotted in Fig. 6.13. The large amount of deformation is clearly visible.

ABAQUS allows to compute the model in linear and nonlinear sense. In Fig. 6.14 the bend and twist (local angle of attack) of linear and nonlinear FEM is compared at constant C_{lift}. The structural deflections at the tip are up to 16% of the span, which reflects again the flexibility of the model. Furthermore it can be observed that the linear FEM exhibits a prolongation of the wing compared to the nonlinear case.

In Fig. 6.15 the local C_{lift} is compared for the highest C_{lift} value. Due to the wing prolongation of the linear case, the lift generated by the inboard part of the wing has decreased. Accordingly it must also be noted, that the outboard loads are lower for the nonlinear model.

Fig. 6.13 Comparison of deformed CFD surface for linear (lin) and nonlinear (NL) FEM at constant $C_{\text{lift}} = 0.85$, additionally the JIG shape is plotted
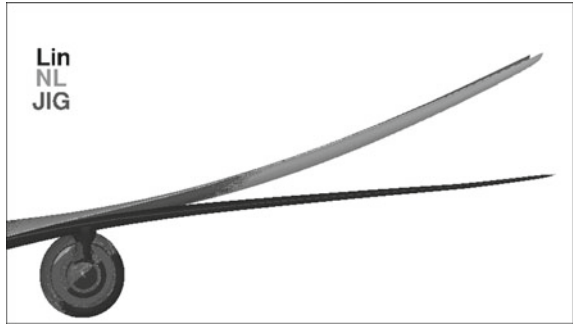
Fig. 6.14 Comparison of bend and local angle of attack (rot-y) for linear (lin) and nonlinear (NL) FEM at constant C_{lift}
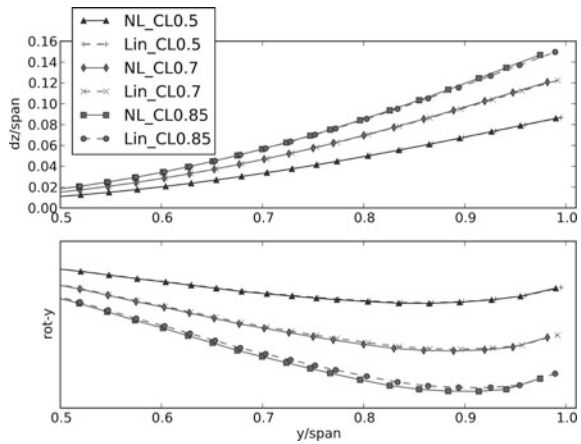
Fig. 6.15 Comparison of local C_{lift} for linear (lin) and nonlinear (NL) FEM at constant $C_{\text{lift}} = 0.85$
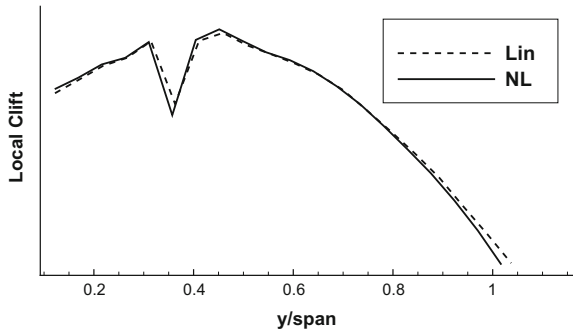
Table 6.1 compares the relative wing prolongations $\Delta\text{span}_{\text{rel}} = (\text{span}_{\text{JIG}} - \text{span}_{\text{Defo}}) / \text{span}_{\text{JIG}}$ and drag differences $\Delta C_{\text{drag,rel}} = (C_{\text{drag,NL}} - C_{\text{drag,Lin}}) / C_{\text{drag,Lin}}$ for the different C_{lift} cases. The linear FEM model span increases up to 1.6% for the highest CL in the deformed state while the nonlinear FEM case shows negligible span increase. This difference is reflected in the drag as well. The drag for the nonlinear computation decreases by up to 1%.

Table 6.1 Comparison of relative wing prolongation and relative drag-difference for linear (lin) and nonlinear (NL) FEM at constant C_{lift}

C_{lift}	$\Delta\mathrm{span}_{rel,lin}$ (%)	$\Delta\mathrm{span}_{rel,NL}$ (%)	$\Delta C_{drag,rel}$ (%)
0.50	0.552	0.0058	−0.059
0.70	1.100	0.0077	−0.268
0.85	1.641	0.0081	−1.094

The results show that for a very flexible wing the selection of an appropriate structural model is essential for accurate CFD-CSM results. And it should be underlined that for more relevant transonic *Mach*-numbers the differences are very likely to be more significant.

6.5 Summary/Conclusion

The paper has presented application examples of high-fidelity aeroelasticity. On aerodynamic side this includes the usage of RANS-CFD. On structural side the accurate inclusion of natural vibrations and different types of nonlinearities was shown.

For the case of flutter investigations the combination of linearised CFD and a simple least-squares ROM allows to use CFD aerodynamics directly without correcting a lower fidelity aerodynamic method.

For static aeroelasticity the focus has been oriented especially on complex structural models including nonlinearities. Here the multi-body model allows to use structural models of very high resolution with nonlinear component movement, while for a different wing-box FEM the importance of including geometric nonlinearities for very flexible wing has been presented.

References

1. E. Albano, W.P. Rodden, A doublet-lattice method for calculating lift distributions on oscillating surfaces in subsonic flows. AIAA J. **7**, 279–285 (1969)
2. H. Barnewitz, B. Stickan, Improved mesh deformation, in *Management and Minimisation of Uncertainties and Errors in Numerical Aerodynamics*, vol. 122, Notes on Numerical Fluid Mechanics and Multidisciplinary Design, ed. by B. Eisfeld, H. Barnewitz, W. Fritz, F. Thiele (Springer, Berlin, 2013), pp. 219–243
3. H. Bleecke, B. Stickan, Industrial comflite applications, in *Computational Flight Testing*, vol. 123, Notes on Numerical Fluid Mechanics and Multidisciplinary Design, ed. by N. Kroll, R. Radespiel, J.W. Burg, K. Sørensen (Springer, Berlin, 2013), pp. 249–256
4. L. Cavagna, P. Masarati, G. Quaranta, Coupled multibody/computational fluid dynamics simulation of maneuvering flexible aircraft. J. Aircr. **48**(1), 92–106 (2011)

5. R.R. Craig Jr., M.C.C. Bampton, Coupling of substructures for dynamic analyses. AIAA J. **6**(7), 1313–1319 (1968)
6. Dassault Systémes. *DS-ABAQUS*, www.3ds.com
7. T. Gerhold, M. Galle, Calculation of complex three-dimensional configurations employing the DLR TAU-code, in *AIAA Paper 97-0167* (1997)
8. H.J. Hassig, An approximate true damping solution of the flutter equation by determinant iteration. J. Aircr. **8**(11), 885–889 (1971)
9. C. Kaiser, R. Thormann, D. Dimitrov, J. Nitzsche, Time-linearized analysis of motionr-induced and gust-induced airloads with the dlr tau code, in *Deutscher Luft- und Raumfahrtkongress* (2015)
10. MSC. *MSC-ADAMS*, www.mscsoftware.com
11. MSC. *MSC-Nastran*, www.mscsoftware.com
12. R. Palacios, H. Climent, A. Karlsson, B. Winzell, Assessment of strategies for correcting linear unsteady aerodynamics using cfd or experimental results (2001)
13. A.A. Shabana, Flexible multibody dynamics: review of past and recent developments (1997)
14. B. Stickan, H. Bleecke, S. Schulze, Nastran based static cfd-csm coupling in flowsimulator, in *Computational Flight Testing*, vol. 123, Notes on Numerical Fluid Mechanics and Multidisciplinary Design, ed. by N. Kroll, R. Radespiel, J.W. Burg, K. Sørensen (Springer, Berlin, 2013), pp. 223–234
15. B. Stickan, J. Dillinger, G. Schewe, Computational aeroelastic investigation of a transonic limit-cycle-oscillation experiment at a transport aircraft wing model. J. Fluids Struct. **49**, 223–241 (2014)
16. B. Stickan, J. Dillinger, J. Nitzsche, Limit-cylcle-oscillation simulations of aerostabil windtunnel experiments 2, in *International Forum on Aeroelasticity and Structural Dynamics (IFASD)*, St. Petersburg (2015)
17. R. Thormann, M. Widhalm, Linear-frequency-domain predictions of dynamic-response data for viscous transonic flows, in *AIAA-Journal* (2013)
18. O. Wallrapp, Flexible bodies in multibody system codes. Veh. Syst. Dyn. **30**(3–4), 237–256 (1998)

Chapter 7
New CFD Practices for Modelling High-Speed Flows

Jan Willem van der Burg, Matthias Lühmann, H. Jakob and J. Benton

Abstract Computational Fluid Dynamics (CFD) is used extensively in modelling high-speed flows for commercial transport aircraft. Current production CFD has deficiencies in modelling specific flow features. In this paper unitary flow cases are considered for specific flow features such as boundary layers, vortical flow, flow separation and shock boundary layer interaction. In the paper new CFD practices in meshing and turbulence modelling are investigated in order to better represent these flow features. In order to measure improvements metrics are introduced which measure an improvement with respect to a reference (from wind tunnel experiment or LES computation). In the paper it is shown that application of new CFD practices give an improved prediction of boundary layer and vortical flow.

7.1 Introduction

Wind tunnel experiments and flight tests are valuable sources for CFD validation. In recent years many CFD validation studies have been conducted for commercial transport cruise configurations. To understand and improve CFD prediction new practices for high-speed flows are studied. A number of new practices in meshing, turbulence modelling and in-tunnel computations are presented in this paper. Each of these practices focusses on a specific aspect of high-speed flow. The improvements will lead to a better representation of specific flow features such as: boundary layers, vortical flow, flow with high streamline curvature, corner flow or the three-dimensional flow field.

J. W. van der Burg (✉) · M. Lühmann · H. Jakob · J. Benton
Airbus Operations GmbH, Airbus-allee 1, 28199 Bremen, Germany
e-mail: jan-willem.vanderburg@airbus.com

M. Lühmann
e-mail: matthias.luehmann@airbus.com

A new practice for modelling high-speed flow studied here is the Reynolds Stress Model (RSM). Currently, the Menter-SST turbulence model [1] is used for CFD production in the Airbus aerodynamic data and design departments. From a theoretical point of view it can be shown that a RSM turbulence model is better able to represent specific physical flow features compared to a *k*-based turbulence model like the Menter-SST model. This is explained in the first part of the paper. The actual implementation of the RSM turbulence model in the DLR Tau code [2] is verified in a number of unit case studies. The RSM based turbulence model has been developed by DLR. A number of improvements have been introduced in recent years in the model, see [3, 4]. Application of the RSM turbulence model to a high-speed wind tunnel model is meant to illustrate the improvement.

Furthermore, two CFD validation studies for shock boundary layer interaction are described. These studies concentrate on the Delery bump in the wind tunnel and the M2155 wing in the wind tunnel under transonic flow conditions. Flow computations using the Menter-SST and RSM turbulence model are discussed and compared to experimental results. The focus here will be as well on practices related to the simulation of the experimental setup, such as boundary conditions, flow conditions and wind tunnel geometry.

7.2 Why a RSM-based Turbulence Model?

Eddy-viscosity models are widely used to compute turbulent flow around commercial transport aircraft configurations. Three considerations described here lead to the conclusion that an RSM based turbulence model is better suited to model complex flows as experienced in low-speed and high-speed flows.

Firstly, an eddy-viscosity model is based on a direct Reynolds stress model that links Reynolds stress to the mean strain rate tensor (Boussinesq hypothesis, 1877). The hypothesis is reasonable for simple turbulent shear flows (e.g., the round jet, mixing layer, channel flow, and boundary layer) where the turbulence characteristics and mean velocity gradients change relatively slowly (following the mean flow). In Ref. [5] it is mentioned that: 'In general, the turbulent-viscosity hypothesis is incorrect'.

Secondly, in the exact formulation of the production term for the k-equation the rotational terms cancel out due to a product of a symmetric Reynolds tensor and an anti-symmetric rotational tensor. This results in a too large level of turbulence in rotating flows and leads to a too rapid dissipation of vorticity. As a consequence for a *k*-based model a vortex will be dissipated more rapidly compared to a RSM turbulence model.

Thirdly, the Boussinesq hypothesis in *k*-based turbulence models fails to predict the normal stress anisotropy at walls, see also [6]. Normal stress anisotropy is considered to be responsible for the development of longitudinal vortices in rectangular ducts and other corner flows features for example a wing-body junction.

To summarize a Reynolds stress based turbulence model allows to better model complex flows compared to a k-based turbulence model.

7.3 Verification of a Modern Turbulence Model

In order to get more confidence in the CFD predictions using the RSM based turbulence model in the TAU code a number of verification studies are performed. The RSM turbulence model is verified here for a number of physical flow features representative for high-speed flows, namely: boundary layer, vortical flow, and flow separation.

Verification of a Zero-Pressure Gradient Boundary Layer for a Flat Plate

In a CFD study performed for a flat plate the computed displacement and momentum defect thickness are compared to the experimental values, see Ref. [7]. The flat plate has a length of 5 grid-units, hence $L_{ref} = 5$, the Reynolds number is $Re = 10.9$ million. In order to assess how well a computed boundary layer matches experimental data a metric is introduced. The metric chosen here is the value of the displacement thickness and momentum defect thickness at $x = 4$. Two meshes are considered for this the study, a current practice hybrid mesh representative of near wall meshing in a high-speed configuration with approximately 30 meshing points representing the boundary layer and a structured mesh with approximately 100 mesh points representing the boundary layer. The structured mesh has a larger boundary layer resolution. The structured mesh is produced by DLR. The numerical results are summarised in Table 7.1. It can be observed that the numerical results using the RSM method on a structured mesh are within 1% of experimental values whereas the Menter-SST based method on a current practice mesh is only within 10% of experimental values, Menter-SST on the structured mesh is within 2.5%. The computed momentum defect thicknesses are shown in Fig. 7.1. This indicates that the agreement with experimental data is improved by increasing boundary layer resolution and applying a RSM turbulence model.

Table 7.1 Computed displacement thickness and momentum defect thickness at $x = 4$ computed with Menter-SST and RSM compared to the experimental value from the Wieghardt experiment

	Displacement thickness	Momentum defect thickness
Experiment Wieghardt	0.0078	0.0059
Menter-SST, current practice mesh	0.00825 (+5.8%)	0.00643 (+9.0%)
Menter-SST, structured mesh	0.00757 (−2.9%)	0.00576 (−2.4%)
RSM, structured mesh	0.00772 (−1.0%)	0.00585 (−0.8%)
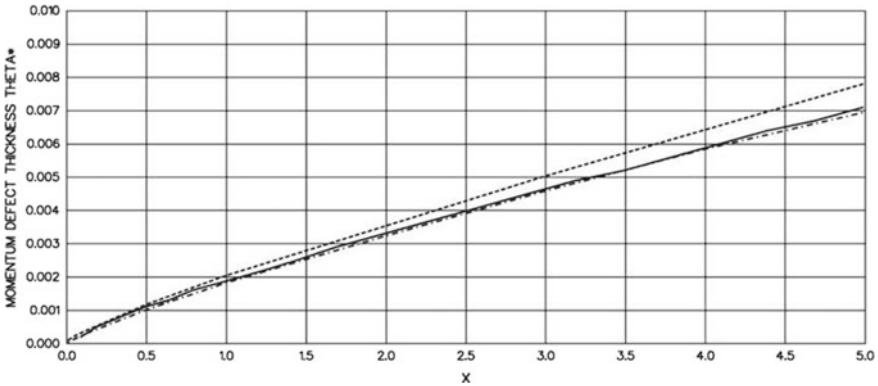
Fig. 7.1 Experimental momentum defect thickness for a flat plate in the Wieghardt experiment (dash-dot) and the momentum defect thickness computed with RSM on a structured mesh (solid line) and computed with Menter-SST on a current practice mesh (dotted line)

Fig. 7.2 Verification of the computed Reynolds stress component R13 in the log-layer (solid line) and its theoretical value (dashed line). The Reynolds stress is taken at a rake position on the outboard upper wing
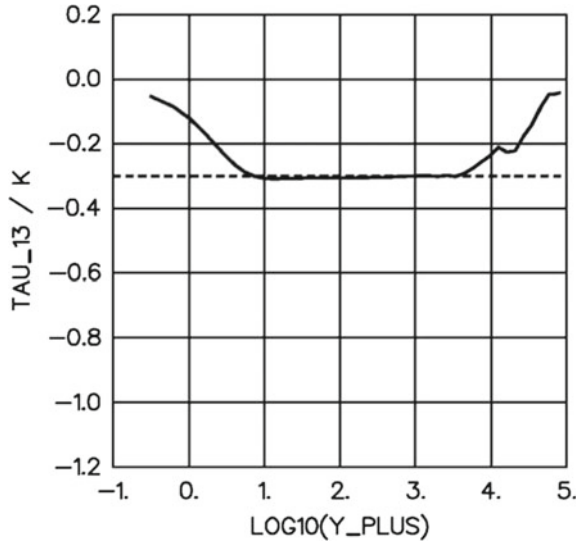
Verification of a Boundary Layer on a High-Speed Wing

To verify the size of the Reynolds stresses in a turbulent boundary layer, the turbulent flow solution for a wind tunnel model of a representative high-speed aircraft is studied. A rake is considered which is placed on the upper outboard wing. The computed Reynolds stresses are compared to theoretical values in the viscous sub-layer and log-layer.

In Fig. 7.2 it is shown that a good agreement in the log-layer between the computed Reynolds stress R13 and its theoretical value is obtained. A similar agreement is found for the normal stress components. It can be concluded that the RSM implementation

is correct and the near-wall meshing is sufficient to resolve the Reynolds stresses. In the viscous sublayer similarly a good agreement is found for the wall normal profiles of k^+ and ω^+ at the same rake position (not shown).

Verification of Vortical Flow for a NACA0012 Wing in a Wind Tunnel

The representation of vortical flow in a turbulent flow solution is studied for the NACA0012 wing mounted in a wind tunnel. A tip vortex is formed by putting the NACA0012 wing under 10 degrees angle of attack. In this study the computed circumferential velocity and the axial velocity distributions are compared to experimental values. Two meshes are considered, a hybrid mesh having prismatic elements near the walls and tetrahedral elements in the remainder in the flow domain and a hybrid mesh with hexahedral elements in the wake at the location of the tip-vortex.

In Fig. 7.3 the flow computations on the hybrid mesh with hexahedral elements in the wake are compared. It can be observed that the RSM turbulence model yields a better agreement with an Oseen–Lamb vortex in terms of vortex spreading than the Menter-SST turbulence model. This is an expected result, since by construction the RSM method should be able to better capture vortical flow compared to Menter-SST. The vortex computed with the Menter-SST method shows less agreement. In terms of metrics the results are summarised in Table 7.2. It can be observed that the RSM turbulence model yields an agreement within 2%.

In Table 7.3 the values of the computed axial velocities on the two meshes are compared to the experimental value at a location 69% downstream of the chord. It can be observed in table the Reynolds stress turbulence model is better able to capture the slope of the axial velocity decay compared to the Menter-SST model which shows a too strong decay of the axial velocity. This is in line with the construction of the RSM
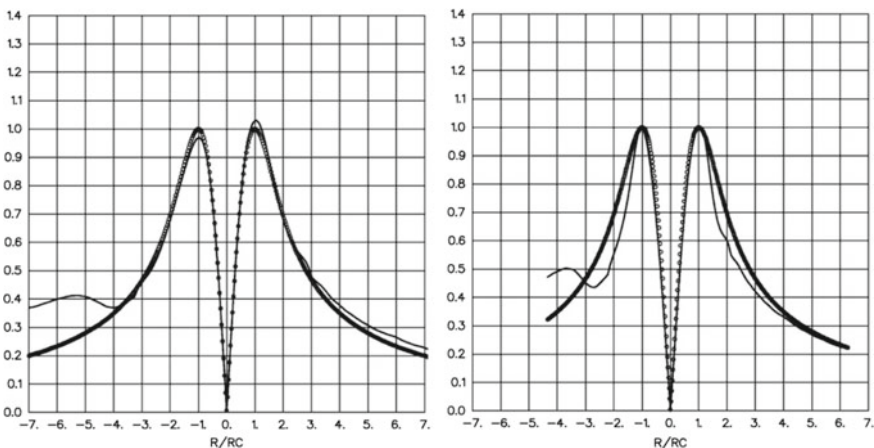
Fig. 7.3 The circumferential velocity profile computed with RSM (left, solid line) and Menter-SST (right, solid line) at 69% chord downstream of the wing is shown is cross-compared with the circumferential velocity profile from Oseen–Lamb theory (dotted line). In the computational hexahedral elements are introduced at the location of the vortex

Table 7.2 Metrics used to assess the representation of a tip vortex at 69% chord downstream of the wing. In the table the spreading rate of the circumferential velocity computed with Menter-SST and RSM at $r = 2$ is compared to the theoretical value based on Oseen–Lamb theory

Method	$V_T / V_{T,max}$ at $r/rc = 2$
Oseen–Lamb (Theory)	0.695
Menter-SST	0.600 (-13.6%)
RSM	0.682 (-1.8%)

Table 7.3 Metrics used to assess the axial velocity at 69% chord downstream of the wing. In the table the computed axial velocity with SST and RSM at 69% chord downstream is compared to the experimental value

Method	u/U_∞ on centre line ($x = 0.826$)
Experiment	1.699
Menter-SST, tetrahedral elements in wake	0.720 (-58%)
Menter-SST, hexahedral elements in wake	0.894 (-47%)
RSM, tetrahedral elements in wake	0.744 (-56%)
RSM, hexahedral elements in wake	1.421 (-16%)

and k-based models (see previous section). The absolute value of the axial velocity along the centerline computed with the RSM turbulence model is still in the order of 16% below the experimental value. Two possible reasons could explain this: either the amount of numerical dissipation is still to high and needs to be reduced by means of for example a matrix dissipation method [8], or the creation of the vortex on the wing is not properly modelled yet. In principle the onset of a vortex on a wing is a flow separation, where mass is taken from the surface to form the vortex. Further studies will be needed to investigate these points. In addition it can be observed that the decay in axial velocity is also too strong for RSM on a mesh with a tetrahedral wake. When applying an unstructured tetrahedral mesh the vortex is diffused and a less good agreement is achieved (for both RSM and Menter-SST). This is believed to be due to the way the gradients are computed in the flow solver. Due to symmetry properties of the hexahedral mesh the truncation error for a green-gauss gradient is smaller compared to the truncation error on a comparable tetrahedral mesh.

So, it can be summarised that the tip vortex can be captured more accurately by firstly introducing hexahedral elements at the location of the vortex and secondly by applying a Reynolds stress model, so that a more physical development (dissipation) of the vortex is guaranteed.

Verification of Flow Separation for the 2D Curved Backward Facing Step

In a study for the two-dimensional curved backward facing step the representation of a flow separation under an adverse pressure gradient is studied. The reference experiment is a LES flow solution which is made available at the turbulence model resource [9]. To this purpose a three-dimensional hybrid mesh using the current mesh practice is defined having prismatic elements near the upper and lower wall
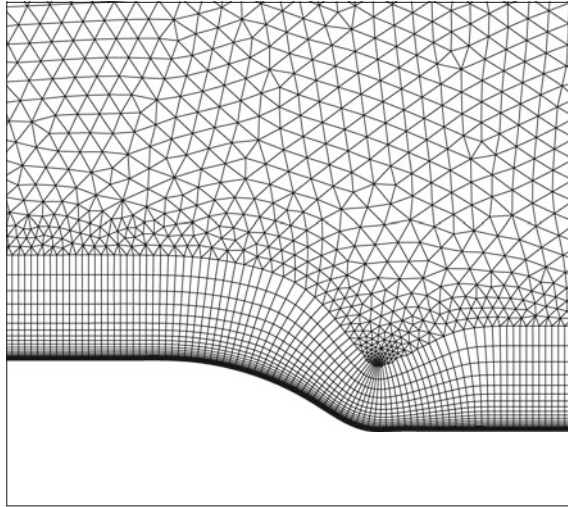
Fig. 7.4 Illustration of two-dimensional hybrid mesh used in the Menter-SST and RSM computation
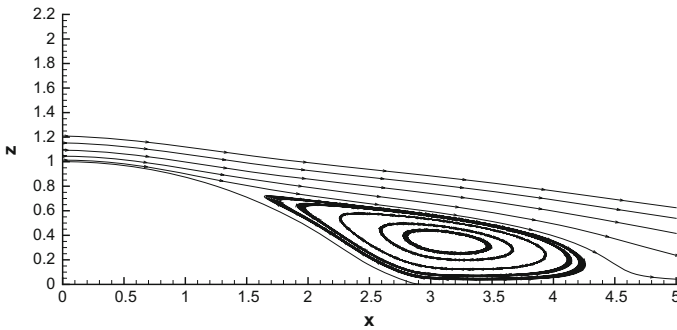
Fig. 7.5 Illustration of the computed streamlines using RSM for the curved backward facing step

and tetrahedral elements in the remainder of the flow domain, see Fig. 7.4. At the inflow plane the quantities of the LES flow solution are enforced. An illustration of the computed flow separation using RSM can be observed in Fig. 7.5. A flow separation is formed at the location of the backward facing step. A smooth surface separation is obtained, the flow separation is not fixated by geometry.

In Table 7.4 the computational results are summarised in terms of metrics. The point of separation and point of reattachment are determined as the point on the surface where the skin friction changes sign. It can be observed that the computed separation length using the RSM method is in agreement with the LES flow solution. Nevertheless, the point of separation and point of re-attachment are shifted. Menter-SST overpredicts the separation length. Further analysis shows that the turbulent

Table 7.4 Metrics used to assess the representation of the flow separation under adverse pressure gradient. Cross-comparison of the point of separation, point of reattachment and separation length in the flow solution computed with LES, SST and RSM

Source	Point of separation	Point of re-attachment	Separation length
LES fow solution	0.85	4.31	3.46
Menter-SST	0.9	3 5.06	4.13
RSM	0.95	4.38	3.43

kinetic energy computed by SST and RSM behind the curved backward facing step underpredict the turbulent kinetic energy computed with the LES method.

A possible explanation for the later point of separation in the RSM computation compared to the LES computation is that due to a different boundary layer development upstream the separated areas are shifted. The current practice mesh has only approximately 30 grid points in wall normal direction. An increase would lead to a better boundary layer representation. Another influence on the turbulent quantities is that in the SST and RSM computation the boundary condition for the specific dissipation rate ω needs to be derived from the LES flow solution. This specification is not straight-forward.

Verification for a High-Speed Aircraft Wind Tunnel Model in ETW

The recently available RSM turbulence model [10, 11] is applied to a high-speed aircraft configuration under ETW wind tunnel conditions. Vortices that appear in the pylon wing area for high angle of attack under transonic conditions are studied here. In Fig. 7.6 the computed flow solution at $M = 0.85$ and $\alpha = 5$ degrees computed using RSM and Menter-SST is shown. It can be observed that in the RSM computation the
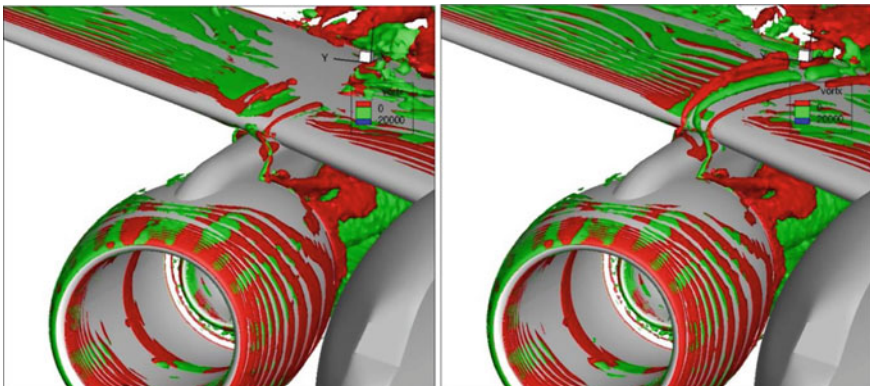
Fig. 7.6 Computed kinematic vorticity number using Menter-SST (left) and RSM (right) at $\alpha = 5$ degrees. The kinematic vorticity number defines the rotation rate divided by the strain rate. Computed flow solutions shown are for a high-speed aircraft configuration with a through-flow nacelle in ETW configuration. High angle of attack
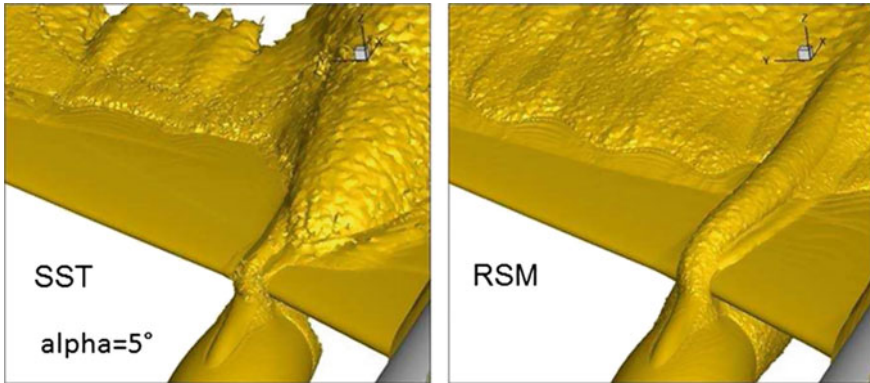
Fig. 7.7 Illustration of the computed flow separation by means of the vorticity for Menter-SST (left) and RSM (right) for a high-speed aircraft configuration at $\alpha = 5$ degrees

vortices are maintained on the upper wing behind the nacelle. In the Menter-SST flow computation these vortices are weakened (as expected by construction) allowing an early flow separation on the upper wing. The result of this flow separation is that a too early lift stall compared to experimental values (not shown) is experienced. The RSM method shows a good agreement between computed and experimental lift even for higher angles of attack. The computed flow separation patterns can be observed in Fig. 7.7.

7.4   Validation of Shock-Boundary Layer Interaction for the Delery Bump

A CFD validation study is performed for the Delery bump [12] in a wind tunnel section. In the CFD study Menter-SST and RSM are applied to verify the flow separation occurring behind the shock. To this purpose metrics are introduced to assess the point of separation, point of re-attachment and the separation length. Boundary conditions specified are inflow and outflow. On the upper and lower wind tunnel wall a viscous boundary layer is specified.

It is verified that the Delery bump in-tunnel results are in good agreement with experimental pressure distributions. Tunnel wall pressure distributions are in good agreement as well. The computed flow separation can be observed in Fig. 7.8. A shock positioned on the bump causes the flow to separate, a separation bubble is formed.

The computed and experimental point of separation, point of re-attachment and separation length are shown in Table 7.5. The value in two experiments for the Delery bump are shown in Table 7.5, see also [10, 11] It can be observed that the computed separation length with RSM is smaller than the experimental separation length.

Fig. 7.8 Illustration of the computed flow separation using the RSM turbulence model; Contour lines of Mach (dotted line) and velocity (solid line) are shown
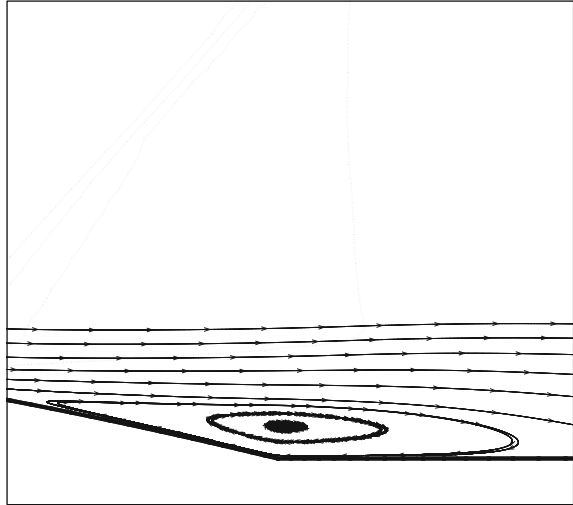
Table 7.5 Metrics used to assess shock-boundary layer separation. Cross-comparison of the point of separation, point of reattachment and separation length (all in [mm]) for two experiments and flow solution computed with SST and RSM

Source	Point of separation	Point of re-attachment	Separation length
Experiment AIAA-2011-479	264.96 ± 1.2	324.96 ± 1.2	60 ± 2.4
Experiment AIAA-2013-2445	262.08	324.48	62.40
Structured mesh, SST	258.00	329.78	71.78
Structured mesh, RSM	260.12	309.31	49.19

Menter-SST computes a larger separation length compared to experiment. This trend is also observed on other computational meshes considered (Centaur and Solar). It should be mentioned that numerical results are affected by the out-flow pressure gradient. This gradient is not sufficiently represented and can be improved by modelling the wind tunnel section downstream of the test section. However, the geometrical shape of the wind tunnel behind the test section is not accessible any longer, since the RAE wind tunnel does not exist anymore.

7.5 Validation of Shock-Boundary Layer Interaction for the M2155 Wing

The aim is to perform a CFD validation study for shock-boundary layer interaction for the M2155 wing [13]. The experimental wind tunnel data for the M2155 wing indicates the occurrence of shock-boundary layer interaction at Mach 0.806 and

Mach 0.854. The M2155 geometry definition consists of a series of two-dimensional profile sections. The final M2155 wing shape should be entirely defined for creating a mesh. A surface loft of the section data is defined based on the two-dimensional sections. In particular the wing tip design requires to fill the space between the sectional data with an three-dimensional surface loft. Sectional data are available in nominal and actual shape. The creation of two-dimensional splines from sectional data is restricted to the nominal geometry because spline quality criteria are not met for the actual data basis. For this reason the mesh generation is based on the nominal surface shape. The three-dimensional wind tunnel shape and location of the model is only known to some degree and has required some additional assumptions for the final shape and setup definition. Meshes for the M2155 geometry are generated by the hybrid mesh generation software Centaur [14].

Viscous wall boundary conditions are utilized on the wing surface and on the tunnel wall attached to the wing. Inflow and outflow condition at the tunnel inlet and exit, the outflow is adjusted to match an experimental pressure value on the tunnel wall close to the tunnel exit. A Mach number adjustment is not performed because of missing data for the Mach number measurement location.

Different approaches for the setup of wind tunnel boundary conditions are studied and it is observed in these studies that the wind tunnel boundary conditions have a significant impact on the numerical results. A good agreement between numerical and experimental results could only be achieved through the utilization of an inviscid wind tunnel boundary condition. For the inviscid tunnel wall boundary conditions the tunnel flow is not effected by the wind tunnel boundary layer. The reduced pressure losses result in a better agreement with experimental data. Wing pressure distributions could reach a sufficient matching of numerical and experimental results only under these constraints. It should be mentioned that the computational pressure losses on the other hand are not considered correctly within the test section.

The application of an inviscid wall boundary is necessary due to a difference between the actual experimental and numerical wind tunnel geometry. The wind tunnel wall has likely a slightly diverging shape, whereas in the numerical computation the wind tunnel walls are modelled by means of a rectangular box (no divergence). This difference of the tunnel shape effects the tunnel boundary layer directly and leads to a wrong flow field at the wind tunnel model location. The experimental set-up and geometric details located inside and outside of the wind tunnel test section contour are not accessible any longer, the wind tunnel does not exist anymore. The inviscid tunnel wall boundary condition can neglect wrong viscous boundary layer effects and provides thereby a better agreement of the numerical and experimental flow close to the model location. For computations using exact tunnel wall shape descriptions a deployment of the viscous wall boundary condition is appropriate.

In a CFD study performed for the two-dimensional Delery bump the validation of results demonstrated a good agreement of numerical and experimental tunnel wall pressure distributions for the viscous tunnel wall boundary condition. In contrast to the Delery bump results a viscous wall boundary condition at the M2155 tunnel wall has not created the correct flow field at the model location. Only an inviscid tunnel wall boundary condition could establish the required adjustment.
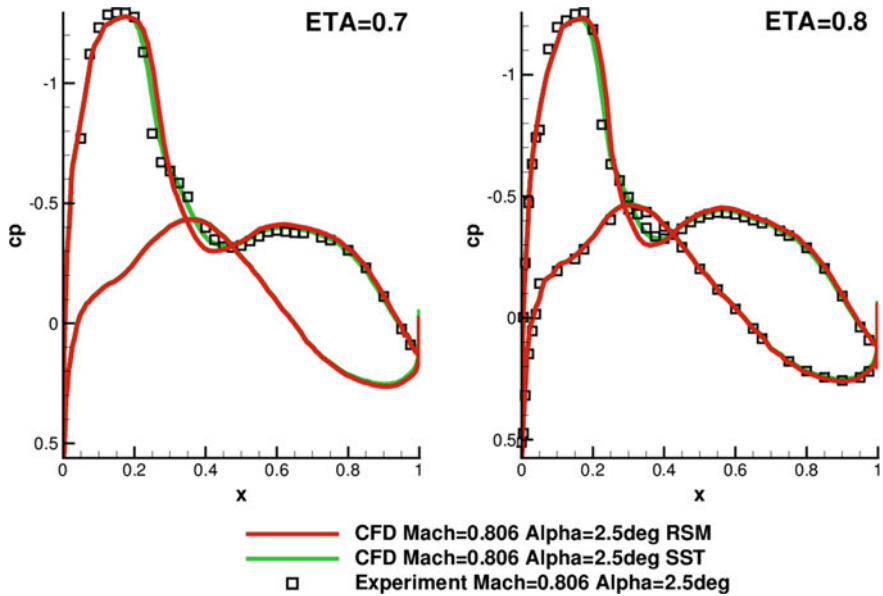
Fig. 7.9 M2155 Wing Pressure Distribution for Mach = 0.806

The turbulent flow computations for M2155 reach convergence. In some cases the number of iterations or the CFL number was modified to achieve convergence. The computed pressure distributions are shown in Fig. 7.9. The agreement with experimental wing pressure distributions is good Fig. 7.9. Differences between RSM and Menter-SST model are small. Figure 7.10 compares the computed and experimental skin friction lines. Consistent with the Delery bump the numerical results computed with the Menter-SST turbulence model (not shown) displays larger area of separation beyond the shock compared to RSM (shown).

On the opposite wind tunnel wall pressure distributions do not display a good agreement with experimental data because of the inviscid tunnel wall boundary condition and the lack of geometrical accuracy of the tunnel wall shape. The actual wind tunnel geometry should be modelled to achieve better agreement. It is believed that a Mach number correction probably would reduce differences between calculation and experiment as well. It was not possible though to use the actual experimental Mach number since information on the wind tunnel correction method and Mach number measurement location are not available.
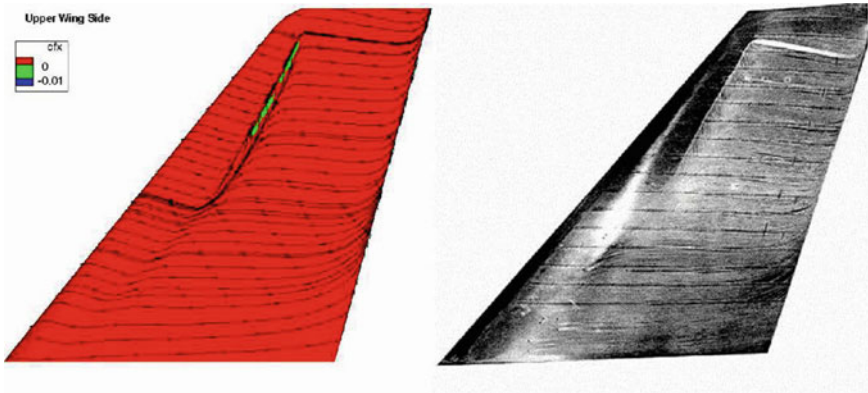
Fig. 7.10 Computed skin friction distribution using RSM (left) and experimental oil visualisation (right) for Mach = 0.806

7.6   Conclusion

New CFD practices in meshing, turbulence model and in-tunnel modelling have been studied for transonic flows. In particular the Reynolds stress model is verified and validated in a number of unit case CFD studies. It is concluded that the current implementation of a Reynolds stress model in the Tau code confirms the expected theoretical behaviour, namely a better representation of boundary layers and vortical flow. For accurate modelling of vortical flow it is concluded that it is necessary to use a structured mesh topology. The underlying reason for this is the way the gradients are computed on the flow solver. RSM turbulence model behaviour for modelling vortical flow is verified for a representative high-speed commercial transport aircraft.

In the validation exercises for shock-boundary layer interaction a definitive conclusion cannot be made. Differences in separation length are observed between Menter-SST and RSM. In order to make a definitive conclusion it is necessary to model the wind tunnel walls in the CFD model. In the current studies the test section is used which is considered to be not enough. For the Delery bump the wind tunnel geometry downstream of the test section needs to be modelled. For the M2155 wing the divergence of the test section and likely wind tunnel geometry downstream of the test section needs to be included in the CFD model.

Further validation exercises for more complex flows are necessary to gain more confidence in the behaviour of the Reynolds stress turbulence model. It is recommended to perform a new wind tunnel experiment in order to generate proper CFD validation data. In the associated CFD validation exercise it is recommended to model a larger part of the wind tunnel geometry, so that for example flow gradients occurring in the outflow area are better represented.

References

1. F.R. Menter, M. Kuntz, R. Langtry, Ten Years of Industrial Experience with the SST Turbulence Model, Turbulence, Heat and Mass Transfer, vol. 4, Begell House, Inc. (2003)
2. A. Beckert, T. Gerhold, G. Gunther, D. Schwamborn, K. Weinman, Application of the DLR-TAU code to fluid-structure interaction on hybrid grids, in *Proceedings of ECCOMAS 2000*, Barcelona, 11–14 Sept 2000
3. V. Togiti, B. Eisfeld, Assessment of g-equation formulation for a second-moment reynolds stress turbulence model, in *AIAA-2015-2925*
4. B. Eisfeld, C. Rumsey, V. Togiti, Second-moment RANS model verification and validation using the turbulence modeling resource website (Invited), in *AIAA-2015-2924*
5. S.B. Pope, Turbulent Flows (2002)
6. B. Eisfeld, Comparison of DRSM and k-based models, DLR-report (2012)
7. K. Wieghardt, W. Tillman, On the turbulent frcition layer for rising pressure, in *1968 AFOSR-IPF Stanford Conference*, vol. II (Department of Mechanicsl Engineering, Standford University, Stanford, CA, Thermosciences Division, 1969)
8. A. Grimminger, Vortical flow correction models in TAU, private investigation (2010)
9. C.L. Rumsey, Turbulence modeling resource, http://turbmodels.larc.nasa.gov. May 2015
10. M. Emory, R. Pecnik, G. Laccarino, Modeling structural uncertainties in reynolds-averaged computations of shock/boundary layer interactions, in *AIAA 2011-0479* (2011)
11. K. Chitale, O. Sahni, S. Tendulkar, R. Nastasi, K.E. Jansen, M. Shephard, Boundary layer adaptivity for transonic turbulent fows, in *AIAA 2013-2445* (2013)
12. J. Delery, Investigation of strong shock turbulent boundary layer interaction in 2 D transonic flows with emphasis on turbulence phenomena, in *14 th American Institute of Aeronautics and Astronautics, Fluid and Plasma Dynamics Conference* (Palo Alto, CA, 1981)
13. AGARD-AR-303 vol. II, Advisory Group for Aerospace Research And Development, 7 RUE Ancelle, 92200 Neuilly-sur-Seine, France, August 1994
14. Data available at CentaurSoft, "CENTAUR", www.centaursoft.com
15. M. Leatham, S. Stokes, J.A. Shaw, J. Cooper, J. Appa, T.A. Blayloc, Automatic Mesh generation for rapid-response Navier-Stokes calculations, in *AIAA Paper 2000-2247* (2000)

Part III
Use-Case OPTIMALE

Chapter 8
Application of Adjoint Based Optimization on a MALE Platform

Kolja Elssel, Kaare Sørensen and Ögmundur Petersson

Abstract Within the AeroStruct project an adjoint based optimization framework has been established based on Reynolds averaged Navier Stokes aerodynamics and FEM structural mechanics analysis using the same geometric model. A parametric geometry kernel (Descartes) has been developed on the basis of the CPACS dataformat as the core of the system. The system has been setup in a flexible and modular fashion such that components can be exchanged and the system can be applied to applications needing only a subset of the functionality. This article describes some of the integration details as well as applications with results.

8.1 Use-Case Optimale

The subject of the AeroStruct project at Airbus Defence and Space was to develop and verify new capabilities in high-fidelity multidisciplinary optimization. The goal was to reduce development time and cost by higher integration of aerodynamic and structural design capabilities. In a conventional aircraft development an aircraft loft and structural layout is found by iteration of sequential work of aerodynamics and structural mechanics until a configuration is found which fulfills the requirements and is agreed. These iterations usually take months and are in the critical path of the aircraft development process thus being very cost and time intensive.

With the development of a high fidelity multidisciplinary optimization framework it is conceived to be possible to reduce costs by starting from a valid design for aerodynamics and structural mechanics and by being able to investigate different configuration layouts simultaneously.

K. Elssel (✉) · K. Sørensen · Ö. Petersson
Airbus Defence and Space, Rechliner Strasse, 85077 Manching, Germany
e-mail: kolja.elssel@airbus.com

K. Sørensen
e-mail: kaare.sorensen@airbus.com

Ö. Petersson
e-mail: oegmundur.petersson@airbus.com

Fig. 8.1 OPTIMALE -
parameterized catia V5
model
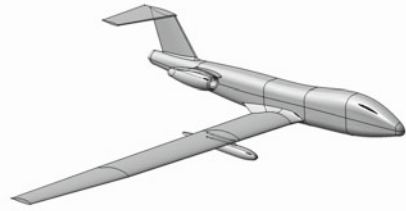
The development scenario that was defined for AeroStruct was a Medium Altitude
and Long Endurance configuration which was to be optimized for maximum range.
The system was to be demonstrated for disciplinary as well as multidisciplinary
optimizations and for single component modifications as well as large configuration
changes.

8.1.1 Setup of Parameterized Model

In order to test the MDA processes being developed between different engineer-
ing teams at Airbus Defence and Space (Aerodynamics and Structures) a common
and representative Use-Case, a generic MALE-type aircraft configuration has been
defined, named the OptiMALE (Fig. 8.1). This model has been designed from scratch
to allow for exchange and cooperation with external partners (TU Munich, TU Braun-
schweig, DLR).

The model has been constructed in an intrinsically parametric fashion. For
instance, the fuselage has been constructed using parameterized sections (Fig. 8.2)
which are positioned along a fuselage line with dimensionless longitudinal position
between zero and one. The absolute position then depends on the fuselage length,
allowing for simple scaling of the model.

A number of parameters of the baseline configuration of the Optimale is externally
available by default, others can easily be added.

- Fuselage (Sections + Length): 28

  - 5 Parameters for 5 Sections
  - 2 Parameter for last Section
  - Overall Length

- Wing (Planform + Position): 14

  - Position, Span, Segmentation: 5
  - Sweep, Twist, Taper: 9

- Total Parameters: 42

Fig. 8.2 Parameterized
fuselage section
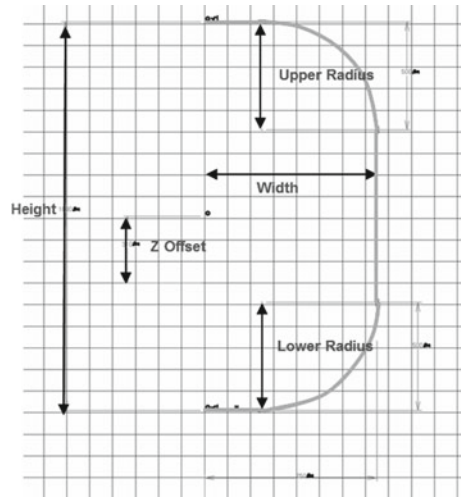
The external shape of OptiMALE is defined by a parametric CATIA V5 loft model, illustrated (for the starboard-half of the symmetric geometry) in Fig. 8.1. The OptiMALE is a conventional low-wing configuration with T-tail and podded engines, pylon-mounted on the rear of the fuselage. It also features an under-wing mounted external fuel tank. Fairing surfaces are defined between the main components (wing-fuselage, fuselage-tail, fuselage-pylon) to have an aerodynamically realistic shape. The wing is defined in its planform by two swept and tapered sections and in its profile by a fixed airfoil.

The baseline design of OptiMALE is sized for a MTOW of 8000 kg, having a wing area of 5 m², a wingspan of 30 m, taper ratio of 0.47 and a sweep of 3° on the inboard section. The wing has a typical laminar airfoil (NASA LRN-1015). The under-wing fuel tanks have a capacity of about 450 liters each. As reference test case for aerodynamic and aeroelastic simulations, a flight condition at Mach 0.4 and 5° angle of attack at 45, 000 ft has been selected.

8.2 Methods and Tools

A modular Optimization and Test Suite has been developed as part of the AeroStruct project to enable an easy integration of different methods and tools used in the optimization process using high fidelity aerodynamics on the basis of the DLR-Tau Code [1] and high fidelity structural mechanics on the basis of Lagrange [2].

Lagrange is an Airbus DS in-house structural mechanics solver and optimization tool. Several developments have been accomplished within the AeroStruct project [3] to extend the solver such as the addition of a time-integration method for transient

fluid-structure simulations [4] and a file as well as an in-memory based interface to the FlowSimulator MDA Framework [5].

8.2.1 Airbus DS - MD Optimization Suite

Three different aspects had to be addressed for the Modular Optimization and Test Suite. The first is to enable the integration of different Tools such as

- Aerodynamic Solvers (CFD, Panel Methods, etc.)
- Structural Solvers (FE, Beamtheory,…)
- Optimizers (Lagrange, Python,)

In order to support such a large scope of methods and tools it was decided to interface all tools via python. The interface should preferably be directly in python, however it is always possible for command line based tools to read values from files or standard output and thereby interface with python.

The second aspect are the different computational requirements, such as

- Direct sequential programs (Optimizer)
- Parallel batch processing (CFD Solver, Adjoint Solver)
- Remote execution (Geometry Processing / CATIA)

The suite has to provide means to submit batch jobs, monitor them and act upon their completion. This is the typical process for CFD Simulations and an automation requires the handling of a large number of failure cases. For a simulation with a run time of weeks, hundreds of batch jobs are submitted and need to be handled. On this scale even problems which occur seldom in regular simulations have to be taken care of in the automated process. Since some of them may be corner cases which are not worth to provide a special handling it is important to have fault tolerance at the highest level and some methodology for retries. The remote execution feature may be needed if tools run on different operating systems (eg. Windows versus Unix) or if licenses for software are only available on specific computers. In comparison the direct sequential execution of program may seem to be a much simpler form. Yet even in this case the program may run as a background program and checks for completion are necessary.

The third aspect is the process control. Again different scenarios need to be covered:

- Sequential Execution
- Parallel Execution - Processes which can be run in parallel
- Combinations of the above which require synchronization within the process

Sequential programs may be executed in parallel (eg. parameter studies), thus means have to be provided which are able to start a number of parallel programs and

- Metadata
- Automatic generation of Analysis models (CFD, FEM, etc.)

- Interface to Meshing tools
- Sensitivities of mesh deformation
- CATIA Interface

Parameterized Geometry

CATIA / OpenCascade

- CFD Geometry
- Changes of Aerodynamic Loft

- Analysis und Optimizationmesh
- Changes of Structural Layout
- Configuration Changes
- Interface for Sensitivity Analysis

Optimizer

Lagrange / Mode Frontier / Python

Aerodynamics

FlowSimulator

LAGRANGE

Structural Mechanics

- CFD Meshing
- CFD Simulation
- Adjoint Sensitivities
- Gust Simulation

- Couplingmethods (Geometry-/Meshbased)
- Time and Spatial coupling between CFD and FEM

- Time Integration
- Structural Dynamics
- Structural Sensitivity and Dimensioning

Fig. 8.3 Airbus DS optimization toolbox flow chart for FSI-MDO

only continue until the last one has completed. In some cases it is even necessary to run a number of batch jobs and run a consecutive batch job for each batch job which has completed (eg. adjoint or postprocessing after primary solution).

8.2.2   Modular Optimization and Test Suite Architecture

The Airbus DS MD-Optimization Suite addresses all of the above requirements and standard modules for the handling of CATIA remote execution, parallel meshing, and TAU batch jobs have been created.

The flowchart (Fig. 8.3) shows the combined high fidelity optimization of an aerodynamic loft with structural layout and sizing. Each step of the optimization is one cycle of the chart.

The starting point is an initial design which is fed into the parametric geometry subsystem. This provides one or more (i.e. perturbed) geometries which are then provided to the aerodynamic subsystem and the structural mechanics subsystem. The aerodynamic subsystem uses a sequential process for the generation of unperturbed and perturbed meshes. The unperturbed mesh is then submitted into the batch system for a primary solution. Once this is completed adjoint solutions are being computed for each target function. The structural mechanics subsystem is using a sequential process for computation of a FE solution and corresponding gradients.

The optimizer is by itself a subsystem which receives objective function values and gradients with respect to parameters and issues a new design point vector. Due to the simple interface any optimizer interfacing with python or a batch system can
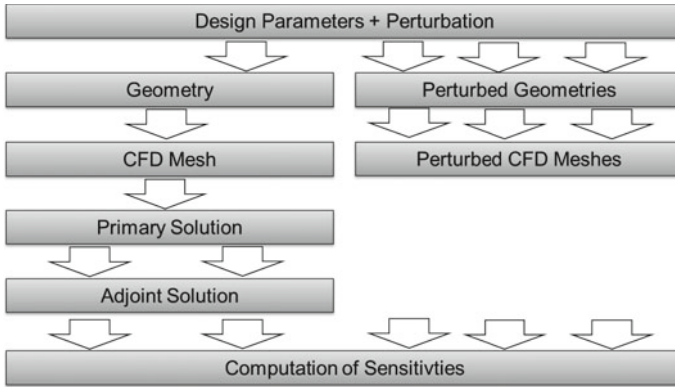
Fig. 8.4 Adjoint computation process flow

be used. In case of Lagrange an SQP algorithm is used and the optimizer stays in memory during the process. This is required because an approximate hessian is computed in the process and no intermediate state values thereof are stored.

8.2.3 Aerodynamic Computation Subsystem Process Flow

The aerodynamic computation in conjunction with the adjoint is the most complex part in the process. This is due the number of dependencies. Yet, despite of these dependencies a significant amount of the overall computation can be done in parallel. The adjoint computation flow chart (Fig. 8.4) describes in the vertical direction the dependencies of the computations. All steps next to each other which can be performed independent of each other. Multiple arrows indicate that several computations (i.e. for each parameter) can be performed in parallel.

8.3 OptiMALE Winglet Optimization

As a test-case for the aerodynamic part of the MDO Framework a disciplinary component optimization was selected. A winglet was designed for the Optimale and an optimization run setup with the properties

1. The influence of the winglet on the overall lift and drag coefficients is significant
2. The physical influence of the winglet parameters on the objective function is relatively easy to assess

The OptiMALE configuration with winglet (Fig. 8.5) has a fuselage length of 14 m and a halfspan of 15 m.

Fig. 8.5 OptiMALE with
parameterized winglet
(initial parameter values)

8.3.1 Winglet Parameterization

The winglet has been designed as a 90° upwards bended wing extension. The tip profile of the winglet is fixed in a 90° angle to the wing tip profile. The size and shape of the winglet can be adjusted with five parameters (Fig. 8.6)

- Angle: The angle of winglet wing-tip in the xy-Plane (z-Axis)
- Scale: The scaling factor of the winglet tip profile versus root profile
- Coordinates X, Y, Z: The position of the winglet tip profile leading edge point relative to the position of the wing tip leading edge point

All parameters have minimum and maximum values as well as initial values. The parameter ranges are defined to keep the designs within a predefined range and to ensure a valid geometry. For instance, the scaling factor minimum value prevents the wingtip to degenerate into a point.

8.3.2 Aerodynamic Winglet Optimization

The first setup was configured as a single disciplinary aerodynamic optimization. This allowed for the test of the computational fluid dynamics subsystem for integration and reliability. The results could then be used to check for physical validity. In subsequent optimizations the minimal and maximal parameter boundaries were extended and some rudimentary structural mechanics aspects integrated.

The setup for the aerodynamics optimization of the glide ratio was configured as

Objective Function :
$$\max \text{GlideRatio} = \max \frac{\text{Lift}}{\text{Drag}}$$

Parameters :
$$\text{Angle}$$
$$\text{Scale}$$
$$\text{CoordinateX, CoordinateY, CoordinateZ}$$

The parameter initial values were:

Fig. 8.6 The parameters of
the OptiMALE winglet
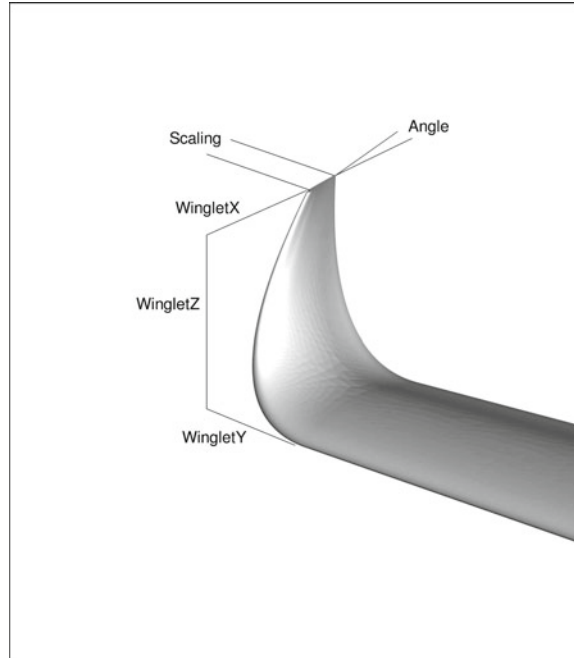
$$\text{Angle} = 0°$$
$$\text{Scale} = 0.5$$
$$\text{CoordinateX} = 1000\,\text{mm}$$
$$\text{CoordinateY} = 750\,\text{mm}$$
$$\text{CoordinateZ} = 1000\,\text{mm}$$

Testing showed that the meshing and solver interfaces needed significant changes for error handling to cope with failed meshing and aborted residual or adjoint computations.

With respect to the physical validation it should be noted that the parameter CoordinateY generally corresponds to an increase in wingspan.

Due to little experience with convergence criteria the optimization was setup to run for a fixed twenty iterations. The optimization algorithm chosen was a steepest gradient descent algorithm for the sake of simplicity. This way restarts could be implemented much easier and the verification of the line search easily possibly.

Parameters were limited by range and aerodynamic coefficient gradients were computed using the adjoint method.

The convergence of the coordinate parameters (Fig. 8.7) show a steady increase of WingCoordinateZ and a steady decrease of WingCoordinateX. This leads to an increase in winglet height and a forward displacement.

The objective function which is in this case identical to the glide ratio shows an expected behavior in the sense that it is increasing with the optimization iterations.
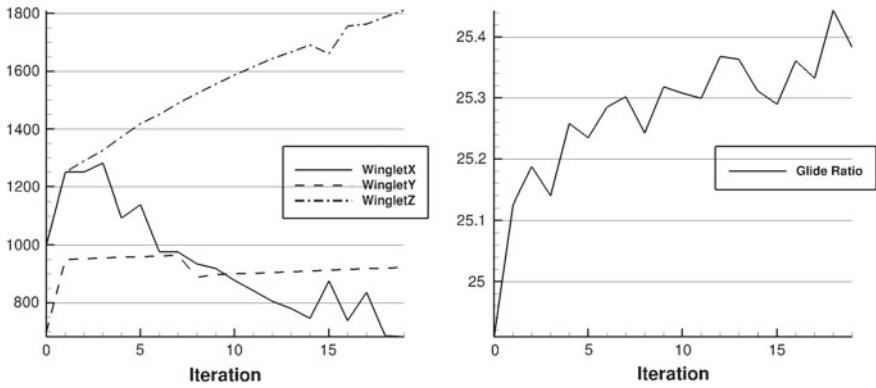
Fig. 8.7 Winglet optimization: parameter convergence and objective function over iteration

Fig. 8.8 Winglet design iterations (0 = Initial, 10, 15, 19 = last design)

Thus, the optimization setup, tools, and processes are consistent and gradients have in principle the right direction. However, it is assumed that the optimization is moving towards a local optimum since the parameter CoordinateY did move toward the upper range limit.

The shape of the winglet (Fig. 8.8) changes over the iterations to a more pointy wingtip. The scaling parameter, which defines the taper ratio of the winglet, reached the minimum allowed value for the parameter. The changes in parameters CoordinateX and CoordinateZ are easily recognized in the images.

Fig. 8.9 Winglet
optimization primary
solution (2)

8.3.3   Aerodynamic Winglet Optimization (2)

The initial aerodynamic optimization of the OptiMALE winglet has shown that the
process works and the results are valid. As a next step the process has been improved
and a restart capability introduced.

The first optimization showed a steady increase in parameter CoordinateZ so
one of the changes for a second optimization was the limitation of CoordinateZ to
1500 mm.

The objective function was again the glide ratio which was to be maximized by
the optimizer at constant angle of attack. The five parameters were set to the same
initial values, however the step size for the adjoint solution has been adjusted.

The optimization went for 19 iterations (Fig. 8.9), large design changes however
seize after five iterations.

The objective function (Fig. 8.10) levels off after four iterations at about a glide
ratio of 26.2. All subsequent iterations have only marginal effect on the objective
function.

The parameter convergence shows that similarly to the last iteration the Coor-
dinateZ parameter increases quickly and is then stopped at the 1500 mm parameter
limit. Also similar to the first optimization there is a forward movement of the winglet
leading edge (Fig. 8.11).

In contrast to the first winglet optimization this time the implicit wingspan increase
through parameter CoordinateY is used by the optimizer. As expected the parameter
change is nearly proportional to the increase in glide ratio.
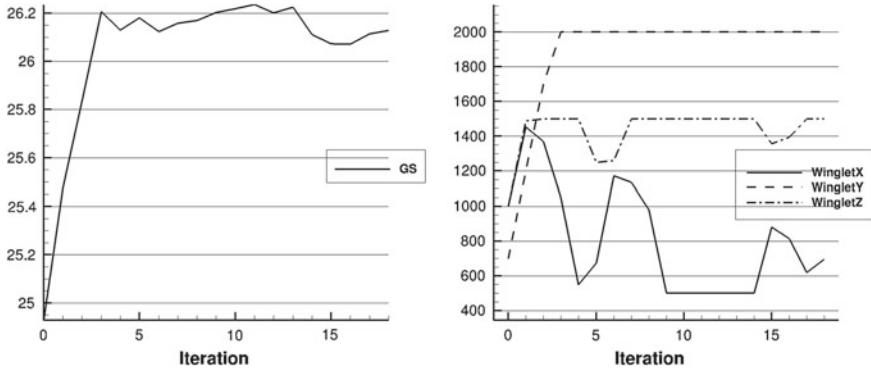
Fig. 8.10 Objective function (Glideslope) and parameters over optimization iterations for winglet optimization (2)

Fig. 8.11 Winglet design iterations (0 = Initial, 2, 4) for winglet optimization (2)

8.3.4 Aerodynamic Winglet Optimization (3)

The previous optimization ran into both parameter limits for CoordinateZ and CoordinateY for which limits of 1500 and 2000 mm respectively have been set. Since the optimizer generates a new geometry and cfd mesh for each design point, no problems are expected with increasing CoordinateY and CoordinateX beyond the current parameter limits. Thus, for the next optimization run these parameters have been increased to values the optimizer should reasonably not reach.

It is expected that the optimizer will increase the parameter CoordinateY limited only by the maximum step size and the number of iterations. However, problems in geometry generation and meshing of highly distorted geometries may stop the optimization early (Fig. 8.12).

The design changes over the iterations (Fig. 8.12) are as expected dominated by the increase of the CoordinateY parameter. The parameter CoordinateZ which cor-
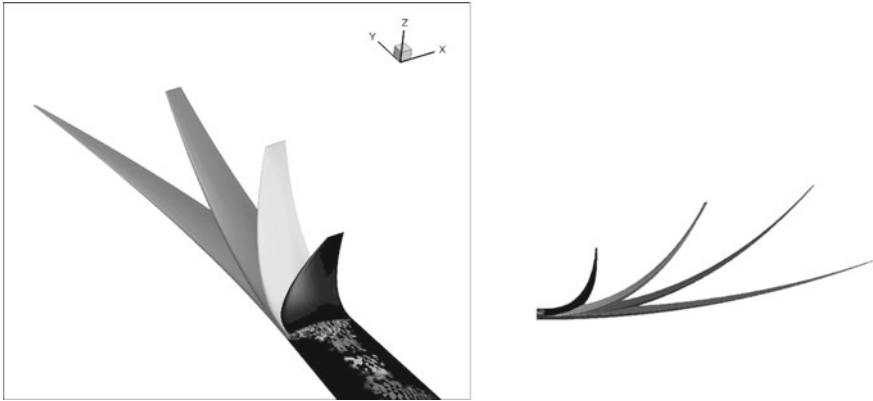
Fig. 8.12 Winglet design iterations (0 = Initial, 3, 6, 9) for winglet optimization (3)

Fig. 8.13 Objective function
(Glideslope) over
optimization iterations for
winglet optimization (3)
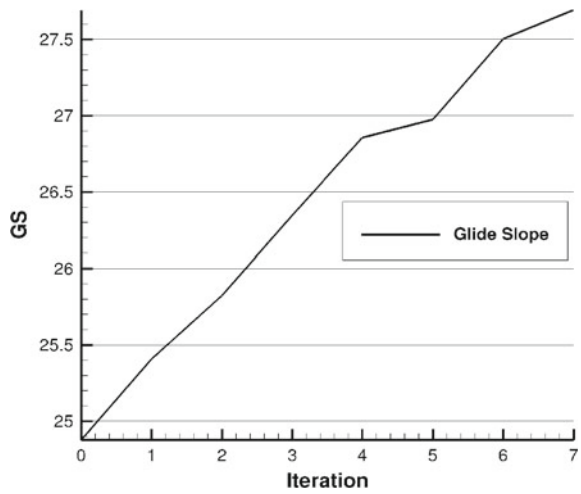
responds to the height of the winglet is steadily increasing at first and then decreases
again even below the initial value. The first increase maybe due to the effect that it
corresponds with an increase of the wing length (and area). Later in the optimization
due to the limit of the scaling parameter the trade-off between height and wingspan
is decided towards wingspan.

The objective function (Fig. 8.13) changes as expected proportional to the para-
meter CoordinateY. The glide ratio increase is in total about 10% compared to the
initial design, which also matches quantitatively very well the increase in wingspan
(Fig. 8.14).

Fig. 8.14 Pressure distribution of design iteration 7 for winglet optimization (3)

8.3.5   Multidisciplinary Optimization of Wing with Winglet

The next step in the validation of the modular multidisciplinary optimization system is the integration of rudimentary structural mechanics into the optimization. As part of this next step also the number of parameters is increased as this is a fundamental advantage of the adjoint approach for the computation of the gradients. The model used for this MDO has, in addition to the five winglet parameter, eleven parameters for the wing planform and twelve parameters for the sectional profiles (thickness and camber) of the wing (Fig. 8.15) resulting in a total of 28 simultaneously active shape parameters.

In this optimization the wing shape parameters are all true multidisciplinary parameters, that is they influence both the aerodynamic and structural mechanics analysis models.

The simplified structural mechanics model uses beam theory for each of the four sections in spanwise direction. The loads were assumed to have an elliptical distribution and are applied accordingly within each section.

The objective function is a minimization of cruise drag

$$\text{CruiseDrag} = \frac{\text{Mass}}{\text{GlideRatio}} = \text{Mass}\frac{\text{Drag}}{\text{Lift}} \tag{8.1}$$

where the angle of attack is included as a parameter into the optimization. For this parameter an additional constraint has been added such that lift equals weight. This has been included into the objective function as

$$\min \|\text{Lift} - \text{Weight}\| \tag{8.2}$$
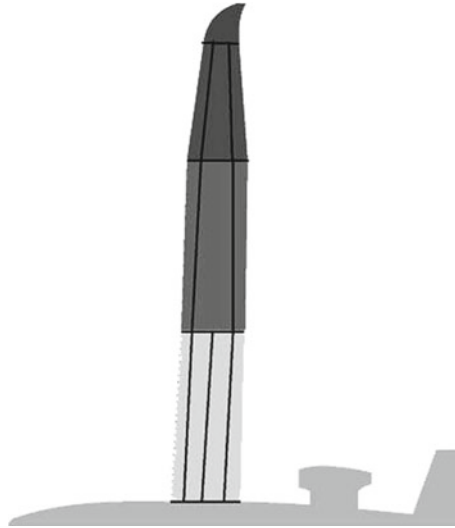
Fig. 8.15 Wing + Winglet MDO - simplified structural mechanics model of the OptiMALE
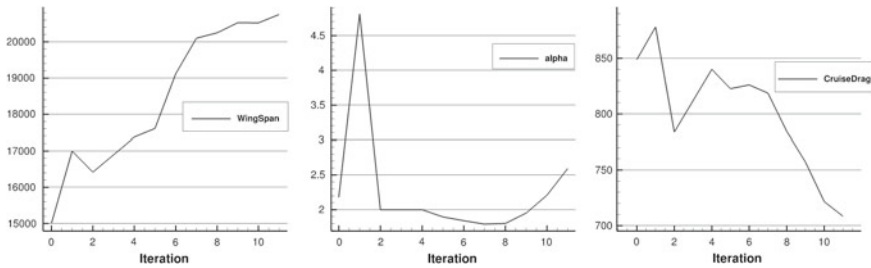
Fig. 8.16 MDO wing + winglet - parameters halfspan, angle of attack and objective cruise drag over iterations

with a trimming of the angle of attack to equalize the lift with the weight. It should be noted that it is not a real trimming as the pitching moment is not included. In order to include the pitching moment a horizontal tail plane (HTP) adjustment would be necessary.

The optimizer increases the halfspan while keeping the angle of attack approximately constant (Fig. 8.16). This indicates that the lift stays about the same, but the drag is decreased.

The objective function (cruise drag) decreases over the number of iterations.

The change in geometry in the course of the optimization (Fig. 8.17) shows an increase in wingspan as well as a backward facing kink in the wing planform. This backward facing kink is a result of the simplified structural model, which does include loads across section boundaries, but does not penalize a directional change of the

Fig. 8.17 Wing + winglet MDO - design iterations and pressure distribution of final design

main spars. This would normally result in added weight due to higher moment loads between sections. Thus, the optimizer found and used a weakness in the structural mechanics modeling.

References

1. D. Schwamborn, T. Gerhold, R. Kessler, DLR-TAU Code - an overview, in *1st ONERA/DLR Aerospace Symposium* Paris, 21–24 June 1999
2. G. Schuhmacher, F. Daoud, Ö. Petersson, M. Wagner, Multidisciplinary Airframe Design Optimisation, in *28th International Congress of the Aeronautical Sciences* (Brisbane, Australia, 2012)
3. K. Elssel, F. Daoud, Ö. Petersson, CA-AeroStruct - Multidisziplinäre Simulation and Optimierung zukünftiger Hochleistungsplattformen - 4, Zwischenbericht (2014)
4. H. Rieger, K. Elssel, F. Daoud, Ö. Petersson, CA-AeroStruct - Multidisziplinäre Simulation & Optimierung zukünftiger Hochleistungsplattformen - 3, Zwischenbericht (2013)
5. M. Meinel, G. Einarson, The flow simulator framework for massively parallel CFD applications, in *Para 2010* (Reykjavik, 2010)

Chapter 9
Treating Non-conforming Sensitivity Fields by Mortar Mapping and Vertex Morphing for Multi-disciplinary Shape Optimization

Altuğ Emiroğlu, Roland Wüchner and Kai-Uwe Bletzinger

Abstract This study investigates the sensitivity filtering properties of the Mortar Mapping method and correlates it to the Vertex Morphing method in order to demonstrate the advantages of such a procedure in the context of shape optimization. It points out the importance of a common design control approach in a Multi-Disciplinary Optimization (MDO) environment. In particular, individual components of MDO have nonmatching interfaces when Fluid-Structure Interaction (FSI) problems are of interest. Since the numerical models of dissimilar discretizations deliver nonconforming sensitivity fields with respect to the design variables defined at their interfaces, the shape optimization of the common surfaces necessitates a third field which unifies the optimization variables and acts as a control field. This approach not only covers this necessity by facilitating the Mortar Mapping method but also reveals that such a procedure acts as a sensitivity filter similar to the Vertex Morphing method without altering the optimality of the solution.

9.1 Similarity of the Filter and Mapping Operators

The Vertex Morphing is a modular and robust sensitivity filtering method due to its explicit nature and applicability in industrial applications without causing a costly procedure. The method was initially proposed in [1]. It introduces a complementary control field which describes the surface design. The relation between the control and the design fields are accomplished through a linear map. A variety of possibilities for defining the control field in discrete sense are

A. Emiroğlu (✉) · R. Wüchner · K.-U. Bletzinger
Lehrstuhl für Statik, Technische Universität München, Arcisstr. 21, 80333 Munich, Germany
e-mail: altug.emiroglu@tum.de

R. Wüchner
e-mail: wuechner@tum.de

K.-U. Bletzinger
e-mail: kub@tum.de

already mentioned in [1]. The construction of the mentioned linear map for the case where the discretized fields have a common grid was previously shown in [2].

In the newly proposed approach, the similarity between the linear transformation operator of the Vertex Morphing and the Mortar Mapping methods is revealed. The method makes use of the Mortar Mapping method to construct the link between the control and design fields. This method could either be used by facilitating a coarsely discretized control field, which drives the shape evolution, or it could be used successively in order to retrieve a filtered sensitivity field on the original design surface, which allows performing node based optimization.

9.1.1 Vertex Morphing Method

For clarity and a definition of a unified notation with the Mortar Mapping, the Vertex Morphing method for the 1D case is briefly presented here. The shape optimization problem could be stated as follows;

$$\min_{s} \quad J(x, u) \tag{9.1}$$
$$s.t. \quad R(x, u) = 0$$
$$g_j(x, u) \leq 0; \quad j = 1, \ldots, k$$

where J, R, g_j are objective function, state equations in residual form and constraint functions respectively. x, s, u are then the design, the control and the state variables. In addition, $x(\xi) \in V$, $V : (-1, 1) \to \mathbb{R}$ is the design surface field which is described by a control field $s(\xi)$, $s \in V$ in combination with an inner product $\mathscr{A}(s, \xi)$, $\mathscr{A} : V \to V$ as stated in [1]. As a result, design surface at a given coordinate ξ_x could be reconstructed through;

$$x(\xi_x) = \mathscr{A}(s, \xi_s) \tag{9.2}$$

where $\mathscr{A}$ is defined by an inner product of $s(\xi_s)$ with a chosen kernel function -namely the filter function- A as;

$$x(\xi_x) = \mathscr{A}(s, \xi_s) = \int_{-1}^{1} A(\xi_s, \xi) \, s(\xi) \, d\xi, \quad A : \bar{\mathbb{R}}^2 \to \mathbb{R}. \tag{9.3}$$

Here it is important to note that the first argument ξ_s of the filter function denotes the surface coordinate of the filter function support in the surface coordinates and is not restricted to coincide with the surface coordinate ξ_x of the surface design handle to be reconstructed. In the case of $\xi_x = \xi_s = \xi_0$, the formulation falls back to the node based Vertex Morphing method.

The control field serves as a master field where the optimization is performed. Thus, it is necessary to compute the sensitivity of the objective function w.r.t. the control variables when gradient based optimization is of interest.

$$\frac{\mathrm{d}J}{\mathrm{d}s} = \frac{\partial J}{\partial s} + \int_{-1}^{1} \frac{\partial J}{\partial x\,(\xi)} \frac{\mathrm{d}x\,(\xi)}{\mathrm{d}s} \mathrm{d}\xi \tag{9.4}$$

It can be clearly seen that the second term of the integral in (9.4) can be treated as a variable transformation -or a mapping- between the control and the design fields. Moreover, making use of (9.3) and the fact that $\frac{\partial J}{\partial s} = 0$, the following can be stated:

$$\delta x\,(\xi_x) = \int_{-1}^{1} A\,(\xi_s, \xi)\,\delta s\,(\xi)\,\mathrm{d}\xi \tag{9.5}$$

$$\Rightarrow \quad \frac{\mathrm{d}x\,(\xi_x)}{\mathrm{d}s} = A\,(\xi_s, \xi) \tag{9.6}$$

$$\frac{\mathrm{d}J}{\mathrm{d}s} = \int_{-1}^{1} \frac{\partial J}{\partial x\,(\xi)} A\,(\xi_s, \xi)\,\mathrm{d}\xi \tag{9.7}$$

Equation (9.6) reveals that the filtering function is indeed nothing else than a mapping between the control and the design fields.

Discretization of Design and Control Fields

In practice, in order to apply numerical methods and solution procedures to the optimization problems, it is necessary to apply spatial discretization to the state equations as well as the design field of interest and the control field. Accordingly, a discrete set of coordinates $\mathbf{x} = [x_1, x_2, \ldots, x_n]$, $\mathbf{x} \in \mathbb{R}^n$ are defined for the determination of the design surface. As the parametrization of the control field is kept free of choice and size, there exists another set of control parameters $\mathbf{s} = [s_1, s_2, \ldots, s_m]$, $\mathbf{s} \in \mathbb{R}^m$.

Having the discretization in mind, (9.7) could be rewritten in the discrete form.

$$\frac{\mathrm{d}J}{\mathrm{d}s_i} = \frac{\mathrm{d}J}{\mathrm{d}x_j} \frac{\mathrm{d}x_j}{\mathrm{d}s_i} = A_{ji} \frac{\mathrm{d}J}{\mathrm{d}x_j} \tag{9.8}$$

$$\frac{\mathrm{d}J}{\mathrm{d}\mathbf{s}} = \mathbf{A}^T \frac{\mathrm{d}J}{\mathrm{d}\mathbf{x}} \tag{9.9}$$

The sensitivity analysis of the objective function w.r.t. the surface perturbations delivers $\frac{\mathrm{d}J}{\mathrm{d}\mathbf{x}}$. The matrix $\mathbf{A}^T$ serves as a filter by mapping the sensitivities onto the discretized control field $\mathbf{s}$. Once the optimization iteration is performed on the control parameters, the surface design variation can be recovered through the discretized version of (9.5):

$$\delta\mathbf{x} = \mathbf{A}\delta\mathbf{s} \tag{9.10}$$

Regardless of the discretization of the design and the control fields, the operator $\mathbf{A}$ is used successively and in an explicit manner. Once the nodal surface sensitivity information is retrieved, a backward filtering is applied by mapping them onto the discretized control field using the operator $\mathbf{A}^T$. After the optimization iteration is

performed and the variation of the control field is obtained, it is filtered forward -or mapped onto- the surface design field with operator $\mathbf{A}$ to retrieve the design surface.

As stated in [1], the choices of dimensions for the s and the x fields result in a reparametrization of the shape. If the dimension of s is chosen less than the dimension of x, the shape is controlled by a coarser field that filters out the noisy sensitivities and consequently the undesired rugged surface designs.

Optimality Condition

The effect of filtering operation on the optimality condition should be further discussed in order to judge if the obtained shape is actually an optimum of the original problem as well. Using Taylor series expansion for the objective function w.r.t. the control variables until the second order term renders;

$$\widetilde{J} = J + (\nabla_{\mathbf{s}} J)^T \delta \mathbf{s} + \frac{1}{2} \delta \mathbf{s}^T \mathbf{H_s} \delta \mathbf{s} \tag{9.11}$$

At a local minimum the stationary condition $\nabla_{\mathbf{s}} \widetilde{J} = 0$ should be satisfied and it is straight forward to show that:

$$\delta \mathbf{s} = -\mathbf{H_s}^{-1} \nabla_{\mathbf{s}} J \tag{9.12}$$

In case the operator $\mathbf{A}$ is a square invertible matrix, (9.10) could be rearranged as $\delta \mathbf{s} = \mathbf{A}^{-1} \delta \mathbf{x}$. On the other hand, for a general case where n design variables are controlled by m control variables, a generalized inverse should be considered to be able to show this relation. Assuming that the columns of the non-square operator $\mathbf{A}$ are linearly independent, the right pseudoinverse can be found as [3]:

$$\mathbf{A}_{right}^{-1} = \mathbf{A}^T \left(\mathbf{A} \mathbf{A}^T \right)^{-1} \tag{9.13}$$

Making use of the transformation in (9.9) and the generalized inverse in (9.13), the Hessian and the gradient terms in (9.12) can be rewritten. Consequently one can obtain the shape variations of the design field from the variations of the control field. For brevity, $\mathbf{R} = \mathbf{A}_{right}^{-1}$ is used;

$$\delta \mathbf{s} = \underbrace{\left(-\mathbf{R} \mathbf{H_x}^{-1} \mathbf{R}^T \right)}_{-\mathbf{H_s}^{-1}} \underbrace{\mathbf{A}^T \nabla_{\mathbf{x}} J}_{\nabla_{\mathbf{s}} J} \tag{9.14}$$

$$\delta \mathbf{x} = \mathbf{A} \delta \mathbf{s} = \mathbf{A} \left(-\mathbf{R} \mathbf{H_x}^{-1} \mathbf{R}^T \right) \mathbf{A}^T \nabla_{\mathbf{x}} J \tag{9.15}$$

$$\delta \mathbf{x} = -\mathbf{H_x}^{-1} \nabla_{\mathbf{x}} J \tag{9.16}$$

Equations (9.14)–(9.16) reveal that the final result of the optimization does not differ from the solution of the original problem, regardless of the choice of the number of discrete control parameters, as long as $n \geq m$. Moreover, the filter function choice effects the properties of the filter operator $\mathbf{A}$, since the linear independence requirement of $\mathbf{A}$'s columns is necessary for the construction of the generalized right inverse.

9.1.2 The Mortar Mapping Method

In this section the Mortar Mapping method is briefly presented without giving details on the implementation aspects. One should refer to [4] and EMPIRE[1] for the implementation details.

Mortar methods could be used to enforce equality constraints or equality of the fields on dissimilar discretizations of the same geometrical entities in a weak sense. In such a case, a transformation of a field f defined on a surface with discretization **x** can be written in the terms of discretization **s** using Mortar methods [5].

Consider the following equality constraint on the minimization problem:

$$f_s\,(\xi) = f_x\,(\xi) \quad \xi \in \Gamma \tag{9.17}$$

This constraint could be enforced with the well-known Lagrange multipliers method by the following extension to the optimization problem in continuous form:

$$\int_\Gamma \lambda\,(f_s - f_x)\,\mathrm{d}\Gamma = 0 \tag{9.18}$$

The mortar method is then defined by choosing the discretization of the Lagrange multipliers field λ, to coincide with one of the discretizations of f_s or f_x. The chosen discretization is then called "the master field", whereas the remainder is named as "the slave field" [6]. Then in discrete form, where for instance the master field is chosen to be the discretization of s, (9.18) takes the following form;

$$\int_\Gamma \hat{\lambda}^T \mathbf{N}_s^T \mathbf{N}_s \hat{f}_s \, \mathrm{d}\Gamma = \int_\Gamma \hat{\lambda}^T \mathbf{N}_s^T \mathbf{N}_x \hat{f}_x \, \mathrm{d}\Gamma \tag{9.19}$$

where $\mathbf{N}_s$ and $\mathbf{N}_x$ are the test functions associated with the respective discretizations of the field f, and the fields denoted with a hat are the discrete nodal values of the Lagrange multipliers λ and the field f. Making use of (9.19), and the fact that the equality condition must hold for any discrete set of $\hat{\lambda}$, the discrete field $\hat{f}_s$ for a given $\hat{f}_x$ can be obtained through the following relation:

$$\hat{f}_s = \mathbf{M}_{ss}^{-1} \mathbf{C}_{sx} \hat{f}_x \tag{9.20}$$

$$\hat{f}_s = \mathbf{A}_{sx} \hat{f}_x \tag{9.21}$$

where it is clear that, $\mathbf{M}_{ss} = \int_\Gamma \mathbf{N}_s^T \mathbf{N}_s \mathrm{d}\Gamma$, $\mathbf{C}_{sx} = \int_\Gamma \mathbf{N}_s^T \mathbf{N}_x \mathrm{d}\Gamma$ and the mapping or variable transformation matrix $\mathbf{A}_{sx} = \mathbf{M}_{ss}^{-1} \mathbf{C}_{sx}$. In the context of Mortar Methods, this mapping operator is also called a consistent mapping operator which preserves a constant field when mapped between different discretizations. It allows computing a weak equivalent of a given discrete field on a different discretization of the same field.

---

[1]EMPIRE is a research tool for co-simulation in the context of field and signal coupling. http://empire.st.bv.tum.de/.

Moreover, computation of the reverse mapping is established similar to (9.19)–(9.21) when the discretization of Lagrange multipliers field -the master field- is chosen as the same as field $\hat{f}_x$, which results in the following form:

$$\hat{f}_x = \mathbf{A}_{xs}\hat{f}_s \qquad (9.22)$$

It is important to note that transpose of the operator $\mathbf{A}_{sx}$ in (9.21) and the operator $\mathbf{A}_{xs}$ in (9.22) are not necessarily identical. This stems from the weak enforcement of the constraint and the weak equivalence of the fields with different discretizations and the choice of the master as well as slave for the integration domain. When a discrete field $\hat{f}_x$ defined on domain x is mapped onto domain s and back onto its original domain, it is clearly modified. They would only be identical in case the fields are discretized in the same way, which results in an identity matrix for the mapping operator. Consider (9.19) and set the discretization of x and s to be identical. This renders; $\mathbf{C}_{sx} = \mathbf{M}_{ss}$ and thus from (9.20), $\hat{f}_s = \mathbf{I}\hat{f}_x$.

9.1.3 The Relation Between the Filter Operator of the Vertex Morphing and the Mapping Operator of the Mortar Method

In this section, the relation between the filter operator mentioned in Sect. 9.1.1 and the mapping operator in Sect. 9.1.2 is revealed. Consider the optimization problem given in (9.1) and introduce an additional equality constraint to the problem as given in (9.17). Now the modified optimization problem reads;

$$
\begin{aligned}
\min_{s} \quad & J(x, u) && (9.23) \\
s.t. \quad & R(x, u) = 0 \\
& g_0(x, s, u) = 0 \\
& g_j(x, u) \le 0; \quad j = 1, \dots, m
\end{aligned}
$$

where the introduced discrete constraint g_0 is:

$$\frac{dJ}{d\mathbf{s}} - \frac{dJ}{d\mathbf{x}} = 0 \quad \text{on} \quad \Gamma \qquad (9.24)$$

Making use of the Lagrange multipliers approach for this constraint, one could write (9.24) in the following form:

$$\int_{\Gamma} \lambda \left(\frac{dJ}{d\mathbf{s}} - \frac{dJ}{d\mathbf{x}} \right) = 0 \quad \text{on} \quad \Gamma \qquad (9.25)$$

Following the procedure defined in (9.18)–(9.21) and enforcing this constraint by making use of static condensation of the Lagrange multipliers through the relation in (9.21), one could write the relation between the sensitivity derivatives of the objective function w.r.t. the control field **s** and the design field **x**, that are discretized in an arbitrarily chosen way:

$$\frac{\mathrm{d}J}{\mathrm{d}\mathbf{s}} = \mathbf{A}_{sx} \frac{\mathrm{d}J}{\mathrm{d}\mathbf{x}} \tag{9.26}$$

The similarity between the expressions (9.9) and (9.26) is obvious and in this way the Mortar Mapping method provides a technique to compute a filtering operator for grid sensitivities. In addition, reconstruction of the discrete surface design update field from the discrete design control update field is straightforward. Making use of (9.10) and (9.22):

$$\delta\mathbf{x} = \mathbf{A}_{xs}\delta\mathbf{s} \tag{9.27}$$

Herein, once again it is important to note that in general $\mathbf{A}_{sx} \neq \mathbf{A}_{xs}^{T}$. This requires definitions of separate mapping operators for forward and backward filtering; one with the design control field chosen as the master field which facilitates the computation of backward filter $\mathbf{A}_{sx}$ and the other with the design field chosen as the master that results in the forward filter $\mathbf{A}_{xs}$.

9.2 Method Demonstration

The demonstration examples are chosen in order to reveal the benefits and effects of using mentioned filtering method in a comprehensive way on small scale cases. Firstly, the benchmark case as mentioned in [1] is chosen since the claim is that the proposed method is comparable to the Vertex Morphing Method. Secondly, filtering of a hypothetical sensitivity field on a planar domain is presented.

9.2.1 2-Dimensional Target Design Generation

The proposed shape optimization problem is generating a target shape, which is a hat function (See Fig. 9.2) defined at discrete points, from a flat initial discrete curve. The target and the design curves are discretized with 40 elements and the control field is discretized with 16 elements (see Fig. 9.1). Linear shape functions are used for the geometrical discretizations of the target, the design and the control fields.

The Objective function of the discrete optimization problem is defined as:

$$J = \sum_{i=0}^{40} \mid x_i^{target} - x_i \mid \tag{9.28}$$

Fig. 9.1 The discretization of the design and control fields
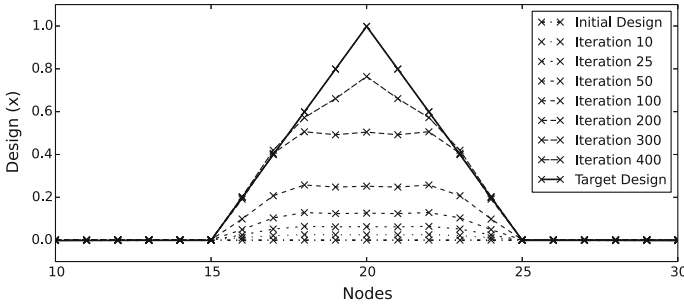
Fig. 9.2 The design evolution of the 2-Dimensional target shape generation problem with sensitivity filtering using Mortar Mapping Method

The sensitivity derivative of the objective function w.r.t. the design handles -discrete nodes- is straight forward to compute:

$$\frac{dJ}{dx_i} = \frac{x_i - x_i^{target}}{| x_i^{target} - x_i |} \tag{9.29}$$

The sensitivity and consecutively the design filtering is achieved through mapping the nodal sensitivity field, that is computed on the design field, onto the control field, computing the design update on the discrete control field and mapping it back onto the design surface. A steepest descent algorithm with a constant step size of 10^{-3} is used for the solution of the optimization problem. Results are presented in Fig. 9.2.

As the discretization of the control field coincides with the design field at the beginning and the end of the hat function span (nodes 15 and 25), the remainder of the domain is not effected from the optimization procedure. This property could be exploited in order to conserve certain design features which might be compulsory due to the manufacturing or design restrictions.

9.2.2 Sensitivity Filtering on a Planar Domain

In order to extend the demonstration of the method, a planar domain could be adopted. A single hypothetical sensitivity vector $(0.1, 0.1, 0.0)$ on a discretized domain is

Fig. 9.3 A hypothetical
sensitivity field defined on
the design field
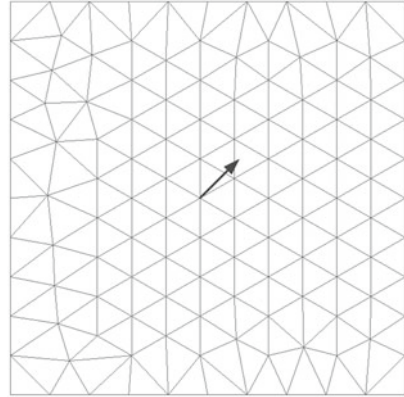
Fig. 9.4 The corresponding
sensitivity field on the
control field
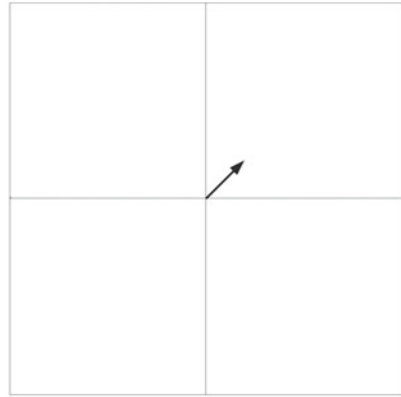
used to present how the method works on surfaces in combination with a steepest
descent algorithm. In this example, the design field is discretized with linear triangular
elements whereas the control field is discretized with bilinear quadrilaterals since
it is required to have coarser discretizations of the control field in order to obtain
filtering properties. The geometrical discretizations of the fields and the assumed
sensitivity field are shown in Figs. 9.3 and 9.4.

As the shape functions of the control field span over a wider range of design
elements, the design update field, that is computed on the control field, also extends
over the portion of the design elements which are covered by the control field's
shape functions. In return, sensitivity and design filtering is achieved by increasing
the continuities of these fields across the design element edges to the control field's

Fig. 9.5 The design update
of the control field computed
with a constant step size 1.0
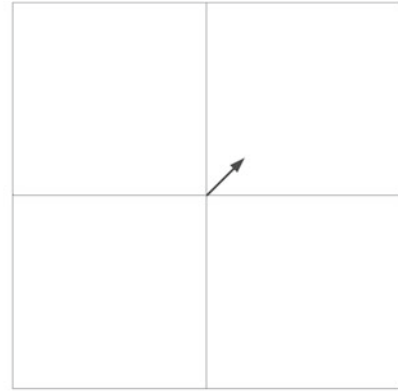
Fig. 9.6 Retrieved filtered
design update field on the
design field
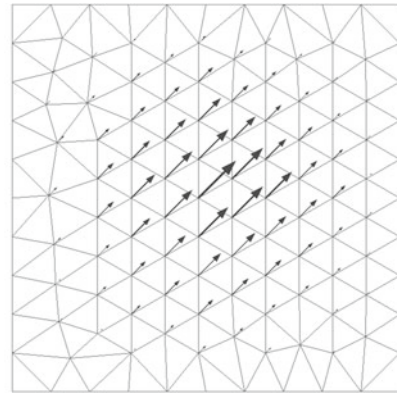
shape functions' continuities. This can also be interpreted as projecting the sensitivity field defined on the C^x continuous design space to the C^s continuous control space (Fig. 9.5). As a result, possible distortions of the design mesh are also avoided (Fig. 9.6).

9.3 Sensitivity Filtering in a Multi-disciplinary Optimization Framework

In this section, the implemented MDO framework with the employed sensitivity filtering method is presented. The shape optimization requires sensitivities of the objective function, which in an aeroelastic environment is often related to the force acting on the interaction surface, and the number of design variables on the interaction surface are often much greater than the number of the objective and the constraint functions. Thus, well-known adjoint method is adopted for the coupled sensitivity analysis. Moreover, due to the suitability to the available software, a Multi-Disciplinary Feasible structure (MDF) [7] is chosen.

9.3.1 Coupled Optimization Problem and Coupled Adjoint Sensitivity Analysis

The considered PDE constrained, steady-state aeroelastic shape optimization problem could be written in the following generic form:

$$\begin{aligned}
\min_{\mathbf{x}} \quad & J(\mathbf{x}, \mathbf{d}, \mathbf{v}, p) \\
s.t. \quad & \Re(\mathbf{x}, \mathbf{d}, \mathbf{v}, p) = 0 \\
and \ B.C.'s \quad & \mathbf{d}_S - \mathbf{d}_F = 0 \quad \text{on} \quad \Gamma_{FSI} \\
& \mathbf{v}_S - \mathbf{v}_F = 0 \quad \text{on} \quad \Gamma_{FSI} \\
& \mathbf{t}_S + \mathbf{t}_F = 0 \quad \text{on} \quad \Gamma_{FSI}
\end{aligned} \tag{9.30}$$

where the design variables, the structural displacements, the fluid velocities and the pressures are denoted by $\mathbf{x}$, $\mathbf{d}$, $\mathbf{v}$ and p respectively. $\Re$ are the steady-state linear elastic structural and the steady-state incompressible RANS equations in residual form:

$$R_S^d = \nabla \cdot \sigma(\mathbf{d}) \tag{9.31}$$

$$R_F^v = (\mathbf{v} \cdot \nabla)\mathbf{v} + \nabla p - \nabla \cdot (\nu D(\mathbf{v})) \tag{9.32}$$

$$R_F^p = -\nabla \cdot \mathbf{v} \tag{9.33}$$

Note that the optimization problem in (9.30) is written w.r.t. the design variable $\mathbf{x}$ rather than the control variable $\mathbf{s}$. Once the nodal sensitivity information is obtained, (9.26) is used to obtain the sensitivities w.r.t. $\mathbf{s}$ in an explicit manner.

A Lagrangian of the PDE constrained optimization problem can be constructed in the following way:

$$\mathcal{L} := J + \int_{\Omega_S} \mathbf{u} \cdot R_S^d \; \mathrm{d}\Omega + \int_{\Omega_F} \mathbf{w} \cdot R_F^v \; \mathrm{d}\Omega + \int_{\Omega_F} q \; R_F^p \; \mathrm{d}\Omega \qquad (9.34)$$

Here $\mathbf{u}$, $\mathbf{w}$, q, refer to structural adjoint displacements, fluid adjoint velocities and adjoint pressures. Making use of the stationary condition for the total variation of the Lagrangian one finds;

$$\delta\mathcal{L} = \delta_{\mathbf{x}}\mathcal{L} + \delta_{\mathbf{d}}\mathcal{L} + \delta_{\mathbf{v}}\mathcal{L} + \delta_p\mathcal{L} = 0 \qquad (9.35)$$

It is necessary to set the variation of the Lagrangian w.r.t. the state variables to vanish in order to derive the coupled adjoint FSI analysis. Consecutively, this enables calculation of the sensitivity derivatives from the partial derivative of the Lagrangian w.r.t. the design variables.

$$\delta_{\mathbf{d}}\mathcal{L} + \delta_{\mathbf{v}}\mathcal{L} + \delta_p\mathcal{L} = 0 \qquad (9.36)$$
$$\delta\mathcal{L} = \delta_{\mathbf{x}}\mathcal{L} \qquad (9.37)$$

Equation (9.36) is the starting point of the coupled adjoint FSI analysis and (9.37) results in the coupled sensitivities respectively. After application of integration by parts and the Gauss theorem on the Lagrangian function (the viscous term in the RANS momentum equation should be treated twice) and introducing the boundary conditions in (9.30), one reaches the adjoint equation systems and boundary conditions. The derivation mainly follows [8] apart from the surface normal shape variation assumption. Due to the arbitrary nature of the shape perturbations' and the interface displacement fields' combination, it is more convenient to assume an arbitrary variation of the shape. This results in a slightly different sensitivity equation and coupling terms respectively [9]. The derived continuous adjoint equation systems are listed below:

$$R_S^u = \nabla \cdot \sigma\,(\mathbf{u}) \qquad (9.38)$$
$$R_F^w = -\nabla\mathbf{w} \cdot \mathbf{v} - (\mathbf{v} \cdot \nabla)\,\mathbf{w} + \nabla p - \nabla \cdot (\nu \mathrm{D}\,(\mathbf{w})) \qquad (9.39)$$
$$R_F^q = -\nabla \cdot \mathbf{w} \qquad (9.40)$$

The coupled adjoint equation systems differ only by the boundary conditions from the uncoupled adjoint equation systems. For clarity, the interface coupling terms for the adjoint fields are presented as follows:

$$\mathbf{w} = \mathbf{u} \qquad (9.41)$$
$$\mathbf{t}^a = \nabla\mathbf{v} \cdot [2\nu\mathbf{n} \cdot \mathrm{D}\,(\mathbf{w}) - q\mathbf{n}] \qquad (9.42)$$

where (9.41) refers to a Dirichlet boundary condition on the adjoint RANS equations and (9.42), namely the adjoint tractions, refers to a Neumann boundary condition acting on the adjoint structural equations. Similar boundary conditions were derived in [10] for a coupled adjoint sensitivity analysis of an aeroelastic problem which is

governed by Euler flow and linear elastic structural equations. It is important to note that a force objective is assumed and such objective functions can also be formulated on the inlet and outlet of the flow domain [11]. As a result, partial derivatives of the objective function w.r.t. the design variables do not appear in the coupling terms but rather on the inlet and the outlet boundary conditions of the adjoint fluid equations. These equations enable a partitioned solution of the adjoint coupled fields similar to the partitioned solution of the coupled primal fields with the so-called Lagged-Coupled Adjoint (LCA) method [12].

Finally, once the coupled adjoint solution is available, grid sensitivities could be calculated from the following equation;

$$\frac{\mathrm{d}J}{\mathrm{d}\mathbf{x}} = 2A \, \nabla\mathbf{v} \cdot [\nu\mathbf{n} \cdot \mathrm{D}\,(\mathbf{w}) - q\mathbf{n}] \tag{9.43}$$

with A being the area effected by the surface perturbations. It is important to note that due to an assumption introduced for the adjoint coupling and sensitivity equations, the structural sensitivities do not directly appear in the final sensitivity equation but indirectly through the coupled adjoint solution [8]. Finally, the sensitivities w.r.t. control field $\mathbf{s}$ can be calculated through (9.43) and (9.26).

9.3.2 Multi-disciplinary Feasible Optimization and Software Framework

In order to realize the optimization workflow, a software coupling environment is necessary. For this purpose, the open-source, in-house software EMPIRE (Technische Universität München) is chosen, which offers a modular and efficient way of software coupling. As EMPIRE handles the connections with other software components in a server-client relation, the resulting workflow remains modular. The components of the workflow could then be replaced with desired software or method given that they comply with the requirements of the employed MDF communication pattern.

In this framework, CFD analysis is carried out with OpenFOAM®.[2] The well-known *SIMPLE* algorithm is employed for the solution of both primal and adjoint flow variables. A new solver is designed to handle both solutions in an iterative manner through EMPIRE's communication capabilities. Furthermore, the structural analysis tool of Airbus Defence and Space (ADS), LAGRANGE® is utilized for CSM analysis thanks to its capabilities in MDO context [14]. Due to the self-adjoint nature of the linear elastic structural equations, a further development in the solvers is not necessary. Thanks to the Python®[3] interface of this software, the workflow could be realized in an adaptive way. The coupled primal and adjoint equation systems are solved in a partitioned manner by making use of the Aitken accelerator [15] that

---

[2]OpenFOAM® is an open-source toolbox for CFD simulations. http://www.openfoam.com/.

[3]Python® is a programming language. https://www.python.org/.
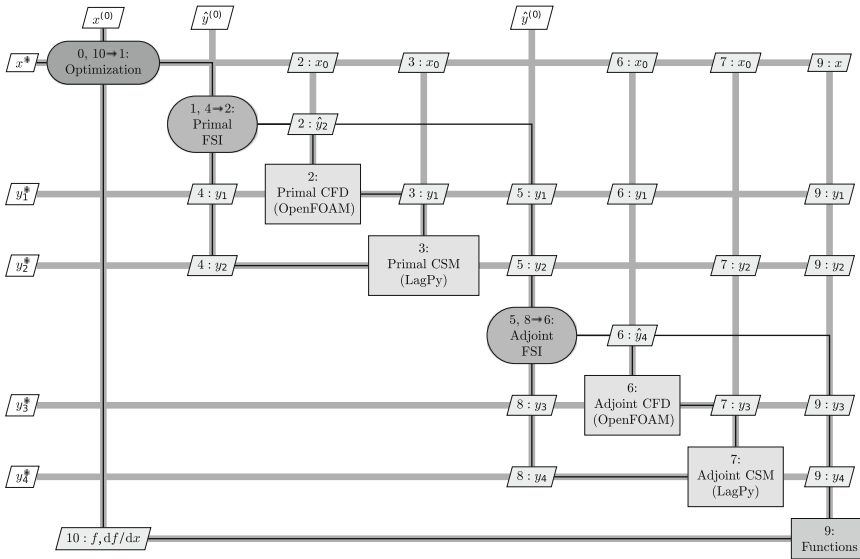
Fig. 9.7 The Extended Design Structure Matrix (XDSM) [13] of the implemented MDO workflow

is available within EMPIRE. Finally, the sensitivity filtering is achieved by making use of the mapping filters of EMPIRE. Having the components of the workflow mentioned, the resulting connections and the communication pattern of the clients are shown in Fig. 9.7.

9.3.3 Results

Making use of the constructed MDO framework, optimization of a symmetric NACA0012 airfoil with 0° angle of attack (AoA) is performed. In order to avoid the implications of frozen turbulence assumption in the adjoint Navier–Stokes derivations, Reynolds number is kept well below the turbulence limit ($Re \simeq 150$) and the optimization iterations are advanced until a steady-state flow solution is not possible. The CFD model is presented in Figs. 9.8 and 9.9. The structural model uses the same geometrical discretization as the fluid model interface (See Fig. 9.10). This choice does not reduce the generality of the intended demonstration of the filtering method but only reduces the possible numerical errors in the primal and adjoint fields that could arise due to different discretizations. In fact for practical problems, where the CFD and CSM interface discretizations are often dissimilar, the necessity for a design control field is more significant, since the design update should be computed on a common surface that drives both numerical models. Shell elements are used to model the structural behaviour which results in a flexible airfoil. A simple support is applied at the model's leading and trailing edges. Finally, a coarser discretization of
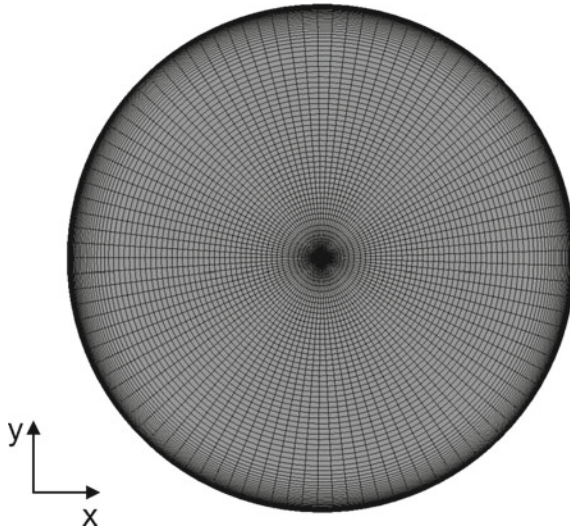
Fig. 9.8 CFD computational domain with outer diameter to chord length ratio: $D \approx 130 \cdot C$
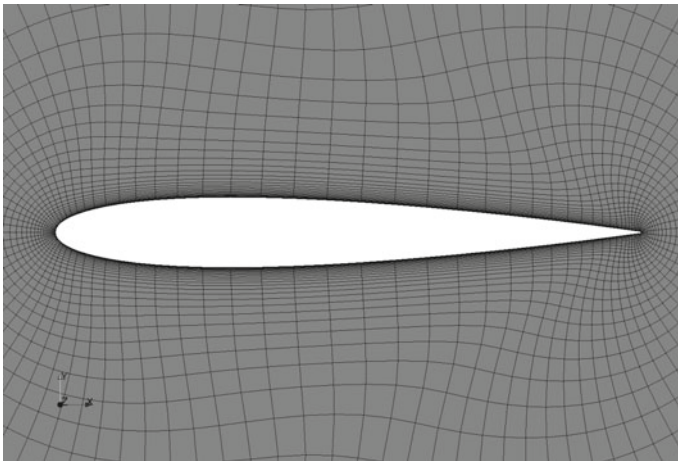
Fig. 9.9 The discretization of the flow domain around the NACA0012 airfoil

the control field with bilinear quadrilaterals is adopted to achieve filtering properties (See Fig. 9.11).

The considered optimization problem is a weighted sum of the drag minimization and the lift maximization problems. The objective function can be written as:

$$J\left(\mathbf{x}, \mathbf{d}, \mathbf{v}, p\right) = w_D \cdot \mathbf{F}_D + w_L \cdot \mathbf{F}_L \tag{9.44}$$

Fig. 9.10 The design mesh of the NACA0012 airfoil
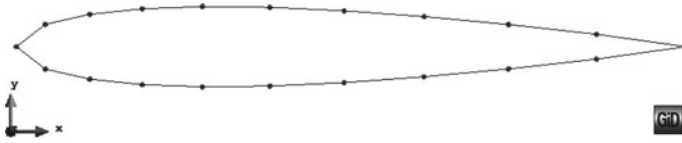
Fig. 9.11 The control mesh of the NACA0012 airfoil
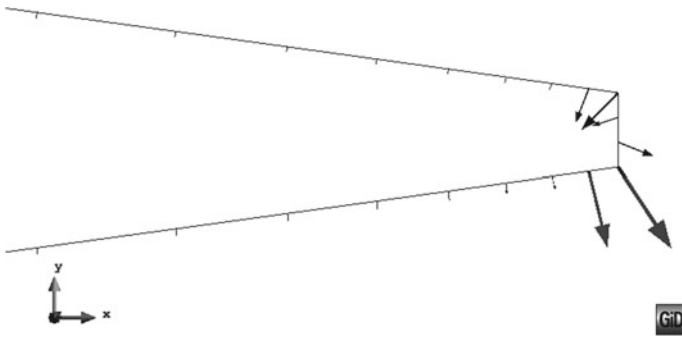
Fig. 9.12 The rugged sensitivity field on the design surface
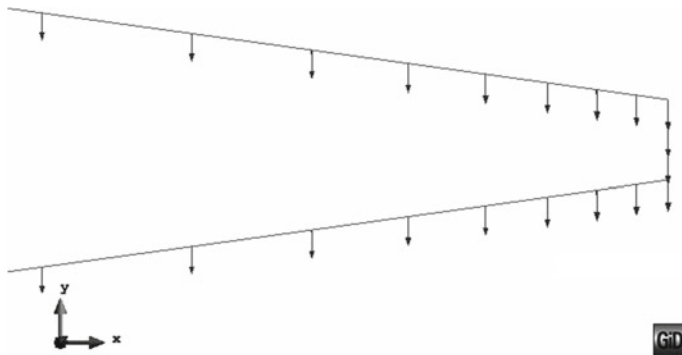
Fig. 9.13 The smooth design update field as a result of filtering operation
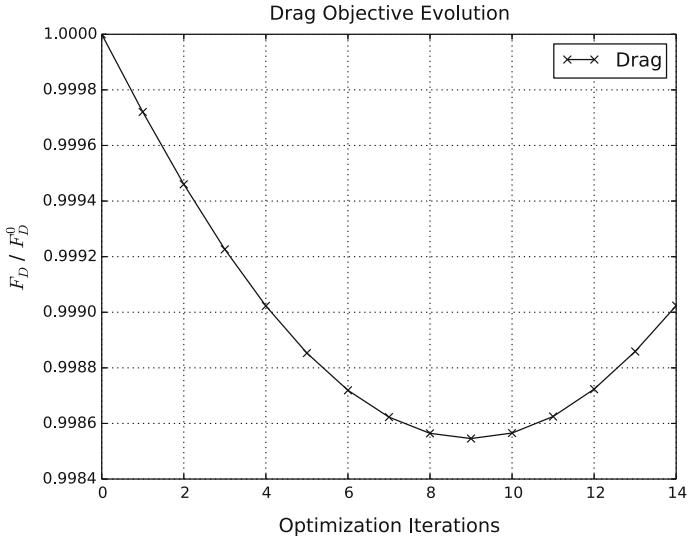
Fig. 9.14 The drag objective evolution throughout optimization iterations. Values are averaged with the initial drag value
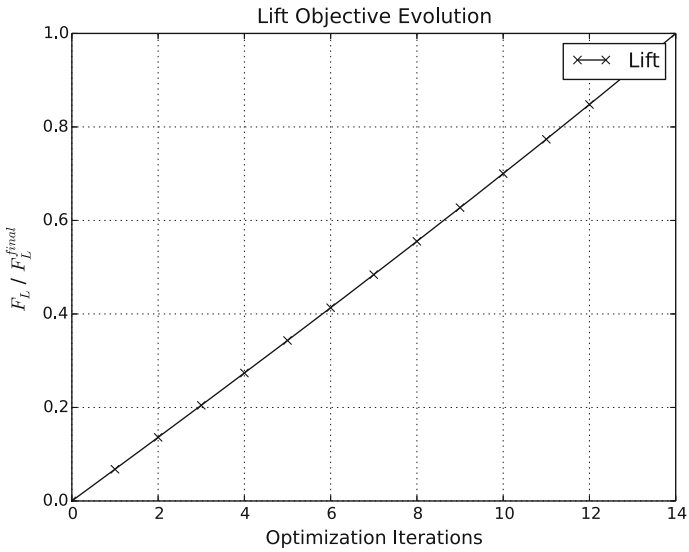
Fig. 9.15 The lift objective evolution throughout optimization iterations. Values are averaged with the final lift value
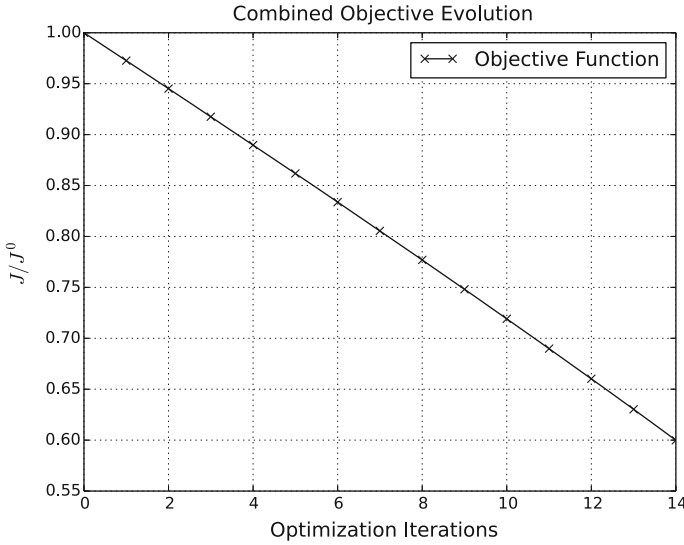
Fig. 9.16 The combined objective evolution throughout optimization iterations. Values are averaged with the initial objective value

where $\mathbf{F}_D$ and $\mathbf{F}_L$ correspond to the drag and the lift forces respectively. Furthermore, equal importance is given to the weights of individual objectives; $w_D = 1.0$, $w_L = -1.0$.

It is clear that if the retrieved grid sensitivities were to be used for the optimization, the interface mesh would be distorted and it would not be possible to perform a CFD simulation on the resulting numerical model (See Fig. 9.12). Making use of the Mortar Mapping technique and the proposed method, sensitivity filtering is achieved and smooth design updates are retrieved (See Fig. 9.13).

The gain from the individual objectives and the weighted sum during the optimization procedure are shown in Figs. 9.14, 9.15 and 9.16. It is predictable that the drag and the lift objectives contradict each other when an optimization is to be performed. This is clearly visible in Fig. 9.14 where the drag force takes a turn to increase while the lift force in Fig. 9.15 keeps increasing. However, the total objective function keeps decreasing as expected (See Fig. 9.16). At the converged FSI state the geometry is forced to evolve towards slenderness due to the drag minimization, while the lift maximization tends to increase the AoA and the camber of the airfoil.

9.4 Conclusions

A method to construct a filtering operator through the Mortar Mapping technique is presented. The method uses the same basic principles with the Vertex Morphing

method and forms the variable transformation through the Mortar Mapping procedure. As the Mortar Mapping is a general procedure for field transfer between different discretizations of the same field, the method is also applicable to CAD models. For instance, the control field could be chosen as the underlying CAD model that describes the geometry and forms a basis for numerical model generation. In that case, since the optimization problem is solved and shape variations are computed in the control space, it would be possible to retrieve a CAD model at the end of the optimization process, too. Moreover, it is shown that the proposed method does not violate the optimality condition of the optimization problem and the claim is supported with the examples of varying complexity. In addition, the applicability of the method to more complex problems is presented utilizing the developed MDO framework. In fact, the necessity of a control field is much more prominent when MDO problems are considered. Often the numerical models of the individual disciplines have non-matching discretizations on their interfaces, which results in dissimilarly discretized sensitivity fields. The proposed method not only closes this gap and acts as a driver for the optimization problem, but also serves as a sensitivity filtering method to improve the quality of the resulting numerical models.

References

1. M. Hojjat, E. Stavropoulou, K.-U. Bletzinger, The vertex morphing method for node-based shape optimization. Comput. Methods Appl Mech. Eng. (2014). https://doi.org/10.1016/j.cma.2013.10.015
2. K.-U. Bletzinger, A consistent frame for sensitivity filtering and the vertex assigned morphing of optimal shape. Struct. Multidisc. Optim. (2014). https://doi.org/10.1007/s00158-013-1031-5
3. R.B. Bapat, *Linear Algebra and Linear Models* (Springer, London, 2012)
4. T. Wang, R. Wüchner, S. Sicklinger, K.-U. Bletzinger, Assessment and improvement of mapping algorithms for non-matching meshes and geometries in computational FSI. Comput. Mech. (2016). https://doi.org/10.1007/s00466-016-1262-6
5. B.I. Wohlmuth, Discretization techniques based on domain decomposition, in *Discretization Methods and Iterative Solvers Based on Domain Decomposition*, vol. 17, Lecture Notes in Computational Science and Engineering, ed. by M. Griebel, D.E. Keyes, R.M. Nieminen, D. Roose, T. Schlick (Springer, Berlin, 2001), pp. 1–84
6. C. Farhat, M. Lesoinne, P. LeTallec, Load and motion transfer algorithms for fluid/structure interaction problems with non-matching discrete interfaces: momentum and energy conservation, optimal discretization and application to aeroelasticity. Comput. Methods Appl. Mech. Eng. (1998). https://doi.org/10.1016/S0045-7825(97)00216-8
7. J.R.R.A. Martins, A.B. Lambe, Multidisciplinary design optimization: a survey of architectures. AIAA J. (2013). https://doi.org/10.2514/1,J051895
8. R. Najian-Asl, D. Baumgärtner, K.-U. Bletzinger, Towards shape optimization of steady-state fluid-structure interaction problems using vertex morphing, in *16th AIAA/ISSMO Multidisciplinary Analysis and Optimization Conference*, Dallas, TX, 22–26 June 2015. https://doi.org/10.2514/6.2015-3356
9. E.M. Papoutsis-Kiachagias, K.C. Giannakoglou, Continuous adjoint methods for turbulent flows, applied to shape and topology optimization: industrial applications. Arch. Comput. Methods Eng. (2014). https://doi.org/10.1007/s11831-014-9141-9

10. A. Fazzolari, An Aero-Structure Adjoint Formulation for Efficient Multidisciplinary Wing Optimization. Dissertation, Technische Universität Braunschweig (2005)
11. C. Othmer, A continuous adjoint formulation for the computation of topological and surface sensitivities of ducted flows. Int. J. Numer. Methods Fluids (2008). https://doi.org/10.1002/fld.1770
12. J.R.R.A. Martins, J.J. Alonso, J.J. Reuther, Complete configuration aero-structural optimization using a coupled sensitivity analysis method, in *Proceedings of the 9th AIAA/ISSMO Symposium on Multidisciplinary Analysis and Optimization*, Atlanta, GA, 46 Sept 2002, https://doi.org/10.2514/6.2002-5402
13. A.B. Lambe, J.R.R.A. Martins, Extensions to the design structure matrix for the description of multidisciplinary design, analysis, and optimization processes. Struct. Multidisc. Optim. (2014). https://doi.org/10.1007/s00158-012-0763-y
14. G. Schuhmache, F. Daoud, Ö. Petersson, M. Wagner, Multidisciplinary airframe design optimization, in *28th International Congress of the Aeronautical Sciences*, Brisbane, Australia, 23–28 Sept 2012
15. B. Irons, R.C. Tuck, A version of the Aitken accelerator for computer implementation. Int. J. Numer. Methods Eng. **1**, 275277 (1969)

Chapter 10
Interfacing MSC Nastran to the CFD-Solver DLR-Tau for Unsteady FSI Analyses with Nonlinear Aircraft Structures

Matthias C. Haupt, Klemens Lindhorst and Peter Horst

Abstract For the partitioned analysis of fluid structure interactions the coupling of fluid and structural analysis codes is a basic requirement. For this purpose the MSC Nastran solver provides a programming interface OpenFSI, which is used and extended here for a flexible usage. Target is the integration of this nonlinear structural solver into the parallel programming environment FlowSimulator in which the DLR-Tau code is used for fluid analysis. The developed component based architecture and implementation is explained in detail. Two applications show the characteristics of nonlinear behaviour of aircraft structures. A beam-like behaviour shows in the nonlinear aeroelastic loading case a stiffening due to larger deflections and rotations and a correct kinematic shortening of the wing-span. A tin-walled wing structure shows skin buckling, which reduces the overall stiffness of the wing and alters the flowfield locally. Both effects can not be reproduced by the classical linear theory.

10.1 Introduction

The coupling of stand-alone-codes for the analysis of fluid structure interactions (FSI) requires the exchange of coupling values e.g. the projection of displacements and forces between the different surface grids as well as the transport from one code to the other and the control of the coupling process [1]. Figure 10.1 shows schematically the process logic of such a FSI implementation. A typical approach to build up such an implementation is to use the individual solver as black box solver with the capability to solve the governing equations for a given set of boundary conditions. These boundary conditions are derived here from the coupling conditions

M. C. Haupt (✉) · K. Lindhorst · P. Horst
Institute for Aircraft Design and Lightweight Structures,
Hermann-Blenk-Str. 35, 38108 Braunschweig, Germany
e-mail: m.haupt@tu-bs.de

155

Fig. 10.1 Process logic of a partitioned FSI simulation

and are the continuity of surface displacements and the equilibrium of forces [2]. For nonconformal surface discretizations, which is the usual situation, a projection step is required to satisfy the coupling conditions via the discrete degrees of freedom of the different surface discretizations. The projection of the grid values is done via seperate components. Finally, a top-level programming is needed to steer the components and to manage the iteration to fulfill the coupling conditions on the common boundary and the consistent advance in time of the individual solvers. In such an environment each individual function is handled by an individual software component.

MSC Nastran uses a slightly different approach, because using the solution type 400 MSC Nastran solves the nonlinear and transient structural problem with its own solution techniques and is able to use surface loads from e.g. a CFD solver for the current deformation state in the actual nonlinear iteration step and for the actual time step. In this sense MSC Nastran takes over the control of the coupling process and the FSI implementation requires only the supply of the actual displacement state to the fluid solver and the extraction of the resultant loads to be used by MSC Nastran.

The incorporation of these boundary values in the MSC Nastran solution sequence is shown in Fig. 10.2 refering to the programming interface OpenFSI provided by MSC Nastran for such purposes [3]. The OpenFSI interface has some methods to be implemented which are called during different phases of the nonlinear and transient solution process. The `initialize` method is called in the beginning of a MSC Nastran run for initialization purposes. Before a new time step is evalued the `initializeTime` method is called whereas the `finalizeTime` method is called after the successful timestep evaluation. Most important are the methods `getWettedNodeForces`, in which the forces determined here by the CFD code need to be applied, and `putWettedNodeDisplacementAndVelocities`, in which the actual displacements and velocities on the surface grid are available for further use. In order to use this interface a c++ class has to be written that possesses these particular methods prescribed by MSC Nastran. For details about this c++ class the reader is referred to the [4].

Fig. 10.2   Data flow for an OpenFSI MSC Nastran simulation

Nevertheless the adaptation of a stand alone code to this c++-interface requires some effort and a suitable software concept.

10.2   Component Architecture

The developed software concept is based on a distributed component architecture, in which the MSC Nastran solver component runs as an individual process as well as the other codes especially the CFD solver. The information exchange via an interprocess communication must by understood with a proper adapter by all involved components and should support heterogeneous computers and networks. A widely-used interprocess communication technique like CORBA or xml-rpc [5] enables as a middleware the different components to be implemented with different programming languages and ensures a great flexibility to adapt easily new codes to this environment. For this purpose xml-rpc was selected because of its easy usage.

Because the program flow of MSC Nastran is strictly defined and to avoid error-prone synchronisation mechanisms in the implementation of the MSC Nastran com-

Fig. 10.3 Architecture of
the MSC Nastran server
component
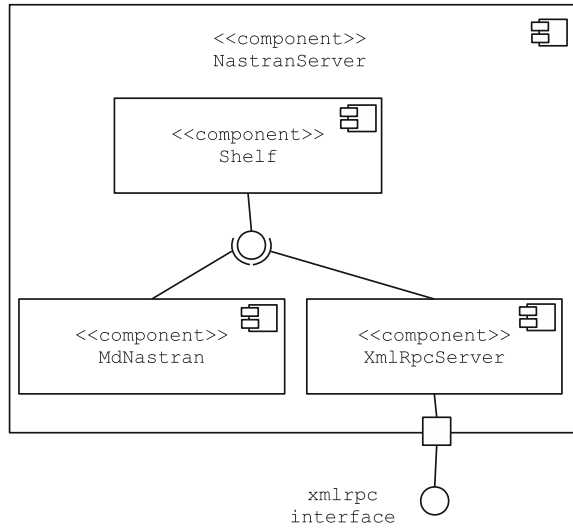
ponent was designed as a server for other client components, see Fig. 10.3. The
xmlrpc server provides services to access a data pool - the shelf - to get the data
which are available via the OpenFSI interface or to set data which are required by
the OpenFSI interface. The Get/Set methods of the xmlrpc server provides access to
control flags defining the actual program state and program advance, the grid points
and the element connectivity of the structural surface grid and to query or define
vectors of interface quantities without the need to write these into files. To make
these services available while MSC Nastran is working the server and the shelf are
implemented in a separate thread and the OpenFSI methods are accessing this shelf
in the same way as the server methods do.

There advantages of this approach are summarized as follows:

- Clear component based architecture in design and implementation
- Simple access to MSC Nastran program with server based service and a lean and
  extensible interface
- Neutral xmlrpc based communication to be used with a various programming
  languages
- Data transfer via network service supporting heterogeneous computers and net-
  works
- Fast data exchange compared to file based communication
- Simple and robust synchronisation of the coupled analysis via control flags

The c++ implementation of the MSC Nastran server component with the xmlrpc
server via OpenFSI is explained in Sect. 10.3 in detail. In Sect. 10.4 an example of a
client connection written in python is given.

10.3   OpenFSI Implementation

For coupled fluid structure interaction analyses MSC Nastran provides a programming interface called OpenFSI with the already mentioned methods. In order to use this interface a c++ class `iflsOpenFSI` was written that implements the particular methods specified in the abstract class `OpenFSIBase`. Furthermore, the class `iflsOpenFSI` is inherited from a class `iflsXmlrpcDataServer`, see Fig. 10.4. This class possesses an instance of a xmlrpc server - here based on the Abyss HTTP server - provided by the xmlrpc-c library [5]. Moreover, in the constructor method of the class `xmlrpcDataServer` the xmlrpc server is equipped with get- and set-methods for the xmlrpc interface for scalar values and array data respectively by using the class-own method `AddMethod`. The particular xmlrpc server methods has to be defined as classes inherited from the class `xmlrpc_c::method`, which is the reason why the `xmlrpcDataServer` class owns a class for each get- and set-method, see Fig. 10.4.
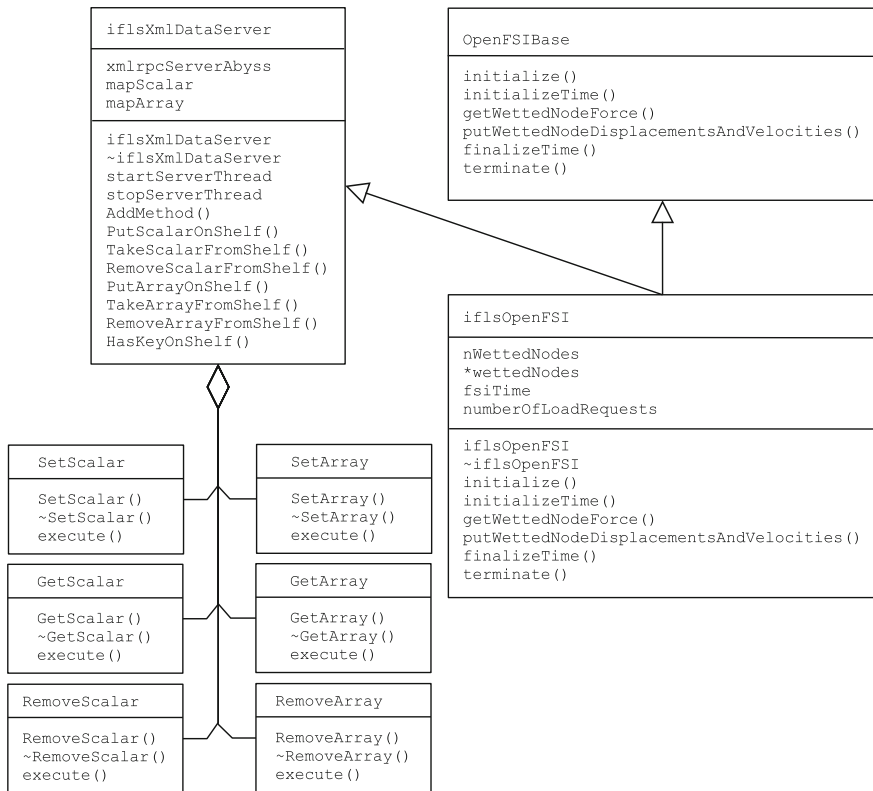
Fig. 10.4   Class diagram of the OpenFSI based MSC Nastran server implementation

For synchronisation with the MSC Nastran process some control flags are available, to query the currents MSC Nastran run state and to steer its progress:

- `Initialize.Finished`: Indicates that the `initialize` method is finished, i.e. MSC Nastran is launched successfully and the xmlrpc server is initialized with model data such as nodal coordinates, node IDs and element connectivity.
- `Time.Set.Flag`: Monitors the time stepping. Before starting the next time step its value is `0` (set in methods `initialize` and `finalizeTimeStep`) and `1` while the time step solution has started (set in `initializeTimeStep`).
- `Solution.Finished`: A value of `1` indicates that MSC Nastran has finished the last solution step and the calculated results (displacements and velocities) are accessible in the server (set in `putWettedNodeDisplacementsAnd...` method). A value of `0` needs to be set by a client after accessing the results to identify the availability of new results.
- `Force.Set.Flag`: A value of `1` (set by a client) indicates, that the force array is set by the client process, e.g. the CFD code, and a MSC Nastran solution step is launched after assigning the forces to the MSC Nastran data structures. A value of `0` (set in the `putWettedNodeDisplacementsAndVelocities` method) makes the `getWettedNodeForces` method waiting for forces.
- `Terminate.Flag`: A value of `1` indicates, that the coupled analysis has reached final time step respectively the `terminate` method and MSC Nastran is terminated in the following.

In addition to these control flags values of the current physical time in the MSC Nastran solution and the next timestep size are accessible via the server by the variable names `End.Time` and `Delta.Time`.

10.4   FSI Architecture

To set up a FSI analysis the component architecture shown in Fig. 10.5 is developed. It consists of two analysis code components (`StructureCode` and `FluidCode`), the component for the projection between the different surface discretizations (`Projection`) and finally the component to steer the components and to exchange data between the components (`ControlCode`). Both analysis code components provide a unified interface (`code interface`), so that the codes are handled in the FSI environment in a unique way and can be easily exchanged by an other code implementing this interface.

For the integration of the MSC Nastran solver into the architecture the structural code component consists of an adapter (`StructureCodeWrapper`), to implement the code interface and to adapt it to the MSC Nastran server capabilities, and a component to communicate with the MSC Nastran server, which is done with a client (`XmlRpcClient`) using the MSC Nastran server interface.
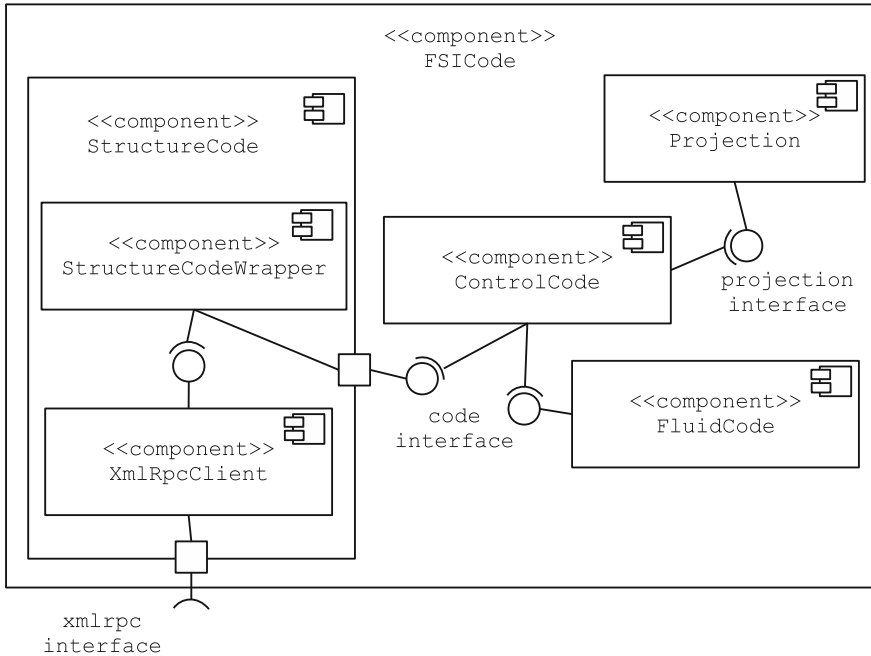
Fig. 10.5 Component diagram of a FSI analysis architecture

The python implementation of the components presented in the following is only an example for a client connection to the xmlrpc server. It is possible to use any programming language that supports a xmlrpc client connection.

10.5   FSI Implementation

The implementation of such FSI analysis was done on top of the FlowSimulator framework [6], which already provides basic techniques to control and steer analysis codes, especially CFD codes, in a parallel environment. Advantageously, the FlowSimulator environment supports the Python programming language, which was used here for the high level programming of the different components. The class diagram in Fig. 10.6 gives an overview over the design.

The xmlrpc client component and in this way the connection to the xmlrpc server is realized with the *xmlrpclib* python package. A class FSNastranClient is implemented that instantiates a xmlrpc server proxy object in order to provide the connection to the server. Moreover, the class FSNastranClient provides simple methods to send, receive and remove scalars and arrays in analogy to the get/set methods of the server. These methods are used by the class FSStructureCode for
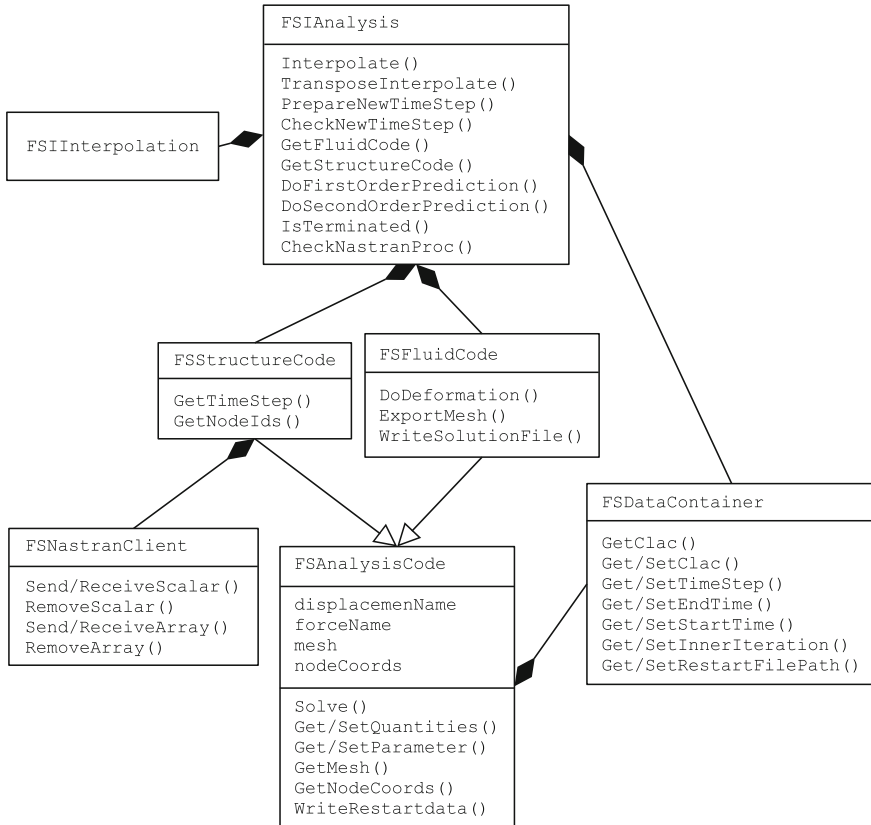
Fig. 10.6 Class diagram of a FSI analysis implementation

data transfer. Furthermore, the class `FSStructureCode` implements the unified code interface `FSAnalysisCode` and in addition some code specific methods, e.g. to handle restarts. `FSAnalysisCode` defines a set of standard methods of analysis codes so that the codes with this interface behave equally and can be replaced easily be an alternative code implementing this interface. The adaptation of the fluid solver - here the DLR-Tau [7] code is used - with the code adapter `FSFluidCode` is done analogous.

The class `FSIAnalysis` provides some high level to the user: FSI specific functions, e.g. the evaluation of a predictor or the set up of the involved codes for a new time step. Furthermore, methods for the projection of forces and displacements between the surface grids are included, using the proper functions of the projection software. In this paper the advanced splining module of the FlowSimulator environment was used. These high level functions hide the detailed set up from the user and the resultant control code is clean and clear. This is explained with an example script of a FSI analysis using the simple Dirichlet–Neumann iteration:

Listing 10.1 FSI initialization

```
1  # Parameters for CFD solver TAU
2  fluidParam = {'ParamFile': "NLR7301.param07",
3                'GridFile': "fluid.grid",
4                'CFDSurfaceMarkers': CFDSurfaceMarkers}
5
6  # Parameters for NASTRAN
7  structParam = {'NastranFile': 'structure.dat',
8                 'SCA_PATH': 'PathToServices/NastranServices',
9                 'NastranExecutable': 'mdnast20101'}
10
11 # Parameters for interpolation module FSAdvancedSplining
12 interpolParam = {"Groups": [{"Name": "WR", "CFDMarker": [3],
13                  "Splines": {"ALL": {"Type": "RBF_TPS", ... }}
14                             ... }
15
16 # Instantiation of FSI class object, fluidCode and structureCode
17 FSI = FSIAnalysis(fluidParam, structParam, interpolParam)
18 fluidCode = FSI.GetFluidCode()
19 structCode = FSI.GetStructureCode()
```

In the lines 1–13 of listing 1 dictionaries are filled with class specific parameters. In the instantiation of the FSI analysis (line 16) the structure and fluid code objects are created as well as the object of the projection. Lines 17 and 18 give direct access to the analysis codes.

Because MSC Nastran controls the time step and iteration control, the analysis loop continues until MSC Nastran terminates the analysis. This is checked in line 1 of listing 2. The intended block starts with the setup of a new time step initializing some data and calculates a second order predictor (line 9) if MSC Nastran is still running. The current displacements are projected on the fluid grid in line 12 and used as boundary conditions for the fluid code in line 15. In line 16 the fluid solver calculates the solution of the configured Dirichlet problem with theses boundary conditions and in line 17 the resulting surface forces are extracted.

Listing 10.2 FSI time stepping loop

```
1  while not FSI.IsTerminated():
2
3      # check for new time step
4      if FSI.CheckNewTimeStep():
5          # Prepare new time step
6          FSI.PrepareNewTimeStep()
7          if FSI.CheckNastranProc():
8              # use structural predictor
9              structDefoVecs = FSI.DoSecondOrderPrediction()
10
11     # interpolate displacements from structure to fluid grid
12     fluidDefoVecs = FSI.Interpolate(structDefoVecs)
13
14     # solve the fluid problem
15     fluidCode.SetQuantities(fluidDefoVecs, fluidCode.displName)
16     fluidCode.Solve()
17     fluidForces = fluidCode.GetQuantities(fluidCode.forceName)
18     fluidCode.WriteRestartData()
19
20     # interpolate forces from fluid to structure grid
21     structForces = FSI.TransposedInterpolate(fluidForces)
22
23
```

```
24      # solve the structural problem
25      if FSI.CheckNastranProc():
26          structCode.SetQuantities(structForces,structCode.forceName)
27      structCode.Solve()
28      StructDefoVecs = structCode.GetQuantities(structCode.displName)
29      structCode.WriteRestartData()
```

In line 21 follows the projection of the fluid forces onto the structural grid. The structural boundary conditions are set in line 26 and line 27 let MSC Nastran perform a solution step. In line 28 the surface displacements are accessed from the structural code. Usually a convergence check should follow in a Dirichlet–Neumann cycle but here MSC Nastran does this during its own nonlinear solution and decides how to proceed.

With this high level implementation the user is able adapt e.g. an other structural code and can use this environment to implement more sophisticated FSI coupling schemes easily.

10.6 Examples

Target of the MSC Nastran integration into the FlowSimulator environment is the capability to investigate structural nonlinear applications. Therefore, two cases are considered in the following sections.

10.6.1 Beam Structure

In the first example a high aspect ratio wing with constant cord together with a simple beam model representing the structure is investigated in cooperation with the DLR Göttingen. The structural parameter of the beam model are taken from [8] and summarized in Table 10.1. Figure 10.7a shows the structural model consisting of a finite element beam and the wetted surface in grey color. The aerodynamic profil is given in Fig. 10.7b. The aerodynamic conditions are given in Table 10.2.

The first four eigenmodes in z-direction are shown in Fig. 10.8. The beam is modeled symmetrically meaning the structural behaviour in x direction equals the behaviour in z direction. Therefore, for each eigenmode shown in Fig. 10.8 a second mode with the same frequency and with an identical shape in x direction exists. The largest amplitude of all modes is observed at the wing tip. The first four eigenfrequencies are nearly doubled from one frequency to the next.

Subject of this test case is the quantification of the structural nonlinearities within the coupled FSI analysis. Because the focus is on the structural nonlinearities large deformations are of major interest. In general, structural nonlinearities are expected, if the bending deformation of the free beam end reaches 10% of the beam length. In consequence, the wing tip should exceed a bending deflection of $u_{z,Tip} > 1.6$ m.

Table 10.1 Parameters of the structural model

Parameter	Value	Parameter	Value	Parameter	Value	Parameter	Value
m	749.2 kg	b	16 m	ν	0.33	ρ	2800 $\frac{\text{kg}}{\text{m}^3}$
E	71000 $\frac{\text{N}}{\text{mm}^2}$	G	26700 $\frac{\text{N}}{\text{mm}^2}$	GE	$3.033 \cdot 10^8$	A	$1.67 \cdot 10^{-2}\,\text{m}^2$
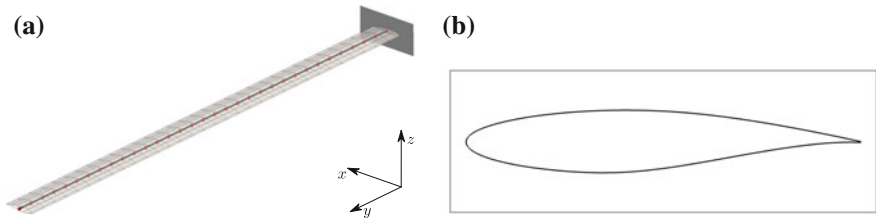
Fig. 10.7 **a** Beam model with wetted surface definition; **b** Aerodynamic contour of the airfoil

Table 10.2 Aerodynamic parameters of the investigated case

Parameter	Value	Parameter	Value	Parameter	Value
Ma	0.58	T_∞	260 K	ρ_∞	0.8 $\frac{\text{kg}}{\text{m}^3}$
p_∞	59696 Pa	U_∞	187.465	α	1.5°
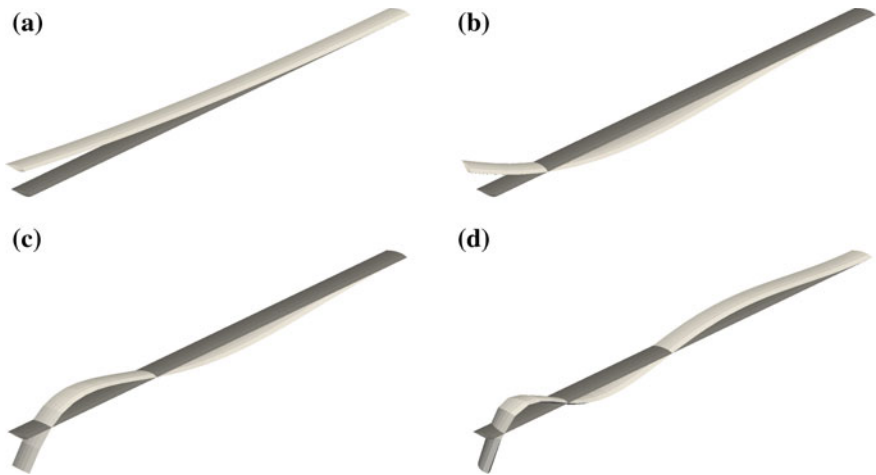
Fig. 10.8 Eigenmodes of the beam: **a** 1st mode with $f_1 = 1.503$ Hz; **b** 1st torsion mode with $f_2 = 5.820$ Hz; **c** 2nd bending mode with $f_3 = 13.053$ Hz; **d** 3rd bending mode with $f_4 = 23.348$ Hz
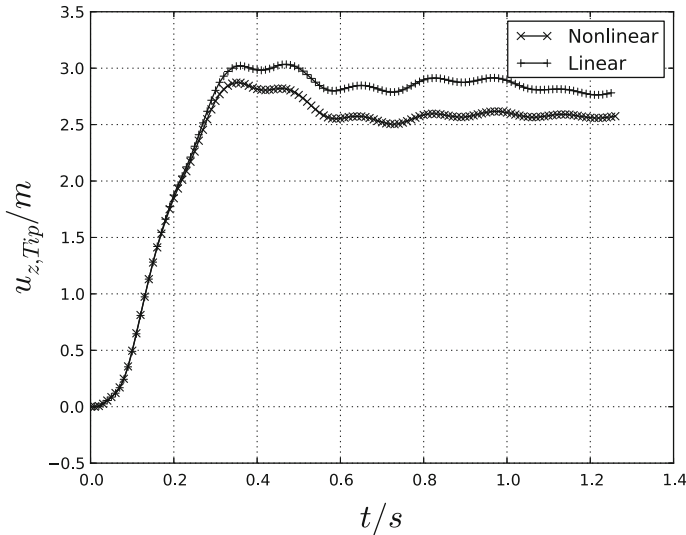
Fig. 10.9 Vertial tip node displacement of transient analysis with linear and nonlinear structure

In the transient analysis the wing starts moving from the undeflected initial state. 1500 time steps with the step size $\Delta t = 0.001$ s are calculated. Figure 10.9 shows the bending definition of the wing tip for the solution with and without inclusion of the structural nonlinearities. Significant differences between the linear and nonlinear behaviour occur for times larger than $t = 0.2$ s. This observation matches the expectation above. After reaching a bending deformation with an amplitude of nearly $u_{z,Tip} = 3$ m the wing tip oscillates with the second eigenmode around a constant value of the stationary limit with a deformation shape close to the first eigenmode. The amplitude of the nonlinear case is smaller compared with the linear case due to the fact, that the additional nonlinear terms stiffen the beam structure. Nonlinear aerodynamic effects play no role.

Important for the understanding is the realistic kinematic deformation of the nonlinear solution, because the nonlinear analysis keeps the deformed beam length constant and in consequence the nonlinear analysis shows a negative displacement in axial y direction, which is not negligible (see Fig. 10.10). The projection of the deformed beam on the y axis is shorted in the order of 2%. The linear analysis shows only a small axial deformation because of the bending induced rotations of the beam cross section and in consequence aerodynamic load components in axial direction.
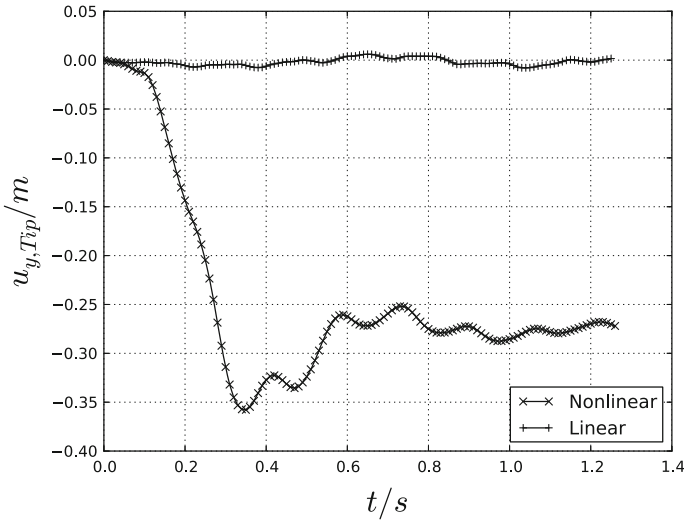
Fig. 10.10 Axial tip node displacement of transient analysis with linear and nonlinear structure
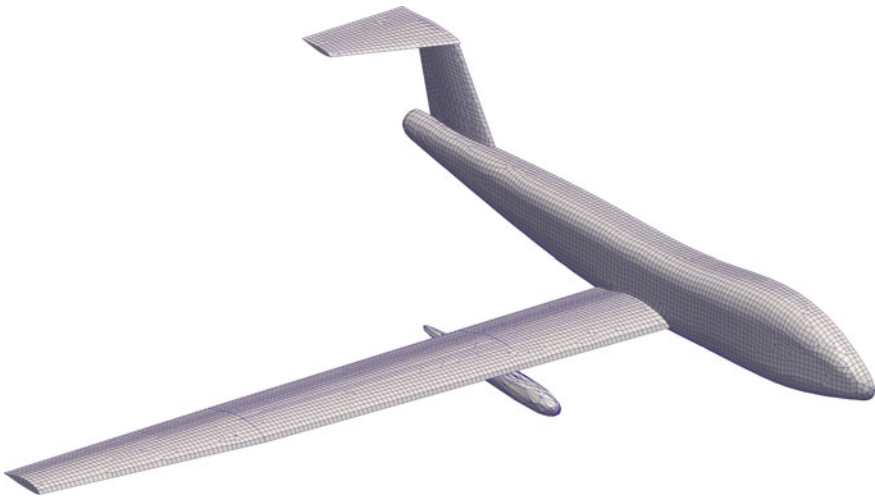
Fig. 10.11 Surface discretization of the structural finite element model

10.6.2 Shell Structure

This test case was developed in cooperation with Airbus Defense and Space and considers a complete aircraft configuration of an unmanned aerial vehicle with a nearly rectangular wing. Figure 10.11 shows the wetted surface of the structural MSC Nastran finite element model, which basically consists of shell elements. The additional
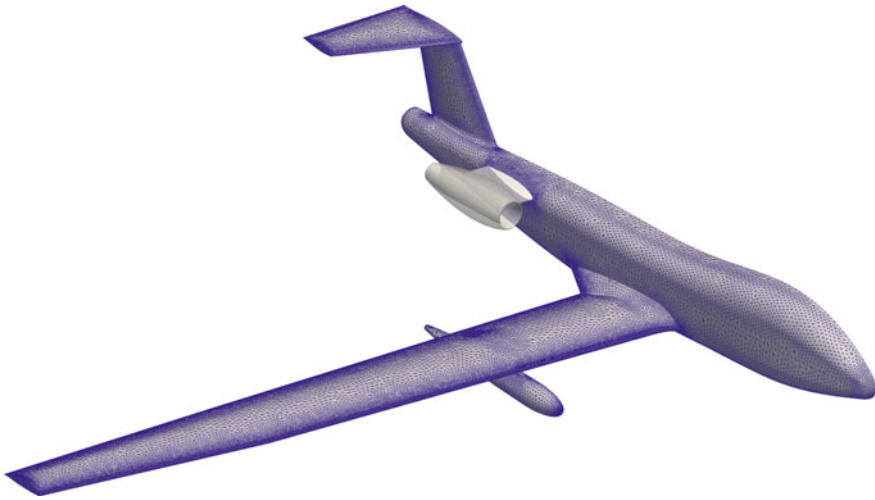
Fig. 10.12 Surface discretization of the aerodynamic model

store tank is represented by a mass point which is connected to the wetted surface elements of the MSC Nastran model (`WETELEME` card) by multipoint constraints (`RBE3` card).

The wetted surface discretization of the aerodynamic grid is shown in Fig. 10.12. The subgrid around the engine is excluded from the analysis, because of the missing structural counterpart and the missing aerodynamic thrust modeling. Because the flight conditions are fixed and the focus is on quality of the wing bending this aspect is negligible.

The flight conditions of Mach number $Ma = 0.4$ at altitude $H = 11$ km provide at an angle of attack of $\alpha = 8.086°$ a lift of the rigid aircraft which is in balance with its weight of nearly $m = 6,000$ kg for the completely fueled configuration. With this angle of attack and empty tanks (wing, center and store) a coupled FSI analysis results in deformations in a reasonable magnitude. Figure 10.13 shows the aeroelastic equilibrium using a linear and a nonlinear structural model. The upper wing skin tends to a wavy bending deformation under the compression close to the wing root. This leads to a further loss of stiffness and to buckling of the skin, which can be modelled only by the nonlinear theory. This local stiffness reduction has a larger bending deflection of the complete wing as consequence. The wing tip deflection of the nonlinear model is with $u_{z,Tip}^{NL} = 0.594$ m 13.58% larger than for linear model with $u_{z,Tip}^{L} = 0.523$ m. The global lift coefficients for both model types are $c_A^L = 0.8426$ and $c_A^{NL} = 0.8391$, which is a deviation of 0.415%. The reason for this is the wing span reduction in the nonlinear model and the altered flow field due to the skin buckling.

With these stationary cases as initial state a transient gust analysis is performed using the DLR-Tau gust generator [9]. The vertical gust is of the 1-cos type with a
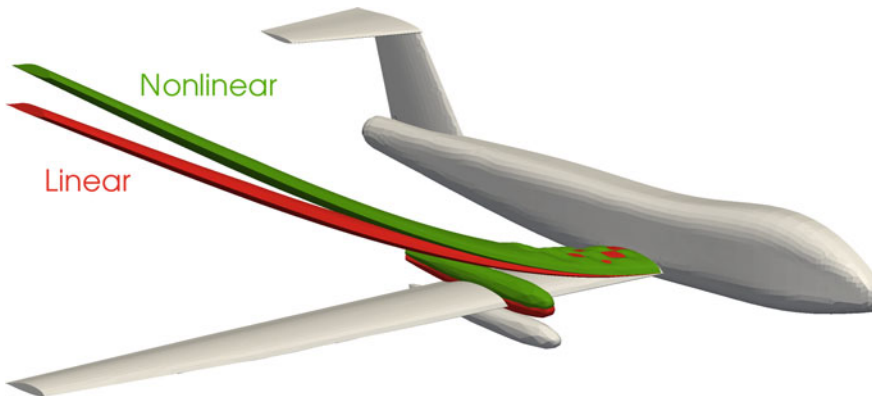
Fig. 10.13 Comparison of stationary aeroelastic deformations (amplified by a factor of 10)
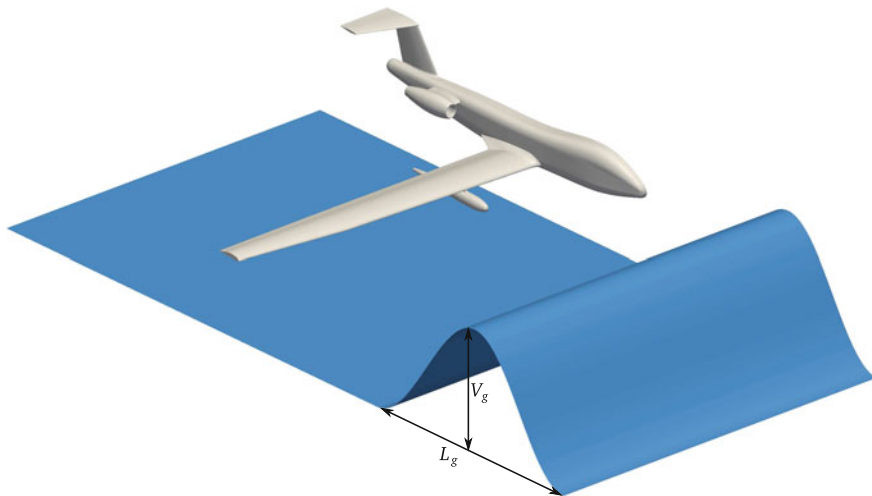
Fig. 10.14 Illustration of the gust parameters

length of $L_g = 10$ m, a maximum gust velocity of $v_g = 10$ m/s and moves with the velocity of $U_g = 139.3$ m/s (see Fig. 10.14). At the beginning of the analysis the gust is positioned at the aircraft nose, i.e. the initial distance is $x_{g,init} = 0$ m.

Figure 10.15 shows the history of the wing tip deflection for both models. The initial deformations reflect the different static aeroelastic equilibriums. The dynamic responses show two superposed oscillations stemming from the first two eigenmodes. This happens with slightly different frequencies because of the different stiffnesses especially due to the skin buckling in the nonlinear case. Similar to the static analysis the lift coefficient is not influenced so much (see Fig. 10.16), because the gust excites primarily the bending and both theories do not show discrepancies in the torsional behaviour. For swept wings this may be more significant.
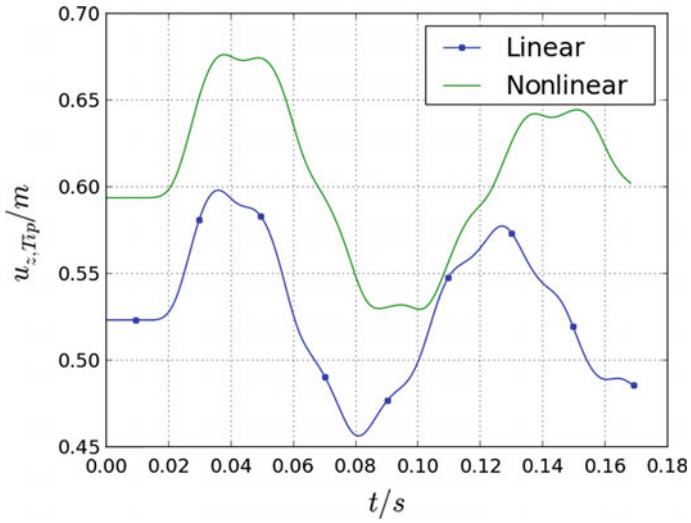
Fig. 10.15 Vertical wing tip displacement due to gust loads
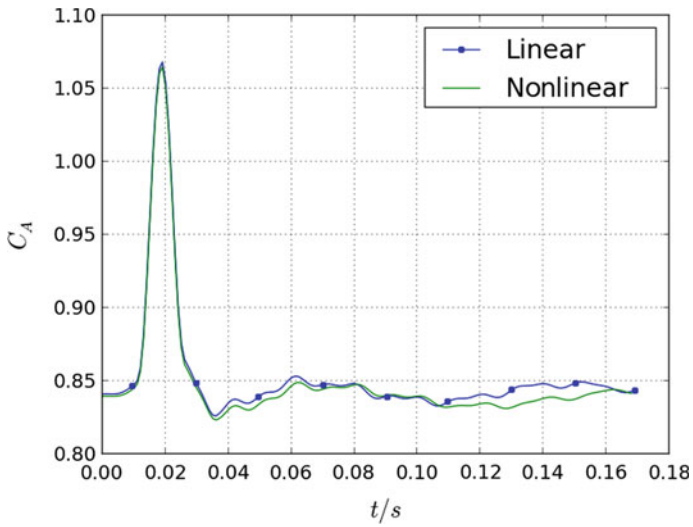
Fig. 10.16 Global lift coefficient due to gust loads

10.7 Conclusion

In this contribution the adaptation of the MSC Nastran solver to the CFD DLR-Tau solver was explained. A server-client concept was developed and implemented for a flexible MSC Nastran usage in FSI analyses. Furthermore, the design of an integration into a FSI framework based on the FlowSimulator software was explained.

The focus of the demonstration examples lies on the nonlinear structural behaviour and its impact on the FSI. Two examples show two import effects. First, the bending of a beam-like structure leads to smaller bending deflections in the nonlinear case. But if the wing has no sweep angle, the overall lift coefficient is only influenced by the realistic shortening of the wing span due to this shortening. Second, the local nonlinear behaviour of the wing skin under compression leads to a local buckling with a decreasing stiffness of the wing in this section. This causes a larger overall deflection of the wing. Possibly, the aerodynamic state may be influenced by such a buckling under certain conditions.

If wings become lighter and more flexible the global and local nonlinear structural behaviour becomes more important in FSI analyses. The presented approach shows the capability to configure such simulations and the applications shows the importance of nonlinear structural models.

References

1. M. Haupt, R. Niesner, R. Unger, P. Horst, Computational aero-structural coupling for hypersonic applications. *9th AIAA/ASME Joint Thermophysics and Heat Transfer Conference*, (AIAA 2006-3252, 5–8 June, San Francisco, California, 2006)
2. R. Unger, M. Haupt, P. Horst, Coupling techniques for computational non-linear transient aeroelasticity. J. Aerosp. Eng. **222**, 435–447 (2008)
3. MD Nastran OpenFSI Tutorial, MSC. Software Corp. (2010)
4. MD Nastran 2010 - User Defined Services, MSC. Software Corp. (2010)
5. E. Kidd, User Manual for XML-RPC (2005), http://xmlrpcc.sourceforge.net/doc/
6. M. Meinel, G.O. Einarsson, The FlowSimulator framework for massively parallel CFD applications. Para 2010, *state of the art in scientific and parallel computing*, (Reykjavik, Iceland, 6–9 June 2010)
7. D. Schwamborn, T. Gerhold, V. Hannemann, On the Validation of the DLR-TAU Code, in *New Results in Numerical and Experimental Fluid Mechanics*, Notes on Numerical Fluid Mechanics, (Springer, Berlin, 1999), pp. 426–433
8. W. Su, C.E.S. Cesnik, Strain based analysis for geometrically nonlinear beams: a modal approach, *53rd AIAA structures, structural dynamics and materials conference*, (AIAA 2012-1713, 23–26 April 2012, Honolulu, Hawaii, 2012)
9. R. Heinrich, L. Reimer, Comparison of different approaches for gust modelling in the CFD code TAU. *International forum on aeroelasticity and structure dynamics*, (Bristol, UK, 2013)

Part IV
Use-Case DIMENSyon-P

Chapter 11
Numerical Computations of Isolated and Installed Engine Jet Flows

Arne Stürmer, Carlos Màrquez-Gutierrez and Peer Böhning

Abstract The integration of efficient high bypass ratio turbofans under the wing of transport aircraft configurations necessitates a very close coupling between the engine and the airframe. One concern arising from this is the possible increase of the noise emissions due to the interaction of the engine jet with the aircrafts' high-lift system. A coupled aerodynamic-aeroacoustic assessment approach is necessary to help understand the underlying flow physics and also support the optimization of such integration scenarios. In the frame of a comprehensive parameter study, a best practice approach for the use of the DLR TAU-Code to investigate the complex aerodynamics of jet-flap interactions was devised which also ensures the usability of the RANS (Reynolds Averaged Navier–Stokes) results in a subsequent aeroacoustic analysis.

11.1 Introduction

Increasingly demanding economic and environmental requirements along with improved aerodynamic and structural solutions have enabled very large bypass ratio engines to become propulsion sytems of choice for commercial transport aircraft. While these engines enable substantial reductions in both fuel burn and emissions, the inherently necessary tighter coupling of these turbofans with the wing of the

A. Stürmer (✉)
DLR Institute of Aerodynamics and Flow Technology, Braunschweig, Germany
e-mail: arne.stuermer@dlr.de

C. Màrquez-Gutierrez · P. Böhning
Rolls-Royce Deutschland Ltd & Co KG, Blankenfelde-Mahlow, Germany
e-mail: CarlosOmar.MarquezGutierrez@Rolls-Royce.com

P. Böhning
e-mail: Peer.Boehning@Rolls-Royce.com

aircraft as well as the high-lift system raises concerns regarding the noise emissions. While even higher bypass ratio engines will provide lower pure jet noise emissions due to the lower exhaust velocity in the bypass flow resulting from the reduced fan pressure ratio, there is a risk that the more closely coupled engines jet will interact with the aircrafts' high-lift system resulting in increases in jet-flap interaction noise. In order to enable both a highly accurate aerodynamic and aeroacoustic assessment and design tool suite, the aim of the present work was to demonstrate and validate the applicability of the DLR TAU-Code [1, 5] to the numerical simulation of engine and engine-airframe configurations and to develop a best practice approach for these simulations, where the results must be suitable for a subsequent use in a numerical aeroacoustic analysis. The requirements set by this multi-disciplinary analysis necessitate specific approaches to both the mesh generation as well as the physical modeling (i.e. turbulence models) in the RANS (Reynolds Averaged Navier Stokes) simulation to ensure high quality solutions can be achieved.

In a first step a methodolgy in TAU for jet flows of isolated nozzles and nozzles installed under a straight, unswept infinite wing section with high-lift system was establisbed. A reference was made available by Rolls-Royce (RRD) in the form of exisiting simulation results based on the use of the commercial CFD solver Fluent and validation data was provided through PIV (Particle Image Velocimetry) measurements, that were obtained for the configurations under study here in the frame of the EU-funded research project VITAL.

In a second step the methodology was extended to a more realistic swept finite wing. For the validation static pressure data on the wing surface were available.

11.2 Test Case Definition

The test cases specified by Rolls-Royce for use in the project were based on the so-called VITAL BPR9 nozzle. This configuration was wind-tunnel tested which resulted in the availability of PIV data characterizing the development of the engine jet and provides a validation basis for the TAU simulations. Furthermore, Rolls-Royce provided existing simulations for these test cases conducted with the commercial CFD solver Fluent, where the results were viewed as a good point of reference for RANS simulations to be used in a subsequent aeroacoustic analysis.

In total three configurations were investigated, as shown in Fig. 11.1:

1. An isolated nozzle configuration with pylon
2. An installed nozzle configuration, mounted with a pylon in an underwing installation on an unswept cruise configuration wing
3. An installed nozzle configuration, mounted with a pylon in an underwing installation on an unswept wing with a 30° flap defelection

All simulations were done at the wind-tunnel scale, which featured a bypass nozzle diameter of $D = 0.26216$ m. In all cases the symmetry along the engine centerline was exploited, enabling a reduction in the mesh size but also limiting the studies

(a) Isolated nozzle configura-   (b) Installed nozzle with a   (c) Installed nozzle with 30°
    tion with pylon   clean, unswept wing   flap deflection

Fig. 11.1 Overview of the VITAL BPR9 configurations employed for the TAU validation studies

to the wind tunnel test configurations that featured a straight, unswept wing. The test point under study, selected from those also measured in the experimental test campaign, is for a representative high-thrust take-off case.

11.3   Mesh Generation

The existing reference simulations were done using block-structured meshes created using the commercial ICEM Hexa mesh generator. In order to ensure for a good compariability with the reference simulations of these test cases done with Fluent, the meshes from those studies were re-used and adapted as necessary for use with the DLR TAU-Code, as shown in Fig. 11.2. One specific adaptation that became necessary was a smoothing of the meshes at the block boundaries. This was prompted by an observed bad rate of convergence in the TAU-solver runs, which indicated a higher sensitivity of TAU compared to Fluent to locally very small time step sizes in the temporal integration scheme.

All the provided meshes were set up for the use of a wall function model at viscous walls in order to save grid points. While this feature is also available in the TAU Code, its use is not standard practice at DLR. Therefore an additional mesh was generated for the isolated case which included sufficient nodes to adequately resolve the boundary layers in the frame of the RANS approach in order to demonstrate the equivalence of the results obtained with this mesh to those obtained using the wall function model.

The meshes ranged in size from $8.6e6$ to $15.6e6$ nodes for isolated case without and with boundary layer resolution and from $13.2e6$ to $19.9e6$ nodes for the installed cases without and with the flap deflection respectively.

(a) Isolated nozzle mesh for wall function simulations

(b) Isolated nozzle mesh for resolved boundary layer simulations

(c) Installed nozzle mesh

(d) Installed nozzle with 30° flap deflection mesh
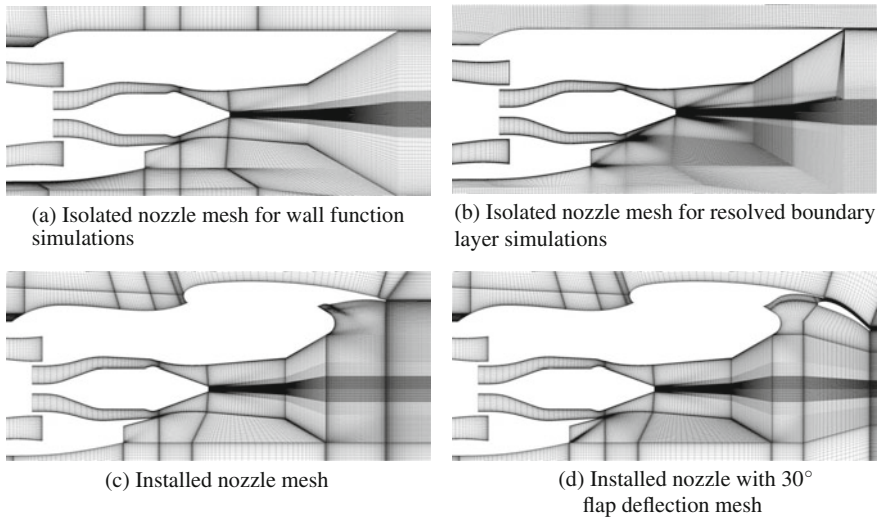
Fig. 11.2 VITAL BPR9 configuration meshes along the engine centerline/symmetry plane

11.4 Numerical Simulations and Parameter Studies

The reference Fluent simulations made use of an upwind scheme for the time integration and employed a $k - \varepsilon$ turbulence model as well as a wall function model on viscous walls. These basic settings were the starting point for the TAU simulations to ensure the best possible comparability. During the course of the studies some adaptations of the numerical approach using the DLR solver became necessary, as will be discussed in the following sections detailing the paramater study on the basis of the isolated VITAL configuration.

Turbulence Model Impact

Presently there is no implementation of the $k - \varepsilon$-model in the DLR TAU-Code. Thus the Menter SST model was chosen for further studies, as this has proven to be the most robust and widely applicable 2-equation turbulence model across a wide range of applications at DLRs Institute of Aerodynamics and Flow Technology [3, 4].

In the simulations it became evident that a shear layer instability at the bypass nozzle occurred in many cases, which had a very detrimental impact on the convergence rate and quality of the CFD solutions. It was found that a switch to the Menter Baseline (BSL) model avoided this issue and ensured both a well-converged RANS simulation as well as a solution quality that was in-line with the requirements set by the subsequent aeroacoustic analysis. Thus this turbulence model was chosen as the standard for use in these types of applications and employed exclusively for all further studies in the frame of the AeroStruct work.

Spatial Discretization Impact

For the initial TAU simulations the meshes of the reference simulations were used. At some of the block interfaces these grids featured some large changes in cell volumes related to specific aspects of the mesh topology. While Fluent was well-behaved in these regions, a strong dependance of convergence rate and solution quality on large cell volume discrepencies was found when running TAU. In order to alleviate these issues and speed up the simulation times the meshes were adapted using ICEM Hexa to have a smoother cell volume distribution across the block boundaries. Using these smoothed meshes, both the convergence behavior as well as the solution quality could be significantly improved in TAU and results achieved a very close agreement with the reference Fluent data.

In most external aerodynamics applications at DLR, the use of the central scheme for the spatial discretization is standard practice [2]. In the present as well as other cases featuring hot engine jets, this model often leads to unphysical total temperature hot spots in the shear layers of the core engine jet with TAU. While not necessarily found to negatively impact the solution quality in terms of the turbulent kinetic enegery (TKE), which is of prime importance for the subsequent aeroacoustic analysis, the use of an upwind scheme is known to avoid these problems. As this choice is also in line with the reference Fluent simulations, a 2. order upwind scheme was employed also for all studies discussed here.

Boundary Layer Resolution Impact

For industrial applications the use of wall functions to resolve boundary layers on no-slip walls is naturally an attractive option to help to reduce the size as well as the effort of generation of the computational mesh and thus also the cost in terms of time and CPU resources of the RANS simulations. However, the applicability of this method is limited to cases with predominantly attached flow around the configuration under study. In particular installed engine cases featuring an aircraft in high-lift configuration at low-speed flight conditions will exhibit large areas of separated flow, which are better handled by adequately resolving the boundary layer flow regions. Therefore DLR decided to also include a case with a mesh featuring a high near-wall mesh resolution to avoid the use of the wall function approach. The aim was to demonstrate that this setup will lead to identical jet development predicitions as found for the reference wall function-based simulations, ensuring that potential future studies for complex aircraft configurations with highly separated flows can be simulated with adequate confidence.

For the isolated nozzle configuration, Fig. 11.3 shows a comparison of the PIV data from the previously conducted wind tunnel tests with the TAU simulation results for both the mesh with and without the high mesh resolution on viscous walls. Plotted are the radial axial velocity and turbulent kinetic energy profiles for the engine jet in the horizontal symmetry plane of the nozzle at an axial position of $x/D = 2.4$ aft of the configuration. The TAU results show essentially negligible differences for the two meshes and approaches and agree well with the experimental results.

(a) Installed nozzle with a clean,
unswept wing

(b) Installed nozzle with 16°
flap deflection
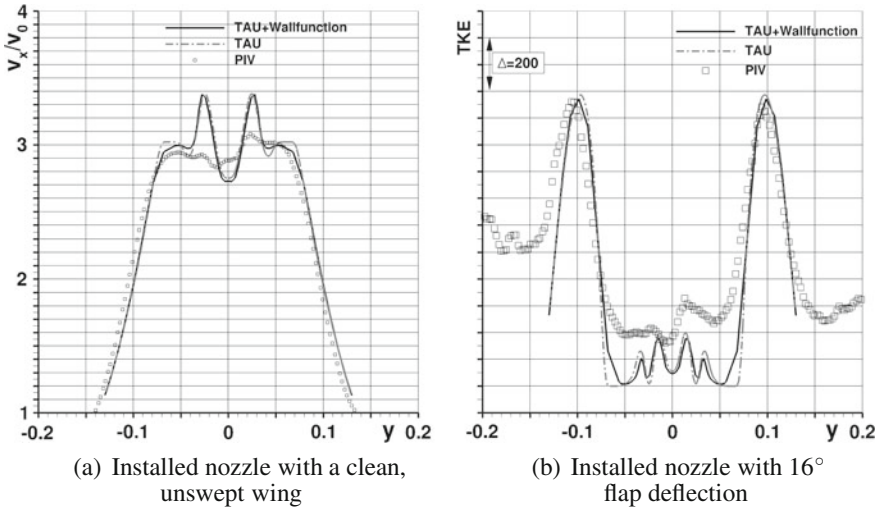
Fig. 11.3 Overview of the VITAL BPR9 configurations employed for the TAU validation studies

11.5 Validation of the TAU Best Practice Approach

For the validation of the RANS results using the best practice for the DLR TAU-Code
simulations, PIV data was available that was obtained in a wind tunnel test in the
frame of the EU R&T project VITAL. This data was measured for the isolated case
and the installed case with the cruise wing at the conditions used in the present study.
In the following sections comparisons between the TAU results, the Fluent results
and the PIV data will be made for these two configurations. For axial locations of
$x/D = 2.4, 3.8, 6.9$ and 8.7 downstream of the nozzle, results will be presented and
discussed for the axial velocity and the turbulent kinetic energy distributions. In all
cases the radial distributions in the engine symmetry plane will be plotted.

11.5.1 Isolated Nozzle with Pylon

For this case the TAU results for both the wall function-adapted as well as the
boundary layer resolving meshes will be compared to the Fluent and the PIV data
(Fig. 11.4).

11.5.1.1 Axial Velocity

The velocity profiles at all axial positions indicate that all numerical results are in
very close agreement and also show a good prediction of the jet development as was
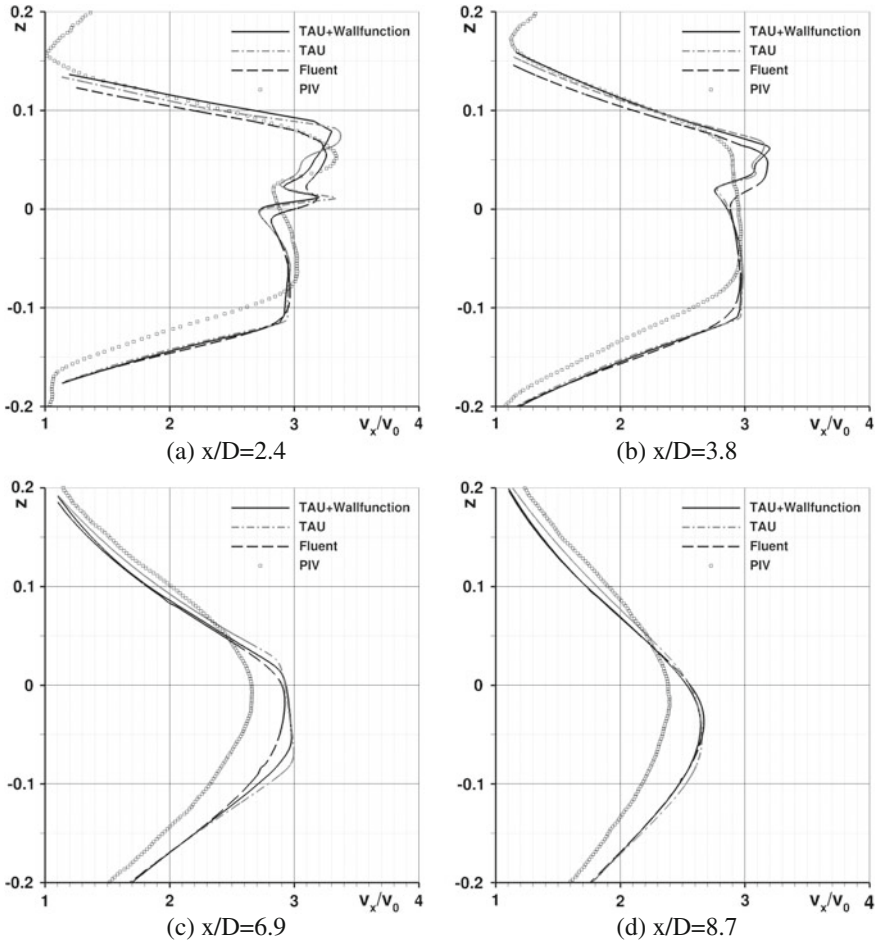
Fig. 11.4 Isolated VITAL configuration jet axial velocity development

determined in the PIV experiments. Generally it can be seen that all CFD results predict a slighly longer potential core length as well as a perturbation of the jet in the upper region by the pylon to larger downstream locations.

11.5.1.2 Turbulent Kinetic Energy

These plots again show a relatively close match between the numerical results and a generally well predicted development of this parameter in the engine jet. In contrast to the axial velocity, the absolute deviations between CFD and experimental data are larger. The impact of the pylon on the jet development in the first few axial positions is seen to lead to the largest differences between the CFD results (Fig. 11.5).

(a) x/D=2.4

(b) x/D=3.8

(c) x/D=6.9

(d) x/D=8.7
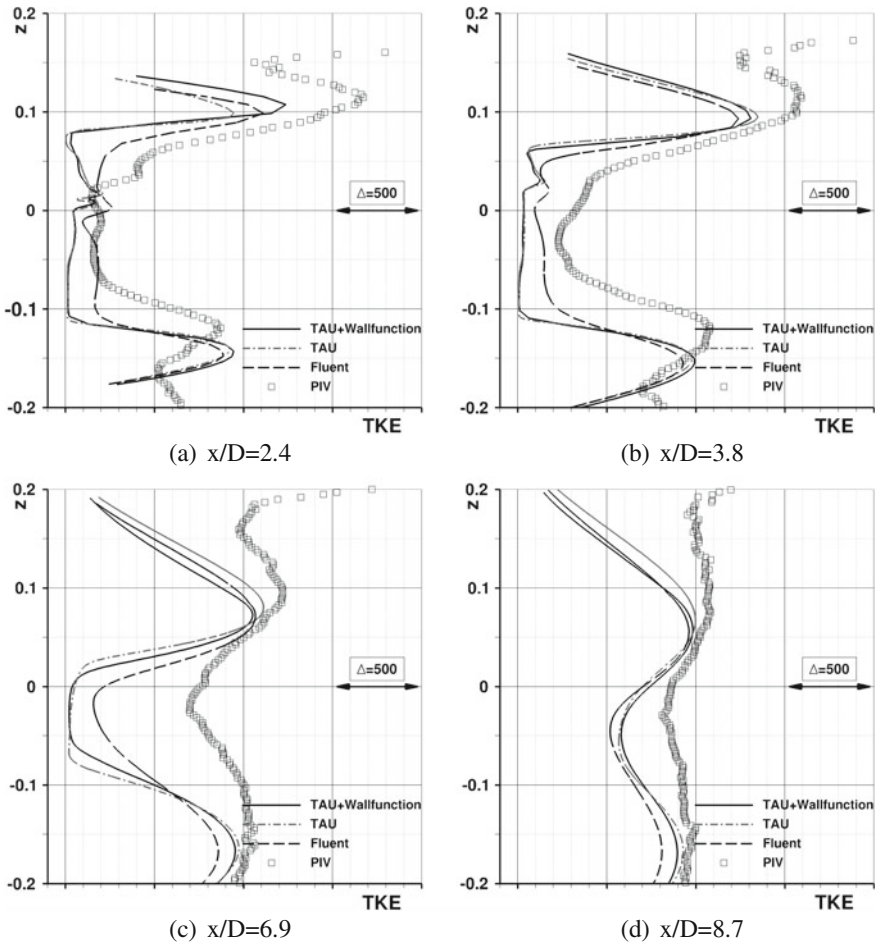
Fig. 11.5 Isolated VITAL configuration jet turbulent kinetic energy development

11.5.2 Installed Nozzle with Clean Wing Configuration

For the installed case with the clean wing, the TAU results will be compared to the
Fluent as well as the PIV data.

11.5.2.1 Axial Velocity

Very much in agreement with the isolated case results, the velocity profiles across
all the axial positions indicate that all numerical results are in very close agreement
and also show a good prediction of the jet development as was determined in the PIV
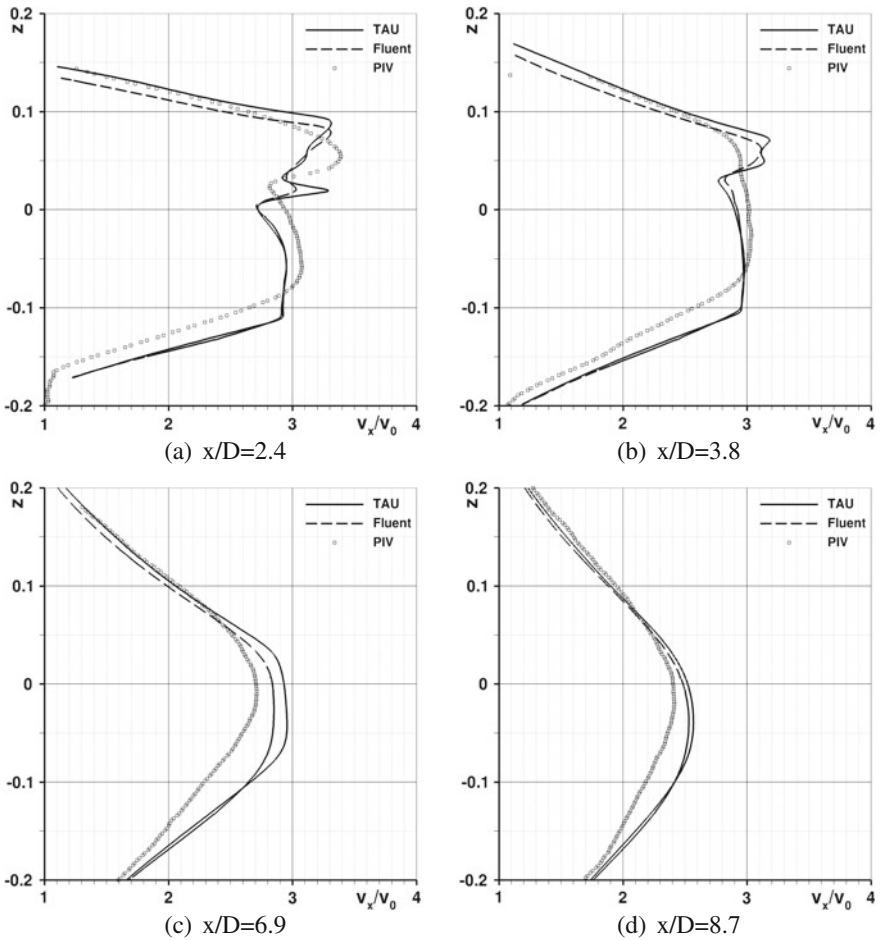
Fig. 11.6 Clean wing installed VITAL configuration jet axial velocity development

experiments. Again, all CFD results predict a slightly longer potential core length as well as a perturbation of the jet in the upper region by the pylon to larger downstream locations (Fig. 11.6).

11.5.2.2 Turbulent Kinetic Energy

The plots of the turbulent kinetic energy again show a relatively close match across the numerical results and a generally well predicted development of this parameter in the engine jet. In contrast to the previously discussed axial velocity data the absolute deviations between CFD and experimental data is somewhat more pro-

(a) x/D=2.4

(b) x/D=3.8

(c) x/D=6.9

(d) x/D=8.7
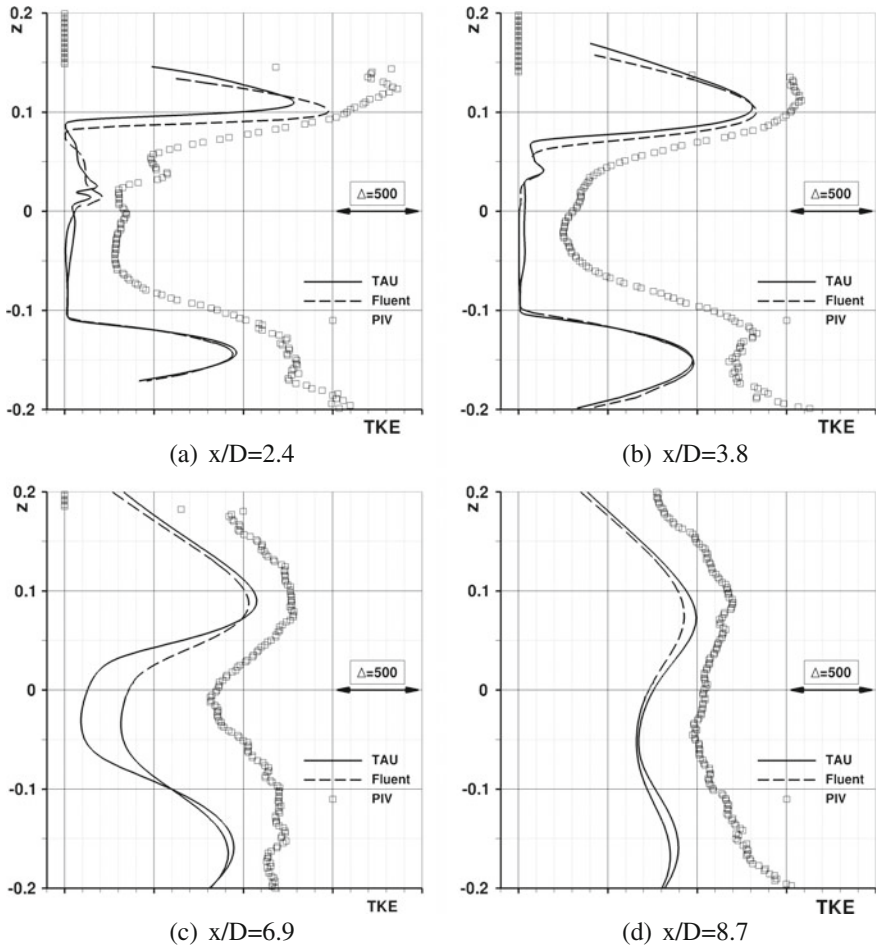
Fig. 11.7 Clean wing installed VITAL configuration jet turbulent kinetic energy development

nounced. Furthermore, the impact of the pylon on the jet development in the first few axial positions is also seen to lead to the largest differences between the various CFD results (Fig. 11.7).

11.6 Application of the Simulation Approach to Complex Aircraft Cases

Two test cases were used to further test the TAU simulation approach for the simulation of complex aircraft configurations with jet-flap interactions. As shown in Fig. 11.8, the basis was the so-called SPWD-S33 configuration (Special Purpose

(a) S33 clean wing configuration   (b) S33 with 16° flap deflection
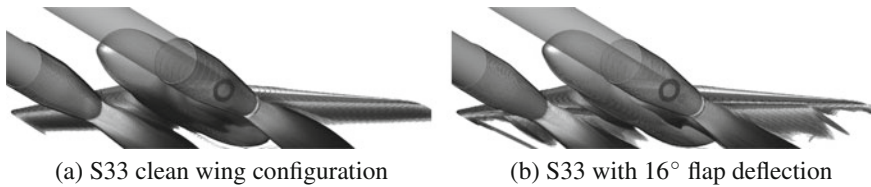
Fig. 11.8 Symphony S33 configuration

Wing Design), which was also wind tunnel tested in the frame of another research project. Both a clean wing case as well as an aircraft with a 16° flap deflection were investigated.

The SPWD wing was a special purpose design to be operated in a wind-tunnel test at zero degree angle of incidence to maintain the orientation of the nozzle and the wing and to avoid significant vortex shedding at the wing root and tip while still generating significant lift to enable a more representative jet-flap interaction. The lower wing surface design of a reference wing was maintained to ensure a representative jet wing interaction and noise reflection scenario could be achieved. These constraints resulted in a complex pressure distribution at the leading edge with the stagnation point moving onto the upper wing surface.

The complexity of these test cases is much greater than was found in the VITAL cases, which featured a straight, unswept infinite wing section only.

Some simplifications versus the wind tunnel test were made, the most notable of which is the simplification to a symmetric aircraft with a symmetry plane along the fuselage centerline, i.e. the fact that the model was sting mounted with a strut attaching to the wing root on one side of the fuselage was not accounted for. Furthermore, a full freestream flow was specified at a farfield boundary, which therefore does not model the limited diameter wind tunnel nozzle flow, which had the tunnel jets shear layers impinging on the wing tip and fuselage of the aircraft. The test point under study, selected from the experimental test campaign, is for a representative high-thrust take-off case.

11.6.1 Mesh Generation

As was the case for the VITAL cases studied in the frame of this work, fully block structured meshes were also used in the analysis of the S33 full aircraft configuration. This was to ensure the to-date established best practice of having smoothly distributed hexahedral elements to resolve the jet shear layers is adhered to also for these studies. The meshes were generated using ICEM Hexa and were created with a mesh density sufficiently fine in the near wall regions to properly resolve the boundary layers. The resulting mesh for the clean wing S33 configuration featured $62.1e6$ and that for the S33 with the flap deflection $64.5e6$ nodes.

11.6.2 Results and Validation

Based on the investigations performed for the VITAL test cases discussed in the previous sections, a simulation strategy for the DLR TAU-Codes application to cases with jet-flap interaction was devised, which ensured good quality RANS results as seen in comparison with other reference simulations as well as wind tunnel test data. Furthermore, this strategy also enabled the use of the obtained flowfield solutions in a subsequent aeroacoustic analysis. This approach was applied to the S33 configuration test cases and was based on the following essential components:

1. Smooth block-structured meshes for the best possible resolution of jet shear layers
2. A 2. order upwind scheme for the spatial discretization to avoid unphysical total temperature hot spots at jet shear layer boundaries
3. The Menter BSL 2-equation turbulence model to enable production of data suitable for the aeroacoustic analysis while also avoiding shear layer instabilities in the RANS simulations

For the validation of the CFD results some pressure distribution data from the wind tunnel test was available for an inboard and an outboard wing section, both at a spanwise distance of 0.09285 m from the pylon location. Figure 11.9 shows a comparison of the numerical and experimental data for these wing sections. The unconventional pressure distribution at the wing leading edge is a results of the special purpose design outlined above. With the exception of the most downstream pressure tap a generally satisfactory agreement between CFD and the wind tunnel test data can be seen - in particular for the inboard section. The larger deviations evident for the outboard section are most likely attributable to the fact that while the simulations assumed the aircraft fully immersed in the $Ma = 0.15$ freestream flow field, the wind tunnel test had a finite tunnel jet, with a likely shear layer impingement on the wing

(a) S33 clean wing configuration   (b) S33 with 16° flap deflection
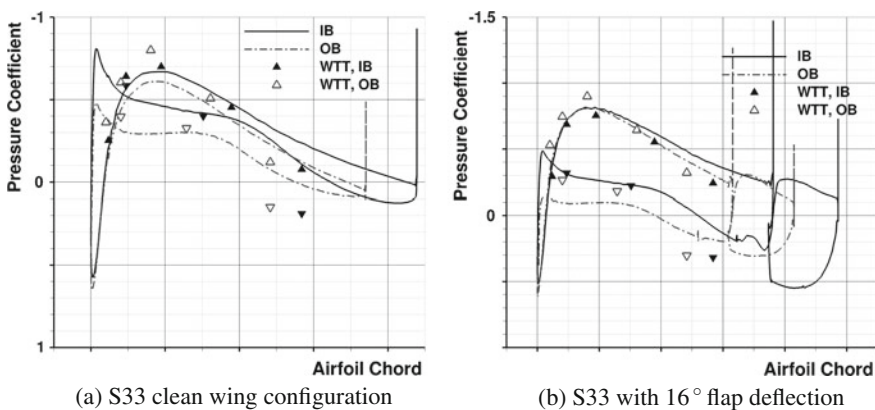
Fig. 11.9 Computed and measured pressure distributions on special purpose designed wing at sections 0.09285 m in- and outboard of the pylon

tip. Thus differences in particular in the outboard wing regions have to be expected. The pressure distributions show the expected increase in wing circulation at constant angle of attack brought about by the flap deflection in the lower pressure levels on the suction side of the wing.

11.7   Summary and Conclusion

In the frame of a comprehensive parameter study the DLR TAU-Code was validated and demonstrated toward its' applicability to the simulation of complex aircraft configurations characterized by strong jet-flap interactions with the added aim of being able to use the RANS results in a subsequent aeroacoustic analysis. Based on the VITAL BPR9 test case a best practice approach to these simulations for both isolated as well as installed configurations was developed, which was in line with the existing reference results utilizing the Fluent CFD-solver.

The investigations showed that the engine jet can be well-predicted using both a full mesh resolution of the boundary layers as well as a wall function model. The most robust turbulence model available in the TAU Code for these applications was found to be the Menter Baseline model. This avoided the occurence of jet shear layer instabilities often encountered with the SST model, while also providing the flowfield data required for the aeroacoustic analysis. TAU was shown to be sensitive to the smoothness of the block-structured meshes that were employed, and requires a gradual distribution in cell volume growth across block boundaries. Spatial discretization was best done using a 2. order upwind scheme, which avoided the occurrence of some unphysical total temperature hot spots at the jet shear layers very often found when using central dissipation schemes.

In future projects and collaborations between DLR and Rolls-Royce the most pressing need is to investigate the usability of hex-dominant unstructured meshes in these types of studies. Through the appropriate use of hexahedral elements, in particular for the resolution of the engine jets, it is hoped that a comparable solution quality can be achieved while also greatly easing the mesh generation effort for complex configurations.

References

1. T. Gerhold, Overview of the hybrid RANS code TAU, in *Megaflow - Numerical Flow Simulation for Aircraft Design*, ed. by N. Kroll (Springer, Berlin, 2005), pp. 81–92
2. A. Jameson, W. Schmidt, E. Turkel, Numerical simulation of the Euler equations by finite volume methods using Runge Kutta time stepping schemes, in *AIAA-81-1259* (1981)

3. F. Menter, Zonal two equation k-ω turbulence models for aerodynamic flows, in *AIAA 93-2906* (1993)
4. F. Menter, Two-equation Eddy-viscosity turbulence models for engineering applications. AIAA J. **32**, 1598–1605 (1994)
5. A. Schwoeppe, The DLR flow solver TAU - status and recent algorithmic developments, *AIAA 2014-0080* (2014)

Chapter 12
Application of Reynolds-Stress-Models on Free Shear Layers

Tim Landa, René-Daniel Cécora and Rolf Radespiel

Abstract This contribution presents the application of the JHh-v2 and JHh-v3 Reynolds-Stress-Model on different test cases with free shear layers. Based on a two-dimensional mixing layer, the need for improvement of the JHh-v2 turbulence model for free shear layers is worked out. An additional sink term within the length-scale equation is implemented and calibrated, resulting in the JHh-v3 model. Simulations of practically relevant test cases with free shear layers are performed using the JHh-v2 and JHh-v3 turbulence models. For comparison, experimental data and results of simulations with the Menter-SST eddy-viscosity model are shown.

12.1 Introduction

Numerical simulations are an important tool for the aerodynamic design process of an aircraft and its components. Through the increasing computational performance during the last decades, it is nowadays possible to simulate complex three-dimensional flows. Nevertheless, still the Direct Numerical Simulation (DNS), where all flow features are resolved by employing the fundamental equations of motion, is too expensive for such flows. For many practically relevant flows it is sufficient to capture the statistical influence of turbulence. Hence, solving the Reynolds-Averaged Navier-Stokes (RANS) equations is a good compromise between accuracy and computational costs. The influence of turbulence on the mean flow within RANS

T. Landa (✉) · R.-D. Cécora · R. Radespiel
Institut für Strömungsmechanik, TU Braunschweig, Hermann-Blenk-Str. 37, 38108 Braunschweig, Germany
e-mail: t.landa@tu-braunschweig.de

R. Radespiel
e-mail: r.radespiel@tu-braunschweig.de

simulation is captured by modeling the Reynolds-stress tensor. The applied turbulence model represents a first order effect on the quality of the simulation.

For industrial applications and practically relevant test cases, so-called eddy-viscosity models (e.g. [1, 2]) are commonly used. These models follow the Boussinesq hypothesis, where the Reynolds stresses are related to the gradients of the velocity components and an eddy viscosity, which is provided by the applied turbulence model. Eddy-viscosity models are quite robust and show accurate results for many applications. Nevertheless, the simplification within the calculation of the Reynolds stresses has drawbacks for the simulation of complex flows (e.g. free shear layers, vortices), where some relevant effects of the turbulence are not accurately captured. Another approach to calculate the Reynolds stresses is to derive exact transport equations from the momentum equations. Closure of the set of equations is again obtained by modelling some terms of the exact transport equations. Turbulence models following this approach are called Second Moment Closure (SMC) models or Reynolds-Stress-Models (RSM). Since exact transport equations are used to determine the Reynolds stresses, these models contain a physically more realistic description of turbulence. Hence, Reynolds-Stress-Models offer potential for complex flows.

Recently, Cécora et al. [3] presented the JHh-v2 turbulence model, which belongs to the class of Reynolds-Stress-Models. Simulations with the JHh-v2 model show promising results for practically relevant aeronautical test cases. Nevertheless, the JHh-v2 model underestimates the development of turbulence in shear layers, which have an inflection point in the velocity profile. This mainly affects free shear layers, which occur for example at backward-facing steps or at jet-like flows behind nozzles. For this reason, an additional sink term was implemented and calibrated by Cécora et al. [4] to compensate this shortcoming. This approach was already successfully tested by Maduta and Jakirlić [5, 6] for a similar Reynolds-Stress-Model. The extended model with the additional sink term is named as JHh-v3 model.

Within this contribution an overview of the JHh-v2 model and the extension to the JHh-v3 model is given. The paper focusses on the length-scale equation, which is the main difference between the models. Both turbulence models are applied on different test cases with free shear layers using the DLR-TAU code as flow solver [7]. A comparison is made with experimental data and the Menter-SST two-equation eddy viscosity model.

12.2 Reynolds-Stress Turbulence Modeling

Reynolds-Stress-Models are based on exact transport equations of the Reynolds stresses. These equations are derived from the momentum equations, reading as follows [8].

$$\frac{\partial \left(\overline{\rho} \widetilde{R}_{ij}\right)}{\partial t} + \frac{\partial}{\partial x_k} \left(\overline{\rho} \widetilde{R}_{ij} \widetilde{U}_k\right) = \overline{\rho} P_{ij} + \overline{\rho} \Pi_{ij} - \overline{\rho} \varepsilon_{ij} + \overline{\rho} D_{ij} + \overline{\rho} M_{ij} \qquad (12.1)$$

The terms within the transport equations of the Reynolds stresses correspond to the physical behavior of turbulence. The production of turbulence is described by the term $(\overline{\rho}P_{ij})$, which can be determined exactly from the equation system. In contrast, the other terms of the right hand side have to be modeled by a turbulence model. These terms are the pressure-strain correlation $(\overline{\rho}\Pi_{ij})$, which represents a redistribution of kinetic turbulence energy to the different directions, the dissipation term $(\overline{\rho}\varepsilon_{ij})$ and the diffusion term $(\overline{\rho}D_{ij})$. The last term $(\overline{\rho}M_{ij})$ describes the effects of compressibility on the transport of the Reynolds stresses. These effects are neglectible for most flow problems including the applications presented within this contribution. For modeling the redistribution, dissipation and diffusion, different Reynolds-Stress-Models exist. Furthermore, most turbulence models contain an additional transport equation for the length scale, which is important to determine the dissipation of the Reynolds stresses. For the simulations presented herein, the JHh-v2 and JHh-v3 models are used, which mainly differ in the formulation of the length-scale equation. These models are briefly described in the following part. As flow solver, the DLR-TAU code has been used, which is a finite-volume solver for the RANS equations on hybrid unstructured grids with second order accuracy.

12.2.1   JHh-v2 Model

The JHh-v2 turbulence model is based on the JHh (Jakirlić Hanjalić homogeneous) Reynolds-Stress-Model, which has been developed by Jakirlić and Hanjalić [9]. The family of JHh turbulence models uses the homogeneous part ε^h of the dissipation rate as length-scale variable. Probst and Radespiel [10] implemented the JHh model into the DLR-TAU code and extended the original length-scale equation of Jakirlić and Hanjalić by two additional source terms, resulting in the JHh-v1 turbulence model. This model shows good results for various subsonic applications. However, shortcomings within simulations of transonic flows with an adverse pressure gradient are observed. For this reason, a recalibration of the JHh-v1 model has been performed by Cécora et al. [3]. This model version is referred to as JHh-v2. An essential part of this model is the transport equation of the length-scale equation, which reads as follows.

$$\frac{D\overline{\rho}\varepsilon^h_{(JHh-v2)}}{Dt} = -\hat{C}_{\varepsilon 1}\frac{\overline{\rho}\varepsilon^h}{\tilde{k}}\widetilde{R}_{ij}\frac{\partial \widetilde{U}_i}{\partial x_j} - \hat{C}_{\varepsilon 2}f_\varepsilon\frac{\overline{\rho}\varepsilon^h\check{\varepsilon}^h}{\tilde{k}} + \hat{C}_{\varepsilon 3}\overline{\mu}\frac{\tilde{k}}{\varepsilon^h}\widetilde{R}_{jk}\frac{\partial^2 \widetilde{U}_i}{\partial x_j \partial x_l}\frac{\partial^2 \widetilde{U}_i}{\partial x_k \partial x_l}$$
$$+ \frac{\partial}{\partial x_k}\left[\left(\frac{1}{2}\overline{\mu}\delta_{kl} + \hat{C}_\varepsilon\frac{\overline{\rho}\tilde{k}}{\varepsilon^h}\widetilde{R}_{kl}\right)\frac{\partial \varepsilon^h}{\partial x_l}\right] + \overline{\rho}S_l + \overline{\rho}S_{\varepsilon 4} \qquad (12.2)$$
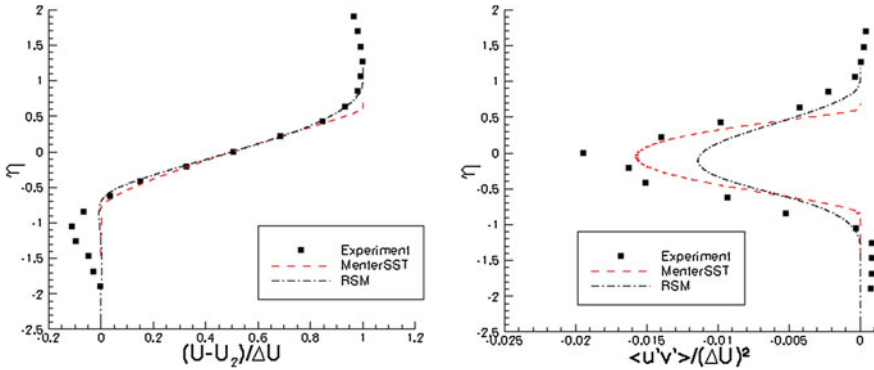
Fig. 12.1 Two-dimensional mixing layer, Case 1: velocity profile (left) and profile of turbulent shear stress (right)

The different functions and the constants within the length-scale equation as well as the modeling of the redistribution, dissipation and diffusion terms of the transport equation of the Reynolds stresses are described in detail in [3]. The JHh-v2 model has been successfully applied to different subsonic and transonic aeronautical problems. The test cases include an oblique shock/boundary-layer interaction, subsonic and transonic airfoil cases including stall conditions, a swept wing at transonic flow conditions and a wingtip vortex at a NACA 0012 half wing. For this test cases, the JHh-v2 turbulence model showed improved results compared to common eddy viscosity models (SAO, Menter-SST). Nevertheless, these test cases include mainly wall-bounded flows. A weakness of the JHh-v2 model becomes apparent in free shear flows. Figure 12.1 (Case 1) and Fig. 12.2 (Case 4) shows results of simulations of two-dimensional mixing layers with the Menter-SST and the JHh-v2 (RSM) model. Case 1 and Case 4 differ with respect to the convective Mach number ($M_c = \Delta U/2a$, Case 1: $M_c = 0.20$, Case 4: $M_c = 0.86$) and the relative difference $(U_1 - U_2)/U_2$ (Case 1: $(U_1 - U_2)/U_2 = 0.275$, Case 4: $(U_1 - U_2)/U_2 = 5.16$). The experimental data come from Goebel and Dutton [11]. Further details of these test cases can be found in [12].

For the lower convective Mach number (Case 1, Fig. 12.1) the Menter-SST model predicts higher absolute values of the turbulent shear stresses in the central part of the mixing layer corresponding to experimental data. In contrast, the JHh-v2 model shows significantly lower absolute values. Nevertheless, in the outer part of the mixing layer, the Menter-SST model underpredicts the turbulent shear stresses, while the JHh-v2 model is in good agreement with the experimental data. Despite the deviations of the turbulent shear stresses, the velocity profile is predicted similar with both turbulence models. However, the experimental data show remains of the boundary layers of the upstream flow ($(U - U_2)/\Delta U < 0$), which is not captured by
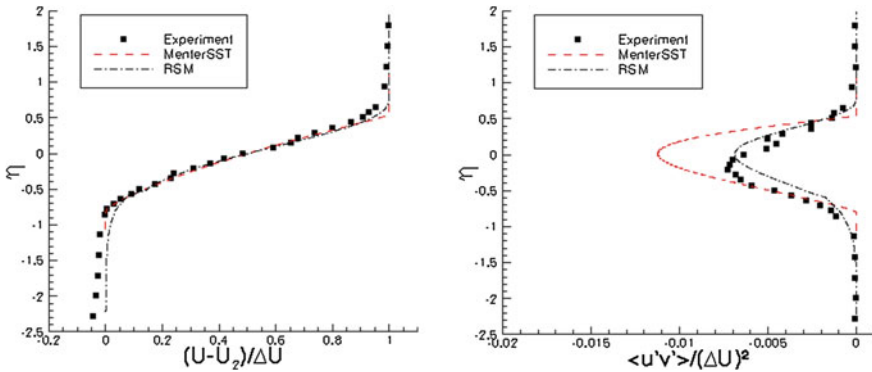
Fig. 12.2 Two-dimensional mixing layer, Case 4: profiles of velocity (left) and turbulent shear stress (right)

Table 12.1 Expansion rate (simulation and experiment) of the two-dimensional mixing layer

db/dx	Case 1	Case 4
Experiment [11]	0.020	0.050
SST	0.021	0.090
JHh-v2	0.016	0.071

the simulations. For a higher convective Mach number (Case 4, Fig. 12.2), a different behavior is observed. Here, the JHh-v2 model predicts turbulent shear stresses, which are in good agreement with experimental data. The Menter-SST model overpredicts the values by about 50%. Again, the velocity profile is predicted similar with both turbulence models.

The mismatch of the shear stresses also influences the expansion rate (db/dx) of the mixing layer which is shown in Table 12.1 for the experiments and simulations.

Corresponding to the underpredicted turbulent shear stresses, the expansion rate is predicted too low with the JHh-v2 model for Case 1. The Menter-SST model shows an expansion rate, which is in good agreement with the experiment. In contrast, for Case 4 both turbulence models overpredict the expansion rate. Particularly, the Menter-SST model shows too high growth of the shear layer.

Overall, the simulations of the mixing layers exhibit shortcomings of both turbulence models. Both models do not accurately capture the turbulent shear stresses for the different test cases. For this reason, an extension for the JHh-v2 model for free shear flows has been implemented and tested.

12.2.2   Extension for Free Shear Flows

An approach to remedy the shortcomings of the JHh-v2 model is to modify the transport equation of the length scale. Therefore, an additional sink term $(-\overline{\rho}P_{SAS})$ has been implemented and calibrated by Cécora et al. [4]. The modified version of the turbulence model is named JHh-v3 model using the following length-scale equation.

$$\frac{D\overline{\rho}\varepsilon^h_{(JHh-v3)}}{Dt} = \frac{D\overline{\rho}\varepsilon^h_{(JHh-v2)}}{Dt} - \overline{\rho}P_{SAS} \tag{12.3}$$

The origin of the additional term is found in the Scale Adaptive Simulation (SAS) concept of Menter and Egorov [13, 14]. Within this concept, the additional term is used as a source term (inverse sign) to locally reduce modeled turbulence to resolve instabilities. Using the term as a sink term, the dissipation is locally reduced in free shear flows with strongly curved velocity profiles. Originally, the SAS concept was developed for two-equation eddy viscosity models. Maduta [6] applied the concept to a RSM model with a ω^h-based length-scale equation. For the JHh-v3 model, which uses an ε^h-based formulation, the additional sink term reads as follows:

$$P_{SAS} = C_{SAS,1} \max\left[P_{SAS,1} - P_{SAS,2}, 0\right] \tag{12.4}$$

$$P_{SAS,1} = 1.755\kappa k S^2 \left(\frac{L}{L_{vk}}\right)^{\frac{1}{2}} \tag{12.5}$$

$$P_{SAS,2} = 3\max\left(C_{SAS,2}\frac{(\nabla\varepsilon^h)^2 k^2 + (\nabla k)^2(\varepsilon^h)^2 - 2k\varepsilon^h\nabla\varepsilon^h\nabla k}{(\varepsilon^h)^2}, (\nabla k)^2\right) \tag{12.6}$$

The turbulent length scale L and the 3D generalization of the classical boundary-layer definition of the von Karman length scale L_{vk} are defined as $L = k^{3/2}/\varepsilon^h$ and $L_{vk} = \kappa S/|\nabla^2 U|$. S is the invariant of the strain-rate tensor.

12.2.3   Calibration of the Additional Sink-Term

The calibration of the constants of the JHh-v3 turbulence model was based on a backward facing step and a zero pressure gradient flat plate [4]. A comparison between the turbulence models and experiments for both test cases is shown in Fig. 12.3.

The simulation of the zero pressure gradient flat plate indicates, that all models predict simple wall bounded flows similarly well. In contrast, the simulation of the backward facing step is improved. The skin friction distribution and the separation length within the free shear layer behind the step is predicted significantly better with the JHh-v3 model. Details of the calibration can be found in [4, 12].
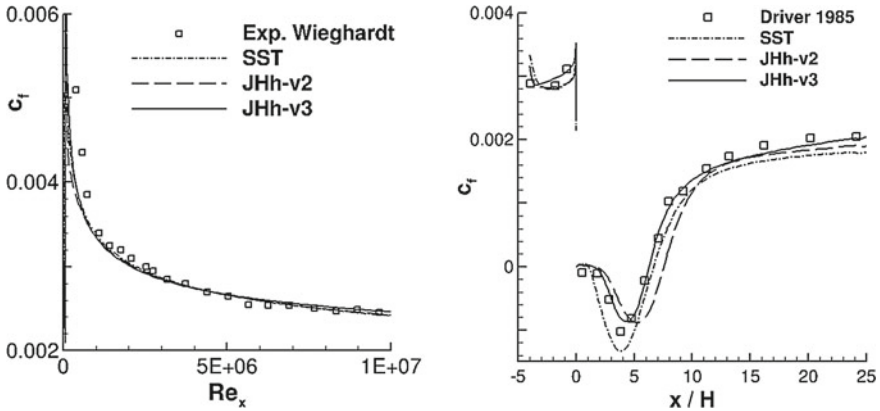
Fig. 12.3 Skin friction distribution of a zero pressure gradient flat plate (left) and a backward facing step (right)

12.3 Application on Test Cases

The JHh-v2 and the JHh-v3 model have been applied on different test cases of aeronautical flows. Within this contribution the main objective is to evaluate the performance of the turbulence models for free shear layers. Hence, simulations of three practically relevant test cases with free shear layers are presented.

12.3.1 Round Single-Stream Jet

The first test case is a single-stream jet emerging from a round nozzle. The geometry of the nozzle and the experimental data for comparison come from [15]. The diameter of the nozzle is $D = 0.05$ m at the exit plane and the Mach number at this position is $M = 0.75$. For reasons of numerical stability, the outer flow in the simulations has a Mach number of $M = 0.01$, whereas the outer flow was at rest in the experiments. Downstream of the exit plane, a free shear layer develops. The computational grid consists of 9.1 million points in total. The computational domain includes the whole 360°-nozzle to avoid spurious effects of periodic or symmetry boundary conditions. Figure 12.4 exhibits some details of the computational grid.

The grid is a structured grid consisting of hexahedral cells. In the region of the jet core, the radial topology of the grid changes to a cartesian topology, which is illustrated in a slice at the nozzle exit plane (Fig. 12.4, right). This method prevents small cells and a singularity at the axis affecting the convergence of the simulation.

Initially, simulations assuming steady flow have been performed with the JHh-v2 and JHh-v3 model. Within these simulations, fluctuations within the shear layer directly behind the nozzle exit arise. Hence, convergence of the steady simulations is not achieved with both turbulence models. In contrast, the fluctuations disappear by
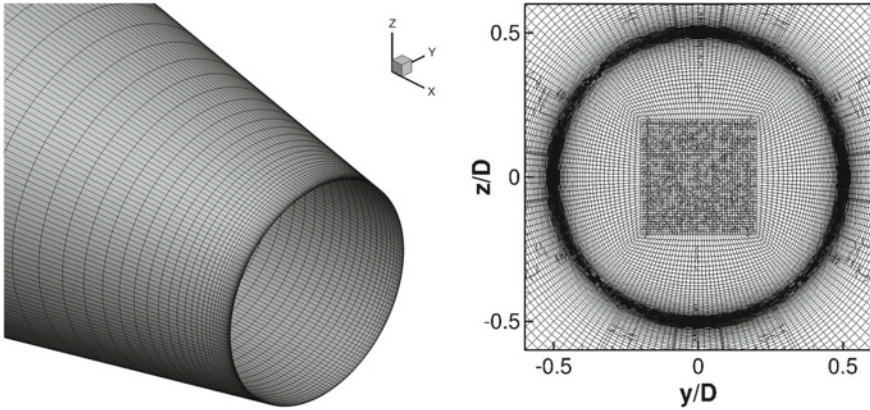
Fig. 12.4 Round single-stream jet. Surface grid on nozzle (left) and grid at the nozzle exit plane x/D = 0 (right)
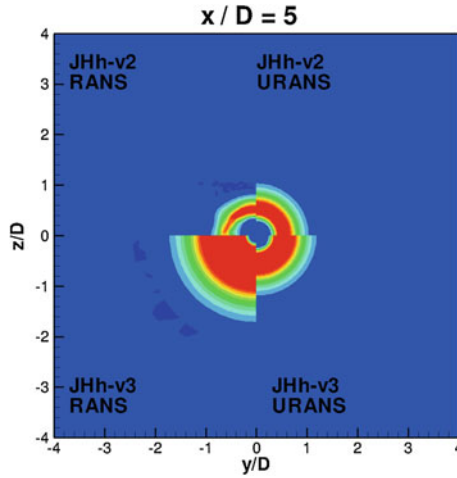
Fig. 12.5 Round single-stream jet. Radial distribution of turbulent kinetic energy (TKE) simulated with JHh-v2 (top) and JHh-v3 (bottom) turbulence models with a steady (RANS, left) and unsteady (URANS, right) solver

performing an unsteady (uRANS) simulation and a converged quasi-steady solution is reached. The influence of the turbulence model and the solver type on the distribution of the turbulent kinetic energy is illustrated in Figs. 12.5 (radial) and 12.6 (axial).

Figure 12.5 clearly shows, that the results of the unconverged steady simulations show significant differences compared to the converged unsteady simulations. Particularly, the steady JHh-v2 simulation does not even exhibit an axisymmetric behavior. In contrast, the converged unsteady simulation is smooth and uniform. Furthermore,
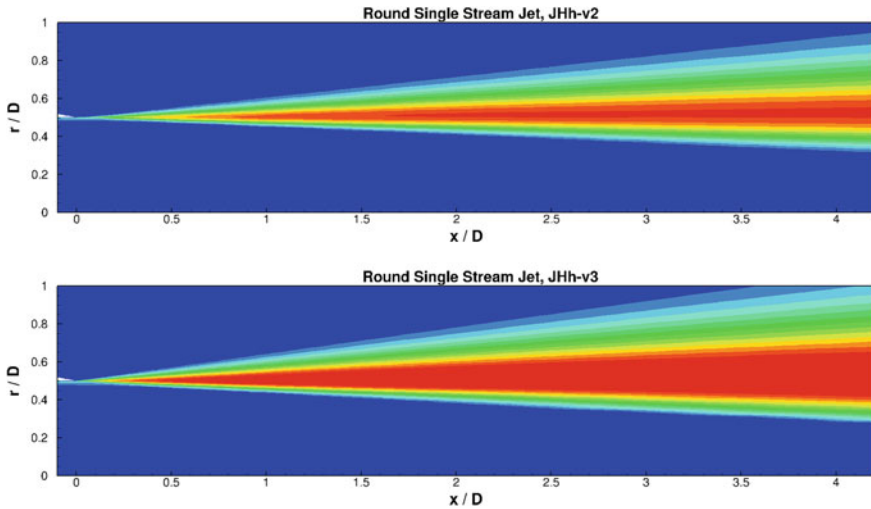
Fig. 12.6 Round single-stream jet. Axial distribution of turbulent kinetic energy (TKE) simulated with JHh-v2 (top) and JHh-v3 (bottom) turbulence models

the effect of the additional sink term becomes visible. As desired, the JHh-v3 model predicts an increased level of turbulence within the free shear layer. Again, this behavior is visible in the axial distribution of the turbulent kinetic energy (Fig. 12.6).

For a deeper insight, Fig. 12.7 shows the radial distributions of the velocity and the turbulent shear stresses for different streamwise positions. For comparison, experimental data and results of simulations with the Menter-SST model are included.

The JHh-v2 model clearly underpredicts the turbulent shear stresses. As a consequence, the shear layer downstream is thinner than observed within the experiments. The JHh-v3 model reveals an improved behavior concerning the shear stresses and velocity profiles. Nevertheless, the JHh-v3 model does not reach the distributions of the experiments or the Menter-SST model.

The axial velocity ratio of the jet along the jet axis (Fig. 12.8) again exhibits an improvement of the results of the JHh-v3 model.

The turbulence models predict a different length of the potential core, which is characterized by $U/U_j \approx 1$. This length is significantly overpredicted with the JHh-v2 model. In contrast, the Menter-SST and JHh-v3 model predict a similar length of the potential core. Furthermore, the rate of decrease of velocity in the core is predicted accurately with both JHh models. In contrast, the Menter-SST model exhibits a too rapid decrease of the core velocity downstream of the potential core.
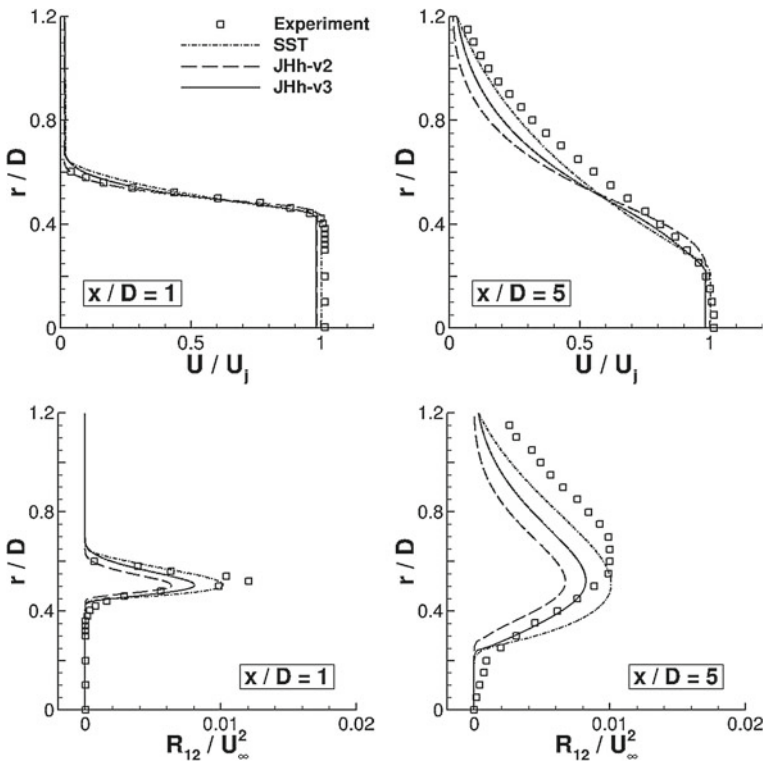
Fig. 12.7 Round single-stream jet. Profiles of velocity (top) and turbulent shear stress (bottom) at two streamwise positions [4]

12.3.2 BLBL

The second test case is an exit geometry of a turbofan engine. The flow contains a hot core jet at a Mach number of $M = 0.9$ and a cold bypass flow at $M = 0.8$. The mixed jet emerges from the nozzle, forming a free shear layer with the moving outer flow ($M = 0.24$). This configuration is named Baseline-Baseline (BLBL), resulting from the round geometry of the mixer between the core and the bypass jets and the round nozzle. The computational grid is a block-structured grid, which has been provided by DLR-Braunschweig. For this case, a 90°-segment of the geometry is considered and symmetry conditions are assumed for the side planes of the computational domain. Furthermore, a radial grid topology is used in the whole computational domain. For the BLBL configuration, again unsteady simulations were performed with the JHh-v2 and JHh-v3 model, since no convergence is reached with a steady solver. In contrast, the unsteady simulations converge to a steady flow field, similar to the round single-stream jet. Figure 12.9 shows the radial distribution of the turbulent kinetic energy downstream of the nozzle exit.
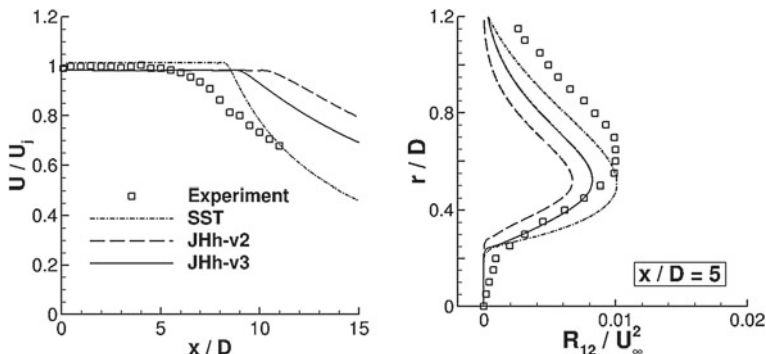
Fig. 12.8   Round Single-Stream Jet. Axial velocity ratio along the jet axis [4]
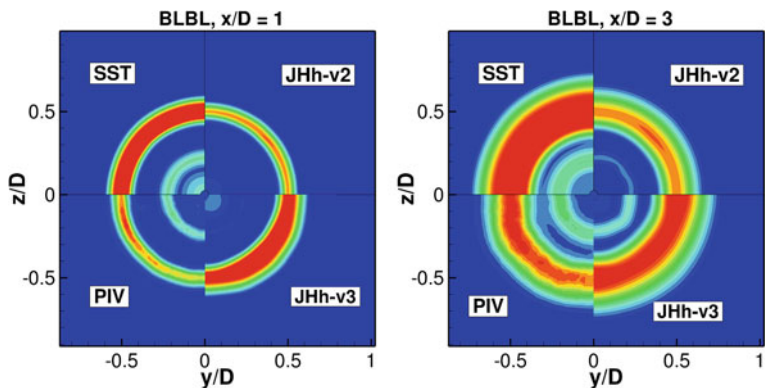
Fig. 12.9   BLBL-configuration. Radial distribution of turbulent kinetic energy (TKE) at two streamwise positions

At a streamwise position of $x/D = 1$ the JHh-v2 model predicts values of the turbulent kinetic energy, which are in good agreement with the PIV data in the mixing layer behind the nozzle exit. The Menter-SST model and the JHh-v3 model show significantly increased values at this position. Nevertheless, the PIV data reveals a region of increased turbulent kinetic energy in the shear layer of the core and bypass jets. This is only captured by the Menter-SST model at this position. Further downstream ($x/D = 0.3$), the turbulence is slightly underpredicted by the JHh-v2 model. In contrast, the JHh-v3 model slightly overestimates the values. Furthermore, the Menter-SST model shows the largest values of turbulent kinetic energy at this position, considerably larger compared to the experimental data. The turbulence in the shear layer of the core and bypass jets is captured by the Menter-SST and the JHh-v3 model, however, the Menter-SST model is closer to the experimental values. Further information about the development of the shear- layer become apparent
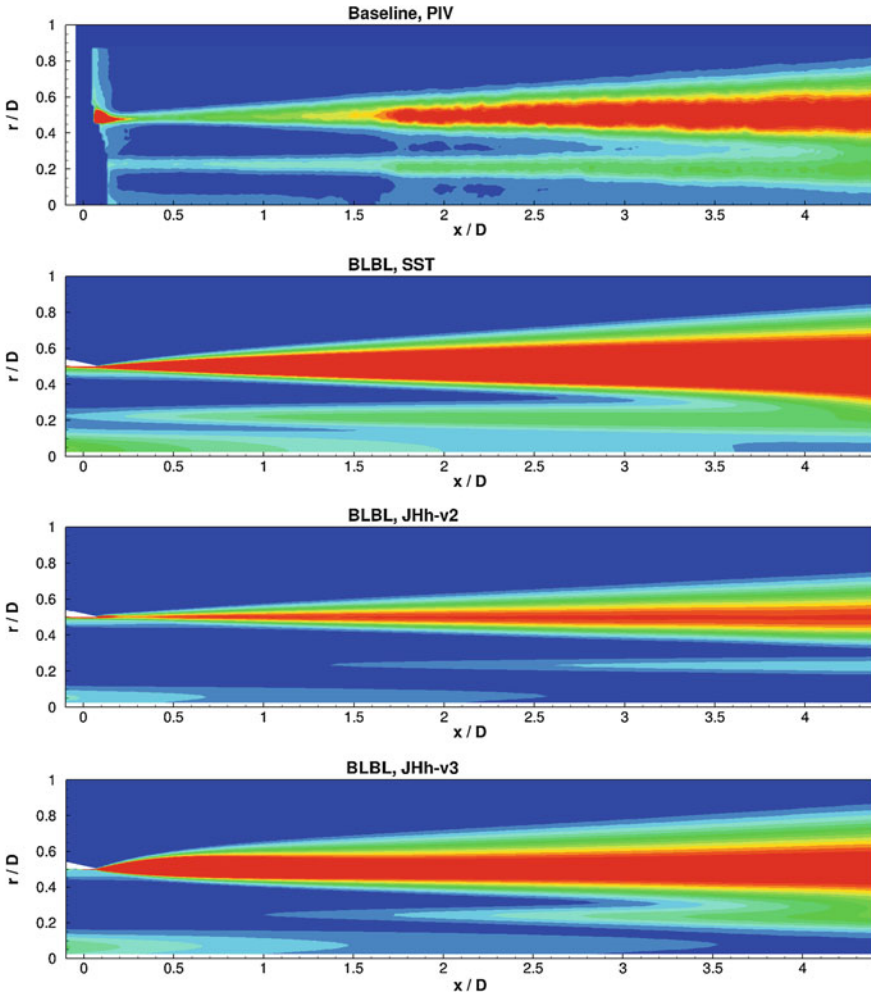
Fig. 12.10 BLBL-configuration. Axial distribution of turbulent kinetic energy (TKE) from PIV measurements and simulations

in the axial distribution of the turbulent kinetic energy of the BLBL configuration (Fig. 12.10).

In a region between $x/D = 1$ and $x/D = 2$, the JHh-v2 model predicts values of the turbulent kinetic energy, which are close to the experimental data. Nevertheless, the development of turbulence is underpredicted further downstream. In contrast, the Menter-SST model exhibits a rapid increase of turbulence at the trailing edge of the nozzle. As a consequence, the turbulent kinetic energy is overpredicted within the whole shear layer. The expansion is predicted similar compared to the PIV data. A different behavior is observed for the JHh-v3 model. In the region directly behind

the trailing edge of the nozzle ($x/D \leq 0.75$), a nonlinear growth of the shear layer becomes apparent. Furthermore, the values of the turbulent kinetic energy increase rapidly here. Further downstream ($x/D \geq 1.5$), turbulence is slightly overpredicted by the JHh-v3 model, which is already observed in the radial distribution at $x/D = 3$. In this region, the shear layer growth is lower and a linear behavior is observed, corresponding to the PIV data. Nevertheless, the locally large growth at the beginning of the shear layer is not shown by the PIV data or the other turbulence models. Furthermore, the simulation of the round single-stream jet with the JHh-v3 model also exhibits a linear growth of the shear layer. For this reason, the behavior close to the trailing edge is further investigated. Figure 12.11 displays the grid and the behavior of the additional sink term in detail for the BLBL configuration and the round single-stream jet.

It appears, that the grid close to the trailing edge (Fig. 12.11, top) of the nozzle strongly differs between both test cases. The resolution in radial and axial direction is significantly lower for the BLBL configuration. A closer examination of the additional sink term P_{SAS} of the JHh-v3 model (Fig. 12.11, middle) leads to the conclusion, that this term is underresolved on the given grid. The distribution of the sink term shows kinks and a volatile behavior corresponding to the individual cell interfaces. In contrast, the sink term at the round single-stream jet reveals a smooth behavior, resulting in a linear shear layer growth downstream. In particular, the second part of the sink term $P_{SAS,2}$ reflects the non-smooth behavior close to the trailing edge.

Altogether, for the BLBL configuration, the effect of an increased turbulence due to the additional sink term becomes apparent. Unfortunately, grid-dependencies significantly influence the development of the shear layer. Nevertheless, the potential of the JHh-v3 modelis indicated by the present results. Although the turbulence is overestimated due to the rapid increase behind the nozzle, the growth of the shear layer further downstream corresponds to experimental data. Here, the turbulence is underpredicted by the JHh-v2 model. Hence, the sink term could improve the prediction of the shear layer on a sufficiently fine grid.

12.3.3 BLSL3

The third test case is a modified version of the BLBL configuration. The mixer for the hot core jet and the bypass jet is identical (BL), whereas the geometry of the nozzle differs. The nozzle of BLSL3 configuration contains a crown of baffles (SL3), which will be called "castellations" in the following. The flow conditions remain unchanged compared to the BLBL configuration. The grid has been generated with Gridgen V15 (Pointwise, Inc.). Again, the computational domain is a 90°-segment of the geometry with symmetry conditions applied at the lateral boundaries. For the castellations, an increased number of grid points is used in circumferential direction to capture the complex flow behavior in this region. For the transition between increased and regular resolution, prism layers are used. The flow around the geometry is mainly resolved
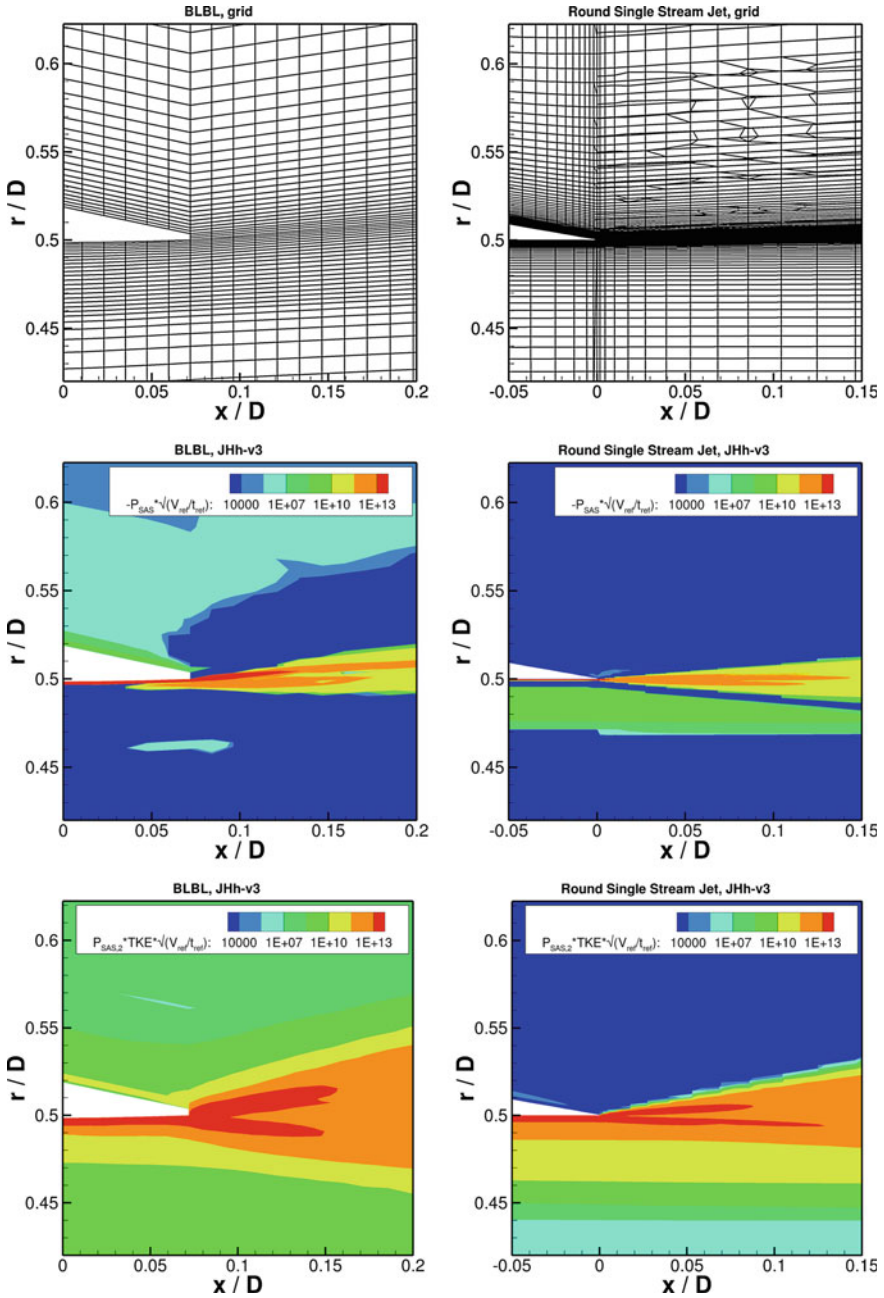
Fig. 12.11 Comparison between BLBL-configuration (left) and Round Single-Stream Jet (right). Top: local grid at nozzle exit, middle and bottom: distribution of additional source term P_{SAS} and the corresponding part $P_{SAS,2}$
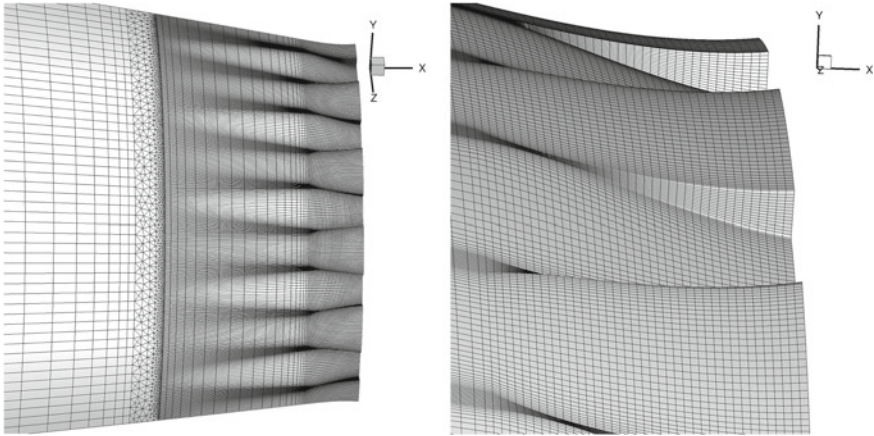
Fig. 12.12 BLSL3-configuration. Surface grid in the region of the castellations
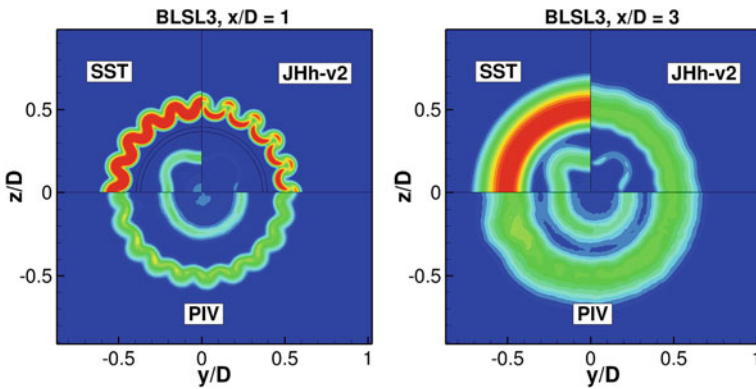
Fig. 12.13 BLSL3-configuration. Radial distribution of turbulent kinetic energy (TKE) at two streamwise positions

with hexahedral cells. Towards the farfield, an unstructured topology consisting of tetrahedrons is applied. Figure 12.12 shows details of the surface grid close to the castellations.

The investigation of the BLSL3 configuration includes simulations using the JHh-v2 model and the Menter-SST model as a reference. Due to lack of time and resources within the project, simulations with the JHh-v3 model have not been performed. The radial distribution of the turbulent kinetic energy at two streamwise positions is presented in Fig. 12.13.

The castellations cause a three-dimensional flow behavior, which is characterized by a wavy structure of the turbulent kinetic energy. Both turbulence models capture this behavior. At a streamwise position of $x/D = 1$, both turbulence model over-predict the kinetic energy of turbulence. However, the Menter-SST model shows
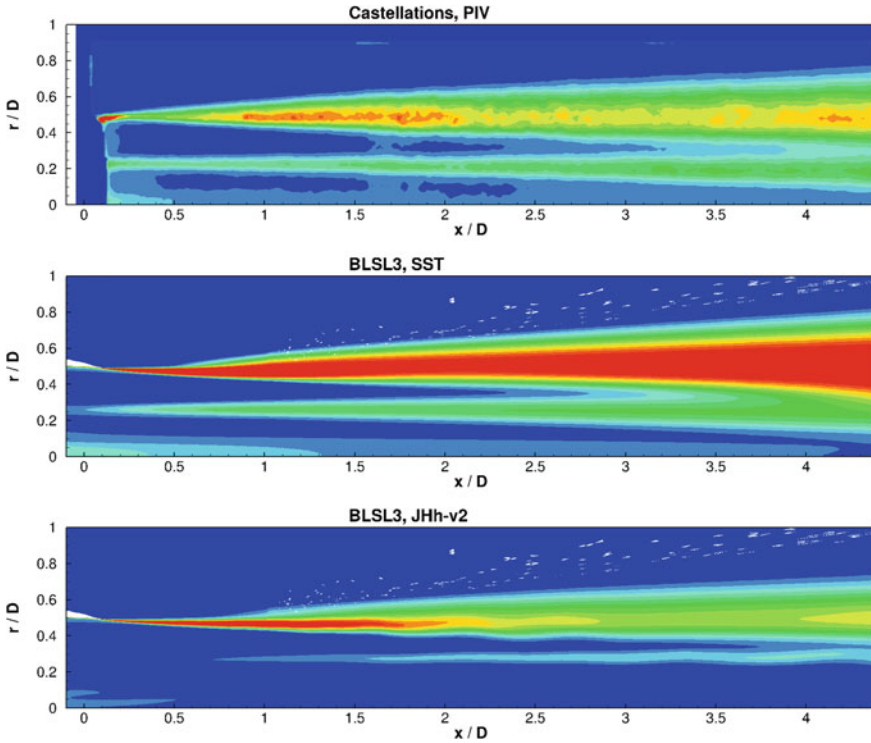
Fig. 12.14 BLSL3-configuration. Axial distribution of turbulent kinetic energy (TKE) from PIV measurements and simulations

strongly increased values compared to the JHh-v2 model. In contrast, the turbulence within the shear layer of the core jet and the bypass jet is accurately predicted by the Menter-SST model. Within the simulations, this shear layer is not axisymmetric, which can presumably be attributed to the influence of the boundary conditions. Further downstream ($x/D = 3$), the wavy structure of the shear layer behind the nozzle disappears and a nearly circular behavior is observed. At this position, the turbulence predicted with the JHh-v2 model corresponds to the PIV data. Again, the Menter-SST model significantly overestimates turbulence. Nevertheless, the values within inner shear layer are again accurately captured by the Menter-SST model. Similar findings arise from the axial distribution of the turbulent kinetic energy, displayed in Fig. 12.14.

For the BLSL3 configuration the free shear layer behind the nozzle is adequately predicted with the JHh-v2 model. In contrast, the inner shear layer between the core jet and the bypass jet is significantly underpredicted. For both shear layers, the Menter-SST model exhibits increased values of the turbulent kinetic energy. As a consequence, the turbulence within the inner shear layer corresponds to the experi-

mental data, whereas the values in the shear layer behind the nozzle are considerably overpredicted.

12.4 Conclusion

With this contribution, the application of two Reynolds-Stress-Models on different test cases containing free shear layers is shown. Shortcomings of the JHh-v2 model were observed in the simulations of two-dimensional mixing layers. For this reason, the model was extended by an additional sink term in the length scale. The application of the new JHh-v3 model on a round single-stream jet shows improved results compared to the JHh-v2 model. Due to the new sink term, turbulence in the shear layer is increased, in agreement with experimental data. In general, the same behavior is observed for an exit geometry of a turbofan engine (BLBL configuration). Here, the JHh-v3 model shows an extraordinary increased production of turbulence within the shear layer. This behavior can be attributed to an underresolved grid at this position. For a second geometry of a turbofan engine (BLSL3 configuration), the JHh-v2 model shows satisfying results, while the Menter-SST model overpredicts turbulence.

Overall, promising results are achieved for free shear layers with the presented Reynolds-Stress-Models. Particularly for the engine test cases, these models show reliable results compared to the Menter-SST eddy viscosity model. Nevertheless, especially the JHh-v3 model is sensitive regarding the computational grid. On underresolved grids, the additional sink term can adversely affect the solution. For this reason, further work is required to exploit the full potential of the JHh models for free shear layers.

References

1. F.R. Menter, Two-equation eddy-viscosity turbulence models for engineering applications. AIAA J. **32**(8), 1598–1605 (1994)
2. P.R. Spalart, S.R. Allmaras, A one-equation turbulence model for aerodynamic flows. La Recherche Aèrospatiale **1**, 5–21 (1994)
3. R.-D. Cécora, R. Radespiel, B. Eisfeld, A. Probst, Differential reynolds-stress modeling for aeronautics. AIAA J. **53**(3), 739–755 (2015)
4. R.-D. Cécora, R. Radespiel, S. Jakirlić, in *Modelling of Reynolds Stress Augmentation in Shear Layers with Strongly Curved Velocity Profiles*, ed. by B. Eisfeld, Springer Tracts in Mechanical

Engineering (Springer, Berlin, 2015). https://doi.org/10.1007/978-3-319-15639-2, ISBN 978-3-319-15638-5

5. S. Jakirlić, R. Maduta, On steady RANS modeling for improved prediction of wall-bounded separation. *52nd AIAA Aerospace Sciences Meeting*, (National Harbor, MD, USA, 2014)

6. R. Maduta, An eddy-resolving reynolds stress model for unsteady flow computations: development and application, Dissertation, TU Darmstadt (2014)

7. D. Schwamborn, A. Gardner, H. von Geyr, A. Krumbein, H. Lüdeke, A. Stürmer, Development of the TAU- code for aerospace applications. *50th NAL International Conference on Aerospace Science and Technology*, (Bangalore, India, 2008)

8. D.C. Wilcox, *Turbulence Modeling for CFD*, 2nd edn. (DCW Industries, La Cañada, CA, USA, 1998)

9. S. Jakirlić, K. Hanjalić, A new approach to modelling near-wall turbulence energy and stress dissipation. J. Fluid Mech. **459**, 139–166 (2002)

10. A. Probst, R. Radespiel, Implementation and extension of a near-wall Reynolds-Stress Model for application to aerodynamic flows on unstructured meshes. *46th AIAA Aerospace Sciences Meeting and Exhibit, AIAA Paper 2008-0770*, (Reno, NV, USA, 2008)

11. S.G. Geobel, J.C. Dutton, Experimental study of compressible turbulent mixing layers. AIAA J. **29**(4), 538–546 (1990)

12. R.-D. Cécora, Reynolds-Spannungsmodell der Turbulenz für Anwendungen der Flugzeugaerodynamik. Niedersächsisches Forschungszentrum für Luftfahrt, Forschungsbericht 2015-27, Braunschweig (2015)

13. F.R. Menter, Y. Egorov, A scale-adaptive simulation model using two-equation models. *AIAA-Paper 2005-1095*, (Reno, NV, USA, 2005)

14. F.R. Menter, Y. Egorov, The scale-adaptice simulation method for unsteady turbulent flow predictions. Part 1: theory and model description. Flow Turbul. Combust. **85**(1), 113–138 (2010)

15. N. Andersson, L.-E. Erkisson, L. Davidson, Large-eddy simulation of a mach 0.75 jet. *9th AIAA/CEAS Aeroacustics Conference*, (Hilton Head, SC, USA, 2003)

Chapter 13
Further Development of CAA Simulation for Isolated and Installed Nozzle Configurations

Andrej Neifeld and Roland Ewert

Abstract A hybrid RANS/CAA approach with stochastic source modeling is used in this work for noise prediction. Previously, this methodology has been successfully applied to isolated configurations of jet and airframe with different source models. For the prediction of jet noise, the source model as proposed by Tam and Auriault has been used for isolated nozzle configurations. A modeling approach for isolated airframe noise configurations is relying on the vorticity based Lamb vector source model. The CAA simulation of installed configurations with the combination of jet and airframe requires however consideration of both noise generation mechanisms simultaneously. Thus, a vorticity based 'Eddy Relaxation' source model has been recently proposed as further development of this methodology, which is expected to capture the installation effect.

13.1 CAA Methodology

For the numerical prediction of jet noise, the DLR's CAA code PIANO is applied in combination with the Fast Random Particle-Mesh (FRPM) method. The both codes are running simultaneously, whereat FRPM is generating the source fluctuations in space and time $(3 + 1 - D)$, which are instantly propagated in the CAA domain with PIANO as acoustical fluctuations. As input, the hybrid RANS/CAA approach requires a precomputed RANS solution, which delivers the mean-flow distribution for consideration of sound convection and refraction as well as statistical quantities of turbulence for the modelling of FRPM sources.

A. Neifeld (✉) · R. Ewert
Technical Acoustics Branch, Institute of Aerodynamics and Flow Technology,
Lilienthalplatz 7, Braunschweig, Germany
e-mail: andrej.neifeld@dlr.de

R. Ewert
e-mail: roland.ewert@dlr.de

The source model of Tam and Auriault (T and A) is used for the modeling of jet mixing noise sources as will be shown for dual-stream nozzles in Sects. 13.2 and 13.3. This source model describes accurately the fine-scale noise of jet shear-layer, but on the other hand is incapable to describe correctly the trailing edge noise. Since the T and A source model is considering only the curl-free part of fluctuating Lighthill tensor (refer to Wu et al. [1])

$$\nabla \cdot R' = \underbrace{\nabla \Phi}_{I} + \underbrace{\nabla \times \Psi}_{II} \tag{13.1}$$

i.e. the term (I), and is omitting the divergence-free part (II), it is not capturing the mechanisms, which is enforced by vorticity fluctuations.

The prediction of trailing edge or rather airframe noise has been performed previously with vorticity modeling in combination with the acoustic perturbation equations (APE) as proposed by Ewert and Schröder [2]. These governing equations are derived from the linearized Euler equations (LEE) which permit to prescribe the vorticity transporation entirely with the source term on the right hand side. However, this approach is not reproducing coherent jet flow dynamics as would be required for coherent jet noise generation.

On the other hand, the vorticity based source model in combination with the LEE would pose a problem, since the right hand side term is not able to dissipate the triggered vorticity fluctuations. In order to ensure an equilibrium between the production and dissipation of vortical fluctuations a sink mechanism is required, too. The annihilation of triggered vortical fluctuations is realizable with negative correlation of these structures, which would act as a vorticity sink. Such an approach is pursued with 'Eddy Relaxation' (ER) source model as proposed by Ewert et al. [3].

As an example, the Fig. 13.1 is showing a CAA computation with ER source model for an installed configuration with jet-flap interaction (Neifeld et al. [4, 5]).
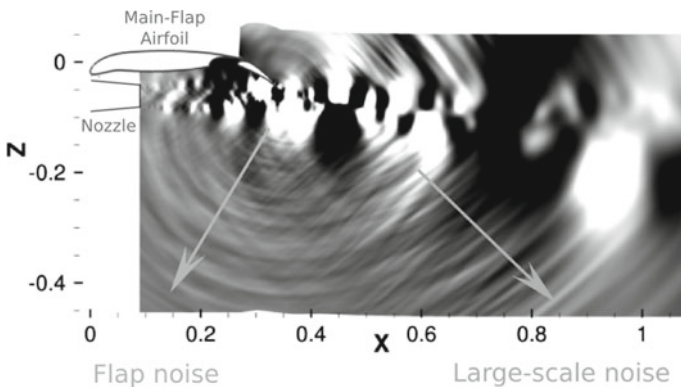
Fig. 13.1 Contour plot of sound pressure fluctuations for a configuration with jet-flap interaction computed with 'Eddy Relaxation' source model

The contribution of different noise generation mechanisms are found in this case. The coherent, fine-scale and trailing edge noise would be all necessary for a correct noise prediction of such installed configurations.

13.1.1   Eddy Relaxation Source Model

The Eddy Relaxation (ER) source model is applicable in combination with linear ($\varepsilon = 0$) or non-linear ($\varepsilon = 1$) Euler equations (13.3)–(13.5). Herein, the flow quantities are decomposed in mean (quantities with superscript 0) and perturbed (prime quantities) part, i.e.

$$\rho = \rho^0 + \rho', \ \ v_i = v_i^0 + v_i', \ \ p = p^0 + p'. \tag{13.2}$$

The full set of governing equations in perturbed formulation with the definition of (13.2) reads

$$\frac{\partial \rho'}{\partial t} + \left(v_i^0 + \varepsilon v_i'\right) \frac{\partial \rho'}{\partial x_i} + v_i' \frac{\partial \rho^0}{\partial x_i} + \left(\rho^0 + \varepsilon \rho'\right) \frac{\partial v_i'}{\partial x_i} + \rho' \frac{\partial v_i^0}{\partial x_i} = 0 \tag{13.3}$$

$$\frac{\partial v_i'}{\partial t} + \left(v_j^0 + \varepsilon v_j'\right) \frac{\partial v_i'}{\partial x_j} + v_j' \frac{\partial v_i^0}{\partial x_j} + \frac{1}{\rho^0 + \varepsilon \rho'} \frac{\partial p'}{\partial x_i} - \frac{\rho'}{(\rho^0 + \varepsilon \rho')\rho^0} \frac{\partial p^0}{\partial x_i} = Q_i \tag{13.4}$$

$$\frac{\partial p'}{\partial t} + \left(v_i^0 + \varepsilon v_i'\right) \frac{\partial p'}{\partial x_i} + v_i' \frac{\partial p^0}{\partial x_i} + \gamma \left(p^0 + \varepsilon p'\right) \frac{\partial v_i'}{\partial x_i} + \gamma p' \frac{\partial v_i^0}{\partial x_i} = 0 \tag{13.5}$$

with the ER source term

$$Q_i = -\varepsilon_{ijk} \frac{\partial}{\partial x_j} \left[\sigma \left(\Omega_k' - \Omega_k^{ref} \right) \right] \tag{13.6}$$

on the right hand side. The non-linear perturbation equations (NLDE) correspond to Navier–Stokes equations in primitive formulation, whereat the fluctuating molecular viscosity terms are neglected in the framework of these studies.

   The right hand side realizes a relaxation source, which adjusts the numerically resolved vorticity

$$\Omega_i' = \varepsilon_{ijk} \frac{\partial v_k'}{\partial x_j} \tag{13.7}$$

to the time-resolved target distribution of Ω_k^{ref}. The time-resolved reference vorticity is provided by FRPM. The relaxation parameter σ defines the coupling rate of

reference to realized vorticity or rather the inverse time constant of deviating regulation. This control of fluctuations is comparable to sponge-layer boundary condition, whereby in case of sponge layer there is no differentiation between curl and divergence. In case of ER source model, the curl of expression in brackets (13.6) selects only the vorticity fluctuations without any influence on acoustical modes.

The production/destruction problem of vorticity source with LEE as mentioned in previous section can be circumvented with the ER source model. The correlation of numerically resolved vorticity fluctuations with stochastically modeled allows to control with the relaxation parameter σ the production and destruction of vortices. This feature becomes evident if the relaxation term (13.6) is split in two parts as

$$Q_i = \underbrace{-\varepsilon_{ijk}\frac{\partial \sigma \Omega'_k}{\partial x_j}}_{I} + \underbrace{\varepsilon_{ijk}\frac{\partial \sigma \Omega_k^{ref}}{\partial x_j}}_{II} \qquad (13.8)$$

where the term (I) is a subgrid scale model (SGS) of Smagorinsky type and the term (II) the contribution of production, which is modeled stochastically. If the relaxation parameter σ is associated with the turbulent subgrid eddy viscosity ν_t, the first term corresponds to the vorticity based SGS 'model 3' of Dantinne et al. [6]. The scaling of production term is also expressed with the relaxation model parameter σ. The equality of both terms can be interpreted as conversion between production and dissipation of the local equilibrium hypothesis.

The ER source model is applicable in two different modes:

 (i) **Deterministic Mode** (deterministic source model): The relaxation parameter is defined as a high constant value, which couples strongly the reference vorticity distribution with the numerically resolved, i.e. the dynamics of vorticity fluctuations are prescribed directly; LEE are used as governing equations
 (ii) **Forced Mode**: The relaxation parameter is defined on the basis of eddy viscosity considering the grid resolution. The self-reinforced flow properties such as secondary instabilities are resolved on the CAA mesh, whereby the stochastic production term is acting as an active forcing term (active back-scattering model); NLDE are used as governing equations

In forced mode, the contribution of production from unresolved scales is transfered to the dynamics of resolved wave-numbers. As an advantage, the energy feeding from unresolved wave-number regime allows to perform scale resolving simulations with significantly coarser grid resolution. This kind of active back-scattering models have been investigated before for example by Leith [7], Schumann [8] and Zamansky et al. [9].

In this mode, the σ parameter is defined as turbulent eddy viscosity due to the FSM model of Speciale (Terzi et al. [10, 11]).

$$\nu_t = \nu_{t,RANS} \cdot f_\Delta \left(\frac{\Delta}{L_k} \right) \tag{13.9}$$

with

$$f_\Delta \left(\frac{\Delta}{L_k} \right) = \left[1 - \exp \left(-\beta \frac{\Delta}{L_k} \right) \right]^n \tag{13.10}$$

and

$$\beta = 0.009, \quad n = 1, \quad L_k = \nu^{3/4}/\varepsilon^{1/4}, \quad \Delta = \max\{\Delta_x, \Delta_y, \Delta_z\}$$

where Δ is the grid cell width, L_k the Kolmogorov length scale, β and n the calibration parameters. The Δ is prescribed with the applied grid resolution. The eddy viscosity and Kolmogorov length scale are obtainable from precomputed RANS solution.

13.1.2 Forcing Test and Benchmark Problem

The test computation of Fig. 13.2 demonstrates the feasibility of "Eddy Relaxation" source term to trigger and to steer precisely the vorticity fluctuations in numerically resolved domain as prescribed with the reference vorticity distribution. The computational domain is set up as a 3-D cuboid with a FRPM patch of the same size. The both plots on the left side are showing the first component of the vorticity vector as a cut through x–y plane. The plot (A) is representing the reference vorticity distribution as generated with the FRPM and plot (B) the corresponding realization with the governing equations. The comparison of both plots reveals an equivalent topology of the appearing structures, i.e. the resolved vorticity fluctuations are closely following the reference distribution.

In order to evaluate the behavior quantitatively, the transfer functions for all three components of vorticity vector are computed on the right side of Fig. 13.2. The ratio of reference to resolved magnitude is plotted in logarithmic scale over frequency. The desired transfer characteristics are found for all three components up to the cut-off frequency of grid resolution.

In a second computation, the ER source model is tested with a benchmark problem of "4th CAA Workshop on Benchmark Problems" [12], which is illustrated in Fig. 13.3. This case describes a hot parallel jet with a thin shear-layer and a constant velocity/temperature profile in axial direction. In vertical direction, the Mach number is $Ma = 0.756$ at the jet axis, which softly blends to $Ma = 0.0$ at approximately $y = 4$. The temperature is $T = 600\,\text{K}$ in the jet core and drops to the ambient temperature in the far-field. The acoustic waves are triggered with a periodic monopole at the coordinates origin with an angular frequency of $\omega = 76\,\text{rad/s}$.

Since the linearized Euler equations are used as governing equations, hydrodynamic instability is triggered by the shear-layer in combination with the periodic perturbations of the monopole. As observable in Fig. 13.3, a linearly growing hydrodynamic pressure fluctuations start to amplify directly after the perturbation source,
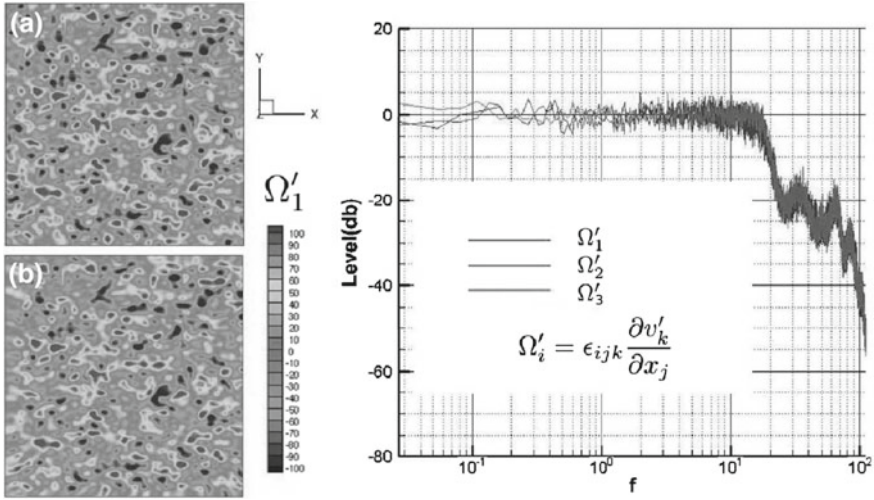
Fig. 13.2 Forcing of vorticity fluctuations with 'Eddy Relaxation' source model; (left) First component of **a** forced vorticity vector and **b** corresponding realization on the left hand side of governing equations; (right) Transfer function between forced and realized for the three components of vorticity vector

- Parallel hot jet with harmonic heat (energy) source
- $T_j=600K$
- $M_j=0.756$
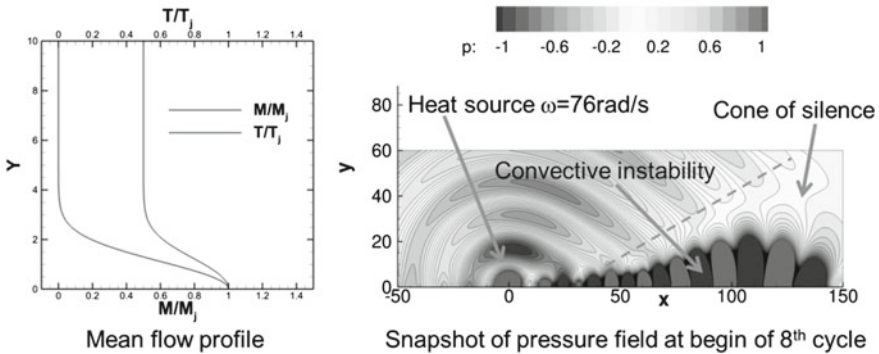
Fig. 13.3 4th CAA workshop on benchmark problems [12], category 4, problem 1: hot unstable jet with a harmonic heat source

which are then damped with a sponge-layer at the end of computational domain. The acoustic waves are refracted with the shear-layer away from the axis which generates a 'cone of silence' with weaker acoustic fluctuations in this region.

The task of this benchmark problem is to suppress the hydrodynamic instability without to influence the accuracy of acoustic solution. In the CAA computation, the ER source is applied without the forcing term, i.e. only the dissipation term is

(a) Unstable jet, $\sigma = 0$

(b) Case 1: $\hat{\sigma} = 0.01$, $x = -50 \ldots 150$, $y = 0 \ldots 5$

(c) Case 2: $\hat{\sigma} = 0.02$, $x = -50 \ldots 150$, $y = 0 \ldots 5$

(d) Case 3: $\hat{\sigma} = 0.03$, $x = -50 \ldots 150$, $y = 0 \ldots 5$
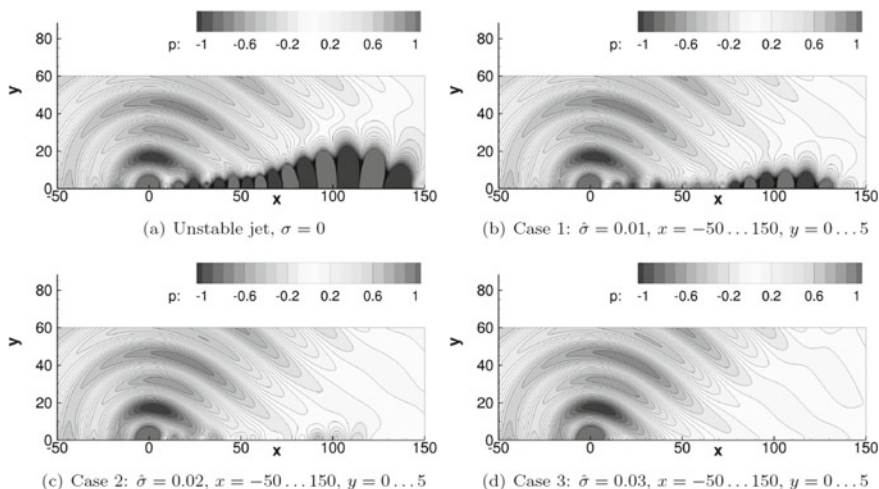
Fig. 13.4 4th CAA workshop on benchmark problems [12], category 4, problem 1: hot unstable jet with a harmonic heat source; variation of forcing parameter σ

holding. With the deactivation of the second term, the ER source is expected to take out the vorticity that triggers the instability without to damp the acoustic fluctuations of monopole.

The σ parameter is distributed over space as a constant value. For the determination of a appropriate value for relaxation parameter, a parametric study has been performed with successively increasing value starting from $\sigma = 0$ (Fig. 13.4a) up to $\sigma = 0.03$ (Fig. 13.4d). As can be seen in the last plot, the hydrodynamic instability has been completely suppressed with $\sigma = 0.03$ without to change the pattern of acoustic wave radiation.

Altogether, the posed task of benchmark problem has been successfully solved with the above described parametric study, which is also proving that the ER source term is able to damp selectively the vortical modes without to influence the acoustics as far as a sufficiently high value of σ parameter is chosen. After the expected behavior of ER source model has been found in these test computations, the method is applied to jet noise configurations as described in the next section.

13.1.3 Isolated Single Stream Jet

The general feasibility to reproduce jet noise with the ER source model in forced mode has been initially tested for a configuration with an isolated single stream jet in 2-D. As mentioned above, two different noise generation mechanisms are expected for an isolated jet, i.e. coherent and fine-scale noise. The fine-scale noise is radiated in polar angle range between $\theta = 60°$ and $\theta = 120°$ (measured from the downstream
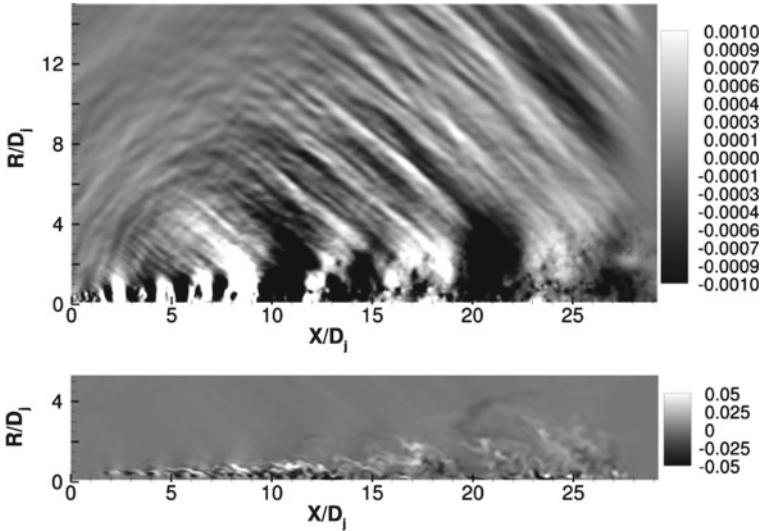
Fig. 13.5 Contour plot of (top) pressure and (bottom) density fluctuations for isolated single stream jet computed with 'Eddy Relaxation' source model in 2-D with the jet axis at $R/D_j = 0$

jet axis). This noise contribution has weak directivity characteristics, which is omni-directional in first principle but is refracted with the shear-layer and thus is slightly amplified around $\theta = 60°$ and reducing to a cone of silence at the jet axis.

The coherent noise appears at shallow angles below $\theta = 60°$ with a distinct radiation direction. These properties deliver a spectrum with a peak at characteristic frequency range, which has typically higher SPL values than the fine-scale noise. As observable in contour plot of Fig. 13.5, the both noise characteristics are found in the 2-D computation with ER source model in forced mode. The acoustic pressure fluctuations in polar angle range $\theta = 60° - 90°$ are rather scattered and with smaller magnitude than below $\theta = 60°$, i.e. with characteristics of fine-scale noise. The noise radiation below $\theta = 60°$ correspond to the expected properties of coherent noise radiation.

Subsequently, 3-D CAA computations with ER source model in deterministic and forced mode are performed for an isolated single stream jet in static condition with a nozzle exit Mach number of $Ma = 0.9$. These computational cases are also described in Neifeld et al. [13]. Depending on the computational mode, the governing equations have been switched either to LEE or to NLDE. The applied CAA setup is illustrated in Fig. 13.6 for a cut in $x - z$ plane. The computational domain is constructed as a truncated cone with roughly the same spreading as of the shear-layer. The CAA mesh comprises in total $9.7 \cdot 10^6$ grid points, which are distributed on 87 blocks as O-topology.

The resulting spectra are plotted in Fig. 13.7 together with the reference spectra from measurement of prime facility as described by Cavalieri et al. [14] and jet noise
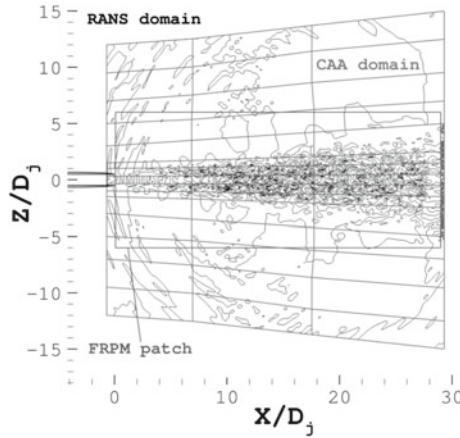
Fig. 13.6 Computational setup for an isolated single stream jet with nozzle exit Mach numer $Ma_j = 0.9$ in 3-D

Fig. 13.7 Comparison of sound pressure level spectra between measurement, analytical and computed with ER source model in forced and deterministic mode for an isolated single stream jet with nozzle exit Mach numer $Ma_j = 0.9$
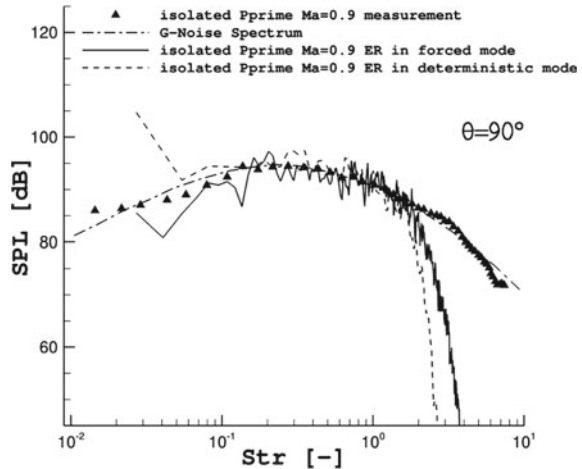
similarity spectrum for a polar angle position at $\theta = 90°$, i.e. for fine-scale noise. The spectrum with the dashed line represents the computation in deterministic mode, which is the case with entirely prescribed vorticity fluctuations. The spectrum with the solid line is obtained from the computation in forced mode, where the vorticity fluctuations are partly triggered stochastically and partly resolved on the CAA mesh.

Both spectra have a relatively good match to the reference spectra, whereby at the lowest frequency bands the deterministic case is rather overpredicting and the forced case underpredicting the targeted values. Similar agreement to the reference spectra is found also at shallow angles for coherent jet noise. The corresponding plots of velocity, density and pressure fluctuations of forced mode are shown in Fig. 13.8. In summary, the applicability of ER source model for deterministic and forced mode in 3-D space has been demonstrated for jet noise of a single stream nozzle.
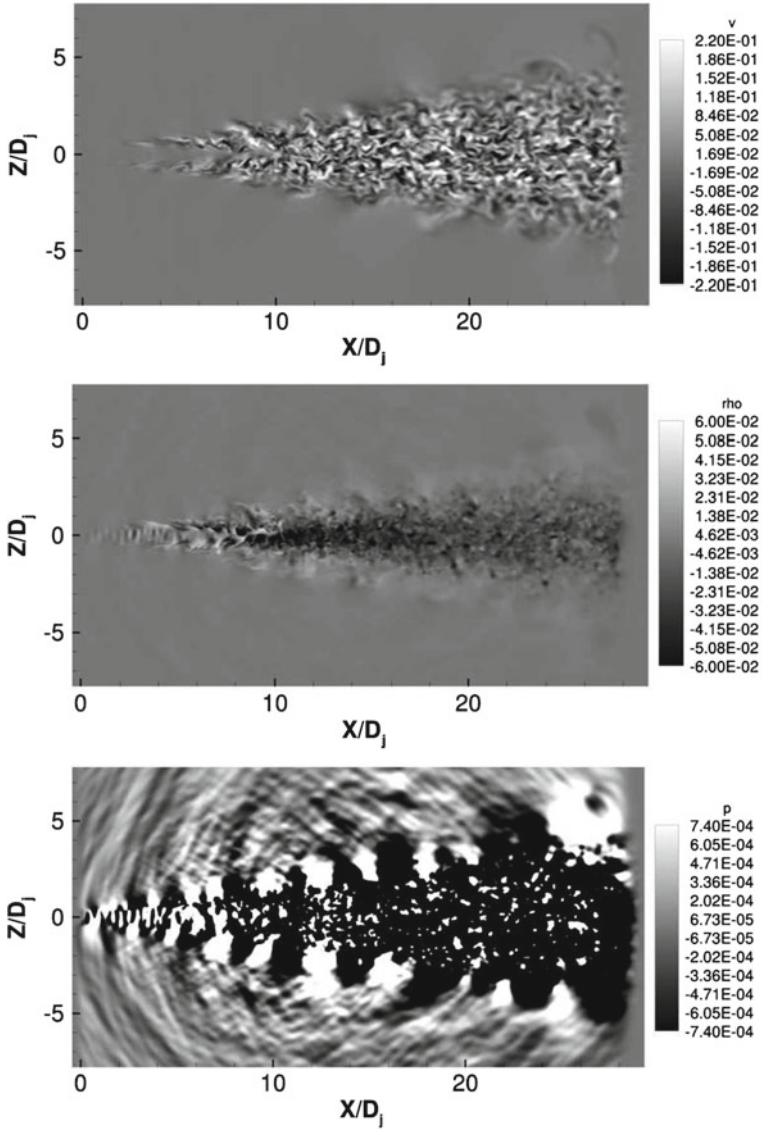
Fig. 13.8 Contour plot of (top) *v* component of velocity fluctuations, (middle) density and (bottom) pressure fluctuations from CAA computation with the setup of Fig. 13.6

13.2 Isolated Dual-Stream Nozzles

Two nozzle geometries of Rolls-Royce Deutschland (RR-D) are used for noise prediction with T and A source model. These configurations represent isolated dual-stream nozzles with ambient free-field velocity $Ma_\infty = 0.24$:

 (i) Baseline configuration of isolated dual-stream nozzle
(ii) Baseline configuration with noise reduction application at the nozzle trailing edge (serrations).

Herein, the configuration (i) serves as reference for the evaluation of noise reduction from the serrations of configuration (ii). In general, the serrations are expected to cause noise reduction in the low- and mid-frequency range. In high-frequency range on the other hand, the serrations produce more noise due to enhanced mixing in the shear-layer at nozzle lip.

The required RANS solutions for CAA computation are provided by institute of fluid dynamics (ISM, TU Braunschweig). Two different turbulence models, i.e. Menter-SST and JHh-v2 RSM have been used to compute the RANS solutions with the DLR's CFD solver TAU, which give in total four solutions for both configurations. Previously, the Menter-SST turbulence model has been used by default for noise prediction of isolated nozzles. This study aims to evaluate the noise prediction capability of the recently implemented JHh-v2 RSM in TAU in comparison to Menter-SST turbulence model.

The CAA computations are performed with the method of azimuthal-modal decomposition based on T and A source model (deterministic category of CAA). As described in Sect. 13.1, this source model predicts only fine-scale noise, i.e. is restricted to the polar angle range $\theta = 60° \dots 120°$. Hereafter, the microphone position at $\theta = 90°$ is evaluated for each configuration. Each CAA computation solves 10 azimuthal modes, which are summed up in the post-processing to a total spectrum that as such corresponds to a spectrum from a 3-D computation. Altogether, four CAA computations are conducted with the same numerical settings.

In order to evaluate the noise reduction, the spectra of configuration (i) are subtracted from the spectra of configuration (ii). This reduces the number of four individual SPL spectra to two SPL difference spectra, whereat one is representing the difference between the both Menter-SST RANS solutions and the second between the both RSM solutions. A third SPL difference spectrum is available from experiments as provided by RR-D, which is plotted together with the both numerical in Fig. 13.9 as octave band spectra.

In the SPL difference spectrum of measurement, the noise reduction of serrations is observable for a broad frequency range up to $f_{1/3} D_j / u_j = 3$. Above this frequency, the penalty noise of serrations starts to rise. This behavior is quite well reproduced with the SPL difference spectrum of both SST RANS computations. The prediction based on both JHh-v2 RSM RANS computations is however less accurate. The overall spectrum shape may be interpreted as similar to the experimental and to the Menter-SST prediction, but delivers at the end an overprediction, i.e. a noise increase instead of noise reduction for configuration (ii).

Fig. 13.9 Comparison of noise reduction between measurement and numerical prediction with SST and RSM RANS solutions
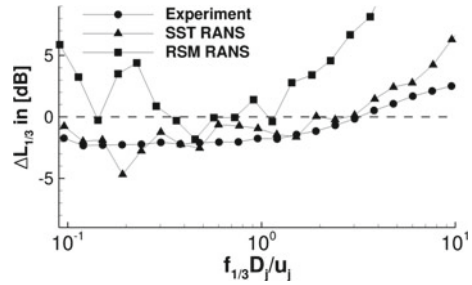
This comparison leads to the conclusion that a RANS solution based on Menter-SST turbulence model provides input data for CAA computation with sufficient accuracy to perform noise reduction prediction. On the other hand, the noise reduction as found in experiments is not properly reproduced with the JHh-v2 RSM RANS solution despite the higher order of turbulence model.

13.3 Use Case DIMENSyon-P

An isolated dual-stream nozzle configuration with pylon has been designed by RR-D for the investigation of pylon influence on jet noise radiation. For CAA computation of this configuration, the hybrid RANS/CAA method is applied again with the T and A source model. However, the computational domain is resolved here in 3-D space, since an azimuthal-modal decomposition of a jet-flow with pylon is not possible.

The required RANS solution for CAA input has been provided by Transport Aircraft Branch of Institute for Aerodynamics and Flow Technology (DLR). This RANS solution is validated with the corresponding PIV measurement. The mean-flow and turbulence kinetic energy are found as appropriate for further CAA computation.

In the azimuthal-modal computations of isolated nozzle configurations as described in Sect. 13.2 has been observed that for a full representation of jet noise spectra, the first 5–10 azimuthal modes are necessary. It means for a 3-D CAA computation that a full resolution in circumferential direction is necessary, whereas a half or quarter CAA domain would be insufficient since first and second azimuthal modes would not be captured.

The provided RANS is solved as a half model with a cut through the symmetry plane of pylon. This RANS solution is mirrored at the symmetry plane to obtain input data for the entire CAA domain. The FRPM sources as triggered in the CAA domain are depicted in Fig. 13.10, which are unsymmetrical due to stochastic seeding of FRPM although a symmetrical input RANS is used. The source domain is resolved with 3 FRPM patches with $1 \cdot 10^6$ each, which are arranged successively along the jet axis.

Two CAA computations are performed with the same setup with the difference in definition of boundary condition on pylon. For the first computation, the pylon wall
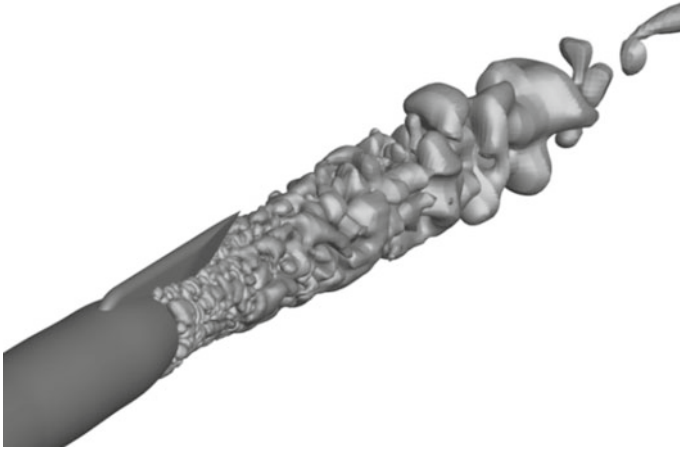
Fig. 13.10 Distribution of FRPM sources computed with Tam and Auriault source model for an isolated dual-stream nozzle with pylon
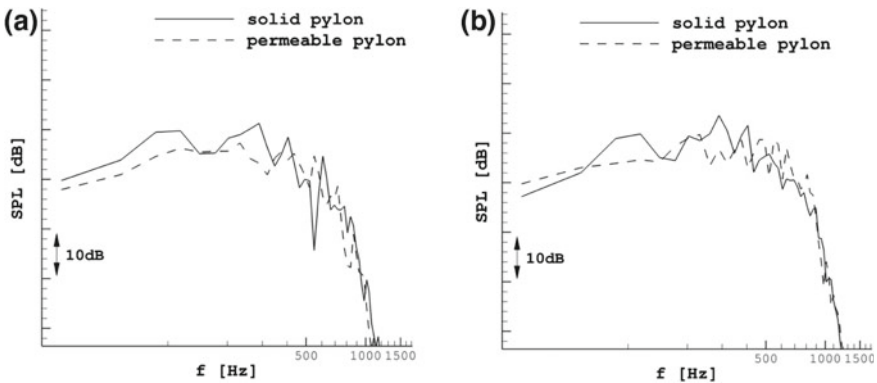
Fig. 13.11 Comparison of numerical spectra between acoustic hard and acoustic permeable pylon at polar angle $\theta = 90°$; **a** lateral and **b** below the pylon

is defined as acoustic porous, i.e. the acoustic waves are leaving the computational domain at pylon wall. In the second computation, the boundary condition of pylon wall is changed to a hard wall, which completely reflects all fluctuations. Thus, the difference of spectra between the both computations would describe the maximum potential to absorb sound by pylon wall. Herein, the effect of pylon on mean-flow remains unchanged, since RANS solution is the same in both CAA computations.

The spectra of both CAA computations are plotted in Fig. 13.11. Two microphone positions are evaluated in a direction (a) lateral to the pylon and (b) below with a distance to the jet axis of $R/D_j = 10$. The polar angle is for both positions $\theta = 90°$. The difference between the both computations for the lateral position is $\Delta SPL \approx$

2 dB. For the position below the pylon in Fig. 13.11b, the difference is less. The smaller difference appears plausible since the surface of pylon wall perpendicular to the lateral position is larger than to the position below the pylon. Thus, stronger reflexion of sound pressure fluctuations to the lateral position would be expectable.

References

1. J.Z. Wu, Y. Zhou, X.Y. Lu, M. Fan, Turbulent force as a diffusive field with vortical sources. Phys. Fluids **11**(3), 627 (1999)
2. R. Ewert, W. Schröder, Acoustic perturbation equations based on flow decomposition via source filtering. J. Comput. Phys. **188**(2), 365–398 (2003)
3. R. Ewert, J. Dierke, A. Neifeld, S.M.A. Moghadam, Linear and non-linear perturbation equations with relaxation source terms for forced Eddy simulation of aeroacoustic generation, in *AIAA Aviation, 20th Aeroacoustics Conference, AIAA 2014-3053* (2014)
4. A. Neifeld, R. Ewert, D. Keller, M. Steger, Towards prediction of jet noise installation effect using stochastic source modeling, in *AIAA Aviation, 20th Aeroacoustics Conference, AIAA 2014-3059* (2014)
5. A. Neifeld, J. Dierke, R. Ewert, J.W. Delfs, Aeroacoustic research in Europe: the CEAS-ASC report on 2014 highlights. J. Sound Vib. **357**, 107–127 (2015). CAA Computation of Generic Jet-Flap (JFI) configuration
6. G. Dantinne, H. Jeanmart, G.S. Winckelmans, V. Legat, Hyperviscosity and vorticity-based models for subgrid scale modeling. Appl. Sci. Res. **59**, 409–420 (1998)
7. C.E. Leith, Stochastic backscatter in a subgridscale model: plane shear mixing layer. Phys. Fluids A **2**(297), 297–299 (1990)
8. U. Schumann, Stochastic backscatter of turbulent energy and scalar variance by random subgrid-scale fluxes. Proc. R. Soc. Lond. A **451**, 293–318 (1995)
9. R. Zamansky, I. Vinkovic, M. Gorokhovski, LES approach coupled with stochastic forcing of subgrid acceleration in a high Reynolds number channel flow. J. Turbul. **11**, 1–18 (2010)
10. H.F. Fasel, D.A. von Terzi, R.D. Sandberg, A methodology for simulating compressible turbulent flows. J. Appl. Mech. **73**, 405 (2006)
11. J. Fröhlich, D.A. von Terzi, Hybrid LES/RANS methods for the simulation of turbulent flows. Prog. Aerosp. Sci. **44**, 349–377 (2008)
12. J.C. Hardin, J.R. Ristorcelli, C.K.W. Tam, in *ICASE/LaRC Workshop on Benchmark Problems in Computational Aeroacoustics (CAA)*, NASA Conference Publication 3300, Hampton, Virginia, 24–25 October 1994, (May 1995)
13. A. Neifeld, D. Boenke, J. Dierke, R. Ewert, Jet noise prediction with Eddy relaxation source model, in *AIAA Aviation, 21st Aeroacoustics Conference, AIAA 2015-2370* (2015)
14. A.V.G. Cavalieri, P. Jordan, W.R. Wolf, Y. Gervais, Scattering of wavepacket by a flat plate in the vicinity of a turbulent jet. J. Sound Vib. **333**(24), 6516–6531 (2014)

Part V
Cross-Cutting Subjects

Chapter 14
Structural Optimization of 3D Wings Under Aerodynamic Loads: Topology and Shell

Volker Schulz, Roland Stoffel and Heinz Zorn

Abstract New methods in manufacturing and novel challenges and usages require the exploration of the potential of new wing designs. This is the goal of this paper. We propose novel computational methods for the robust optimization of wings under aerodynamic loads. We restrict the discussion to the optimization of the linear-elastic properties of wings concerning several load cases and with treatment on deformations and regularization. The degrees of freedom for the design itself are the interior structure of the wing leading to topology optimization aspects and the structure of the wing hull in terms of composite material. Thus, this paper aims at mathematical methods for topology optimization of the wing interior made of isotropic material, the optimization of orthotropic composite material in the wing hull and the proper treatment of practical deformation aspects and multiple loads in this context.

14.1 Introduction

We develop mathematical methods for wings with the abstract coarse structure in Fig. 14.1. The 3D wing consist of two major parts, the interior (light grey), which we denote as Ω_0 and the wing hull (dark grey), which we denote as Ω_1.

We aim at the minimization of the elastic compliance, i.e., the computational treatment of the following optimization problem with constraints in the form of the elasticity equation:

$$\min W_\Omega := \int\limits_\Omega \sigma(u) : \varepsilon(u)dx$$

$$\text{subject to} \quad -\text{div}(\sigma(u)) = 0 \text{ in } \Omega := \Omega_0 \cup \Omega_1$$

V. Schulz (✉)
Steinbeis-Innovationszentrum Modellbasierte Mathematische Optimierung,
Januarius-Zick-Str. 73, 54296 Trier, Germany
e-mail: volker.schulz@uni-trier.de

R. Stoffel · H. Zorn
Trier University, Trier, Germany

Fig. 14.1 Exemplaric
NACA wing illustrating the
coarse structures treated in
this paper

$$\sigma(u) = C\varepsilon(u) \text{ in } \Omega$$
$$u = 0 \text{ on } \Gamma_{\text{fix}}$$
$$\sigma(u)n = g \text{ on } \Gamma_{\text{force}}$$

where $\qquad\qquad \Gamma_{\text{fix}} \cup \Gamma_{\text{force}} = \partial\Omega$

Here, $u : \Omega \to \mathbb{R}^3$ denotes the deformation vector field and ε, σ the strain and stress tensors, furthermore $C : \Omega \to \mathbb{R}^{3\times3\times3\times3}$ the spatially varying stiffness matrix. The boundary Γ_{fix} is the part of the wing boundary, where the wing is attached to the body of the aircraft, and the boundary Γ_{force} is the part, which the aerodynamic loads $g : \Gamma_{\text{force}} \to \mathbb{R}^3$ are acting on. The degree of freedom for optimization is the stiffness matrix, where we—in contrast to free material optimization [1]—do not admit an arbitrary structure. In the interior Ω_0, we rather assume that the stiffness matrix is a scalar multiple of an isotropic tensor, i.e., $C_0 = \rho E_0$, where $\rho : \Omega_0 \to \mathbb{R}$ and E_0 is constant. Furthermore, we assume that the stiffness matrix in the hull, Ω_1, depends locally and orthotropically on the local fiber orientation, i.e., $C_1 = C_1(\alpha)$, where $\alpha : \Omega \to \mathbb{R}$. The subsequent sections focus on Ω_0, Ω_1 and practical aspects.

14.2 Topology Optimization of the Wing Interior

Topology optimization aims at optimal structures or–more precisely–optimal material distributions in the subdomain $\Omega_0 \subset \Omega \subset \mathbb{R}^3$ with respect to minimization of elastic energy (compliance). The amount of material is not allowed to surpass a certain maximal volume, i.e., $\int_{\Omega_0} dx \le V$. A decisive aspect is the representation of the boundary $\Gamma = \partial\Omega_0$, for which the level set method of Osher/Fedkiew [2] or Sethian [3] is a powerful tool. Several approaches exist to topology optimization:

- SIMP method
- shape optimization based on the shape calculus
- topology optimization based on the topological calculus

The *SIMP* (solid isentropic material with penalization) method of Bendsøe and Sigmund [4] uses a homogenization approach to structural optimization. They introduce a pseudo density function $\rho \in \{0, 1\}$. If the density at a point (or in an element of the discretization mesh) is 0, there does not exist any material. If it is 1,

then there exists material there. Based on this interpretation of material structure, gradient based algorithms are used in order to compute a locally optimal density distribution ρ. Additional difficulties resulting from relaxation ($\rho(x) \in (0, 1]$) and potential checkerboarding have to be treated, e.g., by filtering techniques (cf., [4, 5]). However, those techniques are hardy computationally viable on unstructured grids.

Shape optimization based on the shape calculus is used in several industrial applications. The theoretical foundations can be found in [6, 7]. Optimal shapes for fluid flow is considered, e.g., in [8] and also [9–11]. If shape optimization is used for the purpose of topology optimization as in [12], it is assumed that there are already holes (regions without material) in the domain. The aim is to compute the optimal shapes of the boundaries of those holes. The shape calculus is used to compute shape sensitivities on the boundaries. The resulting shape gradient guides the computation towards a (local) optimum. The method uses an explicit representation of the boundaries. A severe drawback is that the number of holes cannot be changed by this approach. This problem can be circumvented by a combination of shape optimization with a level set method. The level set method describes the boundaries of the holes as contour surface (usually the zero contour surface) of a higher dimensional level set function Φ. The evolution of the boundaries is described by the so called level set equation, which is a time dependent convection equation. In this way, holes are enabled to merge. However, this method does not possess a mechanism to create new holes. Good computational performance is achieved for level set functions in the form of signed distance functions, which require frequent re-initialization during the optimization process. Furthermore, the shape gradient, which exists only on the contour surface, has to be somehow propagated on the whole computational domain.

The creation of new holes is enabled by the usage of the so-called topological derivative, which has been introduced by Sokolowski and Zochowski [13] in 1999. The concept of topological derivative is frequently used in image processing and inverse modeling.

The topological derivative compares function evaluations on shapes without a hole and with a small hole in the form of a difference quotient. Thus, it is the limit of the difference quotient and can be related to shape gradients. In this particular case, the topological derivative of the compliance in 3D at the position $x \in \Omega_0$ can be expressed as (cf. [14, 15])

$$D_T W_\Omega(x) = \frac{3}{4} \frac{1-\nu}{7-5\nu} \left[10\sigma(u) : \varepsilon(u) - \frac{1-5\nu}{1-2\nu} \mathrm{tr}\sigma(u)\mathrm{tr}\varepsilon(u) \right](x).$$

where ν is the Poisson ratio of the material. A rather elegant method for structural optimization is the combination of the topological derivative with the level set method as described in [16]. In this approach, the domain Ω_0 is divided in one region with material $\{x \mid \Phi(x) \leq 0\}$ and another region without material $\{x \mid \Phi(x) > 0\}$. The topological derivative is used as an indicator, where material should be added or reduced. A local optimum is reached at a fixed point of this strategy, as soon as the sign of the topological derivative coincides with the sign of the level set function everywhere.

The publication [17] discusses a topological sensitivity analysis for linear elasticity in 2D without level set function approach. The sensitivity analysis in 3D is carried out in [14], again without a level set framework. The level set method of Amstutz with inclusions is described in [16], referencing [18] for the sensitivity analysis. [19] introduces the level set framework together with a penalization of constraints. In [20], augmented Lagrangian approaches for the proper treatment of constraints within a topology optimization context are investigated but in the context of linear elasticity.

The topology optimization approach proposed in this paper consists of the following components:

- discretization and solution of the elasticity equations by usage of the open source software toolbox FEniCS [21].
- 3D implementation of the topological gradient described in [14] for the linear elasticity solver FEniCS in combination with the
- level set approach in [16, 19].
- Furthermore, it is necessary to limit the volume of the optimal structures. For the treatment of additional constraints of this type, we use an augmented Lagrangian technique as described in [16, 19].

In the sequel, we describe numerical results of this strategy for the following testcase: we use a wing in the shape of a NACA prism as in Fig. 14.1. This wing is exposed to a usual pressure profile, which is constant in longitudinal direction. The elasticity equation is discretized in the wing interior on 8 million tetraedral elements with 1.5 million nodes and with linear finite elements. From that result 4.6 million unknowns, for which the discretized elasticity equations are solved on a parallel computing architecture in each optimization iteration. The optimization needs 180 iterations according the optimization approach discussed above. For the interior wing structures, we allow only 10% of the maximum possible material volume, i.e., $V_0 = 0.1 \cdot |\Omega_0|$. Figures 14.2 and 14.3 show the achieved solution from different prespectives. We note that the results of this test case can be geometrically interpreted as longitudinally curved truss-like structures, which challenge the usually used rib structures.

Similar investigations can be performed with wings with a priori rib structures in the interior as in Fig. 14.4.
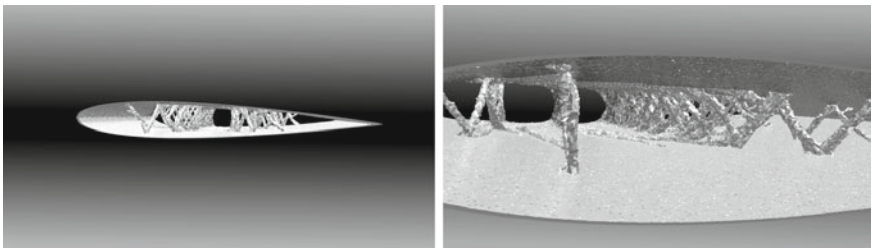
Fig. 14.2 View into the optimized wing tip (left) and in detail (right)
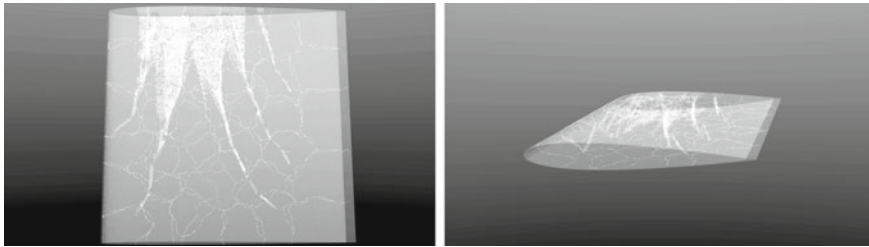
Fig. 14.3 Transparent rendering of the optimal wing from different angles. The thin net-like structures show the domain decomposition for parallel computing

Fig. 14.4 Topological optimization with an interior rib structure. Initial iteration (top) and two different cuts through the optimal solution (middle and bottom)

14.3   Optimization of the Distribution of Orthotropic Composite Material in the Wing Shell

We model the material in the wing shell as an orthotropic material, where one material direction coincides with the normal vector in each point in the shell. The other two material direction are described by a rotational angle around the normal vector. Thus, we optimize the distribution of this orientation angle as a function $\alpha : \Omega_1 \to \mathbb{R}$. This function enters the material properties in the form $C(\alpha) = T(\alpha) C_1 T(\alpha)^{\top}$, where $T(\alpha)$ denotes the transformation of the reference coordinates, which depends on the angle α, and C_1 denotes a fixed orthotropic reference material.

The methods are implemented within the software toolbox FEniCS already mentioned in Sect. 14.2. In a first approach, we applied gradient based methods to the problem of determining the orientation angle distribution α, where the derivative information is produced via an adjoint solution and the optimization itself is performed by a limited memory quasi-Newton method. This approach is viable, although additional regularization techniques have to be applied, but in total is takes up very much computational time. However, in [9] P. Pederson has proposed an analytic approach in a rectangular 2D setting and derived necessary optimality conditions for this specific case. There, for certain materials, the stronger material direction coincides with the direction of maximal stress and strain. We use this characterization in the 3D case in the wing shell and implement it in the form of a fixed point iteration, where each iteration step consists of the following algorithm:

1. Solve the linear elasticity equation
2. Determine in each the eigenvector of the largest stress in each point and project it to the shell manifold
3. Set the orientation angle to the direction from step 2.

For the start, it has shown advantageous, to intialize the iterations at the orientation according the maximal strain. The resulting overall method gives the same solution, however, in a much more efficient way. Investigations into the convergence properties are performed in [22]. In an additional step, we combine this algorithm with the topology optimization approach from Sect. 14.2. This combination is implemented in a simultaneous fashion, where after each topology optimization step a fast approximative solution of the orthotropic material optimization in the wing shell is carried out. The resulting method converges to a joint optimum (for the wing interior as well as for the wing shell). Figure 14.5 shows exemplaric results for the optimal fiber orientation in the wing shell for a wing with two interior ribs.

A detailed analysis of the spatial distribution of the optimal solution shows that it can be separated in two intertwined and smoothly varying scalar fields which lead to two perpendicular orientation angles in each point. Figure 14.6 shows an example of a solution of the coupled problem of topology orientation in the wing interior together with the fiber optimization of the wing shell.
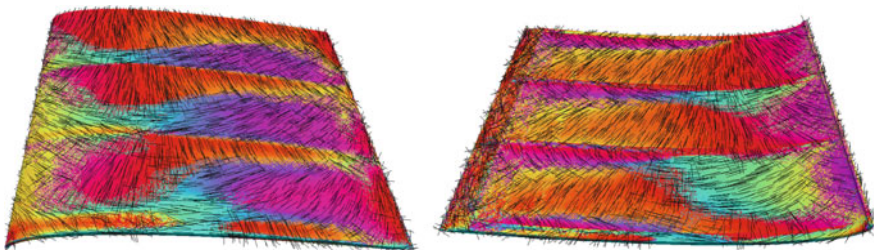
Fig. 14.5 Optimized fiber orientations of a wing with two interior ribs (upper shell left, lower shell right)
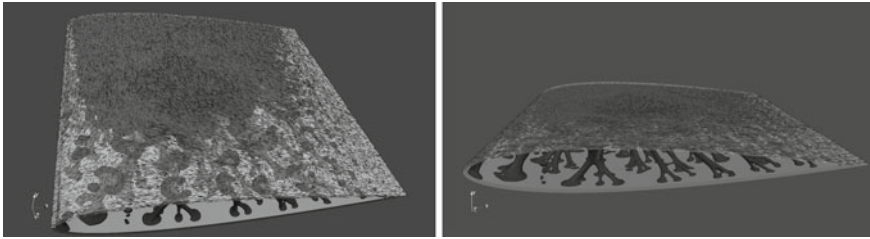
Fig. 14.6 Coupled optimal solution

14.4 Deformation Aspects, Multiple Load Case and Regularization

Wings with interior rib structures show characteristic bulges, when aerodynamic forces bend the whole wing. Those bulges are to be reduced by an appropriate orientation distribution of the orthotropic composite material. Thus, a multicriteria optimization problem arises with the two goals global compliance reduction and local reduction of the bulges. Here, we use again the wing shown in Fig. 14.5 with rib structures as illustrated in Fig. 14.7.

On this wing, the following boundary value problem is solved:

$$-\mathrm{div}(\sigma(u)) = 0 \ \text{in} \ \Omega$$
$$\sigma(u) = C(\alpha)\varepsilon(u) \ \text{in} \ \Omega$$
$$u = 0 \ \text{on} \ \Gamma_D$$
$$\sigma(u)n = 0 \ \text{on} \ \Gamma_{\text{tip}}$$
$$\sigma(u)n = pn \ \text{on} \ \Gamma_N$$

where p denotes the aerodynamic pressure. The resulting bended wing is shown in Fig. 14.8, where the bulges are scaled in order to illustrate the investigated effects.
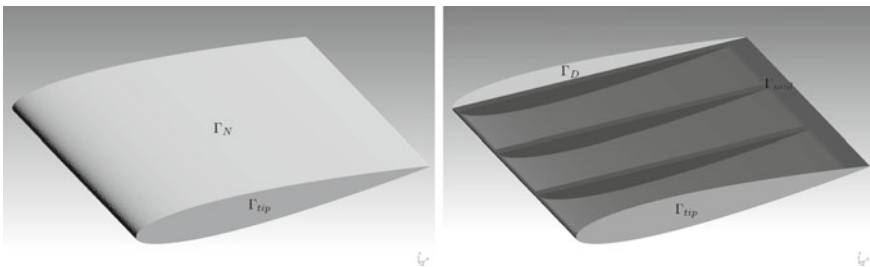
Fig. 14.7 Wing with rib structure as used in the numerical computations

Fig. 14.8 Wing bending with scaled bulges

Fig. 14.9 Pure bulge deformation of the wing (b, scaled)

The deformation $u : \Omega \to \mathbb{R}^3$ is compared with a resulting deformation $v : \Omega \to \mathbb{R}^3$ which bends the wing in the same way (prescribed by Dirichlet condition on the interior plane) but without the action of aerodynamic forces, i.e., as the solution of the boundary value problem

$$-\mathrm{div}(\sigma(v)) = 0 \text{ in } \Omega$$
$$\sigma(v) = C(\alpha)\varepsilon(v) \text{ in } \Omega$$
$$v = u \text{ on } \Gamma_{\mathrm{tip}} \cup \Gamma_{\mathrm{mid}}$$
$$v = 0 \text{ on } \Gamma_D$$
$$\sigma(u)n = 0 \text{ on } \Gamma_N$$

From this result, we compute the pure bulge deformation as $b := u - v : \Omega \to \mathbb{R}^3$ without a global deformation of the wing, as shown in Fig. 14.9.

The vector field $w := v + \lambda b$ ($\lambda \in \mathbb{R}$) corresponds to a deformation of the wing with scaled bulges (scaling factor $\lambda = 50$ in Fig. 14.8). The optimal fiber orientation according to the algorithm sketched above und with usage of w instead of u leads to the effect that the bulges are reduced, if the scaling factor λ is increased—sacrificing compliance to some extent. It should be noted that the overall algorithmic effort is only increased by a factor of 2: two elasticity problem are to be solved in each iteration (u and v), but the optimization algorithm yields the same performance. The resulting Pareto diagramm is shown in Fig. 14.10.

Figure 14.11 shows two optimized fiber orientation distributions, where the color code matches the one in Fig. 14.5.

In order to achieve results which are robust under uncertainties with respect to the specific aerodynamic forces, we consider furthermore the multiple load case. It is obvious that the algorithmic approach discussed above of guiding the fiber orientation with the direction of maximal stress cannot be carried over to this problem
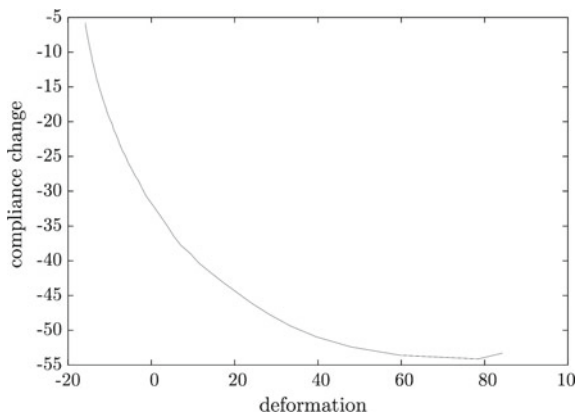
Fig. 14.10 Pareto front of compliance reduction versus bulge reduction ($0 \leq \lambda \leq 60$), shown are percentage values of the difference in comparison to the reference solution with overall constant fiber orientation
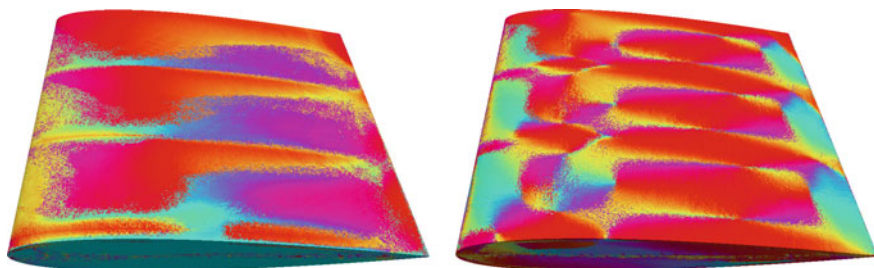
Fig. 14.11 Two optimal fiber orientation distributions: left $\lambda = 1$, right $\lambda = 40$

formulation. Here, we develop the following different approach which is computationally more expensive but can be generalized to the multiple load case. It is related to the methods discussed in [23] for the 2D case only. We represent the compliance as a trigonometric polynomial in the form

$$W_\Omega = \int_\Omega W(\alpha)dx = \int_\Omega a_0 + a_1 \sin(2\alpha) + b_1 \cos(2\alpha) + a_2 \sin(4\alpha) + b_2 \cos(4\alpha)dx$$

(14.1)

where the coefficients a_0, a_1, b_1, a_2, b_2 are scalar functions depending on the location $x \in \Omega$ which are composed of the (constant) material tensor and the strains $\sigma : \Omega \to \mathbb{R}^3$. In the multiple load case (with index k), we obtain with weights $\gamma_k \geq 0$ the weighted sum of the load cases in complete analogy as

$$\sum_k \gamma_k W_\Omega^k = \int_\Omega \bar{a}_0 + \bar{a}_1 \sin(2\alpha) + \bar{b}_1 \cos(2\alpha) + \bar{a}_2 \sin(4\alpha) + \bar{b}_2 \cos(4\alpha) dx$$

$$(14.2)$$

where, e.g., $\bar{a}_1 := \sum_k \gamma_k a_1^k$, a_1^k being the coefficient of the load case k, and the other coefficients $\bar{a}_0, \bar{b}_1, \bar{a}_2, \bar{b}_2$ are defined analogously. Thus, formally, there is almost no difference between the single load case and the multiple load case. As the necessary condition for optimality, the derivative of the integrand above has to vanish in each $x \in \Omega$. Thus, at most four roots of the (differentiated) trigonometric polynomial have to be computed efficiently by reformulation as a polynomial in the complex plane. The root with the smallest contribution in the objective gives the new fiber orientation. A detailed derivation can be found in [22]. In total, we obtain the following algorithm in each optimization iteration:

1. (parallel) computation of the linear elasticity equation for all load cases
2. (parallel) computation of the distributed coefficients $\bar{a}_0, \bar{a}_1, \bar{b}_1, \bar{a}_2, \bar{b}_2$
3. solution of the local scalar optimization problems for the trigonometric polynomials in the FE grid
4. setting the fiber orientation to the direction from step 3.

In the single load case setting, the overall computational effort for this approach is between the effort for the method discussed in Sect. 14.2 and the approach via an adjoint solver discussed above. It increases linearly with the number of load cases. Furthermore, this approach gives good grid convergence as shown in Fig. 14.12, in all cases.

In Fig. 14.13, we show results for a multiple load scenario.

Figure 14.14 presents the convergence history for the multiload case. For each case (two single loads and one multiload case), we evaluate all three objectives. It can be observed in particular that the multiple load optimization yields a good compromise between the two separate objectives.

In the same way, as Eq. (14.1) is generalized to the multiple load case in Eq. (14.2), it can also be generalized to the incorporation of a regularization. We denote by $\bar{\alpha} : \Omega_1 \to \mathbb{R}$ an orientation distribution of which we plan stay in a vicinity. Since the effect of the orientation is periodic in π, this periodicity has to be reflected also
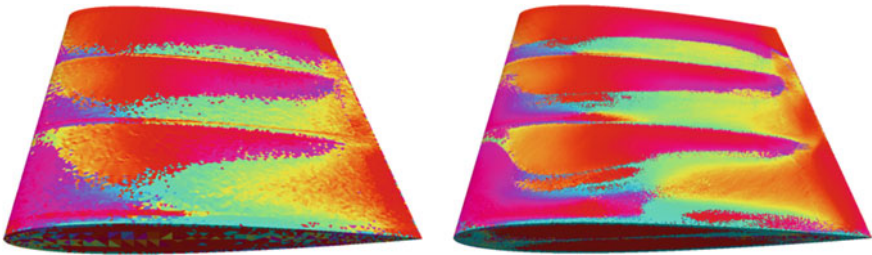
Fig. 14.12 Grid convergence in single load case: left coarse grid, right fine grid
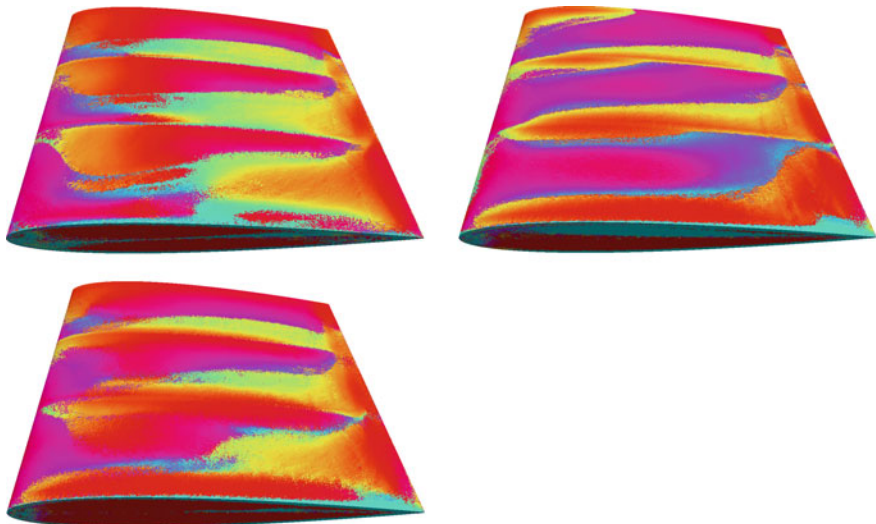
Fig. 14.13 Multiple load results: top row shows optimal solutions in two load cases, bottom shows the optimal solution in the equally weighted load case ($\gamma_1 = \frac{1}{2} = \gamma_2$)
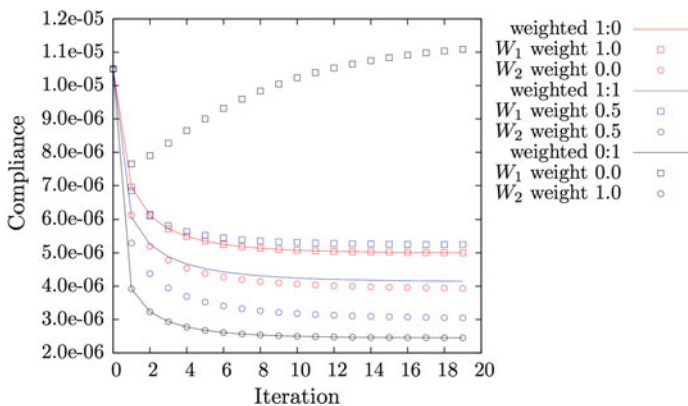
Fig. 14.14 Convergence histories in the multiple load case study

in the regularization term. In a regularized optimization, we use the objective

$$W_\Omega^{pen} := W_\Omega + \mu R(\alpha, \bar{\alpha}), \qquad \mu > 0$$

where $R(\alpha, \bar{\alpha})$ is defined by

$$R(\alpha, \bar{\alpha}) = \int_\Omega \cos\left(-\frac{\pi}{2} - 2\bar{\alpha}\right)\sin(2\alpha) + \sin\left(-\frac{\pi}{2} - 2\bar{\alpha}\right)\cos(2\alpha) + 1dx$$

Fig. 14.15 Regularized result
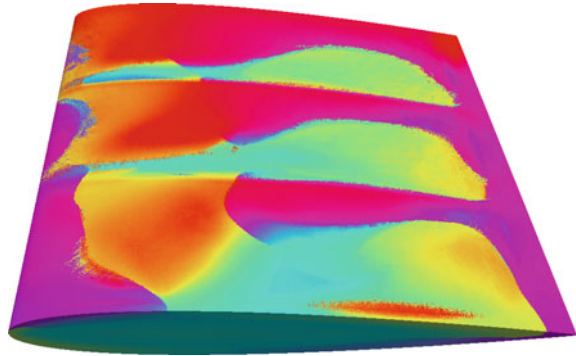
Thus, $R(\alpha, \bar{\alpha})$ periodically penalizes deviations of α from $\bar{\alpha}$, where deviations by $\pi/2$ are penalized most. As a result, the coefficients of the trigonometric polynomial in Eq. (14.1) have to increased as

$$a_0^{pen} := a_0 + \mu \,, \; a_1^{pen} := a_1 + \mu \cos\left(-\frac{\pi}{2} - 2\bar{\alpha}\right), \; b_1^{pen} := a_1 + \mu \sin\left(-\frac{\pi}{2} - 2\bar{\alpha}\right)$$

and analogously in the multiple load case. Figure 14.15 shows a regularized single load case solution on a fine grid, where the regularizing angle distribution $\bar{\alpha}$ has been generated by smoothing an unregularized result with the usage of the Laplace-Beltrami operator. Much clearer separations between the regions of different orientation angles are visible. In the smoothed result, the compliance is deteriorated by roughly 3% only.

14.5 Conclusions

We have developed methods for the topology optimization of aircraft wings, as well as methods for the optimal orientation of orthotropic composite material in the wing shell. Furthermore, practical aspects as reduction of buckling, the multiple load case and regularization have been considered. The numerical results are based on a linear elasticity model for the mechanical behavior of the wing. All implementations have been performed on the basis of FEniCS [21]. The results show a significant performance potential of alternative wing shapes and configurations.

References

1. M. Stingl, M. Kočvara, G. Leugering, A sequential convex semidefinite programming algorithm with an application to multiple-load free material optimization. SIAM J. Optim. **20**, 130–155 (2009)
2. S. Osher, R. Fedkiew, *Level Set Methods and Dynamic Implicit Surfaces* (Springer, New York, 2003)
3. S. Schmidt, V. Schulz, A 2589 line topology optimization code written for the graphics card. Comput. Vis. Science **14**, 249–256 (2011)
4. M.P. Bendsøe, O. Sigmund, *Topology Optimization: Theory, Methods and Applications* (Springer, Berlin, 2003)
5. S. Schmidt, V. Schulz, Shape derivatives for general objective functions and the incompressible Navier-Stokes equations. Control Cybern. **39**, 677–713 (2010)
6. M.C. Delfour, J.-P. Zolesio, *Shapes and Geometries Analysis, Differential Calculus, and Optimization* (SIAM, 2001)
7. J. Sokolowski, A. Zochowski, On the topological derivative in shape optimization. SIAM J. Control Optim. **37**, 1251–1272 (1999)
8. B. Mohammadi, O. Pironneau, *Applied Shape Optimization for Fluids* (Oxford University Press, New York, 2001)
9. P. Pedersen, On optimal orientation of orthotropic materials. Struct. Optim. **1**, 101–106 (1989)
10. S. Schmidt, C. Ilic, N. Gauger, V. Schulz, Airfoil design for compressible inviscid flow based on shape calculus. Optim. Eng. **12**, 349–369 (2011)
11. S. Schmidt, C. Ilic, N. Gauger, V. Schulz, Three dimensional large scale aerodynamic shape optimization based on shape calculus, in *41st AIAA Fluid Dynamics Conference and Exhibit, AIAA 2011–3718* 2011
12. G. Allaire, F. Jouve, A.M. Toader, Structural optimization using sensitivity analysis and a level-set method. J. Comput. Phys. **194**, 363–393 (2004)
13. J.A. Sethian, *Level Set Methods and Fast Marching Methods* (Cambridge University Press, Cambridge, 1999)
14. A.A. Novotny, R. Feijoo, E. Taroco, C. Padra (1992), Topological sensitivity analysis for three-dimensional linear elasticity problem, in *6th World Congress on Structural and Multidisciplinary Optimization Rio de Janeiro, 30 May–03 June 2005* (Brazil, 2005)
15. R. Stoffel, Structural Optimization of Coupled Problems, Dissertation, Universität Trier, 2013
16. S. Amstutz, H. Andrä, A new algorithm for topology optimization using a level-set method. J. Comput. Phys. **216**, 573–588 (2006)
17. S. Giusti, A.A. Novotny, C. Padra, Topological sensitivity analysis of inclusion in two-dimensional linear elasticity. Eng. Anal. with Bound. Elem. **32**, 926–935 (2008)
18. S. Amstutz, Sensitivity analysis with respect to a local perturbation of the material property. Asymptot. Anal. **49**, 87–108 (2006)
19. S. Amstutz, A.A. Novotny, E. de Suza Neto, Topological derivative-based topology optimization of structures subject to drucker-prager stress constraints. Comput. Methods Appl. Mech. Eng. **233–236**, 123–136 (2012)
20. D.E. Campeao, A.A. Novotny, Topological derivative-based structural optimization considering different volume control methods. Technical report, Coordenacao de Matematica Aplicada e Computacional, Laboratorio Nacional de Computacao Cientca LNCC/MCT (Petropolis, Brazil, 2011)
21. A. Logg, K.-A. Mardal, G.N. Wells et al., *Automated Solution of Differential Equations by the Finite Element Method* (Springer, Berlin, 2012)
22. H. Zorn, Optimierung der Materialausrichtung von orthotropen Materialien in Schalenkonstruktionen, Dissertation, Universität Trier, 2017
23. H.C. Cheng, N. Kikuchi, Z.D. Ma, An improved approach for determining the optimal orientation of orthotropic metarial. Struct. Optim. **8**, 101–112 (1994)
24. J. Sokolowski, J.-P. Zolesio, *Introduction to Shape Optimization* (Springer, Berlin, 1991)

Chapter 15
Accelerating Unsteady CFD Simulations Using a Minimum Residual Based Nonlinear Reduced Order Modeling Approach

Matteo Ripepi and Stefan Görtz

Abstract Reduced-order modeling is evaluated as a means to speed up unsteady computational fluid dynamics (CFD) simulations while maintaining the desired level of accuracy. In the reduced order modeling approach, proper orthogonal decomposition (POD) is applied to some computed response time history from a compressible, unsteady CFD solver to compute a set of orthogonal basis vectors. An approximate flow solution for the next time step is predicted by minimizing the unsteady flow solver residual in the space spanned by the POD basis. This is done by solving a non-linear least-squares problem. This approximate flow solution is then used to initialize the flow solver at this time step, aiming to reduce the number of inner iterations of the dual time stepping loop to convergence compared to the conventional choice of initializing with the previous time step solution or an extrapolation in time. This procedure is repeated for all following time steps. Results for the pitching LANN wing at transonic flow conditions show a more than twofold reduction in the number of inner iterations of the flow solver to convergence. Despite the overhead caused by evaluating the reduced-order model (ROM) at every time step, the method results in a 38% savings in computational time without compromising accuracy, thus improving the overall efficiency for unsteady aerodynamics applications. Finally, several means to further improve the performance are also discussed, including updating the POD basis after every new time step.

15.1 Introduction

Reduced-order models (ROMs) are being used to replace computationally expensive full-order models in different fields of application, including computational fluid dynamics (CFD). Typically, ROMs are of interest in situations where the same

M. Ripepi · S. Görtz (✉)
DLR Institute of Aerodynamics and Flow Technology, Braunschweig, Germany
e-mail: stefan.goertz@dlr.de

M. Ripepi
e-mail: matteo.ripepi@dlr.de

full-order model is to be evaluated many times for different parameter settings, such as different flow conditions. The goal is to make many predictions at lower computation cost, hence efficient but nonetheless sufficiently accurate ROMs are typically sought after.

A powerful tool currently considered state of the art in reduced-order modeling of linear and nonlinear systems is proper orthogonal decomposition (POD), a technique which has been demonstrated in many fields of application. When applied in the context of CFD, the basic idea of POD is to replace solving the full-order governing equations of fluid dynamics by determining a suitable linear combination of POD basis vectors, which are computed based on flow solution snapshots from selected full-order CFD simulations. There exist various methods for computing the coefficients of such a linear combination, including interpolation [1] and solving a low-order partial-differential equation (PDE) system. Following the approach in [2], effective POD-based ROMs for steady aerodynamic problems can also be obtained by minimizing the POD approximation's defect with respect to the governing equations of fluid dynamics. This minimum residual based nonlinear reduced order modeling approach has been further refined and demonstrated for subsonic and transonic steady aerodynamic applications in [3, 4].

Here, our idea is to extend this approach to unsteady aerodynamic applications by minimizing the unsteady residual. Although derived from high-fidelity unsteady CFD data, the resulting ROM approximation may lead to a substantial error in time in the predicted response and time accuracy is lost. Hence, our second idea is to use the ROM prediction for a given time step to initialize the full-order model at this time step, assuming this is a good initial guess, and then iterating the inner loop of dual time stepping of the flow solver until convergence is achieved for this time step. Ideally, the number of inner iterations to convergence is reduced in this fashion compared to how the inner loop is otherwise initialized. This procedure is conducted repetitively for a series of times steps, whereby for each and every new ROM prediction, the snapshot set and thus the POD basis may be augmented with the latest fully converged time step solution.

This idea of speeding up the computation of a series of computations using a residual-based reduced-order model has already been demonstrated for steady aerodynamic problems [5]. Here, the corresponding strategy is demonstrated for unsteady aerodynamic applications by using the extended ROM formulation.

15.2 Theoretical Background

The developed model order reduction approach for unsteady aerodynamic applications is based on a least-squares minimization of the unsteady residual, which is obtained by approximating the flow solution through modes arising from a Proper Orthogonal Decomposition (POD) of samples data. Given a set of flow solutions to the full order CFD model $\mathbf{w}(t) = [\rho, \rho \mathbf{v}, \rho E^t] \in \mathbb{R}^N$, N being the total number of flow states (number of conservative variables per grid point times number of grid

points n), ρ the density, $\mathbf{v}$ the velocity vector, E the total energy, at different time steps t_k, with $k = 1, \ldots, m$, the POD yields an optimal basis for representing reduced order solutions of the governing equations. The idea of the reduced order modeling approach is to formulate the discretized unsteady equations as a steady-state problem for every time step in a similar fashion as dual-time stepping is used in solving unsteady CFD problems. This yields the so-called unsteady residual:

$$\widehat{\mathbf{R}} \stackrel{def}{=} \mathbf{R}(\mathbf{w}(t)) + \mathbf{\Omega}\frac{\partial \mathbf{w}(t)}{\partial t} = \mathbf{0} \qquad \mathbf{\Omega} : \text{cell volumes} \qquad (15.1)$$

By discretizing the time derivative (assuming equidistant time steps Δt and an invariant computational grid) with a second-order accurate backward difference formula (BDF-2), it is:

$$\widehat{\mathbf{R}} \stackrel{def}{=} \mathbf{R}(\mathbf{w}(t_{k+1})) + \mathbf{\Omega}\frac{3\mathbf{w}(t_{k+1}) - 4\mathbf{w}(t_k) + \mathbf{w}(t_{k-1})}{2\Delta t} = \mathbf{0} \qquad (15.2)$$

15.2.1   Unsteady Residual-Based Reduced-Order Modeling

The idea is to minimize the unsteady residual in the space spanned by the POD basis vectors $\mathbf{U}_r$, which is obtained by applying a singular value decomposition (SVD) to the snapshot matrix $\mathbf{Y} = \mathbf{U}\mathbf{S}\mathbf{V}^{\mathbf{T}}$, and by truncating the matrix $\mathbf{U}$ retaining only the most relevant r eigenvectors (i.e., those associated to the largest singular values). The snapshot matrix is obtained by collecting the flow solutions at different time steps and subtracting the average of the snapshots $\overline{\mathbf{w}} = \frac{1}{m}\sum_{k=1}^{m} \mathbf{w}_k$, i.e., $\mathbf{Y} = [\mathbf{w}(t_1), \ldots, \mathbf{w}(t_m)] - \overline{\mathbf{w}}$. As an alternative to the SVD, an Eigenvalue decomposition (EVD) of the correlation matrix $\mathbf{R} = \mathbf{Y}\mathbf{Y}^T = \mathbf{U}\mathbf{S}^2\mathbf{U}^T$ can be applied to obtain the POD modes. As this space is of reduced size compared to the original problem, the minimization problem is as well.

The problem is formulated by searching for an approximate flow solution $\widetilde{\mathbf{w}}(t_k)$ in the subspace $\mathbf{U}_r \in \mathbb{R}^{Nxr}$, $r \ll N$, where only the r most relevant basis vectors have been retained:

$$\widetilde{\mathbf{w}} = \sum_{i=1}^{r} a_i \mathbf{U}_i + \overline{\mathbf{w}} = \mathbf{U}_r \mathbf{a} + \overline{\mathbf{w}} \qquad (15.3)$$

with $\mathbf{a}$ being the vector of POD coefficients, minimizing the unsteady residual in the L_2 norm:

$$\min_{\mathbf{a}}\|\widehat{\mathbf{R}}(\mathbf{U}_r\mathbf{a} + \overline{\mathbf{w}})\|_{L_2}^2 = \min_{\mathbf{a}} \sum_{j=1}^{N} \Omega_j \widehat{R}_j^2(\mathbf{U}_r\mathbf{a} + \overline{\mathbf{w}}) \qquad (15.4)$$

The arising nonlinear least-squares problem for the POD coefficients $\mathbf{a}$ is solved by using a Levenberg algorithm [7]. So, an iterative procedure is performed where the

increment to coefficients $\Delta \mathbf{a}$ is obtained by solving the linear system:

$$(\mathbf{J}^T \mathbf{J} + \lambda \mathbf{I}) \Delta \mathbf{a} = -\mathbf{J}^T \widehat{\mathbf{R}} \tag{15.5}$$

with $J_{ij} = \frac{\partial \widehat{R}_i}{\partial a_j} \in \mathbb{R}^{N \times r}$ the Jacobian matrix of $\widehat{\mathbf{R}}$ with respect to the POD coefficients $\mathbf{a}$, and the non-negative damping factor λ, which is automatically adjusted at each iteration depending on the convergence rate of the algorithm. Each component of the gradient vector $\mathbf{g} \equiv -2\mathbf{J}^T \widehat{\mathbf{R}}$ can be scaled according to the curvature, here approximated by the pseudo-Hessian matrix $\mathbf{B} \equiv \mathbf{J}^T \mathbf{J}$, in order to avoid slow convergence in the direction of small gradients. Therefore, replacing the identity matrix $\mathbf{I}$ with the diagonal matrix consisting of the diagonal elements of the pseudo-Hessian matrix, leads to the well-known Levenberg–Marquardt algorithm, which solves iteratively the linear problem:

$$(\mathbf{J}^T \mathbf{J} + \lambda \mathrm{diag}(\mathbf{J}^T \mathbf{J})) \Delta \mathbf{a} = -\mathbf{J}^T \widehat{\mathbf{R}} \tag{15.6}$$

The rank-one Broyden's method is used to approximate the Jacobian of the reduced-order system of equations, from the knowledge of the Jacobian matrix (exact or approximated) built at the previous iteration step:

$$\mathbf{J}_{k+1} = \mathbf{J}_k + \frac{\Delta \widehat{\mathbf{R}} - \mathbf{J}_k \Delta \mathbf{a}}{\|\Delta \mathbf{a}\|^2} \Delta \mathbf{a}^T \tag{15.7}$$

so avoiding the time consuming computation of the $\mathbf{J}$ by finite differences at each iteration of the minimization procedure. Moreover, thanks to Broyden's update procedure, the expensive matrix-matrix computation $\mathbf{B} \equiv \mathbf{J}^T \mathbf{J}$ can be avoided. Indeed, by directly substituting Broyden's formula in the matrix product, one can obtain a way to computing also the pseudo-Hessian matrix from the knowledge of its values during the previous iteration step:

$$\mathbf{B}_{k+1} \equiv \mathbf{J}_{k+1}^T \mathbf{J}_{k+1} \tag{15.8}$$

$$= \mathbf{B}_k + \frac{\mathbf{J}_k^T \Delta \widehat{\mathbf{R}} - \mathbf{B}_k \Delta \mathbf{a}}{\|\Delta \mathbf{a}\|^2} \Delta \mathbf{a}^T + \Delta \mathbf{a} \frac{\Delta \widehat{\mathbf{R}}^T \mathbf{J}_k - \Delta \mathbf{a}^T \mathbf{B}_k}{\|\Delta \mathbf{a}\|^2} \tag{15.9}$$

$$+ \Delta \mathbf{a} \frac{\Delta \widehat{\mathbf{R}}^T \Delta \widehat{\mathbf{R}} - \Delta \widehat{\mathbf{R}}^T \mathbf{J}_k \Delta \mathbf{a} - \Delta \mathbf{a}^T \mathbf{J}_k^T \Delta \widehat{\mathbf{R}} + \Delta \mathbf{a}^T \mathbf{B}_k \Delta \mathbf{a}}{\|\Delta \mathbf{a}\|^4} \Delta \mathbf{a}^T \tag{15.10}$$

which can be rewritten in the compact form:

$$\mathbf{B}_{k+1} = \mathbf{B}_k + \frac{\boldsymbol{\omega}_k \Delta \mathbf{a}^T + \Delta \mathbf{a} \boldsymbol{\omega}_k^T}{\|\Delta \mathbf{a}\|^2} + (\boldsymbol{\phi}_k^T \Delta \widehat{\mathbf{R}} - \boldsymbol{\omega}_k^T \Delta \mathbf{a}) \frac{\Delta \mathbf{a} \Delta \mathbf{a}^T}{\|\Delta \mathbf{a}\|^4} \tag{15.11}$$

with $\boldsymbol{\omega}_k \equiv \mathbf{J}_k^T \Delta \widehat{\mathbf{R}} - \mathbf{B}_k \Delta \mathbf{a}$, and $\boldsymbol{\phi}_k \equiv \Delta \widehat{\mathbf{R}} - \mathbf{J}_k^T \Delta \mathbf{a}$.

Using this formula, the computation of $\mathbf{B}$ (done at each iteration of the minimization process, for every physical time step) has complexity $\mathcal{O}(Nr + 16r^2 + N) \cong$

$\mathcal{O}(Nr)$, instead of $\mathcal{O}(Nr^2)$, where N is the order of the high-dimensional model (the number of conservative variables times the number of grid points) and r the order of the reduced order model (i.e. the number of POD modes used). It must be pointed out that this formula for updating the pseudo-Hessian it is not resulting from a direct approximation of **B**, but relies on the approximation of **J** through Broyden's update of the Jacobian matrix.

15.2.2 Initializing the Flow Solver with ROM Predictions

The predicted ROM solution is successively used as a restarting solution, initializing the DLR's CFD code TAU [6] at the time step under consideration. The aim is to reduce the number of inner iterations to converge the residual with respect to the conventional choice of restarting the unsteady computation using the previous time step solution. The ROM is used therefore as a predictor providing an improved initial guess for the iterative process.

The ROM-based initial guess is based on the information of the solutions collected for a certain number of previous time steps, thus realizing a moving window strategy. In other words, the predicted ROM solution is a linear combination of the most energetic POD modes of the snapshots collected progressively during the running simulation. Local ROMs are thus computed by applying the POD on the snapshots taken at the various time intervals, and updated after a certain number of time steps have been computed. Such approach leads to predictions based on the most recent snapshots, and therefore is more adequate for analysis where certain events exist over a relatively short time intervals, so to better capturing transient phenomena. The advantage of such an approach is that the POD is cheap and leads to low-dimensional ROMs, since only few snapshots are considered. However the POD must be applied many times during the simulation, therefore increasing the total online computational cost of the ROM prediction. Moreover, a poor ROM prediction may happen when the POD is computed over a set of TAU snapshots, collected during a certain time interval, which do not contain information about a phenomena or behavior that will be present in the following time steps to be simulated (e.g. the appearance of a shock wave due to a change in the angle of attack). Restarting the CFD solver TAU with such a poor ROM prediction may lead to an increased number of iterations to converge, compared to restarting the flow solver using the TAU flow solution at the previous time step.

Alternatively, a previously computed POD basis (e.g., generated based on data from a training maneuver exciting a broad band of frequencies and amplitudes) may be employed. This approach aims to collect snapshots coming from a time simulation covering a large domain of the solution space where the flow solutions to be predicted are assumed to lie. The drawback is that the POD is applied to a greater number of snapshots compared to the moving-window approach, and the resulting POD basis is larger in size and thus the ROM more expensive to evaluate. However, only one POD has been computed offline and updating during the online prediction is not required.
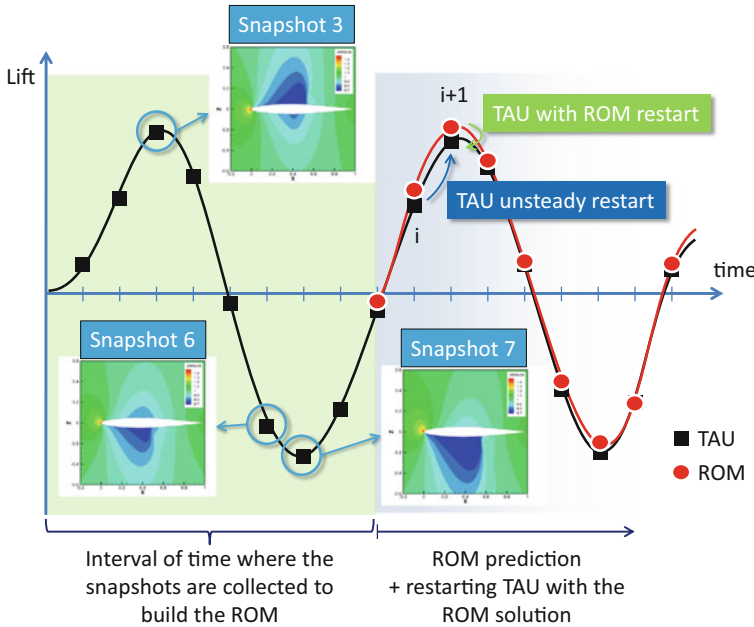
Fig. 15.1 Procedure to initialize DLR'S CFD code TAU with ROM predicted solutions in an unsteady simulation (schematic). In this sketch the ROM is built by applying POD to the TAU snapshots collected during a previous time interval

In the present work, such strategy has been used; indeed, knowing the type of unsteady simulations to be performed (i.e. periodic pitching oscillations at different frequencies), it can be easier to devise a single maneuver covering a broad range of the parameter space of interest (e.g. with a pitching oscillations sweeping in frequency) instead of apply to each single unsteady simulation a moving-windows strategy.

In any case, also for the moving window strategy it is generally recommended to employ an initial POD basis obtained from a generic training maneuver exciting different frequencies and amplitudes, and to then update the basis whenever a new high-fidelity CFD snapshot coming from the time-marching method is available.

Figure 15.1 sketches a restarting process where a ROM is built using snapshots of the flow field collected progressively during a time-marching simulation. In the standard TAU unsteady time marching procedure the solution at the $(i + 1)$th time step is initialized with the solution at the ith time step. Conversely, the ROM-based restarting procedure makes use of the ROM prediction at the $(i + 1)$th time step to initialize TAU at the same time step. Such an approximate ROM solution may be "closer" (depending on the level of unsteadiness of the simulation and on the size of the time steps used) to the final converged TAU solution at the $(i + 1)$th time step than that provided by the solution at the previous time step. Note that a ROM prediction is nothing else that a linear combination of POD modes derived from snapshots. Therefore, it is is only as good as the snapshots used to generate the ROM. It is

not possible to correctly represent flow dynamics or physics not already contained in the snapshots dataset to which the POD is applied. Since the ROM predictions will depend on the training data used to generate the subspace spanned by the POD modes, the building of the ROM must be application driven, i.e., attention must be paid to the training maneuver, which must cover the desired parameter space (e.g. angle of attack range, amplitudes and frequencies) that the simulation will span. It is remarked here, however, that in this context the ROM is used as a pre-processing step in solving the full-order model, and it not intended as a substitute to the CFD solver TAU. Therefore, it must only provide for an approximate solution close enough to the solution to which the iterative procedure will converge, thus reducing the number of inner iterations and the computational cost.

15.2.3   Numerical Test Cases

The ROM-based restarting procedure is applied to the LANN wing, for which the geometrical data are shown in Table 15.1. The LANN wing is defined by two super-critical cross sections at the root and tip chord. Sections between root and tip are derived by linear interpolation. The model has a span of 1 meter and a root chord of 0.3608 m. The quarter-chord sweep angle is 25°. The taper ratio (c_{tip}/c_{root}) is 0.4, the aspect ratio is 7.92 and the airfoil thickness is about 12%. The twist between root and tip is 4.6°.

Table 15.1 Geometrical data of the LANN (Lockheed-Air Force-NASA-NLR) wing model [8]

Model Data		
	half span $s/2$	1.0 m
	c_{tip}	0.1444 m
	c_{root}	0.3608 m
	x_{ref} (pitch-axis)	0.2240 m
	ϕ_{LE}	27.493°
	ϕ_{TE}	16.908°
	$\phi_{25\%}$	25°
	reference area	0.2526 m^2
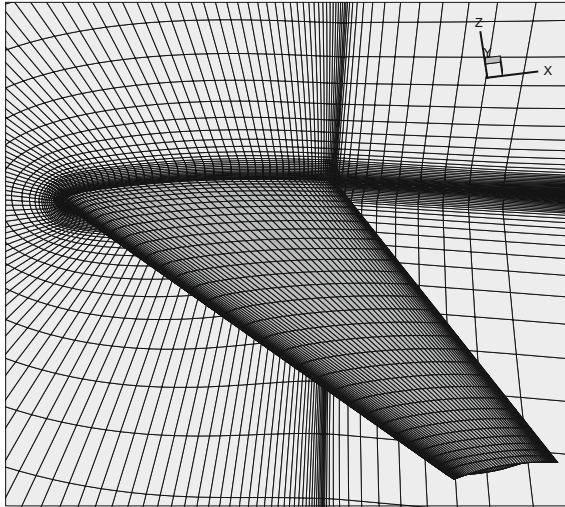
Fig. 15.2 Mesh of the LANN wing

A transonic viscous flight condition at a freestream airspeed of 271.66 m/s, a Mach number of 0.82, a Reynolds number based on c_{root} of $7.31 \cdot 10^6$ and 0.6° angle of attack is considered. At this condition, a periodic pithing oscillation about the unswept reference axis (located at 0.2240 m from the leading edge of the root airfoil) with 0.25° of amplitude and a reduced frequency based on c_{root} of 0.204 has been performed. It must be noted that the ROM-based restarting procedure does not require a periodic state. The procedure is valid for any kind of unsteady maneuver, periodic or not. The ROM can indeed also predict transitory responses.

The RANS equations with the Spalart–Allmaras (negative version) turbulence model have been used to model the flow with the TAU code. A structured mesh having 469, 213 grid points and 450, 560 elements is used for the computation, as showed in Fig. 15.2.

Since a periodic state can be achieved already at the second period, the simulation has been performed for 100 time steps, with 50 time steps per period (which have been shown to be sufficient for a good resolution with respect to time) using a dual time step method with a 2nd order backward difference discretization (BDF2). A study has been performed, where the convergence criterion has been set up to a minimum density residual of $1 \cdot 10^{-4}$, $1 \cdot 10^{-5}$ and $1 \cdot 10^{-6}$, with a maximum number of 100, 200 and 500 inner iterations to converge.
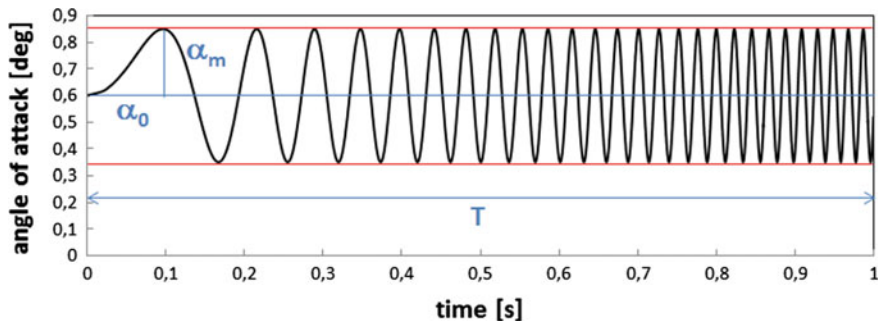
Fig. 15.3 Linear chirp signal used for the time-simulated pitching oscillation manoeuvre

A linear chirp maneuver defined as:

$$\alpha(t) = \alpha_0 + \alpha_m sin(\omega(t)t) \tag{15.12}$$

$$= \alpha_0 + \alpha_m sin\left(\frac{\omega_{max}}{T}t^2\right) \tag{15.13}$$

$$= \alpha_0 + \alpha_m sin\left(\frac{2\pi f_{max}}{T}t^2\right) \tag{15.14}$$

with $\alpha_m = 0.25°$ pitch amplitude and a maximum reduced frequency of $k_{max} = \omega_{max}c_{root}/V_\infty = 0.22$ ($f_{max} = 26.95\,\text{Hz}$), reached at time $t = T = 1\,\text{s}$, has been used as a training signal (see Fig. 15.3). The simulation has been performed using about 20 time steps per pseudo-period, linearly distributed with time over the total length of the simulation, for a total of 500 time steps. From this maneuver flow field snapshots have been collected and POD has been applied to them in order to get the POD modes. The modes have been used to build the ROM, which in turn has been used to predict, at each physical time step, an approximate flow solution for the periodic pitch oscillation. The approximate ROM prediction has successively been used to initialize the inner iterations of the CFD solver TAU.

15.2.4 Numerical Results

The time histories of the lift and moment coefficients of the LANN wing due to the periodic pitch oscillation are shown in Figs. 15.4 and 15.5, respectively. The results shown hereafter refer to the case study with convergence to a minimum density residual of $1 \cdot 10^{-4}$ and a maximum number 200 inner iterations. Both the approximate solution predicted by the ROM, which is used in the inner-loop restarting procedure as an initial guess, as well as the converged TAU solution are shown. The approximate ROM prediction is seen to be quite accurate (see e.g. the lift coefficient at time step 52 in the detailed view in Fig. 15.4), thus providing a better initial guess
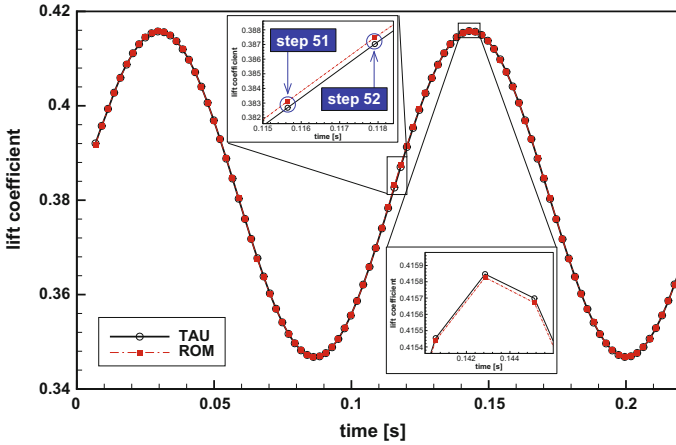
Fig. 15.4 Lift coefficient time history of the full-order model (TAU) and the ROM predictions used in the restarting procedure
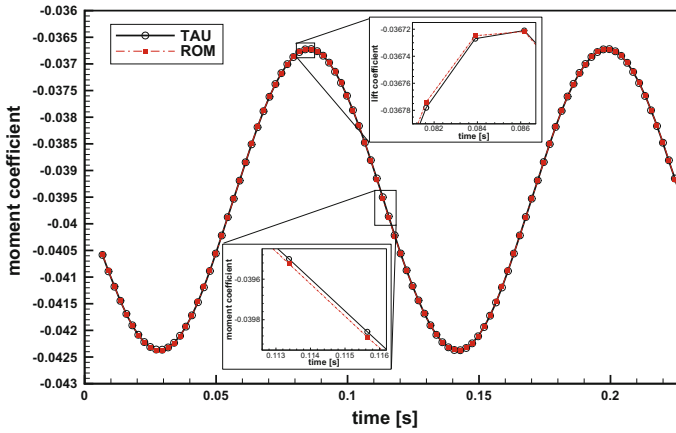
Fig. 15.5 Pitching moment coefficient (about the reference axis) time history of the full-order model (TAU) and the ROM predictions used in the restarting procedure

for TAU than by initializing the time step using the converged solution at the previous time step (see time step 51 in the detailed view in Fig. 15.4).

This is usually more emphasized when the solution presents large temporal gradients, as shown by the comparison of the nondimensional pressure between the approximate ROM solution and the CFD solution for time steps 51 and 52 (corresponding to the maximum time derivative of the solution). The pressure distribution of the wing's upper surface computed with TAU for time step 52 is shown in Fig. 15.6, the ROM prediction is shown in Fig. 15.7, while the TAU solution at the previous time step (51) is shown in Fig. 15.8. Figures 15.9 and 15.10 show the corresponding
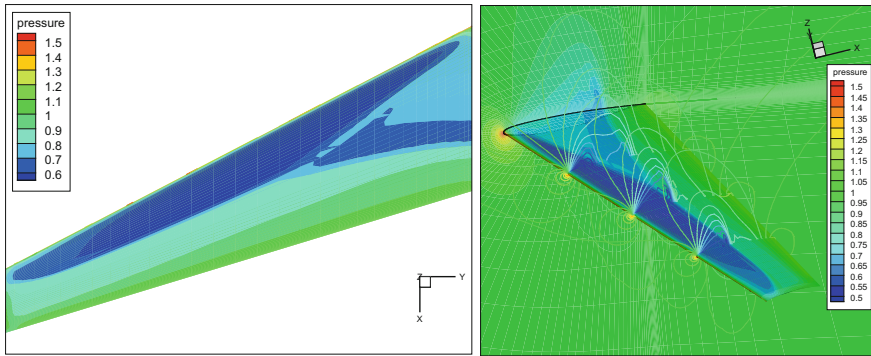
Fig. 15.6 CFD solution at time step 52

Fig. 15.7 ROM solution at time step 52
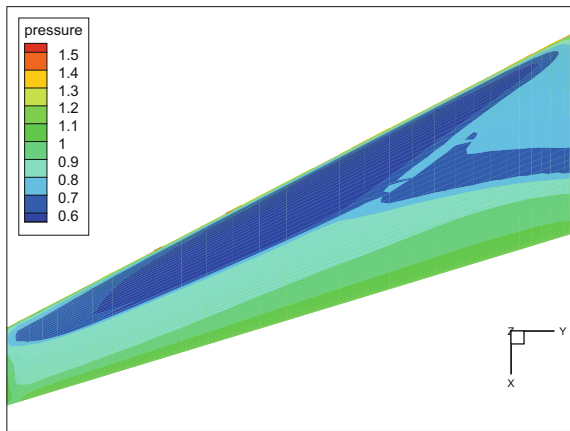
Fig. 15.8 CFD solution at time step 51
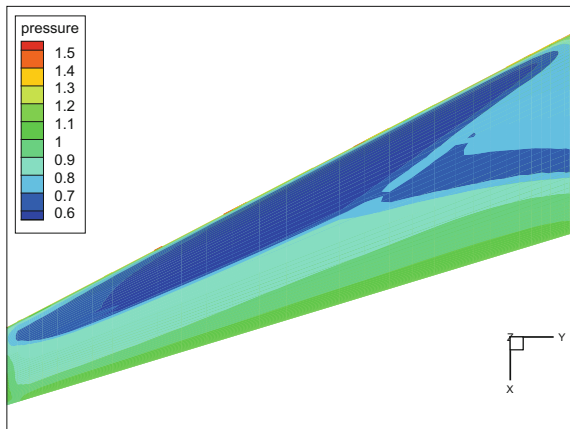
Fig. 15.9 Relative error between the nondimensionalized pressure of the CFD solution at time step 52 and the ROM prediction at time step 52
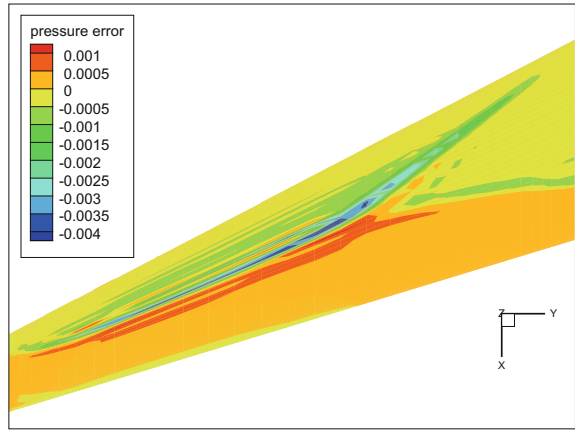
Fig. 15.10 Relative error between the nondimensionalized pressure of the CFD solution at time step 52 and the CFD solution at time step 51
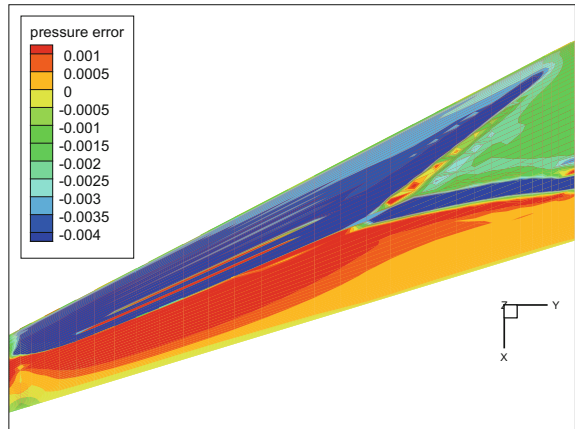
signed relative difference $((p_{TAU}^{52} - p_{restart})/p_{TAU}^{52}$ between the TAU solution at time step 52 and the solution used for initializing TAU with $p_{restart} = p_{ROM}^{52}$ in Fig. 15.9 and $p_{restart} = p_{TAU}^{51}$ in Fig. 15.10. As expected, the difference between the TAU solutions at two consecutive time steps (51 and 52) is much larger than of the difference between the TAU solution and the ROM prediction at the same time step. Such differences are more relevant in the vicinity of the shock wave, which is moving back and forth in the chord-wise direction over the wing during the simulation.

A better initial guess provided by the approximate ROM solution is reflected in the computational cost of the simulation. In particular, using the ROM solution to restart the TAU computation at each time step decreases the number of residual calls (Fig. 15.11), the wall-clock time (Fig. 15.12) and the CPU time (Fig. 15.13) with respect to the standard unsteady restarting procedure.

It must be pointed out that number of residual calls for the TAU+ROM restarting procedure includes: the residual calls needed to build the ROM Jacobian by finite

Fig. 15.11 Comparison of the number of residual calls needed to converge the solution at each physical time step by the standard TAU (black line) unsteady restarting procedure and when TAU is initialized with the ROM inner restart (blue line). The number of residual call needed to solve the nonlinear least squares problem for a ROM prediction are also shown (red line)
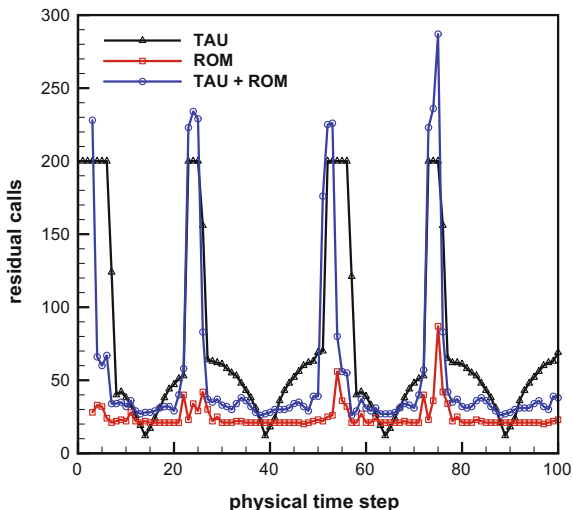
Fig. 15.12 Comparison of the wall-clock time needed at each physical time step by the standard TAU unsteady restarting procedure and by TAU with the ROM inner restart
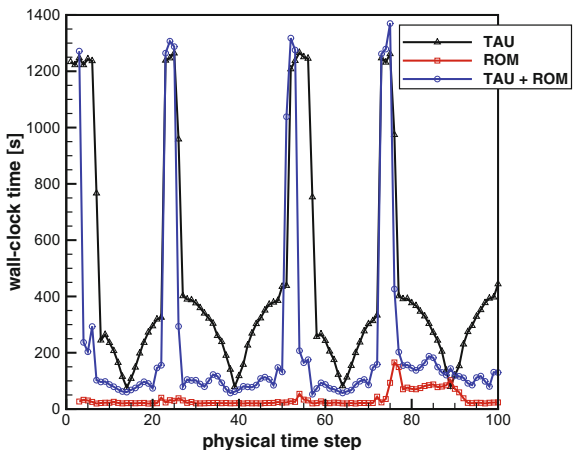
differences (which is equal to the number of POD modes), the residual calls during the nonlinear least squares iterations to minimize the unsteady residual and the residual calls needed for the CFD solver (TAU) to converge to the solution. This is why the total number of residual calls for the TAU+ROM restarting procedure may exceed the maximum number of inner iterations, which has been fixed to 200 in the results shown here, see Fig. 15.11.

When comparing the number of residual calls (Fig. 15.11) and the computational time (Figs. 15.12 and 15.13) it must be noted that the nonlinear least-squares procedure used to compute the ROM predictions makes use of the so-called *residual-only solver* of TAU, whereas TAU makes use of the *flow solver*, which employs a multigrid procedure to converge the flow solution.

Fig. 15.13 Comparison of
the CPU time needed at each
physical time step by the
standard TAU unsteady
restarting procedure and by
TAU with the ROM inner
restart
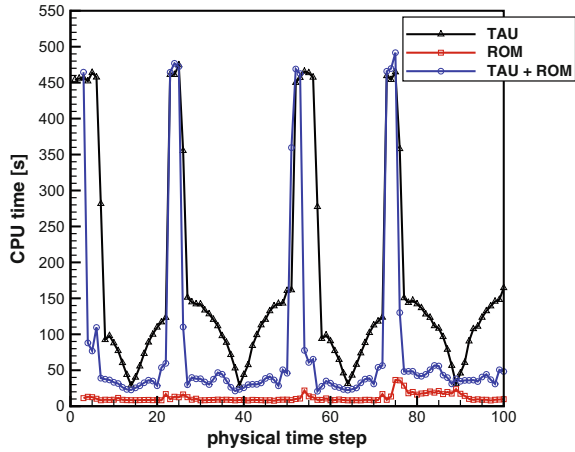
Fig. 15.14 Typical residual
convergence history for a
selected time step
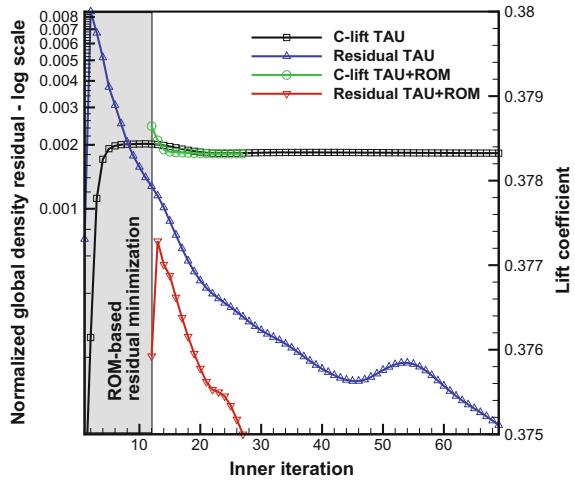
Figure 15.14 compares a typical convergence history of the inner-loop residual (for
a given physical time steps of the unsteady response) when the CFD solver (TAU)
is initialized with the solution at the previous time step (the standard approach)
and when it is initialized with the ROM predicted solution. In the latter case, the
convergence history of the residual starts at the number of nonlinear least-squares
iterations (in general about 10–15 iterations) needed to obtain the ROM solution.
After every iteration of the TAU solver the norm of the residual is computed in order
to monitor the convergence of the solution process. For each control volume a local
residual vector is computed, composed of the residuals of the density, momentum
and energy, and one or more components associated to the turbulence equations.
The global density residual for the monitoring output, normalized with respect to the
global residual of the steady state, is computed as the root mean square value:

$$\|res_\rho\| = \frac{\sqrt{\sum_{j=1}^{N} \frac{res_{\rho,j}^2}{N}}}{\|\mathrm{res}_\rho\|_{\mathrm{steady}}} \tag{15.15}$$

with N being the number of grid points. Here, it is converged to a minimum value of $1 \cdot 10^{-4}$, with a maximum number of inner iterations of 200 per time step. The convergence history of the ROM is not shown because the Levenberg–Marquardt method employed to solve the nonlinear least-squares problem makes use of a different objective function and different stopping criteria to determine the convergence of the ROM solution than the TAU solver. From Fig. 15.14 it can be seen how the first TAU residual computed using the ROM predicted solution as an initial guess is lower than the first residual computed using the TAU solution at the previous time step.

The TAU solver shows some difficulty to converge for time steps with high angular velocity, i.e., the maximum temporal change of angle of attack and thus the maximum change in time of the flow field, as can be seen in Fig. 15.15 where the number of residual calls increases up to the point where the imposed maximum number of inner iterations (i.e. 200) is reached. In these cases, the global density residual shows an oscillating behaviour (Figs. 15.16 and 15.17) and starting with the better initial guess provided by the ROM may (Fig. 15.16) or may not (Fig. 15.17) have a beneficial effect, leading to a faster and oscillation-free convergence.

The convergence behaviour may be improved by choosing a different set-up of the TAU solver, e.g., reducing the CFL number or reducing the time-step size. The current setup has been chosen as a compromise between obtaining accurate results
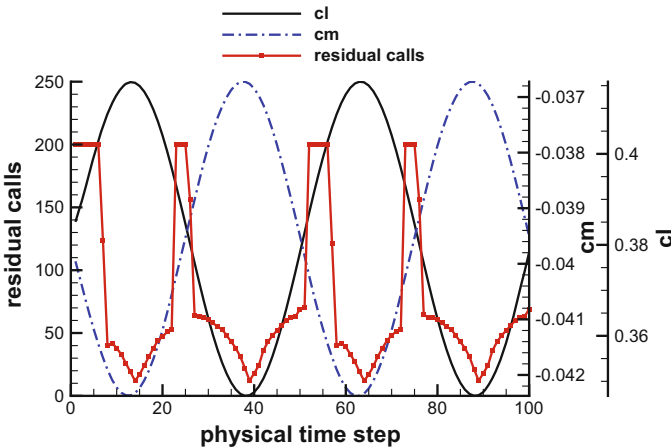
Fig. 15.15 Time history of the lift and moment coefficients and the number of residual calls (i.e. inner iterations) necessary to converge the global density residual to a value of $1e^{-4}$ for the standard unsteady restarting procedure of the TAU solver

Fig. 15.16 Global density residual at a selected time step showing an oscillatory behavior for the standard TAU restarting procedure
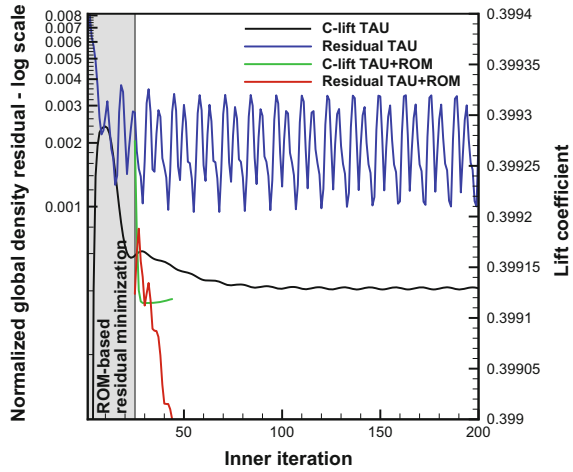
Fig. 15.17 Global density residual at a selected time step showing an oscillatory behavior for both the standard TAU and the ROM-based restarting procedure
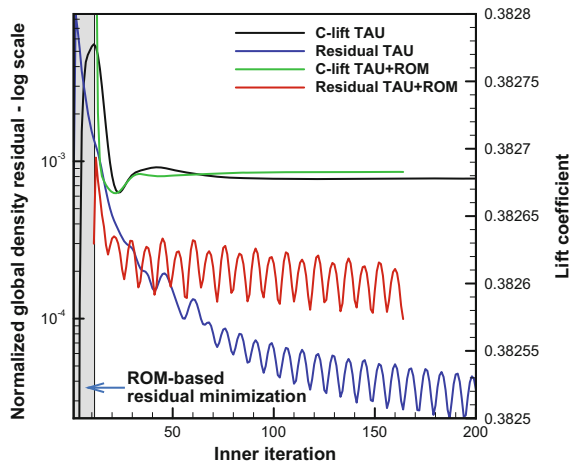
in terms of aerodynamic loads (pressure distribution, lift and moment coefficient) and a reasonable computational time.

Table 15.2 summarizes the performance in terms of computational cost of the unsteady pitching oscillating simulations for different convergence criteria (i.e., minimum residual and maximum number of inner iterations). The *Performance* column shows the speed-up factor and the reduction in the number of TAU iterations (TAU calls). *Total calls* refers to how many residual calls were due to the ROM optimization process plus the following TAU iterations to convergence of the solution. *TAU calls* refers to the reduction in the number of TAU iterations to convergence (initialized with the standard approach or with a ROM predicted solution). The simulations have been performed in parallel using 10 processors.

Table 15.2 Performance of standard TAU and the ROM-based TAU restarting procedure

Convergence criteria		TAU with standard unsteady restart		TAU with ROM-based restart		Performance		
Min. residual	Max. inner iterations	WC time [s]	Residual calls	WC time [s]	Residual calls (TAU+ROM)	Speed-up factor	Total calls reduction	TAU calls reduction
$1e^{-4}$	100	10h 53 min	5482	6h 44 min	4671 (2272 + 2399)	1.62	1.17	2.41
$1e^{-5}$	100	17h 27 min	9466	12h 27 min	6757 (4677 + 2080)	1.40	1.40	2.02
$1e^{-6}$	100	18h 26 min	10000	17h 52 min	10000 (7936 + 2064)	1.03	1.00	1.26
$1e^{-4}$	200	12h 52 min	7341	7h 15 min	5464 (3052 + 2412)	1.77	1.34	2.41
$1e^{-5}$	200	25h 50 min	14238	23h 47 min	15309 (12905 + 2404)	1.09	0.93	1.10
$1e^{-4}$	500	22h 49 min	12379	12h 25 min	8556 (6222 + 2334)	1.84	1.45	1.99

It must be noted that these results do not include information of the offline cost in building the ROM, which must be also considered in the overall evaluation of the efficiency of the ROM-based restarting process. For the case analyzed here the offline cost is the combination of running a TAU simulation, collecting the snapshots and applying a proper orthogonal decomposition. The chirp maneuver used as training simulation was computed using 500 physical time steps, with a maximum of 100 inner iterations and a minimum residual of $1 \cdot 10^{-4}$. The wall-clock time of the simulation was 50h16 min. The proper orthogonal decomposition used to obtain the POD modes lasted for 7 min. The ROM was build using 17 POD modes.

As can be seen from Table 15.2, the number of residual calls of the ROM does not show significant variations with respect to changes in the converge criteria parameters (minimum residual tolerance and maximum inner iterations). Indeed, the ROM predicted solution ($\mathbf{w}_{rom}$) at a generic time step t_{n+1} depends on the TAU solutions ($\mathbf{w}_{TAU}$) at the actual and old time steps, t_n and t_{n-1}, respectively, only through the definition of the unsteady residual vector to minimize, as shown in the equation below:

$$\widehat{\mathbf{R}} \stackrel{def}{=} \mathbf{Res}(\mathbf{w}_{rom}(t_{n+1})) + \mathbf{\Omega} \frac{3\mathbf{w}_{rom}(t_{n+1}) - 4\mathbf{w}_{TAU}(t_n) + \mathbf{w}_{TAU}(t_{n-1})}{2\Delta t} \quad (15.16)$$

If the TAU solutions are properly converged for every minimum global density residual tolerance considered (i.e., $1 \cdot 10^{-4}, 1 \cdot 10^{-5}$, and $1 \cdot 10^{-6}$) then the ROM predicted solution at the generic time step t_{n+1}, which is used to initialize TAU at that time step, is the same for all the convergence criteria considered. Only the number of inner iterations of the TAU solver to convergence changes for the selected tolerance. The more the tolerance is decreased the more iterations and computational time are required. Therefore the performance and effectiveness of the overall ROM-based restarting process are given mainly by two points: first by how accurate the ROM prediction is and second by how much the global density residual of the CFD solver is to be reduced, influencing thus the number of iterations. Requiring a high maximum residual (e.g. $1 \cdot 10^{-4}$) would give an advantage to the ROM-based restarting procedure over the standard one (assuming that the ROM prediction is quite accurate). This is because fewer iterations of the TAU solver will be necessary to converge. Decreasing the desired maximum residual will reduce the speed-up improvement because more TAU iterations (involving multigrid operations) will be required, thus nullifying the effect of the ROM in providing a good initial guess.

15.3   Conclusions and Remarks

An unsteady simulation of a LANN wing in transonic viscous flow has been performed. The motion analyzed is a periodic pitching oscillation which, for the selected amplitude and frequency parameters, does not show a nonlinear behavior in the lift and moment quantities, but it has an important nonlinear behavior of the flow field,

characterized by a moving lambda-shaped shock wave, typical for swept wings under transonic on-flow conditions.

The CFD TAU unsteady simulation where the restarting process make use of the ROM predicted solution as initial guess for computing the flow field at a certain physical time step showed a speed-up, compared to running the CFD TAU solver directly and using the previous time step solution as restarting point.

Such speed-up may vary depending on the convergence criteria set-up for the minimum residual, but it is however not yet fully satisfactory.

It is nevertheless evident that improving the capability of the ROM prediction (e.g. using nonlinear manifold learning techniques, like Isomap) would accelerate the TAU inner-loop convergence in case of unsteady simulations, in particular when the required minimum global density residual is not very demanding.

Further speed-up of the ROM prediction step may be achieved by using hyper reduction techniques (e.g. gappy POD, missing point estimation, empirical interpolation), which make use of a subset of the computational mesh over which evaluate the data, or through sparsity-promoting techniques, which make use of a subset of the POD modes/snapshots having the greatest contribution on the quality of approximation.

An analysis of the ROM-based restarting approach focusing on the convergence of an output of interest (e.g. lift and moment) through the Cauchy convergence criteria would be helpful in understanding the real soundness of the method in an industrial context, where the main purpose of unsteady simulations is to get accurate aircraft loads.

References

1. T. Franz, R. Zimmermann, S. Görtz, N. Karcher, Interpolation-based reduced-order modelling for steady transonic flows via manifold learning, in special issue: reduced order modelling: the road towards real-time simulation of complex physics. Int. J. Comput. Fluid Dyn. **28**(3–4), 106–121 (2014)
2. P. A. LeGresley, J. J. Alonso, Investigation of non-linear projection for POD based reduced order models for aerodynamics, 39th AIAA aerospace sciences meeting and exhibit, AIAA Paper 2001-0926 (2001)
3. R. Zimmermann, S. Görtz, Non linear reduced order models for steady aerodynamics. Procedia Comput. Sci. **1**(1), 165–174 (2010). ICCS 2010
4. R. Zimmermann, S. Görtz, Improved extrapolation of steady turbulent aerodynamics using a non-linear POD-based reduced order model. Aeronaut. J. **116**(1184), 1079–1100 (2012)
5. M. Mifsud, R. Zimmermann, S. Görtz, Speeding-up the computation of high-lift aerodynamics using a physics-based reduced-order model. CEAS Aeronaut. J. **6**(1), 3–16 (2015)
6. D. Schwamborn, T. Gerhold, R. Heinrich, The DLR TAU-code: recent applications in research and industry, ECCOMAS CFD 2006 (2006)
7. J. Nocedal, S.J. Wright, *Numerical Optimization* (Springer, New York, 2006)
8. J.J. Horsten, R.G. den Boer, R.J. Zwaan, Unsteady transonic pressure measurements on a semispan wind tunnel model of a transport-type supercritical wing, Part I general description, Aerodynamic coefficients and vibration modes, AFWAL-TR-83-3039, Air Force Wright Aeronautical Laboratories (1982)

Chapter 16
Surrogate-Based Aerodynamic Shape Optimization of a Wing-Body Transport Aircraft Configuration

Zhong-Hua Han, Mohammad Abu-Zurayk, Stefan Görtz and Caslav Ilic

Abstract Aerodynamic shape optimization driven by high-fidelity computational fluid dynamics (CFD) simulations is still challenging, especially for complex aircraft configurations. The main difficulty is not only associated with the extremely large computational cost, but also related to the complicated design space with many local optima and a large number of design variables. Therefore, development of efficient global optimization algorithms is still of great interest. This study focuses on demonstrating surrogate-based optimization (SBO) for a wing-body configuration representative of a modern civil transport aircraft parameterized with as many as 80 design variables, while most previous SBO studies were limited to rather simple configurations with fewer parameters. The freeform deformation (FFD) method is used to control the shape of the wing. A Reynolds-averaged Navier-Stokes (RANS) flow solver is used to compute the aerodynamic coefficients at a set of initial sample points. Kriging is used to build a surrogate model for the drag coefficient, which is to be minimized, based on the initial samples. The surrogate model is iteratively refined based on different sample infill strategies. For 80 design variables, the SBO-type optimizer is shown to converge to an optimal shape with lower drag based on about 300 samples. Several studies are conducted on the influence of the resolution

Z.-H. Han · M. Abu-Zurayk · S. Görtz (✉)
Aerodynamic Surrogates and Optimization Group, DLR Institute of Aerodynamics
and Flow Technology, Braunschweig, Germany
e-mail: stefan.goertz@dlr.de

Z.-H. Han
e-mail: zhong-hua.han@dlr.de

M. Abu-Zurayk
e-mail: mohammad.abu-zurayk@dlr.de

C. Ilic
Multi-Disciplinary Optimization Group, DLR Institute of Aerodynamics
and Flow Technology, Braunschweig, Germany
e-mail: caslav.ilic@dlr.de

of the computational grid, the number and randomness of the initial samples, and the number of design variables on the final result.

Nomenclature

C_L, C_D, C_M	= lift, drag and pitching moment coefficients
$\mathbf{F}$	= regression matrix for Kriging predictor
L	= likelihood function
m	= number of design variables
Ma	= Mach number
n	= number of high-fidelity sample points
p	= parameter for Gaussian correlation function
Re	= Reynolds number
R	= spatial correlation function
$\mathbf{R}$	= correlation matrix of Kriging model
$\mathbf{r}$	= correlation vector of Kriging model
$\hat{s}(\mathbf{x})$	= standard deviation of Kriging prediction
$\mathbf{S}$	= sampling sites for high-fidelity functions
$\mathbf{V}_{krig}$	= hierarchical Kriging predictor
$\mathbf{w}$	= Kriging weights
$\mathbf{x}, \mathbf{x}'$	= design variables
$\mathbf{x}^{(l)}, \mathbf{x}^{(u)}$	= lower and upper limit of design variables
$\mathbf{y}_S$	= response values
Y	= random function
$Z(\cdot)$	= Gaussian random process
α	= angle of attack
β_0	= coefficient of trend model for Kriging predictor
ξ	= weighted distance for spatial correlation function
μ	= Lagrange multiplier
θ	= hyper-parameter vector for spatial correlation function
δ	= the trust region radius
σ^2	= process variance of Kriging model

Subscripts

init	= initial value
k	= index $\in [1, m]$
S	= sampled data

Superscripts

(i)	= index $\in [1, n]$, referring to i-th sample point
$.'$	= new point
$\hat{.}$	= approximated value
$\tilde{.}$	= redefined value

16.1   Introduction

Over the past two decades, aerodynamic design via high-fidelity computational fluid dynamics (CFD) has received increasing attention in the aerospace community since CFD has matured to an extent that Navier-Stokes (NS) simulations are routinely applied to complex aircraft configurations. The traditional way of applying CFD to aerodynamic design is a manual process in which the designer has to decide what may be a better design based on CFD simulations of the current design. Obviously, the success of this heuristic process depends on the experience and knowledge of the designer and it is particularly hard to reach an optimal design, since the aerodynamic performance can be very sensitive to small (local) shape changes. A more efficient approach to aerodynamic design is based on shape optimization, where a CFD code is coupled with numerical optimization algorithms to automatically get the optimal design. Aerodynamic shape optimization is regarded as a key technology that can contribute to considerable aerodynamic performance improvements when it comes to modern transport aircrafts and may be a key enabler for developing radically new designs.

Despite the maturity of CFD algorithms and continuous progress in high-performance computing, aerodynamic shape optimization driven by high-fidelity and thus computationally expensive CFD is still very challenging, especially for complex aircraft configurations. The difficulties are not only associated with the computational cost of a single CFD computation, but also related to the high-dimensional design space and a potentially highly nonlinear objective function featuring many local optima (particularly for transonic flows). Therefore, the choice of the optimization algorithm is crucial in order to improve the aerodynamic performance as much as possible based on a limited number of CFD evaluations.

Starting from a baseline shape, the most efficient optimization methods use gradient information to find a direction or path towards the nearest (local) minimum of the objective function under aerodynamic and geometrical constraints. Studies using this method for aerodynamic shape optimization were pioneered in the 1970s, with gradients of the cost function evaluated with the finite-deference method. Hicks et al. [1] were first to use this method for airfoil design and then Hicks and Henne [2] extended it to wing design. The evaluation of gradient information using finite-differences suffers from the large computational cost associated with many design variables since each design variable needs to be perturbed separately and then the

flow field needs to be recalculated. This problem can be tackled by employing the adjoint method, which was first applied to transonic aerodynamic shape optimization problems by Jameson [3, 4] in the 1980s. The adjoint method is extremely efficient for gradient evaluation, since the cost of computing all partial derivatives of one objective or constraint function is nearly independent of the number of design variables, requiring one flow solution and one adjoint solution. The adjoint method greatly reduces the computational cost of aerodynamic shape optimization of complex aerodynamic configurations with many design variables and few objectives and constraints. Typically, the optimal shape can be obtained at the cost of 10–100 equivalent CFD evaluations. The adjoint method rapidly gained popularity [5–9], leading to a shift of the focus of aerodynamic design from the heuristic approach to numerical optimization. Nowadays, this method is still one of the most attractive methods for aerodynamic shape optimization of wings [10–12] and complex aircraft configurations [13].

Despite their fast convergence, gradient-based methods can be rather sensitive to the initial guesses or starting point and can easily be trapped in a local optimum [14]. The aerodynamic design space is usually multi-modal with many local optima, which are associated with the non-linear flow phenomena occurring in transonic or separated flows. Therefore, a gradient-free method with global optimization capability needs to be employed to explore the design space (see [15] or [36] for an example). Among the gradient-free methods, guided random search algorithms such as genetic algorithms (GA), simulated annealing (SA), or the particle swarm algorithm (PSA) are capable of finding the global optimum. However, when using this type of algorithms, a single shape optimization usually requires thousands of CFD simulations and the computational cost can easily exceed the available computational budget. This situation becomes even worse when dealing with full aircraft configurations parameterized with a large number of design variables. At DLR's Institute of Aerodynamics and Flow technologies, the subplex algorithm [16] has been the favored gradient-free algorithm in the past since it can deal with noisy objective functions and produces good results at acceptable computational cost for up to 15–20 design variables. Larger numbers of design parameters can make this algorithm very expensive depending on the complexity of the CFD model, especially in its currently employed sequential form.

Recently, surrogate-based optimization (SBO) (see [15, 17, 30, 31]) gained a lot of attention by aircraft design experts because it has been successfully applied to non-local optimization problems in the field of design optimization [18–21]. A surrogate model is a cheap-to-evaluate approximation model of the expensive-to-evaluate objective or constraint function and is built (or trained) based on limited observed data obtained by sampling the design space. To implement SBO, the simplest way is to build a sufficiently accurate surrogate model before the actual optimization process starts and then use it to completely replace the expensive CFD solver during the optimization. However, this is only applicable for low-dimensional problems as the required number of CFD evaluations for building an accurate surrogate model

increases exponentially with an increase in the number of design variables (the so-called curse of dimensionality [22–24]). To tackle this problem, an initial surrogate model can be built at the beginning of the process based on a few samples. Then, the model is adaptively refined with new sample points. The next point for evaluation is selected by optimizing some infill criterion [19], such as maximizing the expected improvement (EI) function [25] or minimizing the lower confidence bounding (LCB) function [26]. Using the computed objective value of the new point, the model is updated and the next evaluation is determined and so forth. As a result, additional sample points are adaptively clustered in promising regions of the design space and the efficiency of converging to the optimum can be dramatically improved compared to evolutionary algorithms. In this type of SBO framework, the role of the surrogate model is not to replace the flow solver in the optimization loop but rather to guide the search of a conventional optimization algorithms [29], either gradient-based or gradient-free, to the optimum by suggesting new sampling sites to be evaluated with CFD. From this point of view, the role of the surrogate model and the infill-sampling criteria is equivalent to that of the conventional optimizers, generating new designs based on known designs. In addition to using infill criteria to adaptively choose new sample points, gradient information [27] and lower-fidelity CFD analysis [28] can used be to enhance the predictions of the surrogate models and to speed up the SBO process, however, this is beyond the scope of this article.

Despite its potential for use in global optimization, application of the SBO-type optimization algorithms in the field of aerodynamic shape optimization of aircraft is currently limited to relatively simple configurations such as airfoils [30–33] or more complex configurations with a rather small number of design variables [34, 35]. There has been some debating whether the SBO-type optimizer can be applied to more realistic aircraft design problems and a few studies set out to compare SBO with its gradient-based counterpart [15, 36, 37]. While previous SBO work at DLR focused on developing and combining different infill criteria, on applying SBO to classical airfoils, natural laminar flow (NLF) airfoils and 2D high-lift configurations [38–40] and on comparing SBO with gradient-free optimization algorithms, this article is motivated by the aspiration to demonstrate an efficient SBO framework for minimizing the drag of a 3D wing-body transport aircraft configuration with as many as 80 design variables. A comprehensive study of the influence of the grid resolution, the randomness and number of the initial samples and the number of design variables is carried out to investigate the performance of the SBO method. An a posteriori study is also carried out to characterize the design space and to identify the important parameters.

The article is organized as follows: Sect. 16.2 gives an overview of the SBO-type optimization framework we are concerned with, with a special focus on the Kriging surrogate model and sample infill criteria used; Sect. 16.3 presents the numerical optimization results for a generic wing-body civil transport aircraft configuration. Section 16.4 details the result of an a posteriori study of the SBO results.

Fig. 16.1 Surrogtae-based optimization framework

16.2 Surrogate-Based Optimization (SBO)

16.2.1 Surrogate-Based Optimization Framework

For an m-dimensional problem, here we are concerned with solving the following single-objective optimization problem

$$
\begin{aligned}
\text{Min.}\quad & y(\mathbf{x}) \\
\text{s.t.}\quad & g_i(\mathbf{x}) \leq 0, i = 1, \ldots, n_c, \\
& \mathbf{x}^{(l)} \leq \mathbf{x} \leq \mathbf{x}^{(u)}
\end{aligned}
\tag{16.1}
$$

where $y(\mathbf{x})$ is the objective function; $g_i(\mathbf{x})$ denotes the constraint with n_c being the number of constraints; $\mathbf{x}$ is the vector of design variables with their upper and lower limits denoted by $\mathbf{x}^{(l)}$ and $\mathbf{x}^{(u)}$, respectively.

In this study we employ a framework for SBO as shown in Fig. 16.1. There are two loops in this framework: the main- and the sub-optimization. The main loop is exactly the same as that in conventional gradient-based or gradient-free optimization, in which the CFD evaluations are directed by the optimizer to find the optimal aerodynamic shape; the sub-optimization is in some way equivalent to the conventional optimizer (such as GA), which suggests the new design(s) to be evaluated by CFD. Note that compared to a conventional optimizer, the SBO optimizer is particularly useful when the objective and constraint functions are expensive to evaluate.

This SBO framework was realized as an object-oriented Python module based on DLR's surrogate modeling for aero-data toolbox, SMARTy [41, 42, 48]. A notable feature of this module is that it can be used as a generic optimizer in a similar way as any currently available gradient-based or gradient-free optimizer in Python. By importing this module, the user can easily set up a specific optimization problem. Here, we set up an aerodynamic shape optimization problem for a wing-body transport aircraft configuration. The basic steps of this process are as follows:

- **Step 1 - Initialization**: Define the objective function and constraints (such as minimizing C_D subject to constant C_L as well as wing thickness constraints); define the design variables and their range by parameterizing the aerodynamic shape using freeform deformation (FFD), the class/shape transformation (CST) method or any other methods.

- **Step 2 - DoE and CFD evaluations**: Design of experiments (DoE) methods [43], such as Latin hypercube sampling (LHS), are used to generate a number of initial sample points in the design space, with each sample representing a candidate aerodynamic shape. Computational grids are generated (or a grid for the baseline shape is deformed) for these candidate shapes and CFD computations are run to obtain the corresponding aerodynamic data needed to evaluate the objective function and constraints. Thereafter, this data is stored in a database. Note that, as an alternative to starting from scratch, it is possible to use and append to a given database, which was generated, for example, during a previous optimization run. This provides the flexibility to the user to terminate the optimization process any time and to restart later or to change the optimization strategy.

- **Step 3 - Building surrogate models**: Based on the sampled database, surrogate models are trained by fitting the model to the data and tuning the parameters. Note that we need to build surrogate models for each objective and constraint function. Once the surrogate models are built, the objective and constraint functions and their mean squared error (MSE) are very cheap to evaluate if compared to the expensive CFD simulations.

- **Step 4 - Solving sub-optimization problems corresponding to user-defined sample infill criteria**: Sample infill criteria determine the mechanism of how to generate new design(s) based on the surrogate model. Different sample infill criteria correspond to different sub-optimization problems, which are to be solved by using a conventional gradient-based and/or gradient-free algorithm. Note that the outcome of the sub optimization problem(s) is the new aerodynamic design(s) to be evaluated with CFD, which is expected to improve the surrogate model in a region of interest, either by further exploring the design or by exploiting a certain region of it.

- **Step 5 - CFD evaluation of new sample point(s)**: The computational grids for the new design(s) are generated (or deformed) and CFD simulation(s) are run to evaluate the aerodynamic performance. This newly obtained data is then used to augment the database.

- **Step 6 - Refinement and termination**: The surrogate models are updated and steps 3–5 are repeated until some termination criterion is satisfied.

- **Step 7 - Posterior treatment**: The optimum design(s) may be analyzed at off-design conditions and the sample-points in the database may be analyzed by other techniques, such as data mining techniques or sensitivity analysis. The posterior treatment may help to refine the settings or to identify key design parameters.

16.2.2 Surrogate Modeling

For an m-dimensional problem with m design variables, suppose we are concerned with the prediction of an expensive-to-evaluate (and unknown) high-fidelity aerodynamic function $y : \mathfrak{R}^m \to \mathfrak{R}$. Assume that the function y is sampled at sites

$$\mathbf{S} = \left[\mathbf{x}^{(l)}, \ldots, \mathbf{x}^{(n)}\right]^T \in \mathfrak{R}^{n x m} \tag{16.2}$$

with the corresponding responses

$$\mathbf{y}_S = \left[y^{(1)}, \ldots, y^{(n)}\right]^T = \left[y(\mathbf{x}^{(1)}), \ldots, y(\mathbf{x}^{(n)})\right]^T \in \mathfrak{R}^n. \tag{16.3}$$

Here n is the number of sampling sites. The pair $(\mathbf{S}, \mathbf{y}_S)$ denotes the sampled data sets in the vector space.

With the above descriptions and assumptions, our objective here is to build a surrogate model for predicting the output of a high-fidelity CFD code for any untried site $\mathbf{x} \in \mathfrak{R}^m$, that is, to estimate $y(\mathbf{x})$, based on the sampled data set $(\mathbf{S}, \mathbf{y}_S)$.

16.2.2.1 Kriging Surrogate Model

Kriging is a statistical interpolation method suggested by Krige [44] in 1951 for which the interpolated values are modeled by a Gaussian process. The theoretical basis for the method was developed by the French mathematician Matheron in 1963 [45]. Kriging gained popularity in design and analysis of deterministic computer experiments after the research work of Sacks et al. [46]. There are different versions of Kriging such as "simple Kriging", "ordinary Kriging" and "universal Kriging". All these versions are available in DLR's SMARTy toolbox. Here we give only a very brief description of ordinary Kriging as quite a lot of literature is available, see [49–51]. Assume a random process corresponding to the aerodynamic function y

$$Y(\mathbf{x}) = \beta_0 + Z(\mathbf{x}), \tag{16.4}$$

where β_0 is an unknown constant and $Z(\mathbf{x})$ is a stationary random process having zero mean and a covariance of

$$Cov\left[Z(\mathbf{x}), Z(\mathbf{x}')\right] = \sigma^2 R(\mathbf{x}, \mathbf{x}'). \tag{16.5}$$

Here, σ^2 is the process variance of $Z(\cdot)$ and $R(\mathbf{x}, \mathbf{x}')$ is the spatial correlation function, which only depends on the Euclidean distance between two sites, $\mathbf{x}$ and $\mathbf{x}'$. Assuming that the aerodynamic function can be approximated by a linear combination of the observed data $\mathbf{y}_S$, the Kriging predictor of $y(\mathbf{x})$ at an untried $\mathbf{x}$ is formally defined as

$$\hat{y}(\mathbf{x}) = \mathbf{w}^T \mathbf{y}_S, \tag{16.6}$$

where $\mathbf{w} = \left[w^{(1)}, \ldots, w^{(n)} \right]^T$ is a vector of weight coefficients associated with the sampled data. Then we can replace $\mathbf{y}_S = \left[y^{(1)}, \ldots, y^{(n)} \right]^T$ with the corresponding random quantities $\mathbf{Y}_S = \left[Y^{(1)}, \ldots, Y^{(n)} \right]^T$. We can also treat $\hat{y}(\mathbf{x})$ as random, and try to minimize its MSE

$$MSE\left[\hat{y}(\mathbf{x}) \right] = E\left[(\mathbf{w}^T \mathbf{Y}_S - Y(\mathbf{x}))^2 \right] \tag{16.7}$$

subject to the unbiasedness constraint

$$E\left[\sum_{i=1}^{n} w^{(i)} Y(\mathbf{x}^{(i)}) \right] = E\left[Y(\mathbf{x}) \right]. \tag{16.8}$$

Solving this constrained minimization problem by the method of Lagrange multipliers, we can get the optimum weight coefficient $\mathbf{w} = \left[w^{(1)}, \ldots, w^{(n)} \right]^T$. In turn, the mean and MSE of the Kriging prediction can be derived. The predicted mean value is

$$\hat{y}(\mathbf{x}) = \beta_0 + \mathbf{r}^T(\mathbf{x}) \underbrace{R^{-1}(\mathbf{y}_S - \beta_0 \mathbf{F})}_{=: \mathbf{V}_{krig}}, \tag{16.9}$$

where $\beta_0 = (\mathbf{F}^T \mathbf{R}^{-1} \mathbf{F})^{-1} \mathbf{F}^T \mathbf{R}^{-1} \mathbf{y}_S$ and

$$\mathbf{F} = [1, \ldots 1]^T \in \mathfrak{R}^n, \mathbf{R} := (R(\mathbf{x}^{(i)}, \mathbf{x}^{(j)}))_{i,j} \in \mathfrak{R}^{n \times n}, \mathbf{r} := (R(\mathbf{x}^{(i)}, \mathbf{x}))_i \in \mathfrak{R}^n. \tag{16.10}$$

Note that the vector $\mathbf{V}_{krig} \in \mathfrak{R}^n$ only depends on the observed data, and it can be calculated at the model fitting stage of Kriging. Once $\mathbf{V}_{krig}$ is obtained, the prediction of the unknown y at any untried $\mathbf{x}$ only requires recalculating $\mathbf{r}^T(\mathbf{x})$. The MSE of the Kriging prediction can be shown to be

$$MSE\{\hat{y}(\mathbf{x})\} \equiv \hat{s}^2(\mathbf{x}) = \sigma^2 \{ 1.0 - \mathbf{r}^T \mathbf{R}^{-1} \mathbf{r} + (\mathbf{r}^T \mathbf{R}^{-1} \mathbf{F} - 1)^2 / \mathbf{F}^T \mathbf{R}^{-1} \mathbf{F} \}. \tag{16.11}$$

16.2.2.2 Correlation Function

The construction of the correlation matrix $\mathbf{R}$ and the correlation vector $\mathbf{r}$ requires the calculation of the correlation function. The correlation function for random variables at two sites, $\mathbf{x}$ and $\mathbf{x}'$, is assumed to only depend on their spatial distance (namely $R(\mathbf{x}, \mathbf{x}') = R(\mathbf{x} - \mathbf{x}')$). A family of commonly-used correlation models is of the form

$$R(\mathbf{x}, \mathbf{x}') = \prod_{k=1}^{m} R_k(\theta_k, x_k - x'_k), \tag{16.12}$$

where $\theta = [\theta_1, \ldots \theta_m]^T \in \mathfrak{R}^m$ are the distance weights (so-called hyper-parameters to be tuned). The most popular form of this correlation function is the Gaussian exponential function. It is of the form

$$R_k(\theta_k, x_k - x'_k) = \exp(-\theta_k |x_k - x'_k|^{p_k}), 1 < p_k \le 2. \tag{16.13}$$

In this article, following the well-known DACE Kriging toolbox [47], a cubic spline correlation function is also employed due to its good performance as well as the feature of being second-order differentiable (a desired feature when gradient information is to be incorporated [48]). It is of the form

$$R_k(\theta_k, x_k - x'_k) = \begin{cases} 1 - 15\xi_k^2 + 30\xi_k^3 & \text{for } 0 \le \xi_k \le 0.2 \\ 1.25(1 - \xi_k)^3 & \text{for } 0.2 < \xi_k < 1, \text{ where } \xi_k = \theta_k |x_k - x'_k|. \\ 0 & \text{for } \xi_k \ge 1 \end{cases} \tag{16.14}$$

16.2.2.3   Hyperparameter Tuning via Maximum Likelihood Estimation

Assuming that the sampled data are distributed according to a Gaussian process, the responses at sample sites are considered to be correlated random functions

$$L(\sigma^2, \theta) = \frac{1}{\sqrt{2\pi(\sigma^2)^n |\mathbf{R}|}} \exp\left(-\frac{1}{2} \frac{(\mathbf{y}_s - \beta_0 \mathbf{F})^T \mathbf{R}^{-1}(\mathbf{y}_s - \beta_0 \mathbf{F})}{\sigma^2}\right), \tag{16.15}$$

where $\beta_0 = (\mathbf{F}^T \mathbf{R}^{-1} \mathbf{F})^{-1} \mathbf{F}^T \mathbf{R}^{-1} \mathbf{y}_S$. The optimal estimation of the process variance

$$\sigma^2(\theta) = \frac{(\mathbf{y}_S - \beta_0 \mathbf{F})^T \mathbf{R}^{-1}(\mathbf{y}_S - \beta_0 \mathbf{F})}{n} \tag{16.16}$$

is obtained analytically, yet depends on the unknown hyper-parameters $\theta = [\theta_1, \ldots, \theta_m]^T$. Substituting it into the associated Eq. 16.15 and taking the logarithm, we are left with maximizing the concentrated likelihood function

$$\theta = \underset{\theta}{\operatorname{argmax}}(-n \ln \sigma^2(\theta) - \ln |\mathbf{R}(\theta)|). \tag{16.17}$$

16.2.3 Sample Infill Criteria and Sub-optimization

Although there are a number of infill criteria available [52], here we are mainly concerned with two of the most popular criteria: one is called MSP (minimizing the surrogate prediction) and the other is called EI (expected improvement).

16.2.3.1 MSP Criterion

For MSP, the mathematical model of the sub-optimization for determining a new sample site is of the form

$$
\begin{aligned}
\text{Minimize} \quad & \hat{y}(\mathbf{x}) \\
\text{s.t.} \quad & \hat{g}_i(\mathbf{x}) \leq 0, i = 1, n_c, \\
& \mathbf{x}^{(l)} \leq \mathbf{x} \leq \mathbf{x}^{(u)}
\end{aligned}
\tag{16.18}
$$

where $\hat{y}(\mathbf{x})$ and $\hat{g}_i(\mathbf{x})$ are surrogate models of $y(\mathbf{x})$ and $g_i(\mathbf{x})$, respectively. Solving this constrained optimization problem by using a conventional optimization algorithm such as a genetic algorithm (GA) or any gradient-based method, we can get the approximated optimal design variables $\hat{\mathbf{x}}_{opt}$. Then, $\hat{\mathbf{x}}_{opt}$ is evaluated by the CFD code to get the corresponding aerodynamic performance coefficient and is compared with what was predicted by the surrogate models. If the error between the two is below a certain threshold, the optimization process can be terminated; if not, the new sample point is augmented to the sample data set and the surrogate model is rebuilt. Note that this criterion is suited for all kinds of surrogate models and is very efficient for local exploitation of promising regions in the design space.

16.2.3.2 Constrained EI Criterion

The Kriging prediction at any untried sample point can be regarded as a Gaussian distribution with the mean given by the Kriging predictor, $\hat{y}(\mathbf{x})$, and the variance given by the mean squared error, $\hat{s}^2(\mathbf{x})$. Then, we can compute the probability that the function value at any untried $\mathbf{x}$ would fall below the minimum among the sample points observed so far. The expected improvement (EI) function [25] can be calculated to account for the improvement of the objective function we expect to achieve at any untried $\mathbf{x}$. The definition of EI is of the form

$$
E\left[I(\mathbf{x})\right] = \begin{cases} (y_{min} - \hat{y}(\mathbf{x}))\Phi\left(\frac{y_{min}-\hat{y}(\mathbf{x})}{\hat{s}(\mathbf{x})}\right) + \hat{s}(\mathbf{x})\phi\left(\frac{y_{min}-\hat{y}(\mathbf{x})}{\hat{s}(\mathbf{x})}\right) & \text{if } \hat{s} > 0 \\ 0 & \text{if } \hat{s} = 0 \end{cases}
\tag{16.19}
$$

where $\Phi(\cdot)$ and $\phi(\cdot)$ are the cumulative distribution function and probability density function of a standard normal distribution, respectively; $y_{min} = Min(y^{(1)}, y^{(2)}, \ldots,$

$y^{(n)}$) denotes the best among the observed data so far. The greater the EI, the more improvement we expect to achieve, thus the point with maximum EI is located by a global optimizer such as a genetic algorithm (GA). Then a CFD computation is performed for this new sample point. For this sample infill criterion, constraints can be handled by introducing the probability that the constraints are satisfied. The corresponding sub-optimization problem can be modeled as

$$\text{maximize} \quad E\left[I(\mathbf{x})\right] \cdot \prod_{i=1}^{n_c} P\left[G_i(\mathbf{x}) \leq 0\right], \qquad (16.20)$$

$$\text{s.t.} \quad \mathbf{x}_l \leq \mathbf{x} \leq \mathbf{x}_u$$

where $P\left[G_i(\mathbf{x}) \leq 0\right]$ denotes the probability that the i-th constraint may be satisfied and $G_i(\mathbf{x})$ is a random function corresponding to the state function $g_i(\mathbf{x})$. Note that $P\left[G_i(\mathbf{x}) \leq 0\right] \to 1$ when the constraint is satisfied and $P\left[G_i(\mathbf{x}) \leq 0\right] \to 0$ when the constraint is violated. The probability of satisfying the constraint at any untried site, $P\left[G_i(\mathbf{x}) \leq 0\right]$ can be calculated by

$$P\left[G_i(\mathbf{x}) \leq 0\right] = \frac{1}{\hat{s}_i(\mathbf{x})\sqrt{2\pi}} \int_{-\infty}^{0} e^{[G_i(\mathbf{x})-g_i(\mathbf{x})]^2/2\hat{s}_i^2(\mathbf{x})} dG_i(\mathbf{x}) = \Phi\left(\frac{-g_i(\mathbf{x})}{\hat{s}_i(\mathbf{x})}\right) \quad (16.21)$$

where $\hat{s}_i(\mathbf{x})$ denotes the estimated standard error corresponding to the surrogate model $\hat{g}_i(\mathbf{x})$.

The optimum sample site $\hat{\mathbf{x}}_{opt}$ obtained by solving Eq. 16.21 is observed by running the CFD code and the new sample point is augmented to the sample date set; the surrogate models are rebuilt and the whole process is repeated until the maximum EI is below a value set by the user. Note that the EI method has the capability of efficiently finding the global optimum and therefore this optimization strategy is also called efficient global optimization (EGO) [25].

16.2.3.3   EI Criterion with Dynamic Search Space Updating

The EI method rapidly gained popularity due to its good capability of finding the global optimum within a limited number of function evaluations (see [30]). However, when the EI method is applied to aerodynamic shape optimization, it turns out that due to the fact that the design space is large and the objective function is complicated it is typically very difficult to obtain the real global optimum. To make this method work, one generally has to choose a baseline shape and then set a very small design space around the baseline shape. Since the design space is restricted to small changes around the baseline, chances of obtaining a more global optimum than a gradient-based method are very limited. To tackle this problem, we propose to use a strategy where we dynamically search the design space for the maximum of the constrained EI function. This method is similar to the trust-region method in [53]. For this method, the sub-optimization problem is modified as

$$\text{maximize} \quad E\left[I(\mathbf{x})\right] \cdot \prod_{i=1}^{n_c} P\left[G_i(\mathbf{x}) \leq 0\right], \tag{16.22}$$

$$\text{s.t.} \ \ \mathbf{x}^* - \delta \leq \mathbf{x} \leq \mathbf{x}^* + \delta$$

This means that for every iteration of the SBO-type optimization process, the maximization of the constrained EI function is restricted to a relatively small space around the best design obtained so far, which is denoted by $\mathbf{x}^*$. Along with the changing $\mathbf{x}^*$, the search space for maximizing the constrained EI function is also moving. In addition, the search radius, δ, can be adaptively modified. By using this modified constrained EI criterion with dynamic search space updating, the chance of obtaining a nearly globally optimal design in a limited number of CFD computations is greatly increased.

16.3 Results for a Generic Wing-Body Transport Aircraft Configuration

16.3.1 Test Case Description and Parameterization

The baseline shape employed for this study is a clean wing-body configuration similar to existing Airbus wide-body transport aircraft. In the DLR research project Digital-X [54], this aircraft configuration was used as a benchmark test case for demonstrating multidisciplinary design optimization of a complete aircraft. Here, we are concerned with the single-point aerodynamic shape optimization of the wing-body configuration (see Fig. 16.2 for the surface grid), at the cruise condition: $Ma = 0.83$, $Re = 43.4 \cdot 10^6$ and $C_L = 0.5$, to demonstrate our newly-developed SBO-type optimizer. The fuselage is fixed and the wing shape is parameterized by free-form deformation (FFD), with a number of control sections along the wing span. See Fig. 16.2 for the schematics of the wing parameterization with 8 control sections along the wing span and 10 nodes for each section, resulting in total number of 80 FFD nodes. The objective here is to minimize the drag, subject to lift and sectional thickness constraint of wing. The optimization mathematical model is of the form.

$$\text{Minimize} \ \ C_D \tag{16.23}$$

$$\text{s.t.} \ \ C_L = 0.5$$

$$\text{Thick}_i = \text{Thick}_i^0, i = 1, \ldots, n_{section},$$

$$x_j^l \leq x_j \leq x_j^u, j = 1, \ldots, m$$

where $n_{section}$ is the number of control sections and m is the total number of design variables. To ensure that all the candidate shapes in the design space satisfy the thickness constraint, we change the corresponding FFD nodes of the upper and lower wing
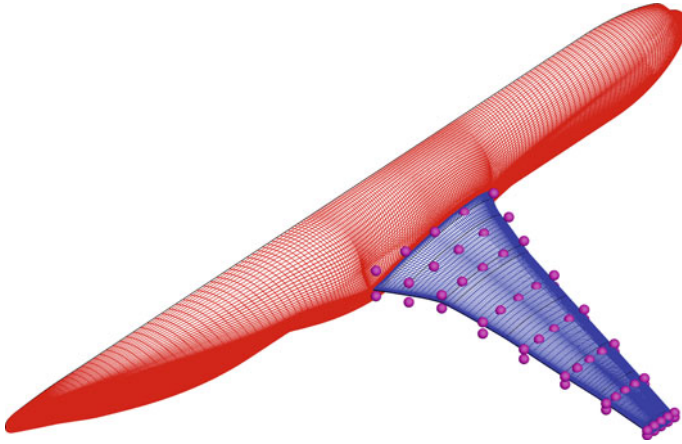
Fig. 16.2 Wing-body transport aircraft configuration and FFD box (8 control sections with 10 FFD nodes for each section, resulting in 40 nodes on upper and lower wing surfaces, respectively)

surfaces simultaneously. This implies, for example, that the number of design variables is reduced to 40 for the parameterization of wing with 80 FFD nodes (see Fig. 16.2). DLR's RANS flow solver TAU [55–57] is used to calculate the aerodynamic performance. Jameson's central scheme is used for spatial descretization and the Spalart-Allmaras one-equation model is used for turbulence closure. The lift constraint $C_L = 0.5$ is handled by the flow solver using a target-lift approach, which internally changes the angle of attack to retain the target lift.

16.3.2 Study of the Baseline Configuration

A study on the grid resolution is a basic requirement set forth by the AIAA aerodynamic design optimization discussion group (ADODG) for its benchmark aerodynamic shape optimization problems. For example, in [58] the first author of the current study conducted a thorough grid convergence study for the baseline RAE 2822 airfoil and for the optimized airfoil to ensure that the variation of the drag coefficient is less than 1 count.

While a full-fledged grid convergence study is beyond the scope of the present study, a set of grids of different size is generated to study the characteristics of the baseline configuration. The grids are block-structured and are generated using a DLR in-house tool, which automatically changes the CAD model of the aircraft and the associated block topology, and applies Pointwise to create the surface and volume grid [60]. Here we study the aerodynamic performance of two representative grids: a
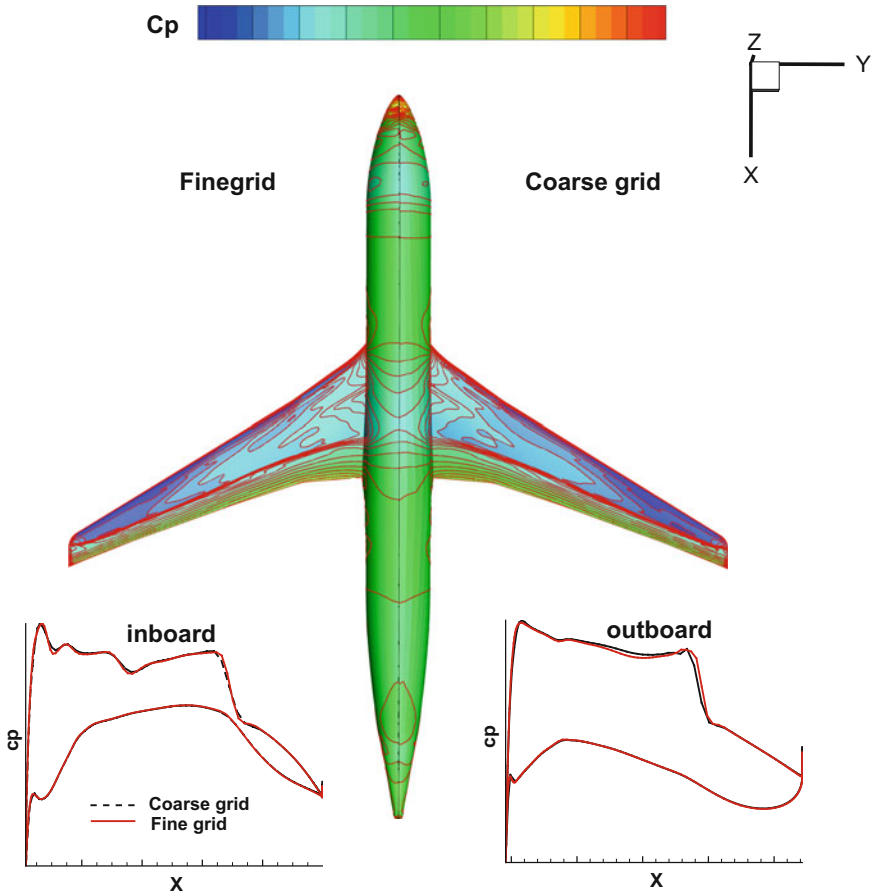
Fig. 16.3 Comparison of surface pressure coefficient contours computed on fine and coarse grids ($Ma = 0.83$, $Re = 4.34E7$, $C_L = 0.5$)

grid with 0.78 million nodes and a finer grid with 3.8 million nodes. The comparison of pressure coefficient contour is shown in Fig. 16.3. From the pressure distribution, one can clearly see that there is a shock wave at around 65% of the chord-wise location, and there is only very small difference between the pressure distributions on the fine and the coarse grids, where the differences can be seen near the shock wave for both grids. Concerning the drag coefficient, there is only 1 count difference (see Table 16.1) between the grids, which enables us to use the coarse grid to run the intensive aerodynamic shape optimizations. Note that the reference point of moment coefficient is at the nose of the fuselage.

Table 16.1 Comparison of aerodynamic force coefficients computed on fine and coarse grids (we should state that the reference is the fine grid)

	C_L	ΔC_D(cts.)	ΔC_M
Coarse grid (0.78 million points)	0.5	1.0	0.0041
Fine grid (3.8 million points)	0.5	0.0	0.0
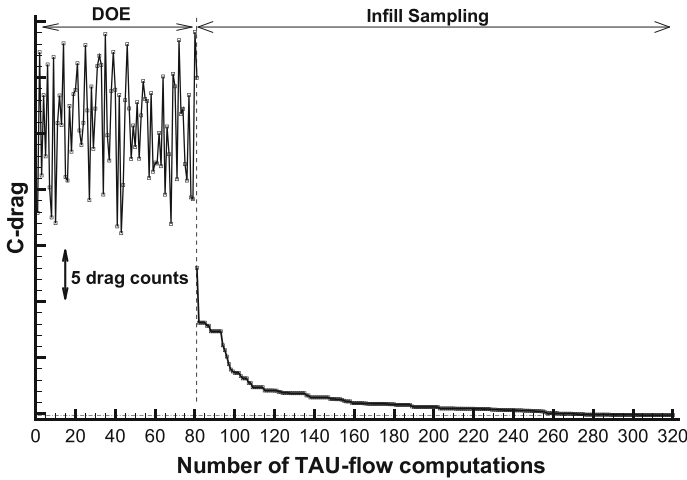
Fig. 16.4 Convergence history of surrogate-based optimization (SBO) (40 design variables, $Ma = 0.83$, $Re = 4.34E7$, $C_L = 0.5$)

16.3.3 Optimization Results

The convergence history of the SBO is shown in Fig. 16.4. Note that we use 81 initial samples for SBO, with 80 samples selected by LHS and one additional sample corresponding to the baseline shape. The optimization reduced the drag by 18 counts. Figure 16.5 shows the pressure distribution of the baseline and the optimized configurations, and we can see that the shock wave is nearly smoothed out by SBO. In addition to being a nearly global optimizer, the potential benefit of SBO can further be explained as: (a) SBO can definitely be an alternative to gradient-based method in the case that fast adjoint gradient is not available, such as the case of laminar wing design considering transition; (b) adjoint gradients can be incorporated in SBO to further improve the overall efficiency, which lends it to the method of gradient-enhanced Kriging (GEK [48]); (c) it is straight forward to extend the SBO framework to robust design, i.e., to design under uncertain flow conditions or random shape variations due to manufacturing tolerances.
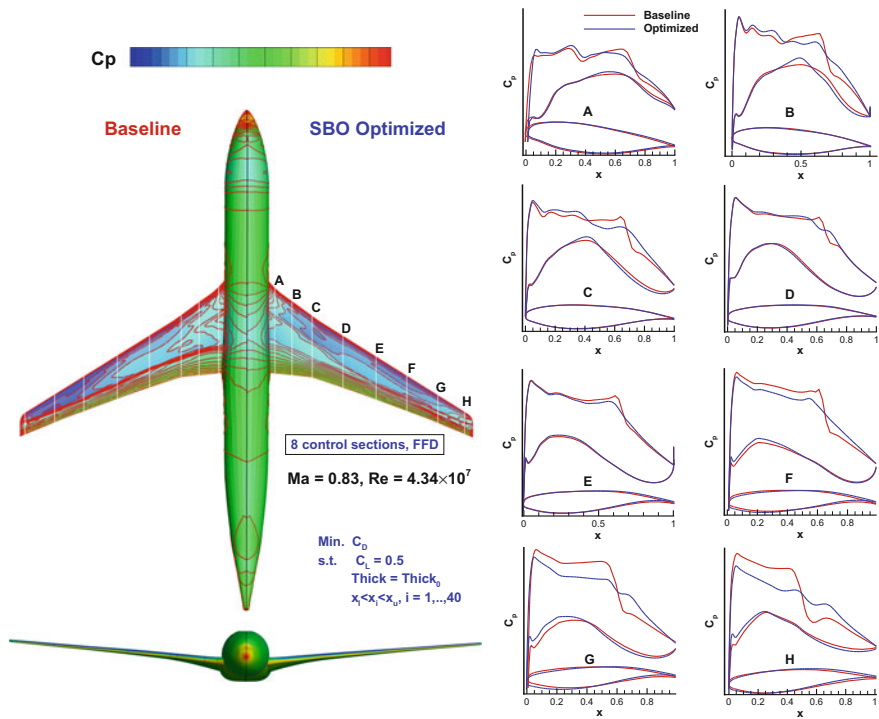
Fig. 16.5 Pressure coefficient distribution of the baseline and SBO optimized configurations ($Ma = 0.83$, $Re = 4.34E7$, $C_L = 0.5$)

16.3.4 Parameter Study

16.3.4.1 Influence of Grid Resolution

Firstly, the influence of grid resolution on the SBO optimization is studied. All the settings except the number of grid nodes are exactly the same. The convergence histories of fine- and coarse-grid optimizations, shown in Fig. 16.6, are very similar. There exists only 1 drag count difference between the optimal shapes obtained by fine and coarse grids, which is consistent with the results of the baseline shape study in Sect. 16.3.2. This study encourages us to use the coarse grid for the rest of study, which is associated with the intensive optimizations of wing-body transport aircraft configuration.

Fig. 16.6 Influence of grid resolution on SBO ($Ma = 0.83, Re = 4.34E7, C_L = 0.5$)
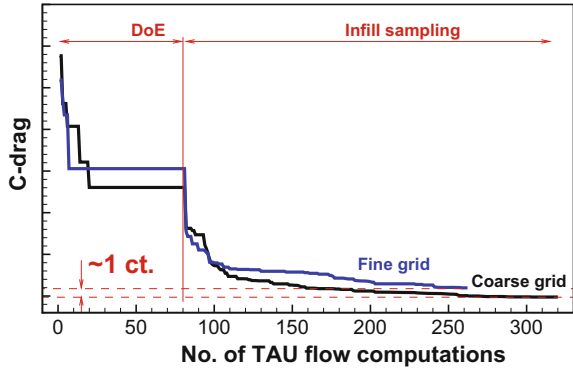
Fig. 16.7 Influence of number of initial sample points on SBO ($Ma = 0.83, Re = 4.34E7, C_L = 0.5$)
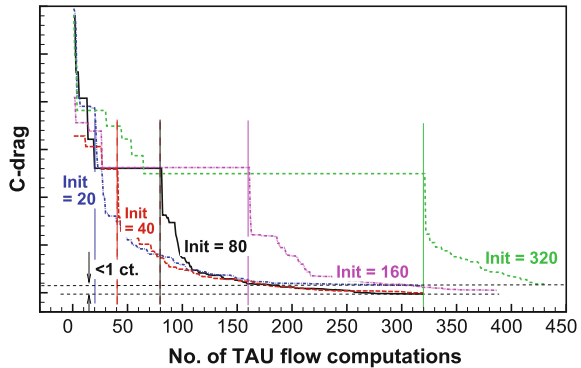
16.3.4.2 Influence of Number of Initial Sample Points

The number of initial sample points is a key issue for a SBO-type optimization. Here for 40 design variables, we used a series of initial sample points, from $0.5n_{dim}$ to $8n_{dim}$. The convergence histories of all these optimizations are shown in Fig. 16.7. The difference between the results is less than 1 drag count. With more initial sample points, the infill-sampling process would be faster. But for the overall computational cost, we suggest using the initial number of sample points of n_{dim} or $2n_{dim}$ (Fig. 16.7).

16.3.4.3 Influence of Randomness of Initial Sampling

When we use DoE method such as LHS, the initial sampling is essentially random. For the same number of design variables, 40, here we repeat the SBO for 5 times. Despite starting from completely different initial samplings, the convergence histories are very similar, see Fig. 16.8. But it is a surprise that the optimized aerodynamics shapes are "quite" different, although there is very little difference considering the drag of optimum shapes (less than 0.6 counts). Further study shows that all the

Fig. 16.8 Influence of randomness of initial sampling on SBO ($Ma = 0.83$, $Re = 4.34E7$, $C_L = 0.5$)
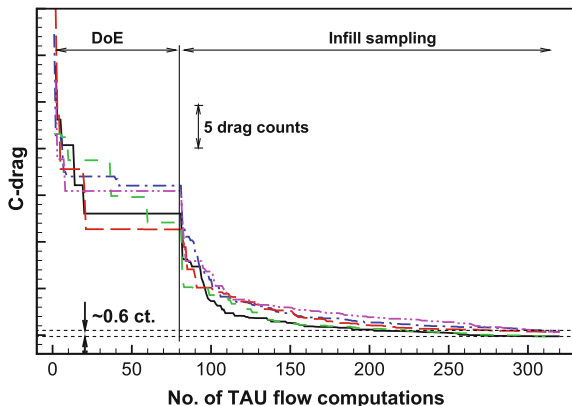
Fig. 16.9 Influence of number of design variables on SBO ($Ma = 0.83$, $Re = 4.34E7$, $C_L = 0.5$)
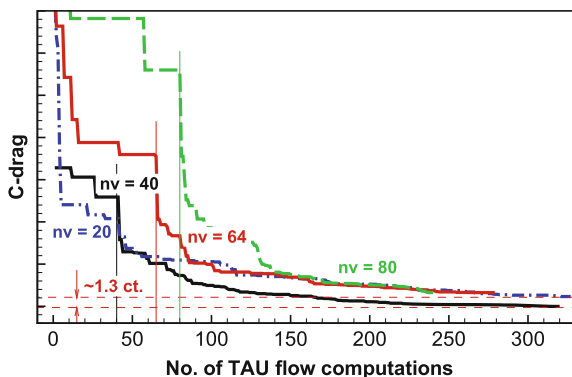
optimums are essentially local optimums. This is a typical feature of aerodynamic shape optimization of airfoil or wing in transonic fully turbulent flows. When the shock wave-drag is reduced to nearly zero, the small change of the aerodynamic shape doesn't have remarkable influence on the total drag coefficient. This is why there are numerous local optimums existing in the design space and it is nearly not possible (or not meaningful) to find the "real" global optimum. But by repeating SBO several times, the chance of getting optimum closer to the "global optimum" can be increased.

16.3.4.4   Influence of Number of Design Variables

At last, we study a very important issue about SBO; the effect of number of dimensions. The optimizations are conducted for the number of design variable of 20, 40, 64, and 80, respectively. According to the best practice obtained in Sect. 16.3.4.2, we used an initial number of sample points equal to the number of design variables. When the number of design variables is increased from 20 to 40, we can see that

Fig. 16.10 Analysis of
design space (40 design
variables, $Ma = 0.83$,
$Re = 4.34E7$, $C_L = 0.5$),
drag coefficient change w.r.t.
Euclidian distance to the
optimum
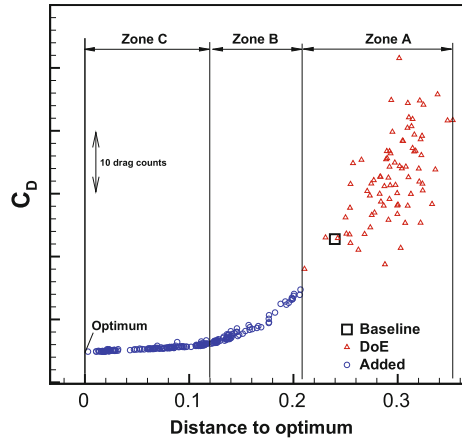
(Fig. 16.9), at the beginning, the improvement with 20 design variables is faster, but
then it slows down. The overall performance when using 40 design variables seems
to be the best, considering both the efficiency and final drag counts. When we con-
tinue to increase the number of design variables to 64 and 80, the convergence is
slowed down again, but the last stage of convergence is similar. Considering the total
computational cost, we can still afford to optimize with our SBO optimizer and using
the settings according to our best practice when the number of design variables is
as large as 80. We expect that the number of design variables can be even larger.
Nevertheless, the number of design variables has notable influence on the optimum
results. The differences observed here may be a combination of different numbers
of design variables and randomness of the initial samples.

16.4 A Posteriori Study of SBO Results

A byproduct of running SBO is that we eventually get a number sample points that
can be post-processed to analyze the features of the design space. Since it is not
possible to directly visualize the high-dimensional design space, we use an indirect
way which measures the Euclid distance between all the sample points and the
optimum point. For a specific optimization, the change of drag coefficient versus
the distance to the optimum point is plotted in Fig. 16.10. The red triangle denotes
the initial sample point chosen by DoE; the black square represents the baseline
shape; the red circle indicates the added sample points determined by solving the
sub-optimization problem. We classify all the sample points into 3 zones: zone A,
B and C. The initial samplings in zone A are far away from the optimum and there
is a large variation of drag coefficient versus the spatial distance, due to the strong
shock wave. Although most of the initial samples have higher drag than the baseline
point, they are necessary for building the initial surrogate model which guides the

optimization toward the promising region. When the optimization enters zone B, the variation of drag versus distance to optimum is reduced due to the fact that the shock wave is weakened. In total, a reduction of 18 drag counts is obtained. As the optimization approaches zone C, the drag coefficient does not change that much with the Euclidian distance to the optimum and only around 1 drag count reduction can be obtained. Although the drag reduction is very small, a more robust aerodynamic shape can be obtained, since the drag coefficient is less sensitive to geometry changes.

The sample points can also be post-processed to identify the key design variables driving the surrogate-based optimization process to the optimum. Maximum Likelihood Estimation (MLE) of the hyper-parameters of the Kriging surrogate model can be used for automatically reducing the number of design variables. The hyper-parameters, θ, are weighted coefficients of the distance along each dimension and indicate how much a variable influences the correlation between two samples. A larger θ-value corresponds to a "more important" variable. If θ approaches zero then the corresponding design variable has little or no effect on the functional variation of the objective function. In other words, automatic dimension reduction can be achieved when the correlation parameters for a chosen correlation model approach zero for certain parameter directions. This approach has been successfully used in high-dimensional optimization problems by Siller et al. [59]. However, "enough" sample points are required to estimate the correlation and an accurate MLE is required.

Here, Kriging with a cubic spline kernel was used and combined with infill sampling based on the EI function. The θ-values were optimized using MLE based on 250 samples. Both 40 and 80 design variables were considered. Based on the optimized θ-values shown as a function of the index of the design variables in Fig. 16.11 and 16.12, the optimization appears to be driven mainly by about 20 design variables. In the case of the parameterization with 80 design variables, it is observed that no more than 65 design variables have any influence on the objective function approximated by the surrogate model and the remaining 15 can be removed from the optimization problem without having any influence on the variation of the objective function. Re-running the optimization with the reduced set of design variables was, however, beyond the scope of the present study.

16.5 Summary and Conclusions

This article develops an efficient surrogate-based optimization (SBO) framework, which is implemented in a Python module called "sbo.py" with objective-oriented programming. It is demonstrated for aerodynamic shape optimization of a generic wing-body configuration, which is representative of modern civil transport aircraft, with as many as 80 design variables. Several studies were conducted to understand the influence of the resolution of computational grids, the number and randomness of the initial sampling as well as the number of design variables (20–80). Some conclusions can be drawn as following:
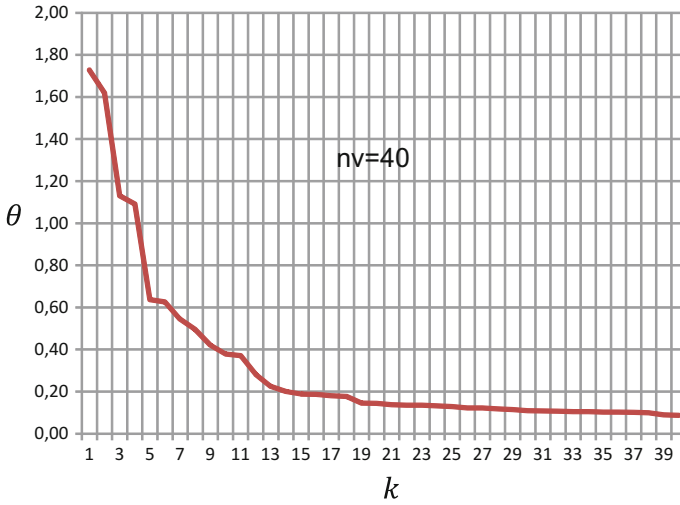
Fig. 16.11 Optimized Kriging hyper-parameters as a function of the index of the design variables (40 design variables)
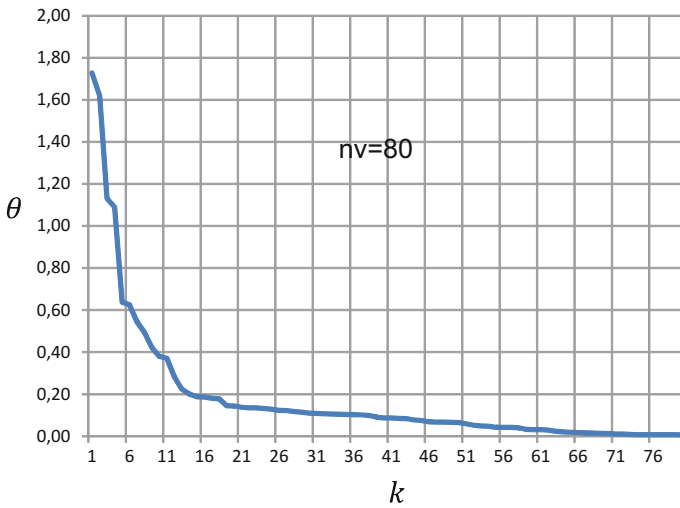
Fig. 16.12 Optimized Kriging hyper-parameters as a function of the index of the design variables (80 design variables)

1. Optimization of the wing-body configuration with SBO is proven successful (18 counts or around 7% drag reduction achieved); SBO is usable for 3D aerodynamic design of wings with as many as 80 design variables.
2. Repeating SBO several times can increase the chance to get a shape which is closer to the "global optimum".

3. For our SBO-type optimizer, small effect can be found for the number of initial samplings. Best practice suggests us to use n_{dim} or $2n_{dim}$ for the number of initial sample points.
4. The number of design variables has dramatic influence on the results as well as the efficiency of SBO. The computational cost increases slowly with increase in number of design variables. SBO is, however, still usable for optimization with as many as 80 design variables.

References

1. R.M. Hicks, E.M. Munnan, G.N. Vanderplaats, *An Assessment of Airfoil Design by Numerical Optimization, NASA TM X-3092* (NASA Ames Research Center, Moffett Field, 1974)
2. R.M. Hicks, P.A. Henne, Wing design by numerical optimization. J. Aircr. **15**(7), 407–412 (1978)
3. A. Jameson, Aerodynamic design via control theory. J. Sci. Comput. **3**(3), 233–260 (1988)
4. A. Jameson, Optimum aerodynamic design using CFD and control theory, in *AIAA Paper 95-1729* (1995)
5. J. Reuther, A. Jameson, J. Farmer, L. Martinelli, D. Saunders, Aerodynamic shape optimization of complex aircraft configurations via an adjoint formulation, in *AIAA Paper 96-0094* (1996)
6. W.K. Anderson, V. Venkatakrishnan, Aerodynamic design optimization on unstructured grids with a continuous adjoint formulation, in *AIAA paper 97–0643, 35th Aerospace Sciences Meeting and Exhibit* (Reno, Nevada, 1997)
7. R. Dwight, J. Brezillon, Effect of approximations of the discrete adjoint on gradient-based optimization. AIAA J. **44**(12), 3022–3071 (2006)
8. J. Brezillon, N.R. Gauger, 2D and 3D aerodynamic shape optimization using the adjoint approach. Aerosp. Sci. Technol. **8**(8), 715–727 (2004)
9. D.J Mavripilis, A discrete adjoint-based approach for optimization problems on three-dimensional unstructured grids, in *AIAA Paper 2006-50* (2006)
10. Z. Lyu, G.K.W. Kenway, J.R.R.A. Martins, Aerodynamic shape optimization investigations of the common research model wing benchmark. AIAA J. **53**(4), 968–985 (2015). https://doi.org/10.2514/1.J053318
11. G.K.W. Kenway, J.R.R.A. Martins, Multipoint aerodynamic shape optimization investigations of the common research model wing. AIAA J. **54**(1), 112–128 (2016)
12. M. Abu-Zurayk, J. Brezillon, Aero-Elastic Multi-Point Wing Optimization Using the Coupled Adjoint Approach, *New Results in Numerical and Experimental Fluid Mechanics IX*, vol. 124, Notes on Numerical Fluid Mechanics and Multidisciplinary Design (Springer, Berlin, 2014), pp. 45–52
13. D. Koo, D.W. Zingg, Progress in aerodynamic shape optimization based on the reynolds-averaged navier-stokes equations, in *AIAA Paper 2016–1292, 54th AIAA Aerospace Science Meeting*, 4–8 January 2016 (San Diego, California, USA, 2016)
14. O. Chernukhin, D.W. Zingg, Multimodality and global optimization in aerodynamic design. AIAA J. **51**(6), 1342–1354 (2013)
15. Y.A Tesfahunegn, S. Koziel, J.R. Gramanzini, S. Hosder, Z.-H Han, L. Leifsson, Application of direct and surrogate-based optimization to two-dimensional benchmark aerodynamic problems: a comparative study, in *AIAA Paper 2015-0265, 53rd AIAA Aerospace Sciences Meeting*, 5–9 January 2015 (Kissimmee, Florida, 2015)

16. J. Wild, On the Potential of Numerical Optimization of High-Lift Multi-Element Airfoils based on the Solution of the Navier-Stokes-Equations, *Computational Fluid Dynamics* (Springer, Berlin, 2002), pp. 267–272
17. W. Song, A.J. Keane, Surrogate-based aerodynamic shape optimization of a civil aircraft engine nacelle. AIAA J. **45**(10), 2565–2574 (2007)
18. N.V. Queipo, R.T. Haftka, W. Shyy, T. Goel, R. Vaidyanathan, P.K. Tucher, Surrogate-based analysis and optimization. Prog. Aerosp. Sci. **41**(1), 1–28 (2005)
19. A.I.J. Forrester, A.J. Keane, Recent advances in surrogate-based optimization. Prog. Aerosp. Sci. **45**(1–3), 50–79 (2009). https://doi.org/10.1016/j.paerosci.2008.11.001
20. Z.-H. Han, K.-S. Zhang, Surrogate Based Optimization, *Real-World Application of Genetic Algorithm* (Intec Book, London, 2012), p. 343
21. S. Koziel, D. Echeverria-Ciaurri, L. Leifsson, Surrogate-based methods, in *Computational Optimization, Methods and Algorithms*, Studies in Computational Intelligence, ed. by S. Koziel, X.S. Yang (Springer, Berlin, 2011), pp. 33–60
22. S. Shan, G.G. Wang, Survey of modeling and optimization strategies for high-dimensional design problems, in *AIAA Paper 2008-5842* (2008)
23. G.G. Wang, S. Shan, Review of metamodeling techniques in support of engineering design optimization. J. Mech. Des. **129**(4), 370–380 (2007)
24. P.N. Koch, T.W. Simpson, J.K. Allen, F. Mistree, Statistical approximations for multidisciplinary design optimization: the problem of the size. J. Aircr. **36**(1), 275–286 (1999)
25. D.R. Jones, M. Schonlau, W.J. Welch, Efficient global optimization of expensive black-box functions. J. Glob. Optim. **13**, 455–492 (1998). https://doi.org/10.1023/A:1008306431147
26. D.D. Cox, S. John, SDO: A statistical method for global optimization, in *Proceeding of the ICASE/NASA Langley Workshop on Multidisciplinary Analysis and Optimization*, vol. 2 (Reston, VA, 1998), pp. 738–748
27. J. Laurenceau, P. Sagaut, Building efficient response surfaces of aerodynamic functions with kriging and cokriging. AIAA J. **46**(2), 498–507 (2008)
28. L. Leifsson, S. Koziel, Y.A. Tesfahunegn, Multiobjective aerodynamic optimization by variable-fidelity models and response surface surrogates. AIAA J. **54**(2), 531–541 (2016)
29. Y. Lian, M. Liou, Multiobjective optimization using coupled response surface model and evolutionary algorithm. AIAA J. **43**(6), 1316–1325 (2005)
30. S. Jeong, M. Murayama, K. Yamamoto, Efficient optimization design method using kriging model. J. Aircr. **42**(2), 413–420 (2005)
31. A.J. Keane, Statistical improvement criteria for use in multiobjective design optimization. AIAA J. **44**(4), 879–891 (2006)
32. A. Vavalle, N. Qin, Iterative response surface based optimization scheme for transonic airfoil design. J. Aircr. **44**(2), 365–376 (2007)
33. S. Koziel, L. Leifsson, Surrogate-based aerodynamic shape optimization by variable-resolution models. AIAA J. **51**(1), 94–106 (2013)
34. K.-S. Zhang, Z.-H. Han, W.-J. Li, W.-P. Song, Coupled aerodynamic/structural optimization of a subsonic transport wing using a surrogate model. J. Aircr. **45**(6), 2167–2171 (2008)
35. M. Kanazaki, T. Imamura, S. Jeong, K. Yamamoto, High-lift wing design in consideration of sweep angle effect using kriging model, in *46th AIAA Aerospace Sciences Meeting and Exhibit*, 7–10 January 2008 (Reno, Nevada, 2008)
36. J. Laurenceau, M. Meaux, M. Montagnac, P. Sagaut, Comparison of gradient-based and gradient-enhanced response-surface-based optimizers. AIAA J. **48**(5), 981–994 (2010)
37. S.J. Leary, A. Bhaskar, A.J. Keane, Global approximation and optimization using adjoint computational fluid dynamics codes. AIAA J. **42**(3), 631–641 (2004)
38. C. Li, J. Brezillon, S. Görtz, A Hybrid approach for surrogate-based aerodynamic optimization with constraints, in *Proceedings International Conference on Evolutionary and Deterministic Methods for Design, Optimization and Control with Applications to Industrial and Societal Problems (Eurogen 2011)*, 14–16 September 2011 (Capua, Italy, 2011)
39. C. Li, J. Brezillon, S. Görtz, Efficient Global Optimization of a Natural Laminar Airfoil Based on Surrogate Modeling, in *New Results in Numerical and Experimental Fluid Mechanics*

IX, vol. 124, Notes on Numerical Fluid Mechanics and Multidisciplinary Design, ed. by A. Dillmann, G. Heller, E. Krämer, H.-P. Kreplin, W. Nitsche, U. Rist (Springer, Berlin, 2014), pp. 53–63. (Contributions to the 18th STAB/DGLR Symposium, Stuttgart, Germany 2012)

40. C. Li, A surrogate-based framework with hybrid refinement strategies for aerodynamic shape optimization, Ph.D. thesis, German Aerospace Center (DLR), Institute Aerodynamics and Flow Technology, DLR-FB-2013-16, 2013

41. Z.H. Han, R. Zimmermann, S. Görtz, Alternative co-kriging model for variable-fidelity surrogate modeling. AIAA J. **50**(5), 1205–1210 (2012)

42. Z.H. Han, S. Görtz, Hierarchical kriging model for variable-fidelity surrogate modeling. AIAA J. **50**(9), 1885–1896 (2012)

43. A.A. Giunta, S.F. Wojtkiewicz Jr., M.S. Eldred, Overview of modern design of experiments methods for computational simulations, in *AIAA paper 2003-649* (2003)

44. D.G. Krige, A statistical approach to some basic mine valuations problems on the witwatersrand. J. Chem. Metall. Min. Eng. Soc. S. Afr. **52**(6), 119–139 (1951)

45. G.M. Matheron, Principles of geostatistics. Econ. Geol. **58**(8), 1246–1266 (1963)

46. J. Sacks, W.J. Welch, T.J. Mitchell, H.P. Wynn, Design and analysis of computer experiments. Stat. Sci **4**, 409–423 (1989)

47. S.N Lophaven, H.B. Nielsen, J. Søndergaard, DACE - A Matlab Kriging Toolbox (Version 2.0), Technical Report IMM-REP-2002-12, Informatics and Mathematical Modelling, DTU (2002), pp. 1–34

48. Z.-H. Han, S. Görtz, R. Zimmermann, Improving variable-fidelity surrogate modeling via gradient-enhanced kriging and a generalized hybrid bridge function. Aerosp. Sci. Technol. **25**(1), 177–189 (2013). https://doi.org/10.1016/j.ast.2012.01.006

49. T.W. Simpson, T.M. Mauery, J.J. Korte, F. Mistree, Kriging models for global approximation in simulation-based multidisciplinary design optimization. AIAA J. **39**(12), 2233–2241 (2001)

50. J.D. Martin, T.W. Simpson, Use of kriging models to approximate deterministic computer models. AIAA J. **43**(4), 853–863 (2005)

51. D.J.J. Toal, N.W. Bressloff, A.J. Kean, Kriging hyperparameter tuning strategies. AIAA J. **46**(5), 1240–1252 (2008)

52. J. Liu, Z.-H Han, W.-P. Song, Comparison of infill sampling criteria in kriging-based aerodynamic optimization, in *8th Congress of the International Council of the Aeronautical Sciences*, 23–28 September 2012 (Brisbane, Australia, 2012). (ICAS2012-11.10ST, 2012)

53. N.M. Alexandrov, J.E. Dennis Jr, R.M. Lewis, V. Torczon, A trust-region framework for managing the use of approximation models in optimization. Struct. Multidiscip. Optim. **15**(1), 16–23 (1998)

54. N. Kroll, M. Abu-Zurayk, D. Dimitrov, T. Franz, T. Führer, T. Gerhold, S. Görtz, R. Heinrich, C. Ilic, J. Jepsen, J. Jägersküpper, M. Kruse, A. Krumbein, S. Langer, D. Liu, R. Liepelt, L. Reimer, M. Ritter, A. Schwöppe, J. Scherer, F. Spiering, R. Thormann, V. Togiti, D. Vollmer, J.-H. Wendisch, DLR project digital-X: towards virtual aircraft design and flight testing based on high-fidelity methods. CEAS Aeronaut. J. **7**(1), 3–27 (2016)

55. T. Gerhold, V. Hannemann, D. Schwamborn, On the Validation of the DLR-TAU Code, in *New Results in Numerical and Experimental Fluid Mechanics*, vol. 72, Notes on Numerical Fluid Mechanics, ed. by W. Nitsche, H.-J. Heinemann, R. Hilbig (Springer Vieweg, Berlin, 1999), pp. 426–433. ISBN 3-528-03122-0

56. N. Kroll, J.K. Fassbender (eds.), *MEGAFLOW - Numerical Flow Simulation for Aircraft Design*, vol. 89, Notes on Numerical Fluid Mechanics and Multidisciplinary Design (Springer, Berlin, 2005)

57. D. Schwamborn, T. Gerhold, R. Heinrich, The DLR TAU-code: recent applications in research and industry, invited lecture, in *Proceedings of the European Conference on Computational Fluid Dynamics (ECCOMAS CFD 2006)*, eds by P. Wesseling, E. Oñate, J. Périaux, (TU Delft, The Netherlands, 2006)

58. Y. Zhang, Z.-H. Han, L.-X. Shi, W.-P. Song, Multi-round surrogate-based optimization for benchmark aerodynamic design problems, in *AIAA Paper 2016–1545, 54th AIAA Aerospace Science Meeting*, 4–8 January 2016 (San Diego, California, USA, 2016)

59. U. Siller, C. Voß, E. Nicke, Automated multidisciplinary optimization of a transonic axial compressor, in *AIAA Paper 2009-0863* (2009)
60. T. Wunderlich, S. Dähne, L. Heinrich, L. Reimer, Multidisciplinary Optimization of a NLF Forward Swept Wing in combination with Aeroelastic Tailoring using CFRP, Deutscher Luft- und Raumfahrtkongress 2015 (2015)

Chapter 17
A Method for the Calculation of Large Deformations in Aeroelastic Applications

Markus Ritter

Abstract A modal-based method that calculates the geometric nonlinear effects in the regime of large deformations of wing-like structures is applied to the modeling of a highly flexible 3D wingbox of high aspect ratio. The proposed method features higher-order stiffness terms and calculates the nodal deformation field not only by normal modes but also by additional modal components. In this way, a nonlinear force-displacement relationship and a geometrically nonlinear displacement field are accounted for. Static and dynamic results for the two configurations are presented together with results from a nonlinear finite element solver. The validations highlight the capability of the method to capture the nonlinear effects and demonstrates its power to model a 3D wingbox structure made of composite shell elements with anisotropic material characteristics.

17.1 Introduction

Future passenger transport aircraft with lower emissions and higher fuel efficiency are the focus of current developments in the aeronautical industry. One of the key design features that supports achieving such goals is a high aspect ratio wing, which lowers the induced drag. However, as the span increases along with the wing's aspect ratio, higher flexibility is the consequence and becomes almost inevitable due to geometrical effects. On the other hand, increased structural flexibility can be advantageous when dealing with external disturbances, such as gust encounters, due to the reduced rigid body acceleration. But it brings several challenges related to the modeling, analysis, and design and it becomes inevitable that the geometrically nonlinear structural nature of the vehicle be taken into account in the earliest phases of design [1].

Industry-standard aeroelastic simulation frameworks are mostly based on a modal description of the airframe using eigenvectors and eigenvalues in the frequency range

M. Ritter (✉)
Institute of Aeroelasticity, Bunsenstraße 10, 37073 Göttingen, Germany
e-mail: Markus.Ritter@dlr.de

of interest to calculate structural deformations in a linear way. These have very limited applicability for the problem of geometrically nonlinear aeroelasticity, where time-domain solutions and coupled aeroelasticity/flight dynamics analysis (due to the coupled nature of the rigid body and elastic response of the aircraft) are sought. Geometrically-exact beam-based formulations coupled with appropriate unsteady aerodynamics are the state of the art for this type of problem [12]. On the other hand, beam formulations are not always sufficient to model complex structural details of transport aircraft wings since the 3D structural model must be condensed to a beam model with equivalent structural characteristics. Using nonlinear FE codes for aeroelastic simulations of entire aircraft can become very costly, especially for dynamic simulations.

A new method, refered to as *Enhanced Modal Approach* was developed to overcome these problems. It is an extension of the classical modal approach towards large deformations that uses a higher order strain energy formulation to consider nonlinear force-displacement relationships and higher-order mode components for the reconstruction of a geometrically nonlinear displacement field [8]. Both enhancements are derived by Taylor series expansions. A series of static, nonlinear structural simulations is necessary to identify the higher-order stiffness and mode components (tensors). Once these components are determined, static and dynamic aeroelastic simulations can be done with a computational effort which is only slightly increased compared to the classical modal approach.

The ability to model complex, highly flexible 3D FEM structures of an aircraft in free flight is seen as the ultimate goal of the enhanced modal approach. A model of this type is shown in Fig. 17.1 as a motivating example. A step by step approach is followed to achieve this goal. To this end, the method is applied to different structural test cases with increasing complexity in order to identify possible issues and improve the method gradually. This work presents applications of the method to a complex, slender 3D wingbox modeled by shell elements made from fiber reinforced material.

Methods for the reduced order modeling (ROM) of nonlinear structures have been addressed by several authors. Mignolet and co-workers have given detailed descriptions for the derivation of static and dynamic nonlinear structural governing equations including higher-order (quadratic and cubic) stiffness terms. The field of application of the method ranges from plate structures to curved beams and the modeling of a complex UAV wing [3, 7, 15].

Kuether and Allen describe methods based on nonlinear normal modes (NNMs) to simplify large, complex structures. NNMs basically describe the resonant frequency and response of a structure as a function of response amplitude or energy [5, 6]. Two substructuring methods that can be used in conjunction with 3D finite element models are presented by Kuether [5], where the second one is based on building a reduced order model of a structure by applying a series of static loads to a nonlinear FE model. Quadratic and cubic stiffness terms are used to account for a nonlinear force displacement behavior and coupling of individual modes.

As will be shown, a geometrically nonlinear displacement field in large deformations of wing-like structures can be reconstructed by shape functions of higher order. The method of quadratic components was successfully applied by Segalman
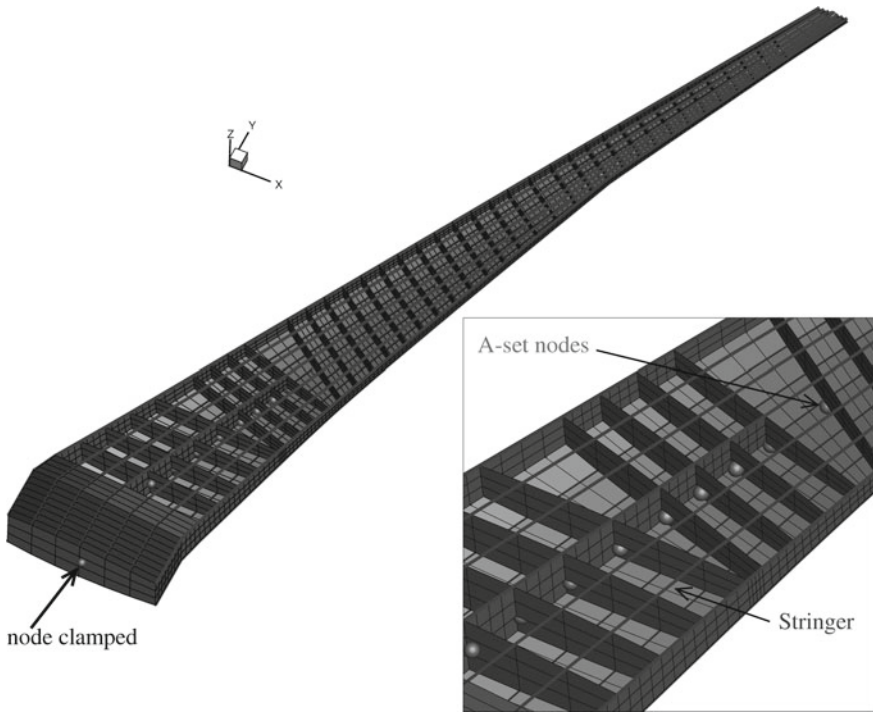
Fig. 17.1 3D FEM model of a transport aircraft wing built with spars, ribs, stringers, and skins as a motivating test case for future application of the method proposed

and Dohrmann to improve the kinematical and dynamical description of rotating structures undergoing large displacements [9, 10]. This method is also used by van Zyl for the calculation of T-Tail flutter [13, 14]. In the approach presented, the concept of structural modes of higher order is further developed to improve the reconstruction of nonlinear, large displacements. Higher-order stiffness terms derived from a higher-order strain energy formulation are used to represent a nonlinear force-displacement behavior.

17.2 Derivation of the Enhanced Modal Approach

The derivation of the enhanced modal approach is given in detail in Ref. [8] and recapitulated in a more compact form in the following.

Compared to the classical modal approach, the proposed method is based upon considering a nonlinear force-displacement relationship by quadratic and cubic stiffness terms and a geometrically nonlinear displacement field based on higher-order mode components up to fourth order. Furthermore, the generalized forces are dependent on the state of deformation and the nodal force field applied.

17.2.1 Static Formulation: Higher-Order Strain Energy

The total potential energy π of an elastic body consists of the sum of the total strain energy U and the potential energy of the applied loads V. This statement is expressed as [11]:

$$\pi = U + V \ . \tag{17.1}$$

Assuming Hooke's law, and neglecting temperature influences, the total strain energy U is given as (using Einstein notation):

$$U = \frac{1}{2} \int_V \tau_{ij} \varepsilon_{ij} \, dv \ (i, \, j = 1, 2, 3) \ , \tag{17.2}$$

where τ_{ij} and ε_{ij} are the stress and strain component pairs, respectively. The work done by the applied loads V can be expressed as:

$$V = \int_V B_i \, u_i \, dv + \int_S T_i^{(v)} u_i \, ds \ , \tag{17.3}$$

where B_i represents the components of the applied body forces, u_i the components of the displacement field, and $T_i^{(v)}$ denotes the traction vector applied on the body surface. Introducing a variation of both the total strain energy and the external work yields:

$$\delta\pi = \delta(U + V) = \int_V \tau_{ij} \, \delta\varepsilon_{ij} \, dv + \int_V B_i \, \delta u_i \, dv + \int_S T_i^{(v)} \delta u_i \, ds \ . \tag{17.4}$$

Invoking the Principle of Minimum Total Potential Energy, i.e., $\delta\pi = 0$, yields:

$$\delta U = -\delta V \ . \tag{17.5}$$

Now the total strain energy, Eq. (17.2), is assumed to be a *nonlinear* and continuously differentiable function of a scalar value q_i of a number of generalized coordinates, m, and expanded in a Taylor series up to the fourth order centered at zero (since the internal energy is zero for zero deformation):

$$U(\mathbf{q}) = \frac{1}{2!} \sum_{i=1}^{m} \sum_{j=1}^{m} \frac{\partial^2 U}{\partial q_i \, \partial q_j} q_i \, q_j$$

$$+ \frac{1}{3!} \sum_{i=1}^{m} \sum_{j=1}^{m} \sum_{k=1}^{m} \frac{\partial^3 U}{\partial q_i \, \partial q_j \, \partial q_k} q_i \, q_j \, q_k$$

$$+ \frac{1}{4!} \sum_{i=1}^{m} \sum_{j=1}^{m} \sum_{k=1}^{m} \sum_{l=1}^{m} \frac{\partial^4 U}{\partial q_i \, \partial q_j \, \partial q_k \, \partial q_l} \, q_i \, q_j \, q_k \, q_l + h.o.t. \qquad (17.6)$$

Using Castigliano's first theorem and applying a differentiation with respect to $\mathbf{q}$ centered at zero yields the governing equation of the structure as function of $\mathbf{q}$ [11]. This governing equation comprises quadratic and cubic stiffness dependencies:

$$\frac{\partial U}{\partial q_p} = \sum_{i=1}^{m} \frac{\partial^2 U}{\partial q_i \, \partial q_p} \, q_i$$

$$+ \frac{1}{2!} \sum_{i=1}^{m} \sum_{j=1}^{m} \frac{\partial^3 U}{\partial q_i \, \partial q_j \, \partial q_p} \, q_i \, q_j$$

$$+ \frac{1}{3!} \sum_{i=1}^{m} \sum_{j=1}^{m} \sum_{k=1}^{m} \frac{\partial^4 U}{\partial q_i \, \partial q_j \, \partial q_k \, \partial q_p} \, q_i \, q_j \, q_k + h.o.t. \qquad (17.7)$$

Introducing the definitions $^{p}G_n$ for the partial derivatives in Eq. (17.7), the following equation in the pseudo-generalized coordinates is obtained:

$$^{p}G_1^{i} \, q_i + \, ^{p}G_2^{ij} \, q_i q_j + \, ^{p}G_3^{ijk} \, q_i q_j q_k = Q^p \quad (p = 1, \ldots, m) \qquad (17.8)$$

Here the summation convention is used again. The idea of the proposed method is to take the $^{p}G_n$ stiffness matrices as generalized stiffnesses and the $\mathbf{q}$ as generalized coordinates. The stiffness parameters G_n can be determined by polynomial fitting or numerical differentiation [8].

17.2.2 Static Formulation: Higher-Order Deformation Reconstruction

The second extension is the reconstruction of the geometrically nonlinear displacement field. As mentioned above, the nonlinear static FE analysis excites nonlinear terms in the strain energy, but also a nonlinear displacement field.

In this work, the nodal deformation field is expanded in a Taylor series centered at zero (similar to the strain energy) which is truncated after the fourth term:

$$\mathbf{u}(\mathbf{q}) = \sum_{i=1}^{m} \frac{\partial \mathbf{u}}{\partial q_i} \, q_i \qquad (17.9)$$

$$+ \frac{1}{2!} \sum_{i=1}^{m} \sum_{j=1}^{m} \frac{\partial^2 \mathbf{u}}{\partial q_i \partial q_j} \, q_i \, q_j \qquad (17.10)$$

$$+ \frac{1}{3!} \sum_{i=1}^{m} \sum_{j=1}^{m} \sum_{k=1}^{m} \frac{\partial^3 \mathbf{u}}{\partial q_i \partial q_j \partial q_k} q_i \, q_j \, q_k \tag{17.11}$$

$$+ \frac{1}{4!} \sum_{i=1}^{m} \sum_{j=1}^{m} \sum_{k=1}^{m} \sum_{l=1}^{m} \frac{\partial^4 \mathbf{u}}{\partial q_i \partial q_j \partial q_k \partial q_l} q_i \, q_j \, q_k q_l + h.o.t. \tag{17.12}$$

Partial differentiation of the displacement field defined in this way with respect to the generalized coordinates and substitution similar as above for the strain energy yields:

$$^p\underline{\Phi} = \frac{\partial \mathbf{u}}{\partial q_p} = {}^p\underline{\Phi}_0 + {}^p\underline{\Phi}_1^i \, q_i + {}^p\underline{\Phi}_2^{ij} \, q_i q_j + {}^p\underline{\Phi}_3^{ijk} \, q_i q_j q_k \tag{17.13}$$

The term $^p\underline{\Phi}_0$ can be seen as the equivalent of the structure's normal modes.

17.2.2.1 The Generalized Forces and the Final Governing Equation

Considering Eq. (17.8), the term on the right hand side of the structure's governing equation is the generalized force Q^p. Applying the principle of virtual work and using the higher order mode components results in an extension of the generalized forces. For simplicity, the approach described by van Zyl is followed here and only the linear and the quadratic mode shape components are considered for the virtual work [13]:

$$\delta V = \delta \mathbf{u}^T \mathbf{f} \ , \tag{17.14}$$

where $\mathbf{f}$ denotes an arbitrary nodal force field. Expansion of the virtual physical displacements $\delta\mathbf{u}$ using the linear and the quadratic mode shapes yields:

$$\delta V = \delta q_p^T \left({}^p\underline{\Phi}_0^{\ T} + {}^p\underline{\Phi}_1^{i\ T} q_i \right) \mathbf{f} \ . \tag{17.15}$$

Thus the generalized forces are given as:

$$Q^p = {}^p\underline{\Phi}_0^{\ T}\mathbf{f} + {}^p\underline{\Phi}_1^{i\ T}\mathbf{f} \, q_i \ . \tag{17.16}$$

Combining Eqs. (17.8) and (17.16) yields:

$$({}^pG_1^i - {}^p\underline{\Phi}_1^{i\ T}\mathbf{f} \,) \, q_i + {}^pG_2^{ij} \, q_i \, q_j + {}^pG_3^{ijk} \, q_i \, q_j \, q_k = {}^p\underline{\Phi}_0^{\ T}\mathbf{f} \ . \tag{17.17}$$

Equation (17.17) is the static governing equation of the enhanced modal approach. Compared to the classical modal approach, the $^pG_1^i$ term is amended by the product of the transpose of the quadratic mode component matrix and the force field. This additional stiffness parameter is proportional to the force field applied to the structure and induces a coupling of otherwise (in the linear sense) uncoupled eigenvectors.

After solving Eq. (17.17), the nodal deformation field is reconstructed as function of the generalized coordinates $\mathbf{q}$:

$$\mathbf{u}(\mathbf{q}) = {}^P\underline{\Phi}_0\, q_p + {}^P\underline{\Phi}_1^i\, q_p q_i + {}^P\underline{\Phi}_2^{ij}\, q_p q_i q_j + {}^P\underline{\Phi}_3^{ijk}\, q_p q_i q_j q_k \ . \qquad (17.18)$$

17.2.3 Dynamic Formulation

The dynamic formulation includes inertia terms in Eq. (17.17). The governing equation is then given as:

$$\mathbf{M}\ddot{q}_i + \left({}^P G_1^i - {}^P\underline{\Phi}_1^{i\,T}\mathbf{f}\right) q_i + {}^P G_2^{ij}\, q_i\, q_j + {}^P G_3^{ijk}\, q_i\, q_j\, q_k = {}^P\underline{\Phi}_0^{\,T}\mathbf{f} \ , \quad (17.19)$$

where $\mathbf{M}$ denotes the generalized mass matrix.

17.3 Numerical Studies

The results of selected static and dynamic simulations obtained with the method described are presented in the following sections. Static simulations without aerodynamic forcing are used to verify the model, and coupled simulations show the power of the method for aeroelastic applications.

17.3.1 High Aspect Ratio Composite Wingbox Test Case

The test case consists of a 20-m span wingbox with a sweep angle of 1.8° made of quadrilateral shell elements. This three-dimensional wingbox resembles a real aircraft wing and is built from three spars, ribs, as well as upper and lower skins. Anisotropic materials (CFRP) are used for all elements of the wing by means of Nastran *MAT2* cards. Furthermore, the thicknesses of the shell elements is reduced along the wing to obtain even curvature in bending deformation for typical aerodynamic loadings. No additional discrete mass elements are used for this test case. The density of all materials is $2700\,\mathrm{kg/m^3}$, the total mass of the wingbox is 489 kg. The model contains 1950 nodes and 2005 elements, 254 different anisotropic materials are used. The structure was generated with the in-house model generator *ModGen* [4]. The outer shape of the wingbox is defined by a NACA 4415 section at the wing's root and a NACA 4412 at the wing's tip. The model is shown in explosion view with details in Fig. 17.2.
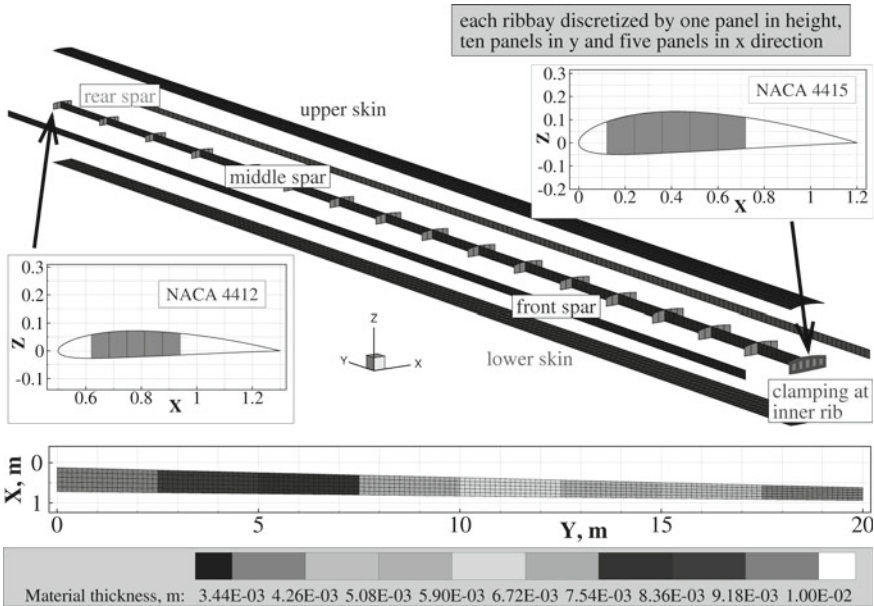
Fig. 17.2 Layout of the CFRP wingbox structural model and material thicknesses

Table 17.1 Eigenvalues of eight selected modes of the generic wingbox model; values were obtained from a FE analysis and from a polynomial reconstruction method

Mode	Type of mode	Eigenvalue FE analysis [Hz]	Eigenvalue reconstructed [Hz]
1	First bending	0.884	0.880
2	First bending in-plane	3.218	3.135
3	Second bending	3.602	3.575
4	Third bending	8.755	8.677
5	Fourth bending	16.18	16.109
6	Fifth bending	25.543	25.612
7	First torsion	28.302	28.386
8	Sixth bending	36.171	37.411

Higher-order stiffness terms and mode components were calculated for eight modes using the method described in Ref. [8]. The reconstructed values are close to the corresponding natural eigenvalues. Table 17.1 lists the types and frequencies of the eight selected mode shapes of the wingbox model obtained from the finite element modal analysis and from the reconstruction method, the corresponding mode shapes are plotted in Fig. 17.3.

Fig. 17.3 Selected normal mode shapes of the wing box test case (corresponding eigenvalues are given in Table 17.1)
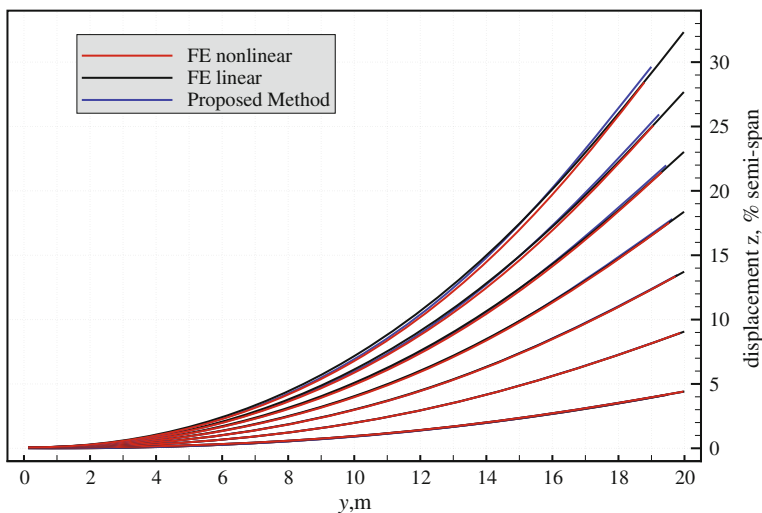
Fig. 17.4 Static displacements from different methods for tip forces with values from 1000 to 7000 N applied along the z direction at the wingtip

17.3.2   Static Simulations and Validations with Nonlinear Nastran Results

A force in the z direction was applied at the outermost rib's nodes (at y = 20 m) with assumed constant values between 1000 and 7000 N to simulate a static tip loading. The results are shown in Fig. 17.4. Again, no follower forces and no gravity have been considered and the force is applied always onto the undeformed initial configuration of the wingbox. In this case, the values were chosen to obtain deformations of the
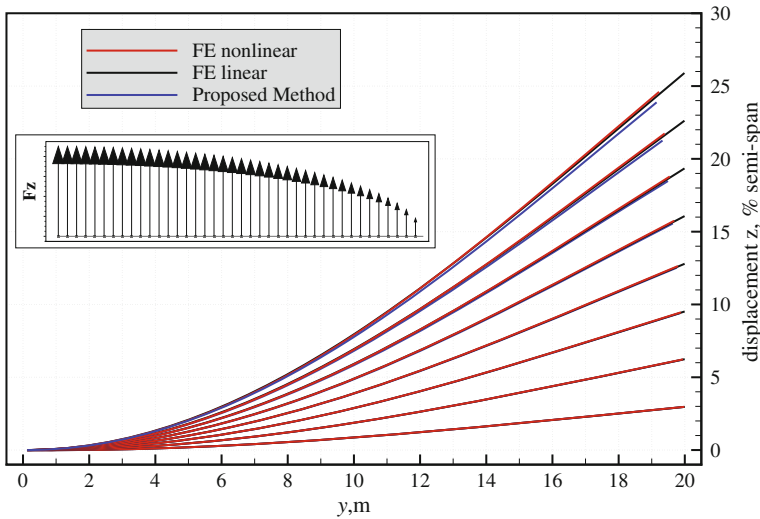
Fig. 17.5 Comparison of the static displacement fields from different methods for different elliptical force fields applied along the z direction at each node of the wingbox

wing beyond the limit of structural linearity (up to almost 30% of the span), as can be seen in terms of the displacements in the z and in the y directions. The linear FE solution yields too large displacements in the z direction and completely omits the deformation in the y direction. The results of the proposed method are in fair agreement with the nonlinear reference data from Nastran. Differences between the nonlinear solution and the enhanced modal approach become large for the last two force fields (6000 and 7000 N). This shows the limits of the method and proves that the method should be seen as an enhancement of the linear solution, roughly in the deformation regime between 10 and 20% of the span for this test case. It must be mentioned that buckling appears in the upper skins of the wingbox (the skins under compression) next to the wingroot if higher forces are applied. This behavior can be simulated by the full nonlinear Nastran solution only since no nonlinear structural solutions including buckling were used for the calculation of the higher-order stiffness and mode components.

The next test uses constant forces at each FE node in the z direction with an elliptical distribution. Thus a loading which is typically obtained from aerodynamic forces is resembled. The magnitudes were again chosen to show the limits of the proposed method. The results of the simulations are presented in Fig. 17.5. As for the first test, the nonlinear reference solution from Nastran and the enhanced modal approach solution show a fair agreement regarding the displacements in the z and in y directions. The limit for the proposed method is at about 20% deformation with respect to the half span of the wingbox.

A more interesting comparison is obtained if the elliptical force field is tilted around the local x-axis of each structural node and thus has a component in the y
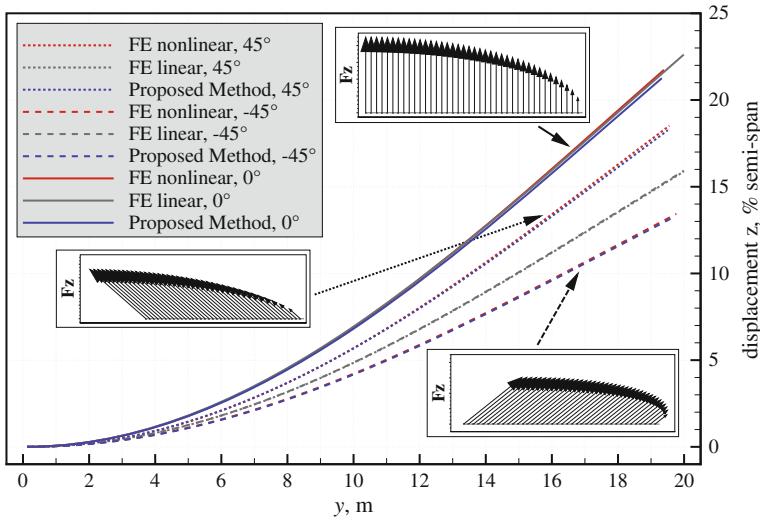
Fig. 17.6 Comparison of the static displacement fields from different methods where elliptical force fields with components in the z and the y direction are applied at each node. Forces are tilted from positive z direction by $\pm 45°$

direction. The proposed method can consider such a loading due to the quadratic mode components and the deformation and force dependent linear stiffness term, cf. Eq. (17.17). The result of this comparison is presented in Fig. 17.6, where the forces in the z direction are tilted in $\pm 45°$ (magnitudes are kept the same). Overall displacements in the z direction are reduced for both the positive and the negative tilt angles. The linear FE solution shows large differences to the respective nonlinear results, because the in-plane component of the force field (the component in the y direction with respect to the undeformed structure) has no effect since it acts in the local axial direction of the structure.

17.3.3 Static Aeroelastic Simulations and Validation with Nastran Results

Static coupling simulations were performed to evaluate the potential of the method presented in terms of large deformations excited by aerodynamic forces. Here, nonlinear aerodynamic forces with respect to structural deformations are considered. In contrast to the doublet-lattice method, the vortex-lattice (VL) aerodynamic model allows unlimited rotations and translations of the aerodynamic panels and calculates aerodynamic loads based on the current panel geometry. The wing is uncambered (for easier comparison with Nastran) and discretized with 64 spanwise panels and
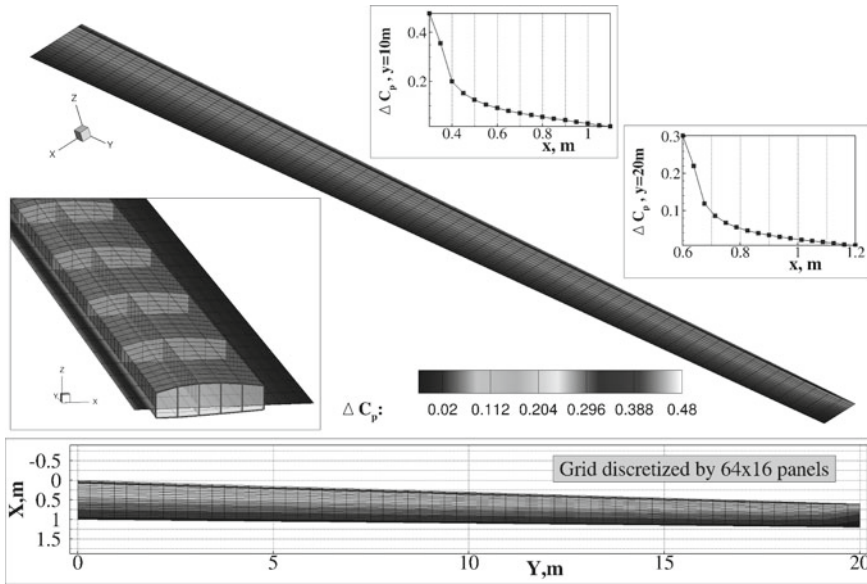
Fig. 17.7 Vortex Lattice aerodynamic model of the wingbox with ΔC_p distribution (dynamic pressure = 3750 Pa, AoA = 1°)

16 chordwise panels. Its aspect ratio is 25. All FE nodes were used to calculate a coupling matrix for force transfer and deformation interpolation.

Aeroelastic results for validation of the method were calculated using Nastran SOL144. A wing having the same geometry and equal panel discretization as the VL-grid was built for Nastran. For the transfer of forces and the interpolation of displacements, a *SPLINE1* method was used. Because Nastran uses a vortex-lattice method for static aeroelasticity and also the spline definitions are similar for both methods, the results are expected to be identical in the linear regime (small deformations). The VL model and a sample aerodynamic solution in terms of the pressure coefficient difference is presented in Fig. 17.7.

The first aeroelastic comparison is shown in Fig. 17.8 in terms of deformations as function of the root angle of attack. Both the VL and the Nastran (SOL144) solution are based on incompressible aerodynamics (the Mach number in Nastran is therefore set to zero in the corresponding aerodynamic card). The dynamic pressure is 3750 Pa. Both the Nastran and the VL solution in combination with a linear structural solution show comparable results – if not exactly the same – for all root angles of attack. The difference is most likely to come from the solution process itself. The VL aeroelastic solution is a static coupling process in which aerodynamic forces and structural deformations are converged iteratively. However, two effects are involved that act against each other. First, the increase in the panel area due to the linear structural solution, shown in Fig. 17.9, and second, the tilting of the aerodynamic lifting forces which results in a component in the y direction. The deformations of
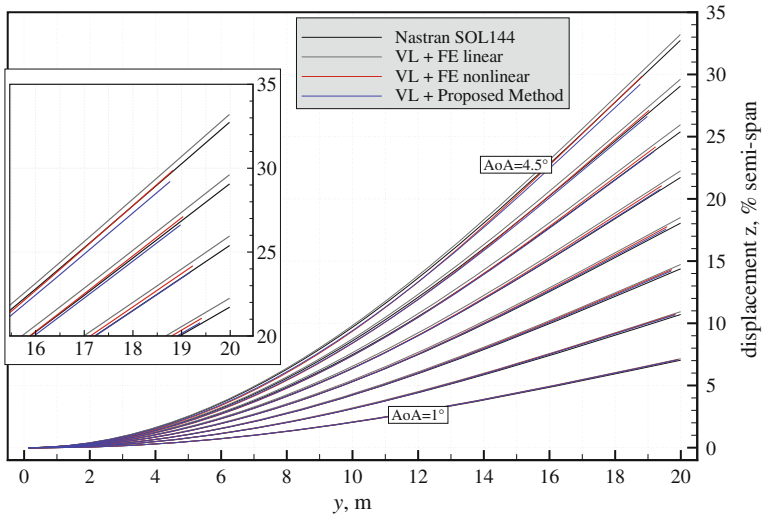
Fig. 17.8 Comparison of aeroelastic (static coupling) results from different methods
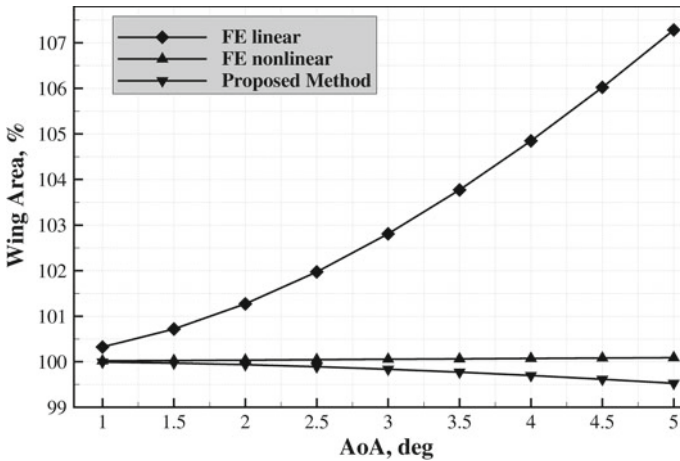
Fig. 17.9 Changes in the aerodynamic grid's surface area due to structural deformations

the nonlinear solution, which were obtained by static coupling of the VL solver with Nastran's SOL400 sequence, and the deformations of the proposed method show good agreement. Differences become significant starting at tip deflections of about 25%.

   Structural loads will be discussed in addition to deformations. This will answer the question of how deformations influence structural loads. Therefore, the forces and moments at the wing root with components in x, y, and z directions are compared as function of the angle of attack at the wing root, as shown in Figs. 17.10 and 17.11.

Fig. 17.10 Summed forces in x, y, and z directions at the wing root as function of the angle of attack
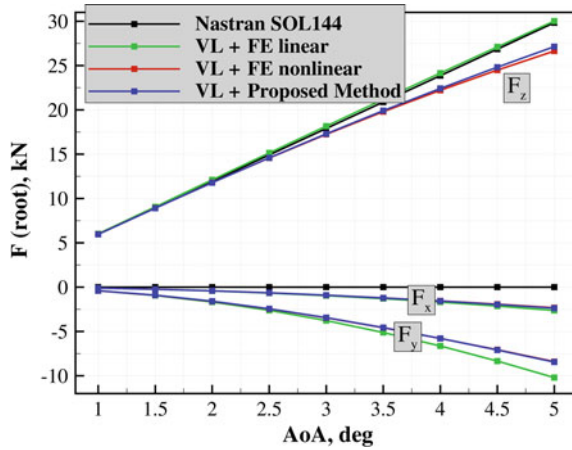
Fig. 17.11 Moments around the x, y, and z axes at the wing root as function of the angle of attack
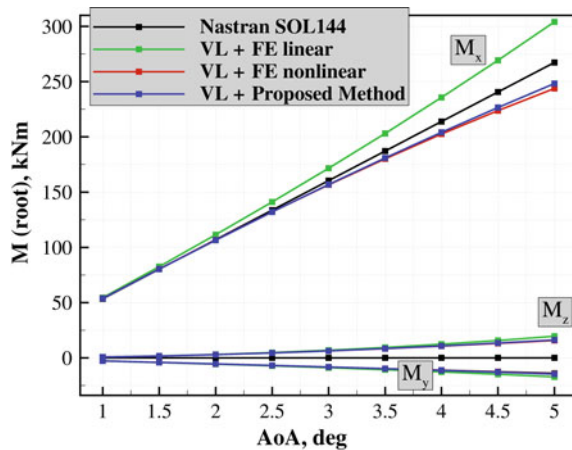
Large differences between the two linear and the two nonlinear solutions are obtained for the shear force F_z at the wing root. The proposed method is in fair agreement with the nonlinear reference solution, although it yields slightly higher loads (which can be seen as conservative, though). The Nastran SOL144 results have no force components in the x and the y directions due to the simplified calculation of the aerodynamic forces. The VL solution calculates the induced drag, though. The loads F_x agree between the three VL solutions, but forces from the VL and linear FE solution in the y direction show large difference. This can be explained with the increase in the surface area, as was shown in Fig. 17.9. As expected, good agreement is obtained between the moments at the wing root around the y and the z axes. It must be mentioned that F_x is negative and thus M_z is positive because in the body fixed system, the lift force has a (positive) component in x direction. The moment around the y axis is negative due to the slight sweep back of the wing. Most important

is the comparison of the wing root bending moment M_x. Here, the VL method with the linear structural solution yields a much higher bending moment compared to the nonlinear and even to the Nastran solution. The tilting of the aerodynamic force vectors, as is considered by the VL solution, keeps them perpendicular to the wing's panels and thus leads to higher bending moments along the wing span and at the root. However, the increase in panel area additionally increases this bending moment. The aerodynamic forces from the Nastran solution only have a component in the z direction, thus the bending moment M_x is decreased even in the case that the panel area is increased. The bending moment from the nonlinear Nastran solution and the proposed method are in fair agreement, but again the enhanced modal approach yields larger values. The most important conclusion from the loads point of view is that an aerodynamically nonlinear solution in terms of displacements (such as the one obtained from the VL method) should not be combined with a linear structural solution. This overestimates the bending moment M_x, as discussed above.

17.3.4   *Dynamic Aeroelastic Simulations and Validation with Nastran Results*

Results and comparisons of different dynamic solution methods are presented in the following. Unsteadiness is introduced by means of unsteady boundary conditions, in this case by a vertical disturbance velocity that superimposes the steady uniform flow field.

The first unsteady test case consists of a 1-cos type gust encounter. The wing is initially at rest, i.e., no steady state deformation is used as initial condition. This is realized in the unsteady VL solution by simply setting the angle of attack to zero degree (the wing's airfoil is uncambered). The uniform flow velocity is set to 50 m/s, the gust disturbance velocity is 14 m/s, and the gust gradient 14 m. The unsteady version of the VL solver, named UVL in the following, uses a wake-stepping method to account for the unsteady circulation on body and wake panels [2]. An implicit BDF scheme is applied to march the coupled solution forward in time. The timestepsize for all unsteady simulations was set to 0.001 s, this value was found to be sufficiently small for a good resolution of the gust in terms of the aerodynamic forces. No stall or other viscous effects are modeled in the UVL solver. The maximum of the time dependent angle of attack during the gust encounter reaches rather high values due to the high gust velocities (which had to be chosen to excite large deformations). This would eventually lead to flow separation from an aerodynamic point of view, but this effect is neglected here. Unsteady reference solutions were obtained by Nastran's SOL146 sequence. This frequency domain method allows the specification of gusts with prescribed disturbance velocities and gust gradients. An inverse Fourier transformation (IFFT) is applied to the frequency domain results within Nastran to obtain time domain results such as displacements of structural nodes.
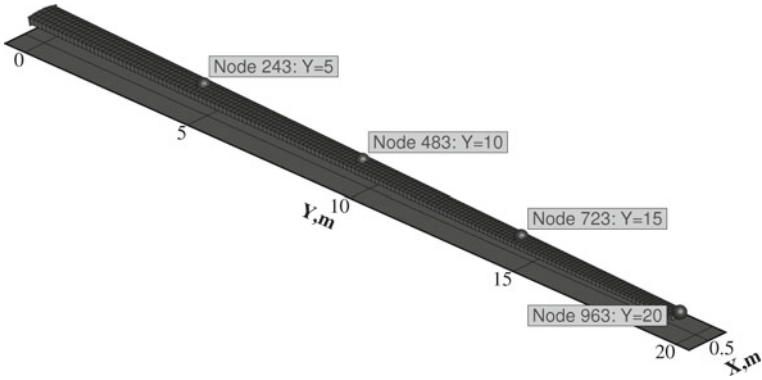
Fig. 17.12 Points on the upper surface of the wing for which time dependent displacements will be presented
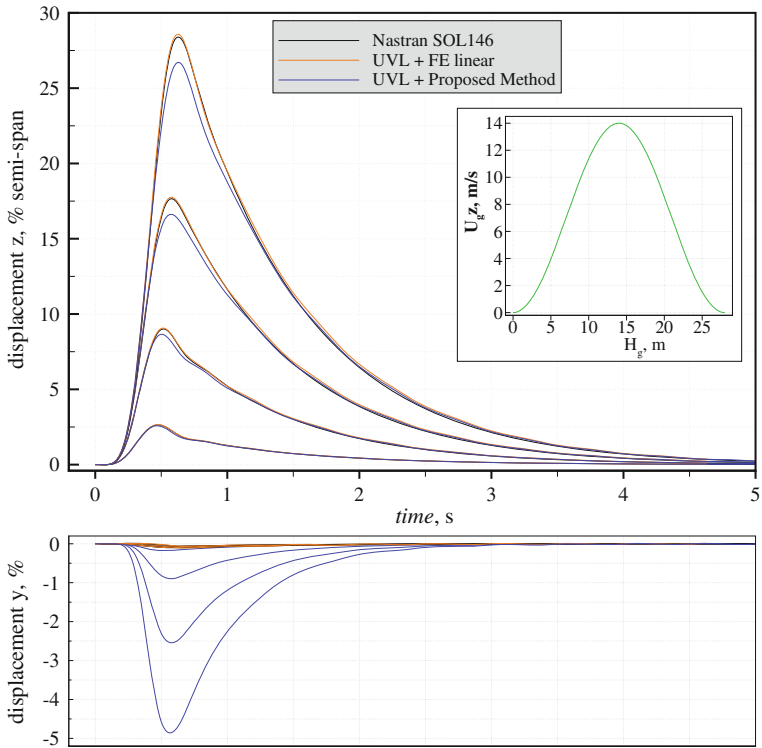
Fig. 17.13 Displacements of four structural nodes as function of time for *1-cos* gust encounter. Disturbance velocity is 4 m/s, gust gradient 14 m
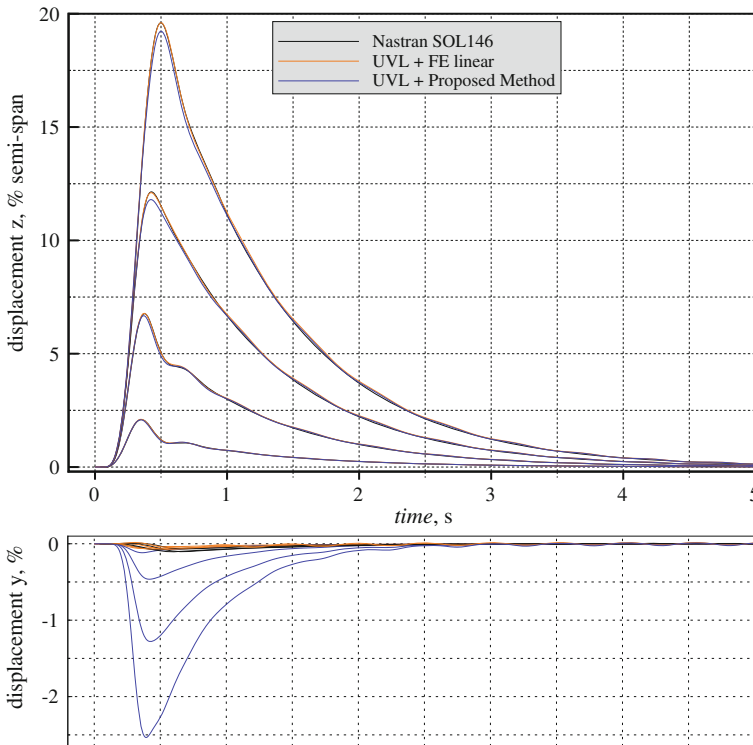
Fig. 17.14 Displacements of four structural nodes as function of time for *1-cos* type gust encounter. Disturbance velocity is 14 m/s, gust gradient 9 m

The results of three different methods (Nastran SOL146, UVL and FE linear, as well as UVL and proposed method) are compared in terms of time dependent displacements of four selected structural nodes. These nodes are located at y = 5, 10, 15, and 20 m on the upper surface of the wing, as is shown in Fig. 17.12. Unfortunately, no fully nonlinear results are available for this comparison. It is intended to couple the UVL solver to Nastran SOL400 in the future. Results of the first unsteady test case are presented in Fig. 17.13. As can be seen, the Nastran and the linear UVL with the linear structural solution are in good agreement, with slightly higher deformations in the *z* direction for the UVL results (similar as for the static coupling results). The motion of the wing is dominated by low frequency structural modes in this case. The proposed method shows smaller deformations in the *z* direction and yields displacements in the *y* direction, as expected. Deformations of this test case reach almost 30% (linear solutions), the proposed method yields about 26% with respect to the span of the wing. The time dependent motion of the nodes is generally in good agreement among the results of the three methods, besides the differences in the displacements due to the different kinematical relationships.
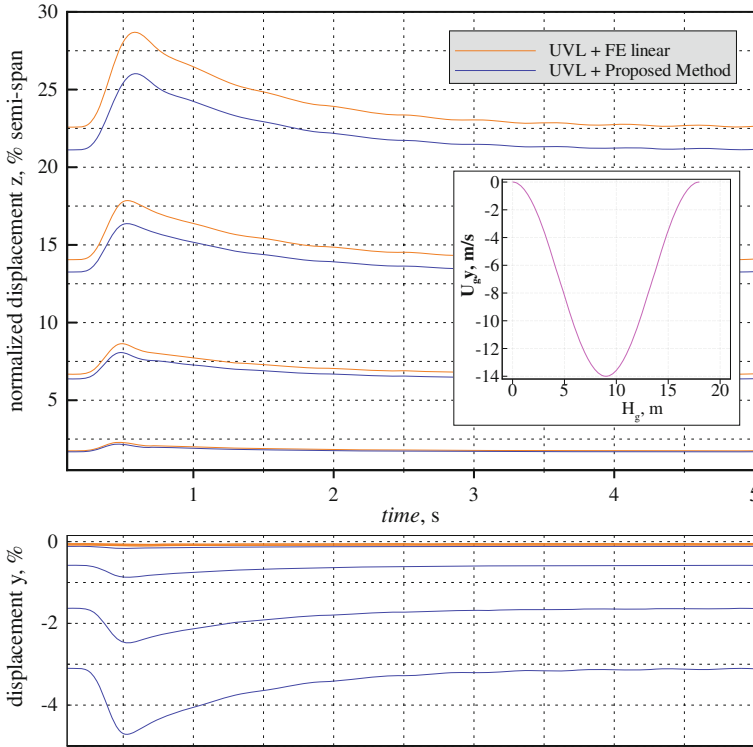
Fig. 17.15 Displacements of four structural nodes as function of time of a lateral *1-cos* type gust encounter. Disturbance velocity is 14 m/s in the negative *y* direction, gust gradient 9 m

The second unsteady test case uses the same vertical gust velocity as before, but the gust gradient is reduced to 9 m. The goal is to excite higher frequency components, the results are shown in Fig. 17.14. Deformations are reduced in this test case (as expected), the maximum tip deflection is close to 20% of the span. The differences between the linear solutions are very small, and the proposed method yields slightly less displacements in the *z* direction, but accounts for the foreshortening effect.

Another test case to demonstrate the power of the proposed method is the simulation of a lateral gust where the gust disturbance velocity acts in the negative *y* direction. This test case is comparable to the steady structural test case in which the force field originally along the *z* direction has been tilted to get components in the *y* direction, cf. Fig. 17.6. The gust of the next test case is again of 1-cos shape, its velocity is 14 m/s in the negative *y* direction, the gust gradient is 9 m. Unfortunately, no reference solution from Nastran is available for this test case, since the wing has no dihedral in the unloaded state and a steady trim solution is not considered in the unsteady solution sequence. The VL solution starts from an initial trim solution which was generated by setting the angle of attack to a certain value. This trim solution serves as initial condition for the unsteady solutions (linear and nonlinear),

and because the wing now has a surface projection in the y direction, the lateral gust acts on the displaced panels and excites aerodynamic forces, mainly in the y direction. Figure 17.15 shows the results of the UVL solver coupled with the linear and the enhanced modal approach solutions. Here, the deformations are increased because the additional gust load leads to higher lifting forces on the wing. Again, the displacements in the y direction are captured by the enhanced modal approach solution only.

17.4 Conclusion and Outlook

A method was presented that enhances the classical modal approach used in aeroelastic applications towards large geometric deformations. Nonlinearities both in the force-displacement relationships and in the geometrically nonlinear deformation field are accounted for by including terms of higher order for the stiffness and the reconstruction of the displacement field. Based on these terms, nonlinear static and dynamic governing equations are obtained where the generalized stiffnesses are depending on the forces applied to the structure. It was proved that the quadratic component of the higher order modes are needed to account for in-plane loadings, which are present in typical aerodynamic force fields when lifting panels are heavily rotated. In this work, the method was successfully applied to a complex wingbox made from composite shell elements. Static and dynamic results showed that the proposed method can acceptably reflect the geometrically nonlinear deformation field at large deformations up to values of approximately 25% of the wing's semi-span. However, also the linear FE solutions showed good results for deformations up to about 10% tip displacement for the test cases presented. From the structural loads point of view, it was shown that geometrically nonlinear aerodynamic methods (such as the VL method) should not be combined with a linear structural solution in the regime of large deformations. Bending moments will be heavily overestimated. The next step for the improvement and validation of the method proposed is the static and dynamic modeling of the complex jet transport aircraft wingbox shown in Fig. 17.1.

References

1. C.E.S. Cesnik, R. Palacios, E.Y. Reichenbach, Reexamined structural design procedures for very flexible aircraft. J. Aircr. **51**(5), 1580–1591 (2014)
2. J. Katz, A. Plotkin, *Low-Speed Aerodynamics*, Cambridge Aerospace Series (Cambridge University Press, Cambridge, 2001)

3. K. Kim, A.G. Radu, X.Q. Wang, M.P. Mignolet, Nonlinear reduced order modeling of isotropic and functionally graded plates. Int. J. Non-Linear Mech. **49**, 100–110 (2013)

4. T. Klimmek, Parameterization of topology and geometry for the multidisciplinary optimization of wing structures, in *Proceedings CEAS, CEAS 2009 - European Air and Space Conference* (Manchester, United Kingdom, 2009), p. 2009

5. R.J. Kuether, M.S. Allen, Nonlinear modal substructuring of systems with geometric nonlinearities, in *54th AIAA/ASME/ASCE/AHS/ASC Structures, Structural Dynamics, and Materials Conference* (Boston, Massachusetts, 2013)

6. R.J. Kuether, M.S. Allen, Substructuring with nonlinear reduced order models and interface reduction with characteristic constraint modes, in *AIAA SciTech. 55th AIAA/ASME/ASCE/AHS/ASC Structures, Structural Dynamics, and Materials Conference* (National Harbor, Maryland, 2014)

7. M.P. Mignolet, A. Przekop, S.A. Rizzi, S.M. Spottswood, A review of indirect/non-intrusive reduced order modeling of nonlinear geometric structures. J. Sound Vib. **332**(10), 2437–2460 (2013)

8. M. Ritter, C.E.S. Cesnik, W.R. Krüger, An enhanced modal approach for large deformation modeling of wing-like structures, in *AIAA SciTech. 56th AIAA/ASME/ASCE/AHS/ASC Structures, Structural Dynamics, and Materials Conference* (Kissimmee, Florida, 2015)

9. D.J. Segalman, C.R. Dohrmann, *Dynamics of Rotating Flexible Structures by a Method of Quadratic Modes* (Sandia National Laboratories, Structural Dynamics Division, Albuquerque, New Mexico, 1990)

10. D.J. Segalman, C.R. Dohrmann, A method for calculating the dynamics of rotating flexible structures, part1: derivation. ASME J. Vib. Acoust. **118**, 313–317 (1996)

11. I.H. Shames, C.L. Dym, *Energy and Finite Element Methods in Structural Mechanics* (Hemisphere Publishing Corporation, New York, 1985)

12. W. Su, C.E.S. Cesnik, Strain-based analysis for geometrically nonlinear beams: a modal approach, in *53rd AIAA/ASME/ASCE/AHS/ASC Structures, Structural Dynamics and Materials Conference* (Honolulu, Hawaii, 2013)

13. L.H. van Zyl, E.H. Mathews, Quadratic mode shape components from linear finite element analysis. ASME J. Vib. Acoust. **134** (2012)

14. L.H. van Zyl, A.N. Sutherland, P.S. Rossouw, *Parabolic mode shapes: What they are, where to get them and what to do with them* (International Forum on Aeroelasticity and Structural Dynamics, Seattle, Washington, 2009)

15. X.Q. Wang, R.A. Perez, M.P. Mignolet, Nonlinear reduced order modeling of complex wing models, in *54th AIAA/ASME/ASCE/AHS/ASC Structures, Structural Dynamics, and Materials Conference* (Boston, Massachusetts, 2013)

Author Index